In situ studies of the growth and oxidation of complex metal oxides by pulsed laser deposition

Chencheng Xu

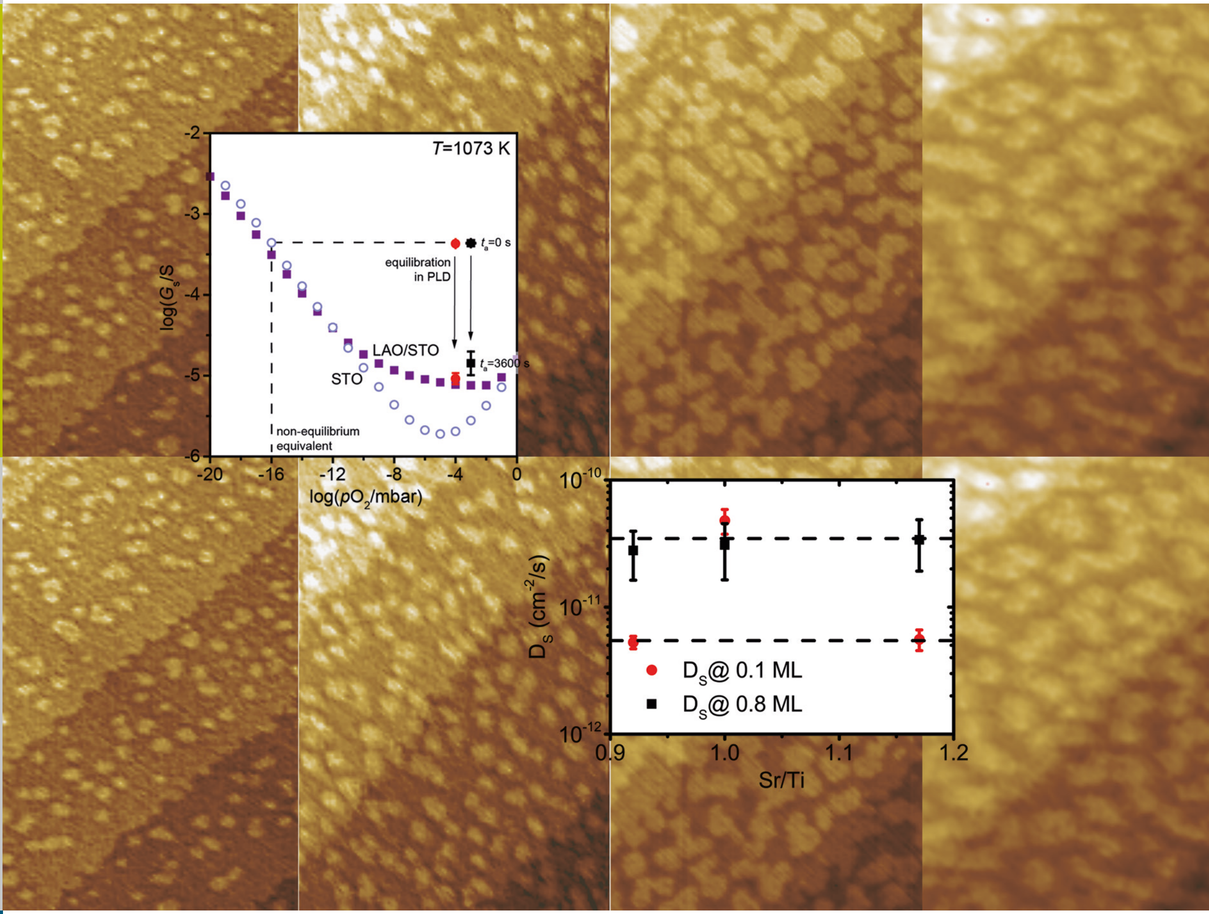

Schlüsseltechnologien /
Key Technologies
Band / Volume 140
ISBN 978-3-95806-204-7

JÜLICH
FORSCHUNGSZENTRUM

Schriften des Forschungszentrums Jülich
Reihe Schlüsseltechnologien / Key Technologies Band / Volume 140

Forschungszentrum Jülich GmbH
Peter Grünberg Institute (PGI)
Electronic Materials (PGI-7)

In situ studies of the growth and oxidation of complex metal oxides by pulsed laser deposition

Chencheng Xu

Schriften des Forschungszentrums Jülich
Reihe Schlüsseltechnologien / Key Technologies Band / Volume 140

ISSN 1866-1807 ISBN 978-3-95806-204-7

Bibliographic information published by the Deutsche Nationalbibliothek.
The Deutsche Nationalbibliothek lists this publication in the Deutsche
Nationalbibliografie; detailed bibliographic data are available in the
Internet at http://dnb.d-nb.de.

Publisher and Distributor: Forschungszentrum Jülich GmbH
Zentralbibliothek
52425 Jülich
Tel: +49 2461 61-5368
Fax: +49 2461 61-6103
Email: zb-publikation@fz-juelich.de
www.fz-juelich.de/zb

Cover Design: Grafische Medien, Forschungszentrum Jülich GmbH

Printer: Grafische Medien, Forschungszentrum Jülich GmbH

Schriften des Forschungszentrums Jülich
Reihe Schlüsseltechnologien / Key Technologies, Band / Volume 140

D 82 (Diss. RWTH Aachen University, 2016)

ISSN 1866-1807
ISBN 978-3-95806-204-7

Zusammenfassung

Pulsed Laser Deposition (PLD) ist ein Abscheidungsverfahren, das sich für die Herstellung von den Dünnschichten und Heterostrukturen aus komplexen Metalloxiden eignet. Der stöchiometrische Transfer zwischen dem Target und dem Substrat erfolgt innerhalb von einem breiten Druckbereich ohne anspruchsvolle Optimierung von Parametern. Infolgedessen dient PLD als das Hauptverfahren für die Herstellung der komplexen Metalloxide Dünnschichten und Heterostrukturen in vielen Laboren.

Trotz der häufigen Verwendung von PLD sind die zugrundlegenden Prozesse während des PLD Wachstums bisher nicht systematisch untersucht worden. Tatsächlich beschränken sich die meisten Forschungsgruppen auf die empirische Parameteroptimierung. Obwohl die Dünnschichteigenschaften auch auf diese Weise optimiert werden können, fehlt ein Verständnis des genauen Zusammenhangs zwischen PLD Wachstum und Dünnschichteigenschaften, das heutzutage immer wichtiger wird. Die zu untersuchenden Aspekte sind spezifisch für die unterschiedlichen Systeme. Das erste Beispiel ist der resistive Speicher (ReRAM) mit komplexen Metalloxiden wie z.B. $SrTiO_3$ (STO) als Dünnschichten, in dem Defekte wie z. B. Kationenleerstellen eine wichtige Rolle spielen. Ein tieferes Verständnis des Schaltverhaltens in solchen Zellen ergibt sich nur dadurch, dass die Bildungsprozesse der Defekte während der PLD Herstellung systematisch untersucht werden. Um die Defektbildung in STO zu verstehen, sind die *in-situ* Beobachtungen dieser Prozesse notwendig. Das zweite Beispiel ist der Bildungsprozess einer leitenden Grenzfläche zwischen zwei Bandisolatoren, z.B. $LaAlO_3$ (LAO) auf $SrTiO_3$ (LAO/STO). Trotz der Entdeckung vor mehr als zehn Jahren ist der Bildungsprozess dieser leitenden Grenzfläche bis heute nicht vollständig verstanden. Der Zeitpunkt zu dem sich die leitende Grenzfläche bildet ist einer der zentralen Fragen. Darüber hinaus kann die Leitfähigkeit von LAO/STO durch Defekte wie Sauerstoffleerstellen beeinflusst sein, die sich durch den Oberflächenaustausch während des Wachstums und Nachglühprozesses ein- und ausbauen lassen.

Diese Arbeit beschreibt die *in-situ* Untersuchung der Bildungsprozesse während der Homoepitaxie von STO. Es konnte gezeigt werden, dass der Grund für die Kationen-Nicht-Stöchiometrie von STO Dünnschichten der bevorzugte Streuungsprozess von Kationen während der Laser-Plume-Ausbreitung ist. Die Dünnschichten von STO mit Kationen-Nicht-Stöchiometrie wachsen im Anfangsstadium im 2D Wachstumsmodus. Die Oberflächendiffusion von STO in diesem Stadium wird verhindert durch die Kationen-Nicht-Stöchiometrie, wobei die Punktdefekte eine Oberflächenspannung erzeugen können. Die Kationen-Nicht-Stöchiometrie führt weiterhin dazu, dass ausgedehnte Defekte generiert werden und der Wachstumsmodus geändert wird. Ein Beispiel dafür ist das Wachstum von Sr reichen STO Schichten, wobei das System zunächst 2D Wachstum innerhalb einer Monolage zeigt und beim weiteren Wachstum ein Terminierungswechsel von TiO_2 nach SrO erfolgt. Anschließend bauen sich Anti-Phasen Grenzen auf und das Wachstum geht langsam in den 3D Wachstumsmodus über.

Der Bildungsprozess einer leitenden Grenzfläche zwischen LAO und STO wurde mit OIRD *in-situ* und *real-time* untersucht, wozu auch die Untersuchung der Ein- und Ausbauprozesse von Sauerstoffleerstellen in LAO/STO Heterostrukturen notwendig waren. Die ersten drei Einheitszellen von LAO verhalten sich dabei anders als die folgenden LAO-Zellen bei den OIRD Messung. Es ergeben sich klare Hinweise darauf, dass der Transfer von Elektronen zu der LAO/STO Grenzfläche während des Wachstums bei Abscheidung der dritten Monolage stattfindet. Der Einbau von Sauerstoffleerstellen findet auch während der PLD-Prozesse statt, wobei der Ausbau von Sauerstoffleerstellen ohne die Einführung von Kationenleerstellen nur während des Nachglühens unter dem Wachstumsdruck und der Wachstumstemperatur möglich ist. Ursächlich für den Einbau der Sauerstoffleerstellen sind Stöße von Partikeln mit hoher kinetischer Energie aus dem Laser-Plume.

Abstract

Pulsed Laser Deposition (PLD) is a versatile deposition technique for complex metal oxide thin films and heterostructures. Without sophisticated parameter engineering, a stoichiometric transfer between target and substrate can take place in a large pressure range of different gas ambient. As a result, PLD is widely applied in many research laboratories.

However, the basic processes during PLD growth are not well understood. Therefore most of the research groups only carry out parameter optimization for PLD empirically. Although the thin film properties can be enhanced by empirical optimization of growth parameters, the exact correlation between PLD growth process and thin film property is hardly known. A better understanding in the correlation between PLD growth and thin film properties is gaining arising attention with its increasing importance for different complex metal oxide based electronics nowadays. The aspects to be investigated are different in various material systems. The first example is the Resistive Random Access Memories (ReRAM) based on complex metal oxides, e.g. $SrTiO_3$ (STO) thin films, where the defects like cation vacancies in thin oxide films play a crucial role for the switching behavior. Only by understanding the defect formation process during the PLD process a rational design of defects in the thin film could be possible. The *in-situ* studies on the defect formation process during STO thin film growth are thus necessary. The second example is the conductive interface between two band insulators, e.g. $LaAlO_3$ (LAO) and STO. Since its discovery one decade ago, the formation process of the conductive interface is not well understood. To understand the physical mechanism behind the conductive interface formation, it is of pivotal importance to learn when the formation takes place. Furthermore, the conductivity of LAO/STO heterostructures are significantly influenced by the defects like oxygen vacancies, which can be incorporated/eliminated both by growth and post-annealing process. So the *in-situ* study on the conductive interface formation and the study on the oxygen vacancy incorporation/elimination process during the growth and annealing process are needed.

In this work the *in-situ* study on the defect formation process during STO homoepitaxy is carried out. The cation non-stoichiometries in STO thin films are introduced by the preferential scattering process during laser plume propagation. STO thin films with cation non-stoichiometry remains at the early growth stage within 2D growth mode. The defects are in this growth stage point defects inhibiting surface diffusion through surface strain. The cation non-stoichiometry leads further to the formation of extended defects as growth proceeds and the growth mode is changed. As an example, the Sr rich STO exhibits firstly 2D growth with subsequent surface termination change from TiO_2 to SrO at low film thickness, whereas the further growth establishes anti-phase boundaries and lead to 3D island growth.

The conductive interface formation process between LAO and STO is studied *in-situ* and *real-time* with Oblique Incidence Reflectance Difference technique (OIRD). In addition, the incorporation and elimination processes of oxygen vacancies in LAO/STO heterostructures are investigated as well. It is observed from the growth process that the first 3 unit cells (u.c.) LAO differ from the rest of LAO unit cells, indicating the electronic transfer happens at 3 u.c. and does not influence the first 3 u.c. LAO. The incorporation of oxygen vacancies into the STO takes place during the PLD growth of LAO, while the elimination of oxygen vacancies in STO is optimal at the growth temperature and pressure. The main reason for the incorporation of oxygen vacancies in STO is the impinging particles with high kinetic energy.

List of Abbreviations

Acronym	**Explanation**
2DEG	Two-Dimensional Electron Gas
AFM	Atomic Force Microscopy
APB	Anti-Phase Boundary
CC	Cold Cathode Gauge
CVD	Chemical Vapor Deposition
EBE	Electron-Beam Evaporation Tool
EOC	Electronic Oxide Cluster
ICCD	Intensified Charge Coupled Device
IMFP	Inelastic Mean Free Path
IR	Infra-Red
LAO	$LaAlO_3$
LEED	Low Energy Electron Diffraction
MBE	Molecular Beam Epitaxy
MS	Mass Spectrometer
OIRD	Oblique Incidence Reflectance Difference
PALS	Positron Annihilation Lifetime Spectroscopy
PLD	Pulsed Laser Deposition
PPMS	Physical Properties Measurement System
ReRAM	Resistive Random Access Memories
RHEED	Reflection High Energy Electron Diffraction
RP	Ruddlesden-Popper
RS	Rock-Salt
sccm	standard cubic centimeters per minute
STO	$SrTiO_3$
SXRD	Surface X-Ray Diffraction
TEM	Transmission Electron Microscopy
TMM	Transfer Matrix Method
u.c.	unit cell
UHV	Ultra-High Vacuum
UV	Ultra-Violet
XPS	X-Ray Photoelectron Spectroscopy
XRD	X-Ray Diffraction

Acknowledgement

This work would not be present without the help and support from many people, to whom I want to express my gratitude.

Firstly, I want to thank Prof. Rainer Waser who gave me the great opportunity to work in the Electronic Oxide Cluster Lab in PGI7 at Forschungszentrum Juelich (FZJ). Great thanks go to Prof. Georg Roth, who agreed to be the doctor father and the first reader of my thesis.

Special thanks to Prof. Regina Dittmann as supervisor of my PhD study and the second reader of my thesis, who has supported my research with fruitful discussions and supervision on the whole research to keep the work in the right track.

For the technical support I would firstly thank Prof. Xiangdong Zhu from UV Davis in USA, and Thomas Seller for establishing the OIRD system and special thanks go to Stephan Masberg for the helpful suggestions by my mechanical construction for improvement of OIRD system.

Secondly I would thank Georg Pickartz who helps a lot by the problem solving in Electronic Oxide Cluster lab. Also special thanks to Dr. Paul Meuffels, Jochen Friedrich, Cerstin Makovicka, Marcel Gerst and René Borowski, who help solve so many technical problems by bringing my theory into experimental reality.

Lots of thanks go to all the fellow in our PLD group. Dr. Sebasitan Wicklein has instructed me in many details for the working with PLD and *in-situ* AFM at the beginning of my PhD time. Without his efforts I would never carry out so many sophisticated experiments on PLD. Dr. Felix Gunkel has given lots of both technical and theoretical suggestions on the LAO/STO system, which help me in great extent. Also great thanks on Dr. Anja Herpers, Dr. Annemarie Koehl and Dr. Christian Lenser who have supported my beginning of PhD time with technical and theoretical support for various aspects. To Nicolas Raab, Christoph Baeumer and Katherina Skaja, who have worked together with me on so many challenging tasks with great efforts although my PhD time, I owe my special thanks. Furthermore, I would like also thank Felix E. Hensling, who was the master student of me and now a new member in the PLD group, for the great support by challenging experiments in the last year of my PhD time.

From the scientific side, I would like to thank Prof. Jan Aarts and A. J. H. van der Torren from University of Leiden in Netherlands for their help on the LEED and LEEM measurements. Thanks for Dr. Hongchu Du, Prof. Chunlin Jia from FZJ and Prof. Joachim Mayer from Central Facility for Electron Microscopy (GFE) in Aachen University, who have supported the STEM measurements in my work. I would also like to thank all the scientists in our institute, with whom I learned so much and improved my views in great extent.

Thanks to Maria Garcia, Michaela Ott and Luise Snyders for the help in administrative questions during my time at the institute.

For the friends who have given so much help in the daily life, I would also thank you on this occasion. Special thanks on my best friends Hehe Zhang, Yizhi Wu and Jizu Zhang, who helped me surviving the daily life that is much more challenging than scientific research for me.

Finally, I would like to thank my father Hongde Xu and my mother Shimei Liang for their steady support, without which I would never keep the courage to face the difficulties during my whole study and the PhD time.

Contents

1 Introduction

Complex metal oxide thin films have complex electronic structures resulting in applications for different fields like ferroelectrics, magneto electronics, optoelectronics, thermoelectronics and novel memory devices. These properties can be strongly dependent on the crystal structure and the particular growth conditions. Moreover, the functional heterostructures with novel interface/surface properties like LAO/STO are also dependent on the fabrication process. To achieve a controlled growth of complex metal oxide thin films, the two most applied growth techniques are molecular beam epitaxy (MBE) [1, 2] and pulsed laser deposition (PLD) [3]. Unlike MBE, which requires sophisticated setups, PLD is capable of fabricating different complex metal oxide thin films like ternary or even quaternary oxides without complex parameter engineering. Therefore PLD is the most widely applied technique in research laboratories for the fabrication of complex metal oxide thin films.

Due to the high potential of PLD for the fabrication of complex metal oxide thin films, different efforts have been taken trying to understand PLD processes, which can be divided into three main parts: the laser-material interaction, which is also called ablation, has been studied by XPS on the ablated target [4]; the plume propagation process has been extensively studied by optical emission spectroscopy and time of flight mass spectrometry [5-7]; the surface diffusion and thin film growth have been studied by RHEED [8, 9] and surface X-ray diffraction (SXRD) [10]. Despite all these works, there are a large amount of questions awaiting answers for the PLD processes. So far most of the groups are employing purely empirical techniques to optimize thin films rather than approaches based on a deeper knowledge of the deposition technique. Within this thesis, we pay attention to the fundamental processes during the thin film growth with different *in-situ* and *real-time* techniques, trying to rationally optimize the PLD process based on the understanding of the basic processes.

The first important aspect is the ***defect formation during the epitaxial PLD growth***, which is important for multiple processes. Two examples are listed in the following:

1) the control of defect concentration in the thin film. Novel electronic devices like resistive memories [11] require not only epitaxial thin films, but thin films with a specific defect concentration. To not only control the epitaxial growth but also control the defect density in the thin film, a more systematic study has to be carried out to understand the fundamental PLD processes that are related to the defect formation. In PLD growth, the cation non-stoichiometry can be tuned by varying the deposition parameters such as laser fluence and oxygen pressure [12]. The cation non-stoichiometry in complex metal oxides is accommodated by different types of defects and thereby strongly influence the crystal structure. These defects can change the dielectric [13], optical [14] and thermal [13] properties of the complex metal oxide thin films. However, the defects accommodation in the thin film can vary as the growth proceeds and is strongly coupled to the growth mode. Therefore the investigation of the growth process of complex metal oxides with respect to the cation non-stoichiometry and the resulting lattice defects is of pivotal importance. In this thesis the

homoepitaxial growth of the model system $SrTiO_3$ was chosen to perform a detailed and systematic study of the growth process and the resulting defect formation process.

2) the control of defects in the heterostructure with a functional interface, e.g. the LAO/STO. The defects can strongly influence the electronic property of this heterostructure [15-17], which indicates the importance of controlling the defects during the PLD growth. For the electrical properties of heterostructures fabricated by PLD, an important aspect is the incorporation of oxygen or oxygen vacancies during the PLD process. Since the oxygen vacancies in some perovskites like STO can strongly influence the conductivity, the processes during the PLD growth related to the generation or elimination of oxygen vacancies can be responsible for the electrical conductivity change. Several possible sources for the change of the oxygen vacancy concentration during PLD can be suggested: the reduction under low oxygen partial pressures and reoxidation under high oxygen partial pressures; the reduction through UV-radiation from the laser plume; and the bombardment by the impinging particles high kinetic energy from laser plume resulting in an oxygen ejection. In this thesis the impact from the listed factors and especially the interplay between each of them are discussed to reach a better control over the PLD process with respect to these factors.

The second important aspect is ***the formation of the functional interface between complex metal oxides*** during the PLD growth. Considering the conductive interface generation between LAO and STO as one example, the conventional method is to study the electrical [18] or optical properties [19] for LAO/STO with different LAO thicknesses *ex-situ*. With these methods, a critical thickness of 4 u.c. LAO has been suggested for a conductive heterostructure. However, it has not been verified if the conductive interface between LAO and STO is formed during the growth process or after the growth process. In this thesis, the *in-situ* and *real-time* OIRD study is carried out to follow the property changed during the growth, trying to identify the formation of the conductive interface.

Outline

The fundamentals of the materials used in this thesis, namely LAO and STO are presented in chapter 2. The description of the different types of defects, the basic aspects of PLD and the current knowledge about LAO/STO heterostructures is also presented in chapter 2.

In chapter 3, the experimental setup for the *in-situ* analysis methods during PLD growth and the characterization methods employed in this thesis are shown. Moreover, a preparation method for well-defined SrO/TiO_2-termination ratios of STO substrates developed with the help of angle dependent XPS is described.

In chapter 4, the discussion on the correlation between defect formation and thin film growth is carried out with the homoepitaxial growth of STO as a model system. Firstly the origin of cation non-stoichiometry and the possible control over cation non-stoichiometry by varying the laser fluence and the oxygen pressure are investigated. Subsequently, the impact of the cation non-stoichiometry on the surface diffusion and island coalescence is studied at an early growth stage. The defect formation processes during the growth of STO is thereafter investigated for the intermediate growth stage. In particular, the formation of anti-phase-boundaries in Sr rich STO is discussed. At the end of this chapter, the growth modes for different cation non-stoichiometries are discussed.

In chapter 5, the transient OIRD signal is investigated during LAO growth on STO. In particular, the influence of the post-annealing process and the growth pressure on the electrical properties of the LAO/STO interface is investigated.

In chapter 6, the redox processes taking place during PLD growth are investigated. The impact of the oxygen pressure on the conductivity of the STO substrates during the annealing processes is firstly discussed. To distinguish between UV-radiation and the particles with high kinetic energy of the LAO laser plume on the STO substrate, the electrical properties of only UV irradiated STO and particle bombarded STO samples are investigated. The interplay between the impinging particles and the defect equilibria expected in thermodynamic equilibrium for the LAO/STO heterostructure is discussed as well.

In chapter 7 the conclusions are drawn and the outlook can be also found in chapter 7.

2 Fundamentals

2.1 Properties of the Materials

2.1.1 $SrTiO_3$

Strontium titanate ($SrTiO_3$) has a cubic perovskite structure with the space group Pm-3m. The lattice constant c_0 of one cubic unit cell is 0.3905 nm at room temperature. Figure 2.1 shows the unit cell of $SrTiO_3$. The Ti atom is in the center of the cubic structure. The corners consist of Sr-atoms. The oxygen atoms are accommodated on the 6 faces of the cubic structure, which form an octahedral structure with the Ti atom in the center. In the [001] direction, the $SrTiO_3$ can be interpreted as a stacking of neutral SrO and TiO_2 layers.

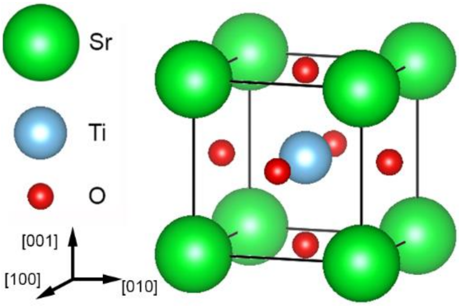

Figure 2.1 *The structure of STO drawn with the help of VESTA program. The principle of VESTA can be found in ref. [20].*

2.1.2 $LaAlO_3$

Lanthanum aluminate ($LaAlO_3$) has a rhombohedral crystal structure at room temperature with the space group R-3c. The structure is similar to the cubic perovskite structure, where only the octahedral of AlO_6 is slightly rotated [21]. Hence the crystal structure of LAO at room temperature can be treated as a pseudo cubic perovskites structure with $c_0 = 0.3789$ nm. At 810 K, a transition from rhombohedral to cubic Pm-3m [21] takes place. In the [001] direction, $LaAlO_3$ can be interpreted as stacks of $(LaO)^+$ and $(AlO_2)^-$ in a simple ionic picture. The charges in the layers derive from the valence states of the La^{3+}, Al^{3+} and O^{2-} ions. As there is only a small deviation from the perovskite structure of STO the crystal structure of LAO unit cells is not shown here.

2.2 Defects in $SrTiO_3$

According to their dimension defects can be divided into four types: (1) zero dimensional defects (0D) like point defects. (2) one dimensional defects (1D), like dislocations, (3) two dimensional defects (2D), like grain boundaries, antiphase boundaries or domain boundaries. (4) three dimensional defects (3D), like segregations and defect clusters. The 1D, 2D and 3D defects are also called extended defects. All these different defects have a strong impact on the properties of the complex metal oxide. In the following the basics for the possible defects in STO will be illustrated with respect to their dimensionality, namely the point defects and the extended defects. The 3D defects are not to be discussed here since they are of minor relevance for this work.

2.2.1 Point defects in STO

Point defects are either interstitials or vacancies. If an atom leaves the ordinary lattice site to arrive at an interstitial site, the resulting defect is called Frenkel pair. If two atoms with opposite charges leave the lattice at the same time, it is called Schottky pair. For the dense packing of atoms in the perovskite of the space group Pm-3m, the Schottky pair is energetically more favored. Point defects are differently charged with respect to the lattice in ABO_3 perovskites and can be described in the so called Kröger-Vink notation. As an example, in undoped STO possible point defects are negatively charged cation vacancies, e.g. Sr vacancies (V_{Sr}'') and Ti vacancies (V_{Ti}'''') and positively charged anion vacancies as oxygen vacancies ($V_O^{\bullet\bullet}$).

Combining the charge neutrality, mass conservation and law of mass action of chemical reactions, the defect chemistry model can predict to a large extent the defect generation and annihilation of specific defect types at a given temperature and oxygen partial pressure [22, 23]. Therefore the defect concentration for each type can be predicted by this model. More importantly, the electronic charge carrier concentration can be determined, as the charge carriers are generated by different defect reactions. Thus the electronic conductivity of the complex metal oxide is determined.

For temperatures lower than approximately 450 °C, all ions are immobile and reactions involving ion motion can be neglected in STO. Only electronic processes are possible like the generation of electron-hole pairs and ionization of already existing neutral vacancies. Electrons and holes are generated at thermodynamic equilibrium as:

$$e^- + h^\bullet \leftrightarrow 0 \tag{2.1}$$

, where the electron- and hole concentration (n and p, respectively) follow the law of mass action:

$$n \cdot p = N_n(T) N_p(T) \exp(-\frac{E_{g_0} - ßT}{k_B T}) \,. \tag{2.2}$$

N_n(T) and N_p(T) are the density of states in the conduction band and valence band at a given temperature T in Kelvin, respectively. E_{g0} is the band gap of STO at 0 K and $ß$ is the factor describing the decrease of the

STO band gap upon temperature increase. k_B is the Boltzmann constant. The factors $N_n(T)$, $N_p(T)$, E_{g0} and *ß* are studied in great detail in ref. [24].

For temperature between 450 °C and 950 °C, the oxygen ions are mobile while the cations stay immobile. At high oxygen partial pressure the STO lattice is oxidized as following:

$$V_O^{\bullet\bullet} + \frac{1}{2} O_2 \rightarrow O_O^x + 2h^\bullet \tag{2.3}$$

, where the oxygen atoms are incorporated into STO lattice with a simultaneous generation of holes. The relation between concentrations of different species follow the law of mass action:

$$\frac{p^2}{(pO_2)^{\frac{1}{2}} \left[V_O^{\bullet\bullet}\right]} = K_0^{ox} \exp\left(-\frac{\Delta H^{ox}}{k_B T}\right) \tag{2.4}$$

, where the p is the hole concentration, pO_2 the oxygen partial pressure, $[V_O^{\bullet\bullet}]$ the concentration of oxygen vacancies, K_0^{ox} the temperature independent reaction constant and ΔH^{ox} the oxidation enthalpy.
At low oxygen partial pressure the STO lattice is reduced as following:

$$O_O^x \leftrightarrow V_O^{\bullet\bullet} + \frac{1}{2} O_2 + 2e^- \tag{2.5}$$

, where the oxygen atoms leave the lattice and the oxygen vacancies and electrons are generated in the lattice.

The concentration of different species follows the law of mass action as well:

$$n^2 \cdot (pO_2)^{\frac{1}{2}} \cdot \left[V_O^{\bullet\bullet}\right] = K_0^{red} \exp\left(-\frac{\Delta H^{red}}{k_B T}\right) \tag{2.6}$$

, where K_0^{red} is the temperature independent reaction constant and ΔH^{red} is the reduction enthalpy.

At temperatures higher than 950 °C, both anions and cations are mobile and cation vacancies can be generated. This simultaneous generation of cation and anion vacancies generates Schottky defects and is called Schottky equilibrium. More specifically, since the formation energy of Ti vacancies is rather high [25, 26] only Sr vacancies form in the SrO sublattice, which leads to a partial Schottky reaction:

$$Sr_{Sr}^x + O_O^x \rightarrow V_{Sr}'' + V_O^{\bullet\bullet} + (SrO)_{sp}\ . \tag{2.7}$$

The secondary phase $(SrO)_{sp}$ will form either on the surface as segregation [27, 28] or in the bulk of STO as Ruddlesden-Popper-type defects [29], which will be discussed in detail as 2D defects in the following.

The excess of Sr atoms in the lattice will drive the reaction towards the product direction, which will be discussed in chapter 4.

The equilibrium concentration of defects in STO is also strongly dependent on the pO_2. We take acceptor ($A^{\bullet}$) doped STO as an example (Figure 2.2). For the temperature regimes with active (> 950 °C) and inactive Schottky equilibrium (450 °C < T < 950 °C) the defect concentrations are different, whereas the charge carrier density (*n* or *p*) behaves the same for both situations.

If the Schottky equilibrium is not activated, at ***low oxygen pressures***, the oxygen vacancy concentration is much higher than the acceptor concentration. Thus the positive charge from the oxygen vacancies can only be compensated by ***electrons***, thus the increase of oxygen pressure reduces the electron density. This is called ***intrinsic compensation*** (the left region in Figure 2.2 (a)). For an ***increased oxygen partial pressure***, where the oxygen vacancies can be compensated by ***acceptors***, the increase of oxygen pressure increases the hole concentration and decreases the electron concentration. This is called ***extrinsic compensation*** and can be divided into n-type and p-type according to the majority of charge carriers (the middle and right region in Figure 2.2 (a)).

If the Schottky equilibrium is activated, Sr vacancies will follow the oxygen vacancy concentration: starting at low oxygen pressures, the increase of the oxygen pressure decreases the oxygen vacancy concentration and increases the Sr vacancy concentration, while for high oxygen pressures the Sr vacancy concentration is constant as is the oxygen vacancy concentration. However, the Sr vacancy concentration is not involved in the electron or hole generation process and thus does not influence the concentration of electrons and holes at all. Thus the pressure dependence of the *n* and *p* concentration is identical for an active and inactive Schottky equilibrium.

The conductivity is summarized in Figure 2.2 (b). The electronic conductivity of STO is expressed as:

$$\sigma_{el} = ne\mu_n + pe\mu_p \tag{2.8}$$

, where *n* and *p* are electron and hole concentrations, respectively. μ_n and μ_p are the electron and hole mobility, respectively. The electron and hole concentrations are both exponentially dependent on the temperature at given pressure (Equation (2.4) and (2.6)), while the electron and hole mobility follow the power law [24, 30]. Therefore the total conductivity is mainly dependent on the electron and hole concentration rather than their mobility.

Figure 2.2 (b) shows that the pO_2 increase firstly reduces the total conductivity since the majority charge carrier electrons decrease and the holes increase. The further increase of the oxygen pressure results in an increase of conductivity, where the holes are the majority of charge carriers. A detailed discussion and quantitative description of the pO_2 dependence of the conductivity in STO can be found in ref. [31].

Point defects in complex metal oxides can not only change the electronic but also the lattice properties. One example is the lattice expansion caused by cation vacancies. As illustrated by Ohnishi et. al [12, 32], if STO thin films with cation vacancies are grown epitaxially on STO substrates, the in-plane lattice in *a*- and *b*-direction of the thin film is strained and only the out-of-plane lattice in *c*-direction is expanded. The explanation for this effect is the electrostatic repulsion between the negatively charged cation vacancies and the anions (Figure 2.3). Thus this *c*-lattice expansion (Δc) can be solely attributed to the cation vacancies in STO and is used in this work for the estimation of the concentration of cation vacancies in the epitaxial STO thin film on STO. The experimental steps for the determination of the *c*-lattice expansion will be illustrated in chapter 3.

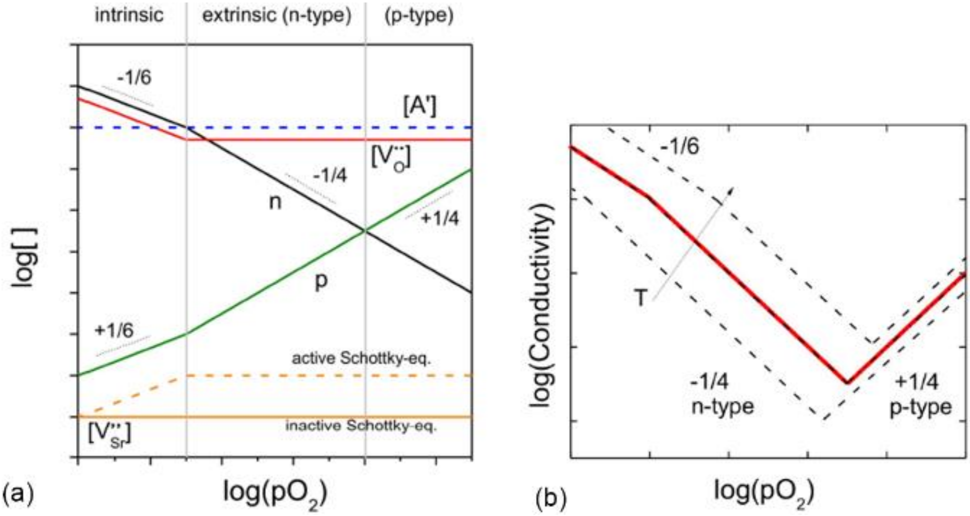

Figure 2.2 *(a) Defect concentration of acceptor doped STO at equilibrium for different oxygen partial pressure. (b) The corresponding conductivity for different oxygen partial pressure. The two pictures are adapted from ref. [31].*

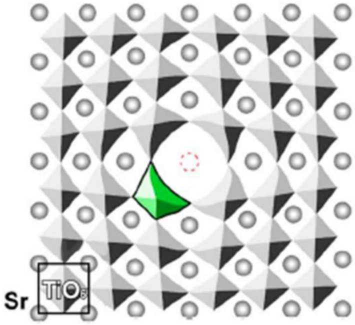

Figure 2.3 *The lattice expansion from the Sr vacancies in STO. Adapted from ref. [32]. The figure is modified.*

2.2.2 1D Dislocations in STO

The representative 1D defects are dislocations including edge dislocation and screw dislocation. Both edge dislocations and screw dislocations have been identified with high resolution TEM [33, 34] as shown in Figure 2.4 together with the corresponding model. The edge dislocation shows a Burgers vector in *a*[001] direction, which is perpendicular to the dislocation core (Figure 2.4 (a)), whereas the screw dislocation shows a Burgers vector in *c*[001] direction that is parallel to the dislocation core (Figure 2.4 (b)).

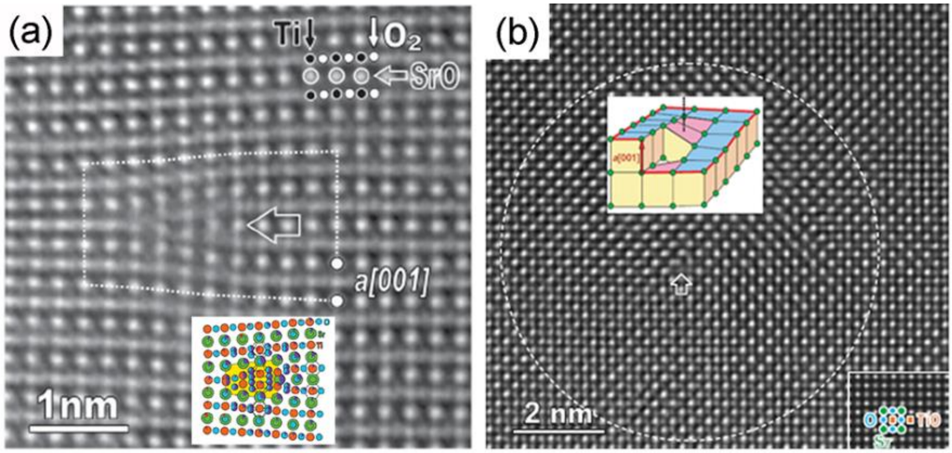

Figure 2.4 *The TEM pictures for (a) an edge dislocation in STO (adapted from ref. [34]) and (b) a screw dislocation in STO (adapted from ref. [33]). The corresponding models to interpret the data are given in the inset.*

2.2.3 2D defects

The most famous and interesting 2D defect in STO is the Ruddlesden-Popper-type defect (RP fault) in STO, since RP fault can strongly influence the STO properties like the thermoelectric properties [35, 36], optical properties [14] and ionic transport properties [37].

The RP fault is different from Ruddlesden-Popper phase (RP phase) of $SrO(SrTiO_3)_n$ [29]. For the RP phase the STO unit cell's translation symmetry is changed with a SrO intercalation after each n STO unit cells in the form of …$(SrTiO_3)_nSrO(SrTiO_3)_n$…. Thus the $SrO(STO)_n$ acts as the new unit cell. The most frequently observed RP phase is in the powder form [38], which can also be produced by MBE growth [39] or PLD [40]. As a simple case of n = 2, a model for the RP phase is illustrated in Figure 2.5 (a). We see a rock salt structure of a SrO double layer formed between two STO unit cells. The lattice vector between two SrO layers is 1/2 $[0\text{-}11]_{RS}$ for the rock salt structure. The subscript RS by 1/2 $[0\text{-}11]_{RS}$ means rock salt.

If the structure of $SrO(STO)_n$ is not periodically reproduced, the rock salt SrO double layer separates only locally two regions of STO with a half Sr-O-Sr bond length shift between both regions. This type of defect is RP fault. As a consequence of the half unit cell shift the SrO from the left region faces the TiO_2 from the right region (Figure 2.5 (b)). Taking the periodicity of one unit cell STO into consideration, this shift is the half period. Thus this boundary formed by the SrO double layer is called anti-phase boundary (APB). It has been observed for Sr rich STO thin films deposited by PLD growth [41].

Although it has been observed for both MBE [14, 42] and PLD [40, 43] that the Sr excess in STO leads to formation of SrO excess layers and the RP phase or APBs, however, the formation process has not been fully understood so far. The study of the formation process of APBs is carried out in chapter 4.

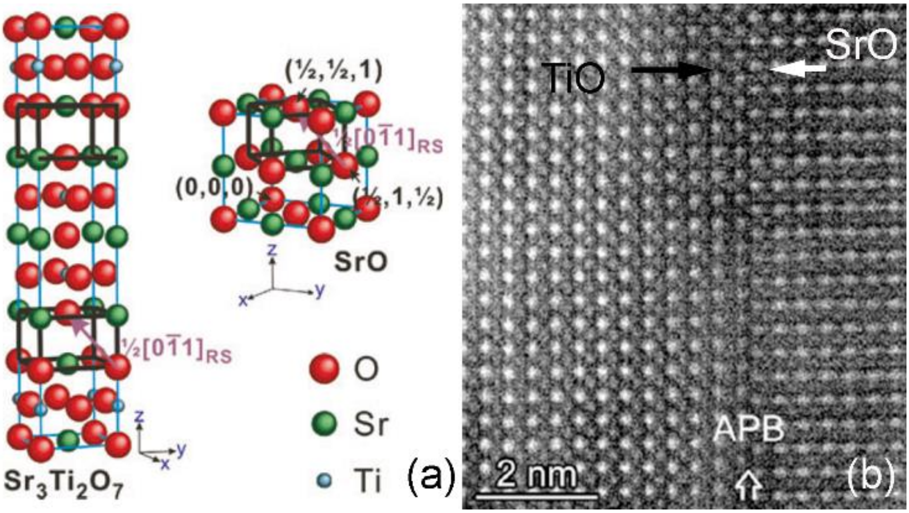

Figure 2.5 *(a) Sketch for Ruddlesden-Popper phase with n = 2 for $Sr_{n+1}Ti_nO_{3n+1}$. The graph is adapted from ref. [38]. (b) A TEM image for Ruddlesden-Popper fault and anti-phase boundary in PLD grown Sr rich STO film. The graph is adapted from ref. [41].*

2.3 Basic processes during PLD growth

As a physical vapor deposition technique, PLD can be applied to many material systems. The most significant advantages are the wide range of applicable gas pressure, the small target size and the nearly stoichiometric transfer within an easily located growth window. In Figure 2.6, a representative illustration of the PLD process is shown. We can see that the PLD process can be divided into three subsequent processes: the ***ablation and plume generation*** within the nanosecond (ns) regime; the ***plume propagation*** process within the microsecond (μs) regime; and the ***surface diffusion and thin film growth*** within the second (s) regime. These three processes will be discussed in the following for homoepitaxial STO growth.

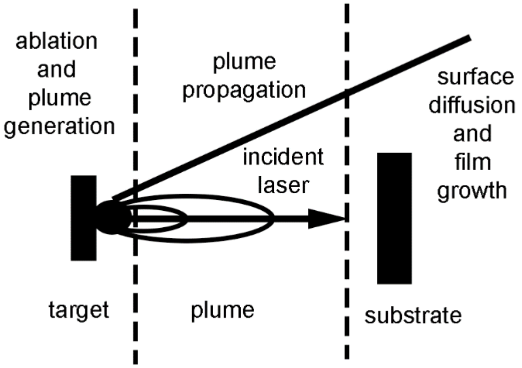

__Figure 2.6__ The working principle of PLD. Three different processes are spatially and temporally separated. For details see the text.

2.3.1 Ablation process and plume generation

The ablation process is the process of releasing materials in the form of atoms, ions and electrons through laser radiation on the target surface. To investigate the ablation process, we have to consider the interaction between photons, atoms and electrons, where the time scale for the interaction processes is important. The electron cooling time (τ_e) is much smaller than the lattice heating time (τ_i) [44], which are both in the range of picoseconds. The electron cooling time is the time for transferring kinetic energy between electrons by collisions till equilibrium, whereas the lattice heating time is the time for the phonons to arrive at equilibrium. The laser duration time (τ_L) has to be compared with both. As for the ns laser duration, it is longer than both, the electron cooling time and the lattice heating time. The processes have to be considered in three time regimes: femtosecond (*f*s), picosecond (*p*s) and nanosecond (*n*s) regime.

In the *f*s regime, only photon induced electronic absorption or electronic excitation can take place, while the thermal conduction can be neglected in this time regime. Once the electrons in the valence band absorb enough energy to jump into the conduction band, they can further increase their kinetic energy and ionize atoms at impact, introducing ***photoionization***. We discuss three possible photoionization processes in two oxide materials used in this work as an example. For photon energies higher than the direct band gap of the material, for example the Kr-F laser (hv ~ 5 eV) on the $SrTiO_3$ single crystal ($E_{g,direct}$ ~ 3.2 eV), the direct ***interband transition*** triggered by the photon energy leads to the formation of an electron-hole plasma with a lifetime in the range of fs. (Figure 2.7 (a)). For photon energies lower than or equal to the band gap, e.g. Kr-F laser on the $LaAlO_3$ single crystal ($E_{g,direct}$ ~ 5 eV), ***multi -photon ionization*** (Figure 2.7 (b)) is activated through the high photon intensity, where the efficiency of ionization is lower than the interband absorption. During the multiphoton ionization with high enough photon intensity, an electron in ground state can absorb enough energy from multiple simultaneously coming photons and arrive an excited state. For crystals with defects on the surface or bulk, ***the ionization via defect energy levels*** is also significant (Figure 2.7 (c)).

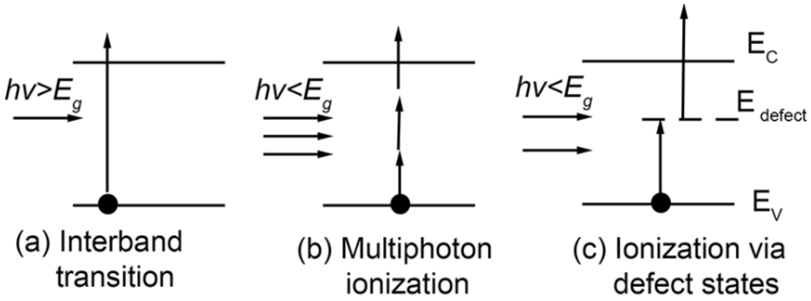

Figure 2.7 *The three mechanisms of photoionization: (a) the interband transition, (b) the multiphoton ionization and (c) the ionization via defect states. The black spot represents the electron, while the horizontal lines represent the conduction band (E_C), valence band (E_V) and defect levels (E_{defect}). The horizontal arrows represent the density of the incident photons required for an efficient ablation.*

In the *p*s regime, two processes in two directions take place. For the direction down into the target, the energy absorbed by the electrons will be transferred to the lattice by electron-phonon coupling. The heat can also be transferred into the target by heat diffusion, which depends on diffusivity and the heat diffusion time. For the opposite direction, free electrons with high kinetic energy can leave the surface leaving ions behind. This separation of two oppositely charged particles generates a strong electrostatic field, which will pull the ions out from the target surface. This is the main ablation process for laser energy densities (fluence) higher than the ablation threshold.

In the *n*s regime, the situation is complicated. As the laser applied in this work has a duration of 25 ns, the interaction between the laser radiation and the already generated plasma is important. The laser will hit the formed plasma and the two dominant processes happening during this process are ***inverse Bremsstrahlung and avalanche ionization*** [45] (Figure 2.8), which can finally lead to a strongly increased free electron density. The neutral atoms in the plasma will be further ionized by colliding with these hot electrons, introducing a stronger ionization degree of the already formed plasma. At the same time, the heat transferred from electrons to the lattice during the ablation process will be increased by the plasma interaction and the evaporation of target material proceeds.

As a conclusion, for the *n*s laser, both, the photoionization process and the thermal evaporation process, are playing important roles. The laser fluence, which is the energy density of the laser on the target in unit of J/cm^2, can strongly influence the ratio between the photoionization and the thermal evaporation. If the laser fluence is high, the main process is the ***photoionization induced ablation***. If the laser fluence is low, the photoionization is weak and the main process is the ***thermal evaporation*** [47]. Nevertheless, these two processes also dependent on the material properties like thermal conductivity and the strength of electron-phonon coupling, which has to be taken into consideration for comparison between different materials.

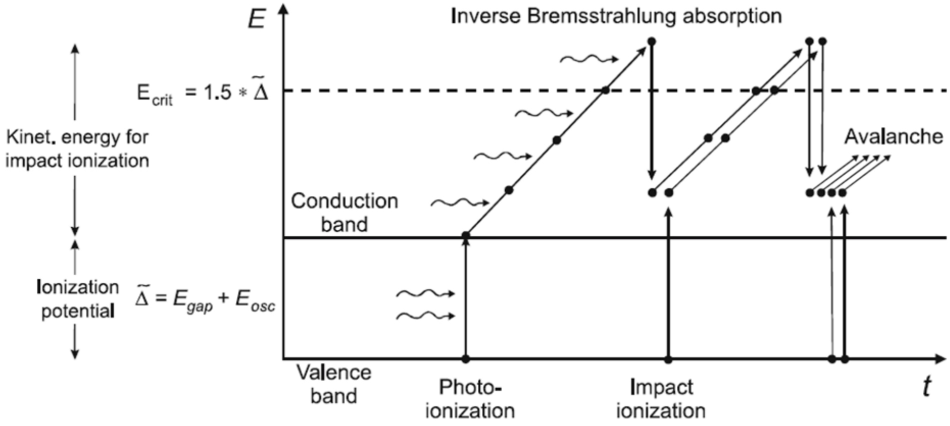

Figure 2.8 *The ionization processes in the ns regime. The most important processes during ns laser radiation are inverse Bremsstrahlung absorption and the avalanche ionization. For the ionization potential, not only the band gap (*E_{gap}*) is important, but the electron oscillation energy (*E_{osc}*) due to the electrical laser field has also to be considered. However, this oscillation energy is by nanosecond laser pulses small and can be neglected [46]. The black dots are the electrons. The figure is reproduced from ref. [46].*

It has to be mentioned that for all multi-elements targets, the ablation process with variation of parameters may introduce non-stoichiometry in the ablated material. For complex metal oxides, the ablation process can be complicated and we discuss the non-stoichiometric ablation with respect to the material properties. Two possible explanations for the non-stoichiometric ablation were suggested for two classes of material systems. For *quaternary oxides* with a complex phase diagram, the explanation for non-stoichiometric ablation is non-congruent melting. For low laser fluence, where the oxide material experiences melting before evaporation, the different melting points of possible phases result in different evaporation rates. Thus the ablated species constitute a composition that differs from the target itself. This effect was first observed in quaternary oxides like $YBa_2Cu_3O_{7-x}$, which shows an incongruent melting [48]. For non-stoichiometric ablation in *ternary oxides* with congruent melting, the explanation is the different diffusion constants for the different elements in the oxide target. For congruently melting materials like $SrTiO_3$ [49], it has been observed that the low laser fluence introduces a Sr rich film, while the high laser fluence produces a Ti rich film. To explain this phenomenon, controversial models have been suggested. As suggested by Dam [4], if the laser fluence is low, the thermal melting and evaporation dominates and the Sr atoms can flow to the surface through the molten region. It makes the surface enriched with Sr and the subsequent ablation is thus Sr rich. However, Wicklein et. al have shown that the non-stoichiometric ablation is rather weak in comparison to the preferential scattering during the plume propagation, which will be discussed in the following.

2.3.2 Plume Propagation

The general model for the plume propagation has been well studied for the simple element plume propagation like Y [50] and Ag [51] in different gas ambient atmospheres. Since the effective pressure of the initial plasma formed by the laser ablation process is around tens of mbar, for the pressures in PLD chamber of lower than mbar a pressure gradient perpendicular to the initial plasma surface is generated. At pressures between vacuum and around 10^{-3} mbar, the interaction between the plume and the gas molecules can be neglected and the plume expands freely. For higher pressures, which are more frequently used for the PLD growth, the interaction between the plume and the gas molecules has to be taken into consideration. One specific feature for the plume propagation in a certain pressure range is the splitting of propagating components, which reveals the complex feature for the interaction between gas molecules and the plume: one component (fast part) comprises high energy particles with little scattering with the surrounding, which is vacuum like; while the other component (slow part) comprises ions that collide with the gas molecules and are slowed down with further propagation. After a certain distance the propagation of the slow part is thermalized and after this distance the propagation is diffusive. The ratio between the two parts is strongly dependent on the pressure in PLD chamber [52], where for the high pressures only the slow part can be observed. The slow part propagation prior to the stop distance can be described well by a hemisphere plume model suggested by Predtechensky and Mayonov [53], where the adiabatic plume expansion with respect to the gas-plume interaction has been considered [51]: The plasma expands and sweeps up the gas molecules, which accumulate at the front of the plasma (from R to R_e, Figure 2.9), while most materials in the plume can be found in a thin hemisphere shell (from R to R_i, Figure 2.9). Within this model, the momentum transfer equation is used to describe the gas dynamics, which can describe how the gas pressure and the increased swept-up gas mass can decelerate the plume propagation. For details see ref. [51] and the following example for the STO plume propagation.

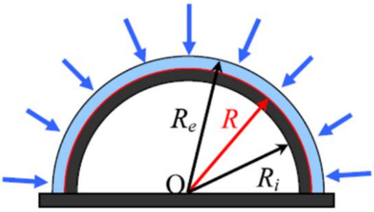

Figure 2.9 *The model for the propagation of the plume in the gas atmosphere. The radius R is the outer boundary of the plume and the R_i is the inner boundary of the plume. R_e is the outer boundary of the swept-up gas. This figure is reproduced from ref. [51].*

In the following we take the STO plume as one example to illustrate the plume propagation influenced by the laser fluence (F_L) and the ambient pressure (p), which is essential for the discussion of homoepitaxial growth of STO on STO as described in chapter 4. The propagation dynamics of the STO plume generated during the PLD process have been studied by using time gated Intensified Charge Coupled Device (ICCD) imaging [54, 55]. This *in-situ* diagnostic was proved suitable to monitor plume expansion during thin film deposition thanks to the advantage of providing spatially-resolved two-dimensional (2D) optical emission intensity maps of different species the plume. It is also possible to investigate the total emission of one plume to compare qualitatively the propagation kinetics between different parameter settings. Although this technique only monitors species which are optically active in the visible range, it has been shown earlier that it provides a description of the laser ablation plume expansion consistent with other different complementary techniques, such as optical emission and absorption spectroscopy as well as ion probe analysis, which can only give local information [6, 50, 56-57].

Figures 2.10 (a) and (b) show examples of the 2D images of the STO plume total emission at different delays after the laser pulse, for deposition in O_2 background gas. In the images of Figures 2.10 (a) and (b), the plume propagation direction is along the vertical z-axis, and $z = 0$ marks the position of the target surface, whereas the x-axis is parallel to the target surface. The corresponding spatially resolved one-dimensional (1D) spectra of the plume species emission (Figure. 2.12) indicate that the plume self-emission is due to many emission lines of Sr and Ti excited atoms in the visible region, and to some emission bands of their oxides [58]. The STO plume images reported in Figure 2.10 allow illustrating the diverse effects of two important PLD parameters, such as F_L, and p. Figure 2.10 (b) shows plume images for three different values of F_L (0.6, 1 and 2 J/cm^2) at $p = 0.1$ mbar. One can clearly observe that at larger values of F_L the plume front reaches the substrate earlier due to the increased initial driving energy of the plume. As the fluence decreases, a more effective braking of the plume propagation occurs, and the plume is actually stopped on a distance of about 2cm from the target surface at the lower fluence. In these conditions the ablated species can reach the substrate only through a diffusive propagation regime in the background gas [52]. Figure 2.10 (a) reports images of the STO plume for four different values of the background gas pressure (1, 0.1, 0.07 and 10^{-3} mbar) at a fixed F_L of 1.5 J/cm^2. The images at $p = 10^{-3}$ mbar are representative of the plume expansion features registered at low pressures. At low-pressure level, the plume is elongated along the direction normal to the target surface ($x = 0$). As the pressure p increases in the 10^{-2}-10^{-1} mbar range, the plume becomes gradually more confined developing into a more spherical shape with the maximum of emission progressively located closer to its front edge. At the high-pressure level of 10^{-1} mbar, an important confinement effect is visible and the plume strongly sharpens while its front effectively brakes (the red area for the high energy particles on the plume front shrinks).

All these phenomena described above result from a rather complex relationship between the plume expansion dynamics and its interaction with a background gas [51, 59-60]. The laser fluence F_L defines both the amount of ablated material and its initial energy, whereas the ambient gas pressure determines the braking/stopping external forces. The interplay between these different quantities regulates the resulting plume propagation dynamics. In the typical conditions used in PLD of epitaxial thin films, the substrate temperature is several hundred degrees. In such cases, the background gas is characterized by a variable, spatial density profile as a consequence of the temperature gradient between the target and the substrate surface (see refs. [61] and [62] for details). The plume expansion dynamics are typically analyzed by following the position of the plume front R along the normal to the target surface as a function of the time t with respect to the laser pulse. Figure 2.10 (c) reports the temporal evolution of the STO plume front for two different values of F_L. This data has been interpreted in the frame of a model based on the balance between plume linear momentum variation and the external pressure force which takes into account the spatial profile of the background gas [61, 62]. The model considers the plume and adjoins the background gas as a hemispherical thin layer of radius R moving at velocity u and experiencing the force due to the background gas pressure p, as expressed by the equation:

$$\frac{\mathrm{d}}{\mathrm{d}t}\left\{\left[M_{\mathrm{p}} + M_{\mathrm{g}}(R)\right]u(R)\right\} = -2\pi R^2 p \qquad (2.1)$$

, where M_{p} is the driving plume mass and $u(R)$ is given by $u(R) = \frac{\mathrm{d}R}{\mathrm{d}t}$. The mass of the background gas swept away by the expanding plume at a distance R at the time t is given by $M_{\mathrm{g}}(R) = 2\pi\int_0^R \rho(r) r^2 \mathrm{d}r$, where $\rho(r)$ is the background density profile as a function of the radial coordinate r.

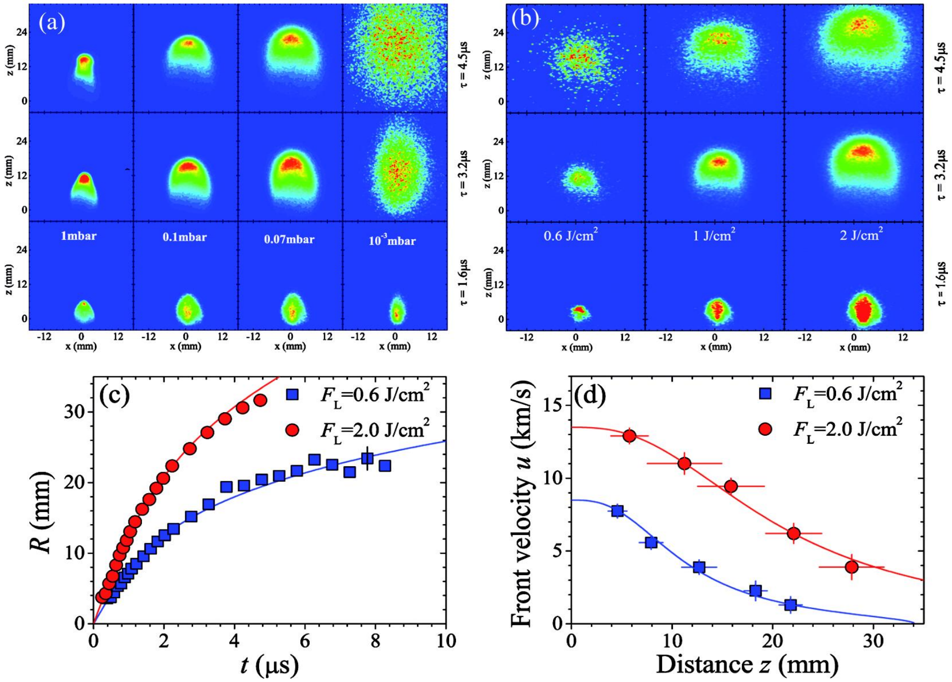

Figure 2.10 *2D images of the STO PLD plume for, (a) different background pressures at different delay times τ with F_L = 1.5 J/cm^2, and (b) different laser fluencies F_L at different delay times τ (same delay times as for (a)) and a background pressure p = 0.1 mbar. (c) Temporal variation of the plume front position R for two different values of the laser pulse fluence F_L at a pressure p = 0.1 mbar. (d) Variation of the plume front velocity u versus distance z from the target position. The solid curves are fits to the model of Equation (2.1). The results were published in ref. [63].*

The solid lines of Figure 2.10 (c) are fits of the experimental data to the propagation model of Equation (2.1), using the driving mass of the plume M_p and the initial velocity u_0 as fitting parameters. The model describes fairly well the experimental plume front dynamics and allows estimating the variation of the plume front velocity u on the distance from the target surface z as reported in Figure 2.10 (d). The fitting procedure provides $M_p = 310$ ng and $u_0 = 8.5$ km/s at $F_L = 0.6$ J/cm^2, and $M_p = 1300$ ng and $u_0 = 13.5$ km/s at $F_L = 2.0$ J/cm^2. This, in turn, indicates an increase of both the driving plume mass and initial kinetic energy with the laser pulse fluence, which eventually defines the consequent plume propagation dynamics. As shown in Figure 2.10 (d) the plume front stops for distances $z \approx 30$ mm at $F_L = 0.6$ J/cm^2.

The plume expansion dynamics allow evaluating the maximum kinetic energy E_k of the cations impinging on the substrate at the plume front, showing the effects of the specific deposition conditions (fluence and background gas pressure). Focusing on wavelengths that come from a specific atom, the kinetic energy of this atom can be investigated and qualitatively represents the influence of the growth condition.

As an example, Figure 2.11 reports the dependence of E_k for the Sr atoms, as a function of the laser fluence F_L for different values of oxygen background pressure ranging from 0.01 to 0.5 mbar at a target-to-substrate distance d_{TS} of 44 mm. The same trends are valid for the Ti atoms, with kinetic energy values reduced by a factor 1.8. We observe that both the fluence and the oxygen pressure influence the maximum kinetic energy of the arriving cations.

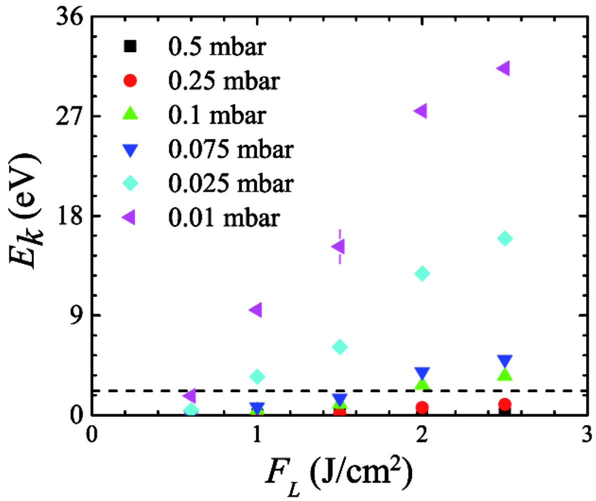

Figure 2.11 *Variation of the maximum kinetic energy E_k of Sr atoms as a function of F_L for various values of the background pressure. The dashed line marks the activation energy for the surface diffusion E_{SD} [8], which we regard as the lower limit below which any influence of the particle energy on the growth kinetics can be excluded. The error bar shows the typical uncertainty of the E_k values as obtained by the accuracy of front velocity curves in Figure 2.10 (d). The target-to-substrate distance is 44 mm. The results were published in ref. [63].*

At a fixed background pressure, the kinetic energy of the ablated species arriving on the substrate can be adjusted by an appropriate selection of the laser fluence. Fig. 2.10 shows the highest energy of nearly 30 eV for the lowest pressure of 0.01 mbar. That is well below 100 eV, which would be necessary to induce significant sputtering effects [64]. However, other kinetic pathways leading to a transition in the growth mode like enhanced intralayer and interlayer adatom transport, direct incorporation of energetic atoms into clusters, and cluster disruption leading to an increased density of nucleation points have to be considered [65]. As described by Willmott et. al [66] the flux of high energetic species can break up small islands of one monolayer height (so called 2D islands) resulting in the creation of new nucleation sites for adatoms. Considering a bond strength of SrO of about 5 eV and 7 eV for TiO bonds [67], respectively, the cracking of 5-fold Ti bonds and 4-fold Sr bonds in the middle of a STO surface island might play a role at the lowest investigated oxygen partial pressure, when a kinetic energy of 30 eV is obtained. Since island fragmentation becomes less likely at energies below 10 eV [66], Figure 2.11 shows that irrespective of the laser fluence this process is inhibited for oxygen partial pressures above 0.025 mbar.

Below the energy range of island fragmentation, the transfer of the kinetic energies of the oncoming particles into enhanced intra- or interlayer diffusion are conceivable processes influencing the growth kinetics of PLD grown films [10, 65, 68]. Since the physical background and the relevant energy range of these processes are still under controversial debate, we introduced the activation energy E_{SD} of surface diffusion (marked in Figure 2.11 as dashed line) as lower limit for the kinetic energy below which any impact of the kinetic energy on the surface diffusion can be excluded. We considered a lower limit of 2.2 eV [69] for E_{SD} but one has to note that there exists some spread of this value in the literature (e.g. 3.3 eV for Sr terminated STO and 3.8 eV for Ti terminated STO [9]).

As can be seen in Figure 2.11 for 0.01 mbar and 0.025 mbar, E_{k} exceeds E_{SD} for all employed laser fluences, except for the lowest value of 0.6 J/cm^2. For 0.075 mbar and 0.1 mbar, E_{k} exceeds E_{SD} at a laser fluence of 2 J/cm^2 and 2.5 J/cm^2, respectively. Above 0.1 mbar enhanced surface diffusion can be neglected for the whole investigated fluence regime. Therefore for the discussion on the surface diffusion in chapter 4 with 0.1 mbar as growth pressure, the enhanced surface diffusion can be neglected.

The laser fluence can strongly change the STO thin film stoichiometry [4, 12-13]. As proven by the former study in our group [58], the laser fluence mainly changes the preferential scattering process and thus influences the final stoichiometry of the plume front arriving at the substrate surface [58]. Figure 2.12 visualizes the relative change of the different components *via* the optical emission spectra at different laser fluences. By tuning the laser fluence from 0.6 J/cm^2 to 2 J/cm^2, we see the optical emissions that correspond to Sr are reduced, while the optical emissions of Ti are increased. The red color represents the maximal concentration of a specific element at corresponding wavelength, while the blue color represents the minimum.

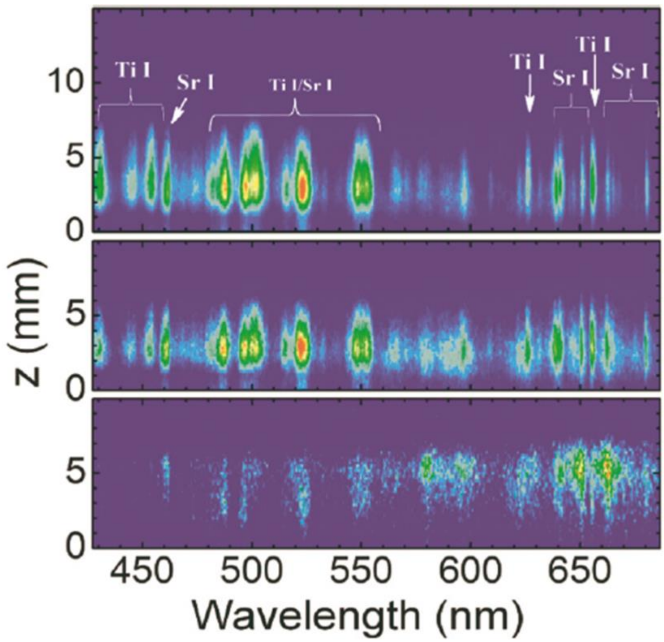

Figure 2.12 *The emission spectra for (upper panel) 2 J/cm^2, (middle panel) 1 J/cm^2 and (lower panel) 0.6 J/cm^2. The oxygen partial pressure in PLD is pO_2 = 0.2 mbar. The figure is reprodued from ref. [58].*

However, the optical emission spectra are strongly influenced by the oxidation process by the ambient oxygen gas. Therefore, in order to see the kinetic processes during the propagation of Sr and Ti species, the optical emission spectra are recorded for the STO plume in Ar. In Figure 2.13 the optical emission ratio of Sr/Ti in Ar is summarized along the plume propagation direction in z axis. We observe a clear increase of the Sr/Ti ratio, which indicates the preferential scattering of the light Ti atoms. Although the oxidation may take place by the oxygen inlet, the kinetic scattering process should be similar to the situation in Ar. So the preferential scattering of the Ti out of the main propagation direction of the plume by the gas atoms is responsible for the Sr rich plume at the low laser fluence, where the nascent plume is stoichiometric. At the high fluence, the nascent plume is Ti rich. The preferential scattering of Ti at the high fluence is not strong enough to reduce the Ti excess to null at a target-substrate distance of around 44 mm, which makes the final film Ti rich. The knowledge of the preferential scattering helps the discussion about the cation non-stoichiometry in chapter 4.

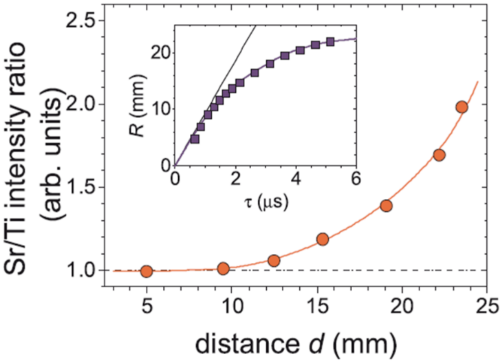

Figure 2.13 *The Sr/Ti ratio (derived from optical emission spectra obtained in an argon atmosphere with a pressure of 0.2 mbar) in the plume along the z-axis. Inset: the distance-time relation for the plume front The two solid curves in the main image and in the inset are guides to the eye. The solid straight line in the inset indicates a trajectory that the free expansion of the plume should follow. This picture is reproduced from ref. [58].*

Besides the surface diffusion and the film stoichiometry, the propagation of the plume can also strongly influence the redox process during growth. First of all, the impinging particles with high kinetic energy of the plume can reduce the STO substrate by selectively sputtering off the oxygen as reported by many groups [70, 71].

Moreover, it has to be mentioned that high energetic photons (e.g. ultra violet radiation, UV) can also be emitted from the laser plume. One example is the Ti II Stark profile at ~ 350 nm observed during PLD growth of TiN layers by Herrmann [72]. The UV-radiation can have an impact on the STO substrates and thin films. It has been reported that at room temperature, the UV-radiation of 325 nm Cd laser [73] can introduce oxygen vacancies or Ti-O vacancy clusters in $SrTiO_3$, which result in conductive $SrTiO_3$. Similar phenomena have been observed by M. Tarun et. al [74]. However, the influence of UV-radiation can be complex. On the one hand, at elevated temperatures like 800 °C for a typical PLD growth, the generation of the defects should be easier with a decreased barrier through thermal activation (see chapter 2.2.1). On the other hand, the measurable UV-radiation influence reported in the literature is carried out with continuous UV-radiation, while the emission time of UV-radiation during the PLD process is much shorter (~ μs) [72], which would reduce the influence of UV-radiation on the STO sample. However, the exact influence of UV-radiation on the STO property change at a nominal growth condition in PLD has not been studied yet.

As a summary for the plume propagation process, the energetic particles in the plume and the UV-radiation from the plume may both influence the oxygen incorporation into STO. Therefore the oxygen incorporation process during the growth of thin films has to be studied, where the impact from the kinetic particles of the plume and the UV-radiation have to be disentangled. The corresponding discussion is carried out in chapter 6.

2.3.3 Surface diffusion

Due to its extremely high deposition rate, the PLD growth is accompanied by a high supersaturation in expression of the chemical potential difference to the equilibrium $\Delta\mu$ [75]:

$$\Delta\mu = k_B T \ln \frac{R}{R_0} \tag{2.2}$$

, where R is the deposition rate and R_0 the deposition rate at equilibrium, T the temperature and k_B the Boltzmann constant. This high supersaturation results in the ***instantaneous nucleation***, where the nuclei are formed in a short time. As indicated by the surface X-ray diffraction, the instantaneous nucleation time of STO crystalline structures on STO substrate should be around several microseconds [10]. In ref. [10], it has been shown that the diffusion time of the nucleated species on the STO substrate is in the range of seconds. Therefore the diffusion of these formed STO crystalline structures should be well separated from nucleation events. This is a distinct feature, which differs from the nucleation process by other techniques like e.g. the continuous nucleation by MBE [76]. This instantaneous nucleation enables the separation of the diffusion process from the nucleation process for PLD.

The surface diffusion process can be interpreted as the hopping of particles between the potential wells formed by the underlying crystal surface. As for complex metal oxides like STO, this hopping process can be simplified as the hopping of STO unit cells on the STO surface by the first approximation. It has to be mentioned that the real process should be much more complex than just hopping of STO unit cells. Since the incoming particles from plasma consist of different neutrals and ions, the coupled multicomponent diffusion has to be considered. Moreover, the diffusing STO structures may consist more than one STO unit cell, which may lead to a distribution of the diffusion time. However, the discussion on the microscopic mechanism of surface diffusion can't be covered in this work. For an illustration for the influence of cation non-stoichiometry on the surface diffusion, the model with STO unit cells can be used and the diffusion coefficient is actually an apparent diffusion coefficient. The advantage for this simplification is that the diffusion can be easily compared with one single apparent diffusion coefficient. The hopping frequency (Γ) is defined as a product of the attempt frequency (ν) and a thermodynamic factor, which is dependent on the diffusion barrier (E_{diff}) and the thermal energy ($k_B T$):

$$\Gamma = \nu \exp\left(-\frac{E_{diff}}{k_B T}\right). \tag{2.3}$$

The attempt frequency (ν) is normally assumed to be the vibrational frequency of the adatoms on the surface, while the diffusion barrier (E_{diff}) is dependent on the binding energy of the adatoms to its neighbors and may differ for local conditions.

Considering the statistical nature of the surface diffusion, the diffusion coefficient (D) is a product of the hopping frequency and the possible area covered by hopping (for the simplest case the square of the lattice constant a_0 for a cubic lattice) in the form of:

$$D = {a_0}^2 \Gamma = {a_0}^2 \nu \exp(-\frac{E_{diff}}{k_B T}). \tag{2.4}$$

For the 2D surface diffusion, the correlation between the diffusion coefficient (D), diffusion length (L_D) and diffusion time (τ) can be established as the Einstein relation [77] derived from Fick's first law:

$$D = \frac{{L_D}^2}{n\tau} \tag{2.5}$$

, where n is the number of nearest neighbors for the diffusion species. For a cubic lattice n should be normally 1 for one particle on the surface, and for a hole on the surface n should be 5. Since only particle diffusion is considered, we take $n = 1$ to simplify the qualitative comparison in chapter 4, which is also used in literature [8]:

$$D = \frac{{L_D}^2}{\tau}. \tag{2.6}$$

The relaxation time of the RHEED intensity (τ) after each laser pulse represents the decrease of the surface roughness (for the details about RHEED see the chapter 3), which can be used to estimate the time necessary for all diffusing units to find an island [8]. Normally, the diffusion takes place on both, the substrate and the formed islands, which leads to a complex analysis of the relaxation time. However, two situations can be simplified: For the low coverage ($\theta = 0 \sim 0.1$ monolayer (ML)), the relaxation time of RHEED represents the diffusion time on the substrate, i.e. $\tau_{0.1\,ML} = \tau_{D,\ substrate}$. For the high coverage ($\theta = 0.7 \sim 1$ ML), the relaxation time can be interpreted as the diffusion time on the formed islands, i.e. $\tau_{0.8\,ML} = \tau_{D,\ islands}$. For both cases the RHEED intensity (I_{RHEED}) can be described as:

$$I_{RHEED} = 1 - \exp(-\frac{t}{\tau}). \tag{2.7}$$

Figure 2.14 illustrates the representative relaxation of the RHEED intensity at low coverage, while the two insets illustrate the surface morphology for the $t = 0$ and $t > \tau$ as indicated by the arrows.

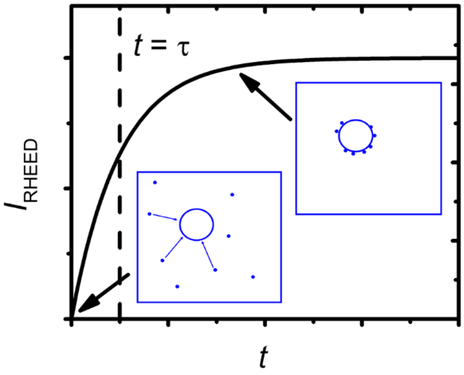

Figure 2.14 *RHEED intensity relaxation for the low surface coverage (black curve) with the relaxation time marked by the broken line. The morphologies at t = 0 and at t > τ are shown in the left and right inset, respectively.*

The diffusion lengths are estimated at surface coverages close to zero or unity ($\theta \sim 0.1$ ML or $\theta \sim 0.8$ ML). For such coverages, the STO unit cells diffuse either to the formed islands (circulars in Figure 2.15 (a)) or to the holes (triangles between three circulars in Figure 2.15 (b)). Therefore the ***diffusion length on the substrate*** can be estimated as half of the averaged distance between the islands ($<L_S>$) at low coverages like $\theta \sim 0.1$ ML (Figure 2.15 (a)):

$$L_{D,substrate} = \frac{\langle L_S \rangle_{0.1ML}}{2} \tag{2.8}$$

, whereas ***the diffusion length on the formed islands*** can be estimated by half of the averaged distance between the holes at high coverages like $\theta \sim 0.8$ ML (Figure 2.15 (b)):

$$L_{D,islands} = \frac{\langle L_S \rangle_{0.8ML}}{2} . \tag{2.9}$$

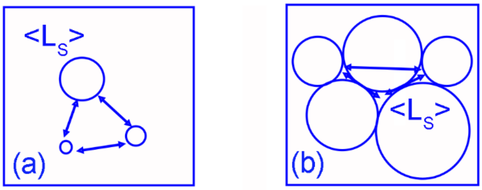

Figure 2.15 *(a) The averaged length between islands at a surface coverage of 0.1 monolayers and (b) The averaged length between holes at a surface coverage of 0.8 monolayers. The circles represent the islands.*

Therefore, with the diffusion time ($\tau_{D,\ substrate}$) and diffusion length ($L_{D,\ substrate}$) on the substrate the apparent surface diffusion coefficient of STO unit cells on STO substrates ($D_{S,\ substrate}$) can be estimated. The diffusion coefficient of STO unit cells on formed STO islands ($D_{S,\ islands}$) can be estimated from the diffusion time ($\tau_{D,\ islands}$) and diffusion length ($L_{D,\ islands}$) on formed islands. This principle is applied in chapter 4 for the discussion of the surface diffusion influenced by the cation non-stoichiometry in STO.

Since the diffusion time can be correlated to the diffusion barrier by combining Equation (2.4) and (2.6):

$$\ln(\tau) \propto \frac{E_{diff}}{k_B T} + C \ . \tag{2.10}$$

The diffusion barrier of STO on STO can be estimated through temperature dependent diffusion time measurements, which have been carried out by several groups [8-9, 78]. Rijnders et. al [8] suggested a barrier of ~ 2.2 eV for an oxygen pressure of 0.2 mbar and ~ 0.48 eV at 0.03 mbar. Lippmaa et. al [9] paid attention to the different terminations of the STO substrate, where on the TiO_2 termination the diffusion barrier is around 3.8 eV and on the SrO termination the diffusion barrier is around 3.3 eV. However, for both studies the influence from the stoichiometry of STO is not considered. This is the point that is to be discussed in chapter 4 with varied cation non-stoichiometry in STO but constant temperature. It has to be mentioned that, to better understand the influence of stoichiometry on the diffusion, temperature dependent depositions with cation non-stoichiometry for homoepitaxial STO are necessary.

2.3.4 Thin film growth modes

There are three classical thin film growth modes for ideal infinite and flat surfaces: the Frank van der Merwe layer-by-layer growth, Volmer-Weber island growth and Stranski-Krastanov layer-plus-island growth [79]. The three growth modes are illustrated in Figure 2.16. For the Frank van der Merwe layer-by-layer growth, the growth stays in the layer-by-layer growth until the end, i.e. the beginning of the next layer takes place after the finishing of the previous layer (Figure 2.16 (a)). Under certain circumstances, e.g. the growth of thin films with slight lattice misfit, the layer-by-layer growth can be sustained in the early growth stage within several unit cells (layer thickness) if the strain is not high enough to relax. However, at increased thicknesses the lattice starts to relax under the stress. Therefore 3D islands are formed and the further growth will be in the 3D mode. This growth with transition from 2D to 3D is called Stranski-Krastanov layer-plus-island growth (Figure 2.16 (b)). If there is no 2D layer-by-layer growth observable and the growth is from the beginning on 3D islands growth, it is called Wolmer-Weber island growth.

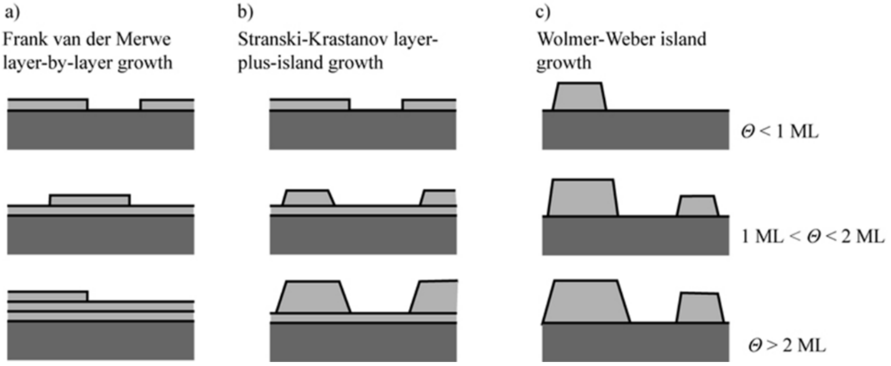

Figure 2.16 *The three growth modes illustrated at different stages: (a) Frank van der Merwe layer-by-layer growth, (b) Volmer-Weber island growth and (c) Stranski-Krastanov growth. The figure is reproduced from ref. [79].*

For a real vicinal surface with terrace edges, which are inevitable for any single crystal substrate with a certain miscut angle, all of the three above mentioned growth modes can be observed on the terraces. Moreover, the terrace edges may act as natural nuclei and the so called step flow growth can be observed: the particles reaching the surface diffuse towards the terrace edges without nucleation on the terrace. The growth of the thin film then proceeds only by the propagation of the terrace front [80]. The principle is illustrated in Figure 2.17. This growth mode can be observed for many complex metal oxide thin film growths with vicinal surfaces, where the surface diffusion length exceeds the terrace length. This growth mode has a positive impact on the thin film properties [81-83].

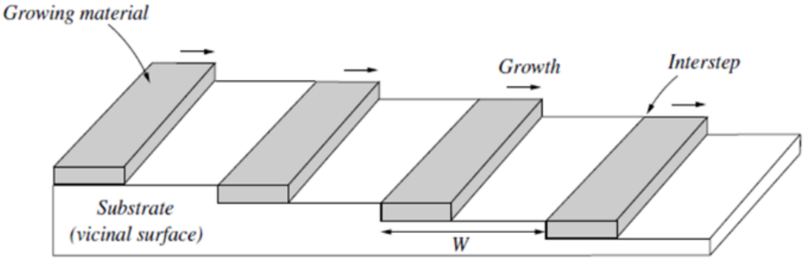

Figure 2.17 *The illustration of the step flow growth mode on a vicinal surface. The figure is reproduced from ref. [80]*

Taking the layer-by-layer growth as an example, the growth of the thin film can be followed by the peak intensity of the specular spot of the RHEED pattern (for details about RHEED see chapter 3) (Figure 2.18). It has been suggested by Kawamura that in theory the RHEED intensity change during thin film growth can be interpreted by the step density model for [84] and applied especially good for the complex metal oxide growth [8, 69]. In this model, the RHEED intensity (I_{RHEED}) can be related to the step density (S):

$$I_{RHEED} \propto 1 - \frac{S}{S_{MAX}} \tag{2.11}$$

, where S_{MAX} is the maximum of step density. The scenario is as follows (Figure 2.18): for the increased density of steps on the surface before island coalescence, the scattering of the specular spot of the electron beam is stronger, which decreases the RHEED intensity. As the island coalescence takes place, the step density is reduced and the RHEED intensity increases.

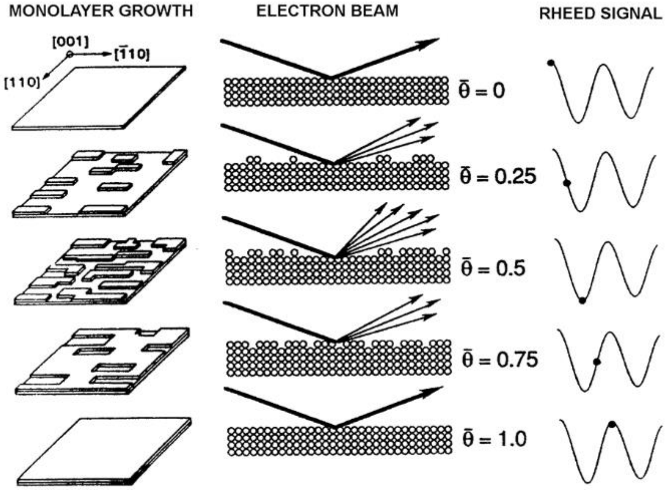

Figure 2.18 *The step density model for the RHEED intensity oscillation. Left panel: development of the surface morphology. Middle panel: the scattering of the electron beams on the surface. Right panel: the RHEED intensity oscillation with dots marking the position for the corresponding time. The figure is reproduced from ref. [85].*

Under the assumption of a circular shape of the 2D islands and an instantaneous nucleation with a constant nucleation density, the development of the step density during the layer-by-layer growth in PLD can be described by a model suggested by Stoyanov (for the derivation see ref. [86]):

$$S(t) = 2\sqrt{\pi N_n}(1-\theta(t))\sqrt{-\ln(1-\theta(t))} \tag{2.12}$$

, where N_n is the nucleation density, θ(t) the surface coverage and S(t) the step density.

This model can explain the step density change derived from the RHEED intensity during most complex metal oxide growths. However, the circular form of the islands requires a high surface diffusion constant, which is not the case for some layer-by-layer growths. The derivation of the assumed circular shape of islands can lead to a change in the RHED oscillations and is to be discussed in chapter 4.

Two aspects have to be considered for the growth modes: From the thermodynamic point of view, the reduction of the total Gibb's free energy of the surface by growth of thin films leads to layer-by-layer growth, while the 3D growth leads to an increase of the surface free energy. This is important for the growth near the thermodynamic equilibrium like for MBE or chemical vapor deposition (CVD). From the kinetic point of view, the time required for different processes is important. The time-related parameters like repetition rate of the laser pulses can thus strongly influence the growth mode [9]. For PLD growth, both aspects have to be taken into consideration, where the kinetics may play a more important role.

For the homoepitaxial growth in PLD, the growth mode can be varied by tuning the growth temperature and the repetition rate. A detailed study on the growth mode mapping within a certain parameter room has been carried out by Lippmaa [9]. However, the influence of the cation non-stoichiometry that can result from the laser fluence variation or pressure variations has not been considered so far. The mechanism behind the growth mode and possible growth mode transitions for STO homoepitaxy with cation non-stoichiometry is discussed in chapter 4.

2.3.5 Peripheral processes introduced by equipment attached to the PLD chamber

It has been shown how important the individual processes during the PLD growth are. However, the PLD growth process is not the only process that happens in the PLD chamber. The impacts from other peripheral processes should also be considered.

As one example of peripheral processes introduced by equipment, the ionized species of the residual gas from the cold cathode can strongly increase the electrons donated to the interface between LAO and STO [87]. The peripheral processes are closely related to the working principle of the equipment. The working principle of the possibly ionizing equipment, cold cathode gauge and mass spectrometer, are illustrated in chapter 3. The effect from the cold cathode gauge and mass spectrometer in the PLD will be investigated for low pressure annealing in chapter 6.

2.4 $LaAlO_3$/$SrTiO_3$ heterostructures

2.4.1 Theorems for the formation of a conductive interface in LAO/STO

It was discovered more than one decade ago that by depositing a polar LAO thin film on a non-polar STO substrate with TiO_2 termination, a conductive interface will be formed despite of the insulating nature of the two materials in single crystal form [88]. This conductive interface is called 2D electron gas (2DEG).

However, since its discovery, the generation of the conductive interface between two oxide band insulator LAO and STO is still not fully understood and remains open despite immense efforts.

Different mechanisms are suggested for the generation of the conductive interface. The first and most important is the polar catastrophe mechanism. It is called "catastrophe" for the sudden electronic transfer compensating ionic polar discontinuity. The straightforward experimental support is the critical thickness of 4 u.c. of LAO for the interface conductivity generation, which is verified by both electrical characterization [18, 89] and optical characterization [90]. In this model, 0.5 electrons per unit cell are transferred to the interface to compensate for the build-in potential which results from the polar discontinuity (Figure 2.19 (a) and (c)). The corresponding sheet electron density should be $n_S \sim 3\text{x}10^{14}\,\text{cm}^{-2}$. Experimentally, the expected number of charge carriers on the interface is not always observed. Normally smaller value is observed with unreduced STO substrate [89].

The second model is the mixing of La into $SrTiO_3$. Since the La doping can make $SrTiO_3$ conductive, the diffusion of La into $SrTiO_3$ during the fabrication process can be a reason for the interface conductivity. Experimentally, the intermixing between $LaAlO_3$ and $SrTiO_3$ is indeed observed [91]. However, this model can't explain the abrupt change of the interface conductivity since the intermixing happens during the whole fabrication process.

Last but not least, the oxygen vacancies generated in $SrTiO_3$ are also suggested for the generation of interface conductivity. This model can explain the absence of the interface conductivity at ***high oxygen pressure grown LAO/STO***, but it is not able to explain the critical thickness for the interface conductivity. It has also been proved by F. Gunkel through the high temperature equilibrium conductance (HTEC) measurement on the LAO/STO samples ***grown at low oxygen pressures*** that the conductive interface survives the ***annealing at oxidizing condition*** [31], which disapproved the oxygen vacancy theory for the conductive interface. Nevertheless, the role of oxygen vacancies on the LAO/STO interface is interesting and is not fully understood yet.

As an important point to test the different mechanisms, the process happening at the critical thickness is of special interest. As a matter of fact, both, changes in STO and LAO at the critical thickness have been observed: the distortion of Ti octahedra [92] and the change of the Ti valence [93] are observed for STO; the optical permittivity change [94] and *c*-lattice constant change [95] for LAO. However, these studies have all been carried out *ex-situ*. As pointed out by Scheiderer et. al [87], molecules like H_2O present in the gas atmosphere can be absorbed on the LAO surface and thus influence the interface conductivity. Therefore, the study of the interface conductivity generation during LAO growth with *in-situ* techniques is necessary to understand the kinetics of different property changes. Therefore, the OIRD signal evolution during growth of LAO on STO is investigated in chapter 5.

It has to be mentioned that the properties of the LAO/STO heterostructure is strongly influenced by the growth conditions. As shown by Brinkman et. al [96], the LAO/STO heterostructure fabricated at different oxygen pressures show different temperature dependent resistance. Especially for high oxygen pressure, the LAO/STO shows high resistance and a Kondo-like minimum, indicating scattering centers on the interface. The most probable explanation is the Schottky equilibrium on the interface involving the Sr vacancies, which act as scattering centers observable at low temperatures [15-17]. For the LAO/STO fabricated at low oxygen pressure, it has been observed by Basletic [97] that the STO substrate is reduced by incorporation of oxygen vacancies. However, no study has been carried out on the Schottky equilibration process or on the process of incorporation of oxygen vacancies during PLD. These two aspects will be investigated in chapter 6.

2.4.2 The difference between TiO_2-and SrO-termination

Experimentally, the electronic properties of LAO/STO heterostructures show a difference in conductivity for different terminations: for the ***TiO_2 termination*** most moderate PLD deposition conditions generate ***conductive*** interfaces, whereas the ***SrO termination never*** shows any comparable ***conductivity*** at all [88, 98-99].

The perovskite structure can be envisaged as a sequence of SrO and TiO_2 submonolayers along [001]. Thus on the surface of single crystal STO two different terminations can be possible: SrO or the TiO_2. These two kinds of terminations have distinct structural and electrical natures [100-102]. For a heteroepitaxial growth of perovskites like LAO in PLD, where the unit cell nucleation on the surface can be finished within short times [10], the incoming oxides can adjust the ordering of LaO^+ and AlO_2^- according to the termination of STO. The interface between $A'B'O_3$ and ABO_3 will be ordered like $A'O/B'O_2/AO/BO_2$ or $B'O_2/A'O/BO_2/AO$ (Figure 2.19 (a) and (b)). For example, if the surface is terminated with TiO_2 (BO_2), the interface ordering should be $AlO_2^-/LaO^+/TiO_2/SrO$. On the contrary, if the surface is terminated with SrO (AO), the interface ordering is $LaO^+/AlO_2^-/SrO/TiO_2$. The two surface terminations of STO do not only influence the structural ordering of the LAO grown on it, but also influence the electronic properties.

For the TiO_2 termination, as discussed above, an electronic transfer to the interface can happen due to the "polar catastrophe" and the accommodated electrons on the interface result in interface conductivity in the form of electronic reconstruction [103] (Figure 2.19 (a) and (c)). However for the SrO termination, the holes will be transferred to the interface but are compensated by the defects or so called "atomic reconstruction" (Figure 2.19 (b) and (d)).

There are two possible methods for the generation of SrO terminated STO: one is through the deposition of a certain amount of SrO on the TiO_2 terminated STO by PLD (or another deposition technique) as shown in chapter 3 and in literature [104], the other is the thermal handling e.g. annealing of STO at a high temperature in oxygen [102].

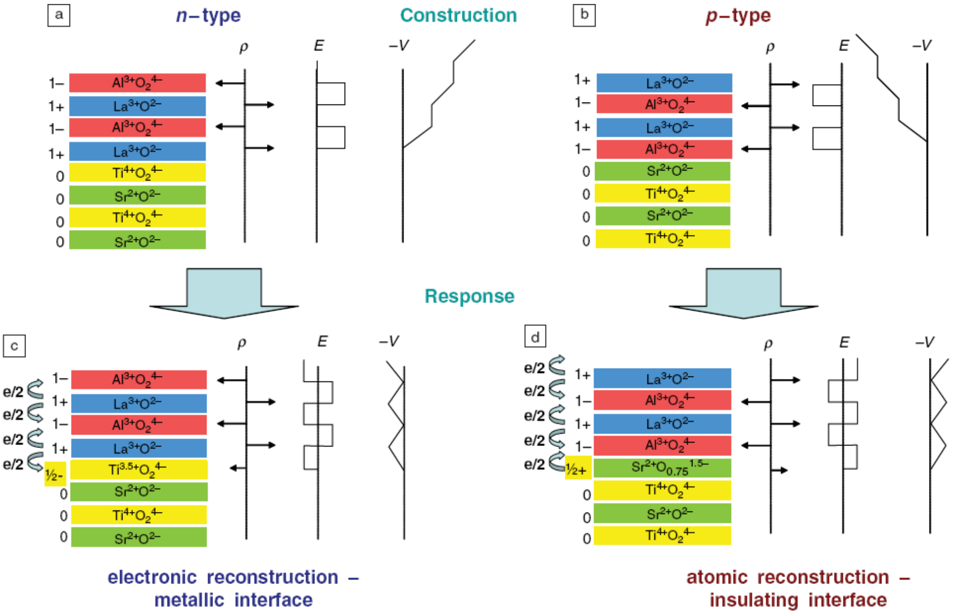

Figure 2.19 *(a) and (c): the principle for the conductive interface generation between LAO and* TiO_2 *terminated STO; (b) and (d): the principle for the absence of conductive interface generation between LAO and SrO terminated STO. This figure is adapted from ref. [103].*

Some other groups have carried out studies on LAO growth on STO with mixed termination in the form of stripes of SrO or TiO_2 on the terrace edges [105]. They intentionally introduced stripes of SrO or TiO_2 by high temperature annealing and then grew LAO on top of the structure. They found the morphology of LAO follows the STO surface and the stripe structure can be observed after growth. Interestingly, this mixed termination introduces anisotropic conductivity. The change of the ratio between SrO and TiO_2 termination can also strongly change the conductivity.

However, for all these discussions the measurements are carried out *ex-situ*, where an insight into the growth process of LAO on STO with different terminations is still missing. Therefore the growth of LAO on STO with 0 %, 55 % and 100 % SrO termination is studied *in-situ* in chapter 5 with OIRD and RHEED.

3 Experimental Methods

3.1 Overview of the Electronic Oxide Cluster (EOC)

The Electronic Oxide Cluster (EOC) is a laboratory with the focus on the material study including fabrication and characterization with all processes under vaccum and well defined ambient. The central parts of this labratory are the ultra-high vacuum (UHV, below 10^{-8} mbar) transfer chamber along with the ultra-high vacuum tunnel. The UHV transfer chamber and the UHV tunnel enable the transfer of the samples between different equipment under continuous UHV condition avoiding the contamination from the absorbates in air. This is extremely important for the study of the fundamental processes during pulsed laser deposition, where the surface and interfaces play a significant role.

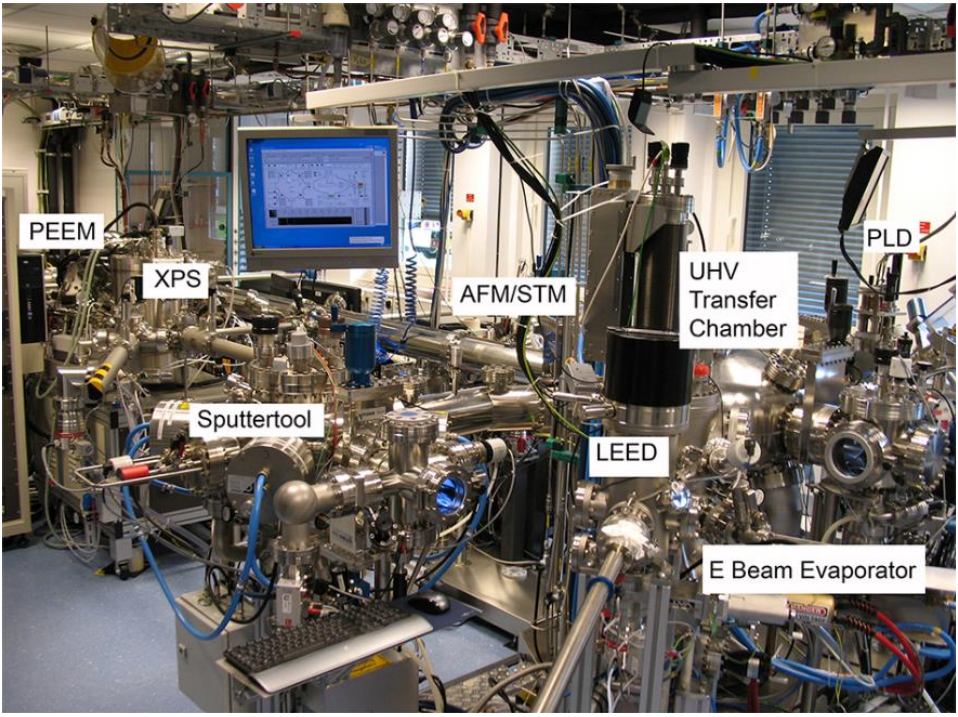

Figure 3.1 *Overview of the oxide cluster tool. All equipment is marked with the corresponding name.*

The whole oxide cluster lab is depicted in Figure 3.1 and comprizes 3 fabrication methods and 6 structural characterization methods. The three fabrication methods are a sputtering tool, an e-beam evaporation tool (EBE) and a pulsed laser deposition chamber (PLD). The sputtering tool is capable of fabricating binary oxide and metal thin films in polycrystalline at low substrate temperature or singlecrystalline states at high temperatures. The EBE supplies poly-crystalline metal thin films as electrodes of devices. The PLD can fabricate metal oxide single crystal thin layers with well controlled layer thicknesses down to sub-monolayer. PLD processes are capable of depositing binary oxides, tenary oxides and even quaternary oxides. In order to have *in-situ* control over the thin film properties, the PLD is equipped with multiple *in-situ* monitoring techniques. The goal is to understand the basic processes like defect formation in thin films and conductive interface formation during the PLD growth, which may lead to the rational design of PLD routines optimizing the desired properties.

Among the six charaterization methods, reflection high energy electron diffraction (RHEED) and oblique incidence reflectance technique (OIRD) are *in-situ* and *real-time* observation techniques for pulsed laser deposition growth. They both are to be discussed in detail in this work to elucidate the correlation between growth and thin film properties during PLD.

Among the other characterization techniques, low energy electron diffraction (LEED) and atomic force microscopy (AFM) analyze the surface atomic structures. X-ray photoelectron spectroscopy (XPS) is capable of measuring (among other properties) the thin film composition and surface termination without lateral spatial resolution.

3.2 PLD and monitoring techniques

3.2.1 PLD

A KrF Excimer Laser from Coherent® with wavelength of 248 nm is used for all the depositions. The initial form of the laser spot is a square with rounded corners. Being tailored with an aperture into a rectangular form, the laser is guided into the PLD chamber by several mirrors. Before entering the PLD chamber, the laser fluence can be tuned by adjusting the transmission of a quartz window with an angle dependent transmission factor in front of the lens of the PLD chamber. The arrangement of the optics on the optical path enables the imaging of the aperture onto a ~ 2x1 mm^2 area on the position of the ceramic target. The principle for the propagation of the laser is illustrated in Figure 3.2.

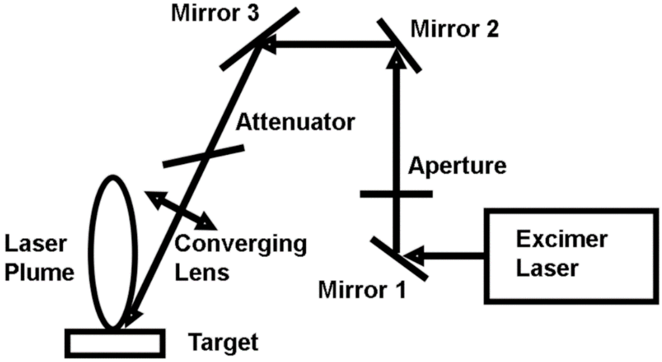

Figure 3.2 *The illustration of the optical path for the excimer laser propagation used in the PLD*

The inside view of the PLD chamber is illustrated in Figure 3.3 (a) with the corresponding photo shown in Figure 3.3 (b). The first process happening in the chamber is the laser plume generation by laser ablation on the target surface. The target can be a ceramic plate with one inch diameter or a single crystal 1x1 cm^2 substrate glued on the one inch diameter metal plate. The target is placed on a rotatable stage of a target carousel, where not only the planetary movement of targets is possible, but also the rotation of a single target is possible. In this way, the homogeneity of the deposited material is improved.

The next step is the plume propagation. The generated plume propagates a certain distance through the predefined ambient, e.g. oxygen, Ar or H_2/Ar mixture with a certain partial pressure that is controlled either by a mass flow controller at an elevated pressure (~ 0.1 mbar with 5 sccm) or controlled with a manual leak value that allows a wider range of gas pressure from 10^{-7} mbar to 10^{-2} mbar. The details about this process has been discussed in the chapter 2.

For the heating of the sample, an infra-red (IR) laser diode is applied in order to offer a high cooling rate by switching off the laser heater. However, the oxide substrates like STO are not able to absorb the IR laser energy given their large bandgap. Therefore a metallic holder is applied as an absorber. A pyrometer is focused on the back side to control the temperature of the backside of the sample holder with a feedback loop to the power output of the IR laser diode. The surface temperature control can be carried out by a pyrometer from a viewport directed to the sample surface, but it is not always accessible for all sample holder designs. This is the case for the sample holder shown in Figure 3.3 (b) which is special for the UV-radiation study shown later in chapter 3.5. For this holder, the temperature difference between substrate surface and back side of the metallic holder is calibrated by a STO reference substrate. The temperature difference for a normal silver paste mounted sample between back side and front side is 30 °C, while for a stack with Ni foil as absorber the temperature difference is 15-20 °C [106]. The two different mounting methods will be applied for the different holder designs in chapter 3.5. The surrounding temperature is measured with a thermocouple on the shutter with a certain distance from the sample holder. The temperature during growth hardly exceeds 100 °C for growths at 800 °C for less than 8 hours. This is important for the other *in-situ* monitoring measurements because of the heat sensitivity of the optical and electronic elements.

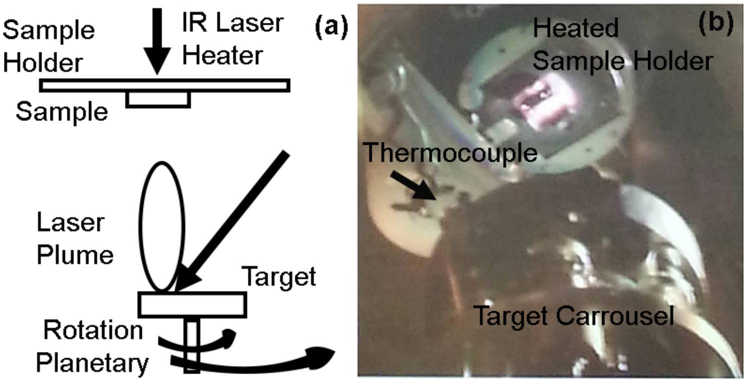

Figure 3.3 *(a) Illustration of the inner construction of the PLD chamber and (b) inside view of the PLD chamber. The temperature of the sample holder can be measured either through the pyrometer from back- or front side. The surrounding temperature is measured through the thermocouple on the shutter that keeps distance from sample during deposition.*

3.2.2 RHEED

Reflection high energy electron diffraction (RHEED) is a standard technique for observing the surface morphology changes during the growth [107]. The method is highly surface sensitive due to the extremely low incidence angle (< 1° by typical measurement), where the short wavelength of the incoming electrons (~ 0.01 nm at 30 keV) leads to big Ewald sphere comprising a large amount of diffraction spots. The working principle of RHEED integrated in a PLD system is depicted in Figure 3.4. The electrons are generated from the electron gun, after which the electron trajectory can be adjusted by electrical field deflection to achieve the maximum intensity. After diffraction on the surface of the substrate, the electron beam hits the phosphor screen and due to fluorescence, green spots can be observed. The CCD camera behind the phosphor screen records the signal during the PLD growth.

The diffraction of the electrons by a periodic lattice follows the Bragg equation:

$$\frac{n}{d} = \frac{2}{\lambda} \sin \varphi \tag{3.1}$$

, where φ is the diffraction angle of the diffracted electrons, λ the de Broglie wavelength of the electrons, d is the distance between two adjacent lattice planes and n the diffraction order. The construction of the Ewald sphere and the reciprocal lattice is a graphic representation of the Bragg equation.

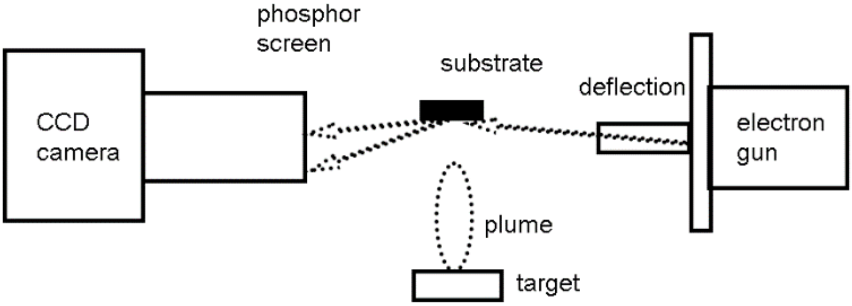

Figure 3.4 *The working principle of RHEED in a PLD system*

For the diffraction on the surface, the reciprocal space rods from the 2D surface lattice can meet the Ewald sphere indicating the constructive interference and the corresponding bright spots can be captured by the phosphor screen. For 2D diffraction, the diffraction spots should lie on a circle known as Laue circle. For the 3D islands on the surface, the incident electron waves experience interference from the 3D lattice. Therefore the pattern on the screen is a product of the Ewald sphere and the reciprocal lattice of the 3D lattice structure from the islands. Summarizing the 2D and 3D diffraction, 2D diffraction leads to rods in reciprocal space and 3D diffraction leads to sharp reflections in reciprocal space.

Figure 3.5 shows the top and side view of a typical diffraction process with the help of the Ewald sphere of the incident electron beam and reciprocal lattice of a simple cubic 2D surface. The specular spot (0 0), first order diffraction ((0 1) and (0 -1)) lie on the zeroth Laue zone. It has to be mentioned that the distances between (0 0), (0 1) and (0 -1) is strongly dependent on the incidence and represents the periodicity perpendicular to the incidence. For a surface with different reconstructions, complex patterns can be visible and analyzed. Especially for a vicinal surface, where the periodicity of the terrace edges introduces additional modulation along the reciprocal rods in reciprocal space both in perpendicular and in parallel directions with respect to the surface normal, each diffraction spot from the diffraction pattern has fine structure [107]. For more details please refer to ref. [8].

During the epitaxial growth process of complex metal oxide by PLD, mostly only (0 0), (0 1) and (0 -1) are observed and the diffraction spots with higher order are too weak. The intensity of the specular spot (0 0) is most frequently investigated. The peak intensity of the specular spot reflects the roughness change of the surface without considering other kinematic effects. If the step density mode is applied as discussed in chapter 2, the time between two maxima in the RHEED oscillation represents the finishing of one monolayer. The number of the oscillations of the RHEED intensity corresponds to the number of the monolayers. The correlation between the RHEED oscillation and the surface morphology change will be discussed in detail in chapter 4.

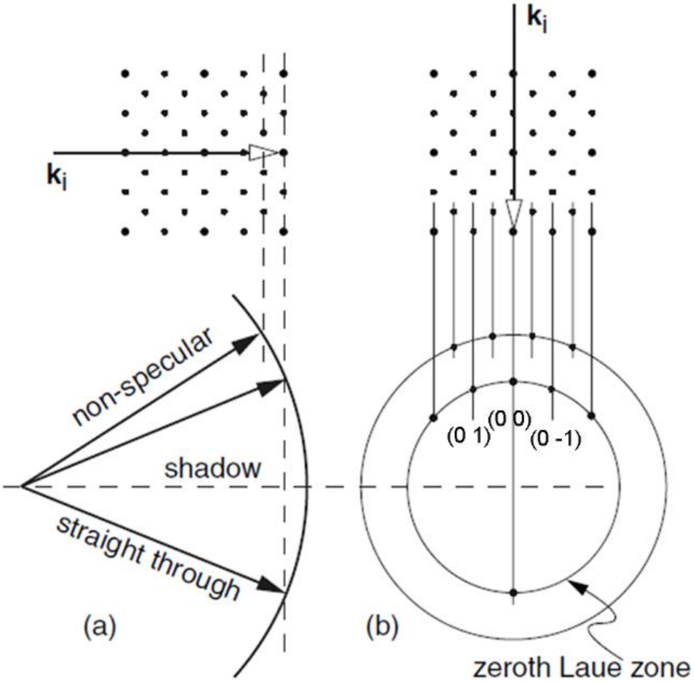

Figure 3.5 *The RHEED diffraction principle of mono-atomic cubic surface (thinner black spots) with c(4x4) reconstruction (thicker black spots) as an example in the (a) side view and (b) top view. The image is reproduced from ref. [107].*

In this work, a kSA 400 RHEED system is applied with the accessibility of high ambient pressure up to 0.1 mbar by utilizing a differential pump [8]. The electron kinetic energy is always fixed at 30 keV.

3.2.3 Oblique incidence reflectance difference (OIRD)

3.2.3.1 Basic principle

The principle of OIRD is based on the changed reflectivity of *p*-and *s*-polarization during the thin film growth process. Utilizing serial optical elements, the *p*-and *s*-polarization can be modulated and focused on the surface of the sample. During PLD growth [108, 109] and annealing [110], the reflectivity is changed and the final polarization direction will be changed, which can be measured by the polarization on one fixed axis. The detailed principle is illustrated in the following.

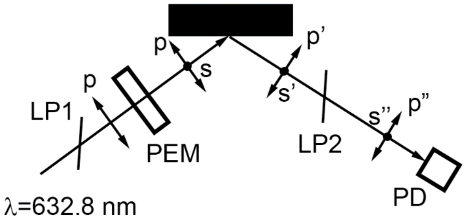

Figure 3.6 *Principle components of an OIRD experiment. The black square is the sample to be studied.*

The two linear polarizers LP1 and LP2, the photo-elastic-modulator (PEM) and the photo-detector (PD) are the main optical elements that are aligned on the optical path (Figure 3.6), whereas an optical chopper is placed directly after the outlet of the laser beam (not shown here) The PEM utilized the photo-elastic effect in quartz crystal, where the quartz crystal is compressed and stretched in one direction periodically with a piezo element and the refractive index in this direction is modulated correspondingly. For OIRD, 50 Hz signal is applied on the two longer sides of PEM plate (Figure 3.7). The LP1 has the transmitting axis parallel to the plane of incidence to let only *p*-polarization enter PEM (*p* in Figure 3.7), while the LP2 has the transmitting axis 45° to the plane of incidence (*j* in Figure 3.7). The PEM plate stays perpendicular to the incidence radiation and the long axis of PEM plate is 45 ° to the *p*-polarization to enable modulation on the *i*-direction.

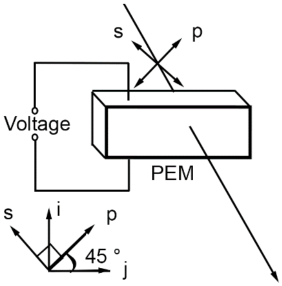

Figure 3.7 *The configuration of p- and s-polarization to PEM. i is the direction where the voltage signal is applied and the polarization is retarded, while j is the optical axis of PEM.*

The following discussion aims at correlating the real and imaginary part of the relative reflectivity change directly to the first and second harmonics of the OIRD signal, respectively.

After emission from the He-Ne source, the electrical field of the 632.8 nm laser will be firstly *p*-polarized with a linier polarizer LP1. To further describe the *s*-polarization and the modulation from other optical elements like PEM, a decomposition of *p*-polarization into two axis parallel (*j*) and perpendicular (*i*) to the PEM optical axis is necessary as illustrated in Figure 3.7. Thus the E field can be expressed as:

$$\vec{E} = \sqrt{2}E_0\hat{p} = E_0(\hat{i} + \hat{j}) \tag{3.2}$$

, where $\hat{p}$ is the unit vector in the positive p-direction, $\hat{i}$ is the unit vector in the positive i direction and $\hat{j}$ the unit vector in the positive j-direction. E_0 is the amplitude of the electrical field.

Since the retardation generated by PEM in i-direction is expressed as

$$\delta = \mathrm{A} \cdot \sin(\omega t) \tag{3.3}$$

, where A is the amplitude of the phase shift set as π/2 for all experiments in OIRD and ω is the frequency of the modulator at 50 kHz, the resulting electrical field is

$$\vec{E} = E_0(\hat{i} \cdot e^{j\delta} + \hat{j}) \tag{3.4}$$

, where j is the imaginary unit.

By decomposing the electrical field into s- and p-polarization, we get:

$$\vec{E} = \frac{\sqrt{2}}{2}E_0(\hat{s} \cdot (e^{j\delta} - 1) + \hat{p} \cdot (1 + e^{j\delta})) \tag{3.5}$$

for the electrical field after modulation *via* the PEM.

The transmission through other optical elements and the viewing port can be represented by t_p for p-polarization and t_s for s-polarization, while the reflection on the surface of the sample can be expressed with r_p for p-polarization and r_s for s polarization. The corresponding phase shift for each transmission or reflection has also to be taken into consideration (δ_{ts}, δ_{tp}, δ_{rs} *and* δ_{rp}). Thus the final electrical field strength for p-polarization is expressed as:

$$\vec{E}_p = \frac{\sqrt{2}}{2}E_0\left[(1 + e^{i\delta})\hat{p} \cdot t_p \cdot e^{i\delta_{tp}} \cdot r_p \cdot e^{i\delta_{rp}}\right] \tag{3.6}$$

, whereas for s-polarization it is:

$$\vec{E}_s = \frac{\sqrt{2}}{2}E_0\left[(e^{i\delta} - 1)\hat{s} \cdot t_s \cdot e^{i\delta_{ts}} \cdot r_s \cdot e^{i\delta_{rs}}\right]. \tag{3.7}$$

The projection of the total electrical field after reflection and transmission onto j direction is:

$$\vec{E}_j = \frac{\sqrt{2}}{2} E_0 \cdot \frac{\sqrt{2}}{2} \cdot \left[(1+e^{i\delta}) t_p \cdot r_p \cdot e^{i(\delta_{tp}+\delta_{rp})} - (e^{i\delta}-1) t_s \cdot r_s \cdot e^{i(\delta_{ts}+\delta_{rs})}\right] \cdot \hat{j} \, . \tag{3.8}$$

Since the intensity of the light can be calculated as:

$$I = \frac{cn\varepsilon_0}{2} \left|\vec{E}_i\right|^2 \tag{3.9}$$

, we have the final intensity of the light for the photodetector as:

$$I = I_0 \cdot ({t_p}^2 \cdot {r_p}^2 + {t_s}^2 \cdot {r_s}^2) \cdot [1 + \cos(\delta) \cdot \cos(2\Phi) + 2 \cdot \sin(\Phi) \sin(\Delta) \sin(\delta)] \tag{3.10}$$

, where $\tan(\Phi) = \frac{t_s r_s}{t_p r_p}$ and $\Delta = (\delta_{tp} + \delta_{rp}) - (\delta_{ts} + \delta_{rs})$. I_0 can be expressed as:

$$I_0 = \frac{cn\varepsilon_0}{4} {E_0}^2 \tag{3.11}$$

, where E_0 is the electrical field of the He-Ne laser directly after emission.

Using the Jacobi-Anger expansion [111], the phase shift by the PEM is expressed as:

$$\sin(\delta) = \sin(\frac{\pi}{2} \cdot \sin(\omega t)) = \sum_{m=0}^{\infty} 2 \cdot \mathrm{J}_{2m+1}(\frac{\pi}{2}) \cdot \sin\left[\left((2m+1)\omega\right) \cdot t\right] \tag{3.12}$$

and

$$\cos(\delta) = \cos(\frac{\pi}{2} \cdot \sin(\omega t)) = \mathrm{J}_0(\frac{\pi}{2}) + \sum_{m=1}^{\infty} 2 \cdot \mathrm{J}_{2m}(\frac{\pi}{2}) \cdot \cos\left[\left(2m\omega\right) \cdot t\right] \tag{3.13}$$

, where $J_i(\pi/2)$ is the Bessel function of the first kind at the point $\pi/2$. m is just an integer order for the summation.

Thus with a lock-in amplifier with 50 kHz (ω) and 100 kHz (2ω) as work frequency, we can extract the corresponding intensity at a certain frequency from (Equation 3.12) as following as ***first harmonics:***

$$I(\omega) = I_0 \cdot J_1(\frac{\pi}{2}) \cdot (\left|r_p\right| \cdot \left|t_p\right| \cdot \left|r_s\right| \cdot \left|t_s\right|) \sin[(\delta_{tp} + \delta_{rp}) - (\delta_{tp} + \delta_{rp})] \tag{3.14}$$

and from (3.13) as ***second harmonics:***

$$I(2\omega) = I_0 \cdot J_2(\frac{\pi}{2}) \cdot (\left|r_p\right|^2 \cdot \left|t_p\right|^2 - \left|r_s\right|^2 \cdot \left|t_s\right|^2) \ . \tag{3.15}$$

Before each experiment, $I(2\omega)$ is adjusted to be < 10^{-4}, which is approaching zero considering the noise level. With this adjustment the reflectivity and the transmission on the optical path is adjusted to:

$$\left|r_{p0}\right|^2 \cdot \left|t_{p0}\right|^2 \cong \left|r_{s0}\right|^2 \cdot \left|t_{s0}\right|^2 \tag{3.16}$$

, which leads to a simplification of the two harmonics during the growth as:

$$I(2\omega) \cong 2I_0 \cdot J_2(\frac{\pi}{2}) \cdot \left|r_{p0}\right|^2 \cdot \left|t_{p0}\right|^2 (\mathrm{Re}(\frac{r_p - r_{p0}}{r_{p0}}) - \mathrm{Re}(\frac{r_s - r_{s0}}{r_{s0}})) \tag{3.17}$$

and

$$I(\omega) = I_0 \cdot J_1(\frac{\pi}{2}) \cdot (\left|r_{p0}\right|^2 \cdot \left|t_{p0}\right|^2) \cdot [\mathrm{Im}(\frac{r_p - r_{p0}}{\left|r_{p0}\right|}) - \mathrm{Im}(\frac{r_s - r_{s0}}{\left|r_{s0}\right|})] \tag{3.18}$$

, if the relative change of the reflectivity on the sample surface and the transmission through the optical assembly parts are not strongly changed. Since the complex reflectivity can be written as $\frac{r_p - r_{p0}}{r_{p0}} = \Delta_p$ and $\frac{r_s - r_{s0}}{r_{s0}} = \Delta_s$, Equation (3.16) and (3.17) can be simplified as:

$$I(2\omega) - I_0(2\omega) \cong 2I_0 \cdot J_2(\frac{\pi}{2}) \cdot \left|r_{p0}\right|^2 \cdot \left|t_{p0}\right|^2 \cdot \mathrm{Re}(\Delta_p - \Delta_s) \tag{3.19}$$

and:

$$I(\omega) - I_0(\omega) = I_0 \cdot J_1(\frac{\pi}{2}) \cdot (\left|r_{p0}\right|^2 \cdot \left|t_{p0}\right|^2) \cdot \mathrm{Im}(\Delta_p - \Delta_s) \ . \tag{3.20}$$

After adjustment of $I(2\omega)$, the optical chopper is applied to determine the pre-factors in Equation (3.19) and (3.20). By applying an optical chopper with a frequency of ω_c = 1 kHz at the beginning of each measurement, the incoming laser intensity is:

$$I_0(t) = \frac{I_0}{2} + \frac{4I_0}{\omega_c \cdot T} \sum_{m=1}^{\infty} \frac{1}{2m+1} \sin((2n+1)\omega_c t) \tag{3.21}$$

, whereas the final intensity with lock-in amplifier is:

$$I_{chopper}(\omega_c) = \frac{4I_0}{\pi} \cdot \left| t_{p0} \right|^2 \cdot \left| r_{p0} \right|^2 . \tag{3.22}$$

Combining (3.19) and (3.20) with (3.22), we get:

$$\frac{I(2\omega)}{I_{chopper}(\omega_c)} \cong \frac{\pi}{2} \cdot J_2(\frac{\pi}{2}) \cdot \mathrm{Re}(\Delta_p - \Delta_s) \tag{3.23}$$

and

$$\frac{I(\omega)}{I_{chopper}(\omega_c)} \cong \frac{\pi}{4} \cdot J_1(\frac{\pi}{2}) \cdot \mathrm{Im}(\Delta_p - \Delta_s) . \tag{3.24}$$

, with $J_1(\pi/2) \sim 0.567$ and $J_2(\pi/2) \sim 0.250$.

Therefore, the real and imaginary part of the relative reflectivity change can be related directly to the first and second harmonics of the OIRD signal, respectively. In the real measurement the background noises $I_0(\omega)$ and $I_0(2\omega)$, which are not dependent on the reflectivity change, have to be considered and are measured for a while before starting real OIRD measurement. Therefore the equations for the data processing of the first and second harmonics signals in OIRD should be:

$$\frac{I(2\omega) - I_0(2\omega)}{I_{chopper}(\omega_c)} \cong \frac{\pi}{2} \cdot J_2(\frac{\pi}{2}) \cdot \mathrm{Re}(\Delta_p - \Delta_s) \tag{3.25}$$

and

$$\frac{I(\omega) - I_0(\omega)}{I_{chopper}(\omega_c)} \cong \frac{\pi}{4} \cdot J_1(\frac{\pi}{2}) \cdot \mathrm{Im}(\Delta_p - \Delta_s) . \tag{3.26}$$

The Equation (3.25) and (3.26) are applied for the data analysis in this work for the OIRD signal.

3.2.3.2 Observation of *in-situ* processes by OIRD

For a thin film system with the film thickness much smaller than the applied wavelength ($d << \lambda$), the phase change of electro-magnetic waves after propagation in the thin film is small. The relation between OIRD signal and the microscopic parameters can be simplified as [112]:

$$\Delta_p - \Delta_s \approx i \frac{4\pi n_0 \cos\varphi_0 \tan^2\varphi_0 \varepsilon_s}{\lambda(\varepsilon_s - \varepsilon_0 \tan^2\varphi_0)(\varepsilon_0 - \varepsilon_s)} \left(\frac{d_f(\varepsilon_d - \varepsilon_s)(-\varepsilon_0 + \varepsilon_d)}{\varepsilon_d}\right). \tag{3.27}$$

This can be used to interpret the thin film thickness change and optical permittivity change during growth or redox processes.

If both the substrate and the thin film have low conductivity, the imaginary part of the optical permittivity is small. Therefore the imaginary part of the reflectance difference dominates. The signal can thus be simplified to:

$$\mathrm{Im}(\Delta_p - \Delta_s) \approx \mathrm{Re}\left(\frac{4\pi n_0 \cos\varphi_0 \tan^2\varphi_0 \varepsilon_s}{\lambda(\varepsilon_s - \varepsilon_0 \tan^2\varphi_0)(\varepsilon_0 - \varepsilon_s)} \left(\frac{d_f(\varepsilon_d - \varepsilon_s)(-\varepsilon_0 + \varepsilon_d)}{\varepsilon_d}\right)\right)). \tag{3.28}$$

The growth process without strong reduction of the film or substrate can thus be interpreted with the imaginary part of the reflectivity difference, i.e. the first harmonics of the OIRD signal. The example for STO homoepitaxy on STO can be found in ref. [109].

If the thin film conductivity or the substrate conductivity is changed strongly during a redox process, the reflectance difference can be simplified to:

$$\mathrm{Re}(\Delta_p - \Delta_s) \approx \mathrm{Im}\left(\frac{4\pi n_0 \cos\varphi_0 \tan^2\varphi_0 \varepsilon_s}{\lambda(\varepsilon_s - \varepsilon_0 \tan^2\varphi_0)(\varepsilon_0 - \varepsilon_s)} \left(\frac{d_f(\varepsilon_d - \varepsilon_s)(-\varepsilon_0 + \varepsilon_d)}{\varepsilon_d}\right)\right)). \tag{3.29}$$

One example for a redox process in STO thin films on STO, studied by OIRD, has been shown in ref. [110].

Other material systems like Xe absorption on Ni and Cu surface can also be studied by OIRD, which is not in the scope of this thesis. For more details please refer to ref. [113]. It has to be mentioned that the OIRD technique is not widely applied in the thin oxide film growth, lacking complementary experiments to prove the observations from OIRD signals. Therefore the study in our EOC lab has the advantage of helping understanding the processes generating OIRD signals during oxide thin film growth. For more details see the chapter 5.

3.2.3.2 Experimental set-up of the OIRD system

The experimental set-up with the electrical and optical elements in OIRD is illustrated in Figure 3.8, which is a home-made equipment with help from Prof. X. D. Zhu in University of California, Davis. Two optical tables are employed to support the optical elements for incident laser and reflected laser, respectively. The red arrows mark the optical path of the laser. For the standard measurement during thin film growth, the He-Ne laser will go through the holes of the static optical chopper. After being spread with a beam splitter, an attenuator with double attenuating glass can tune the intensity of the laser spot. The linear polarizer

1 (LP1) generates the *p*-polarization, while the photo-elastic modulator (PEM) modulates the electrical field of the laser with 50 kHz, which is controlled by the PEM controller. The quarter wave plate (QWP) can retard the phase shift between *p*- and *s*-polarization to guarantee the initial $I(2\omega)$ to approach zero. Being focused onto the sample and reflected from the sample, the reflected laser will be firstly polarized by the linear polarizer 2. The final laser intensity is recorded by the photodetector and transferred to the two lock-in amplifiers: the lock-in 1 has the frequency of 50 kHz, which is the same as the PEM frequency and delivers $I(\omega)$; the lock-in 2 has the frequency of 100 kHz, which is double the PEM frequency and delivers $I(2\omega)$. At the beginning of each deposition, the mechanical chopper is activated and the intensity detected by the photodetector is: $I(\omega_c = 1\ \text{kHz})$.

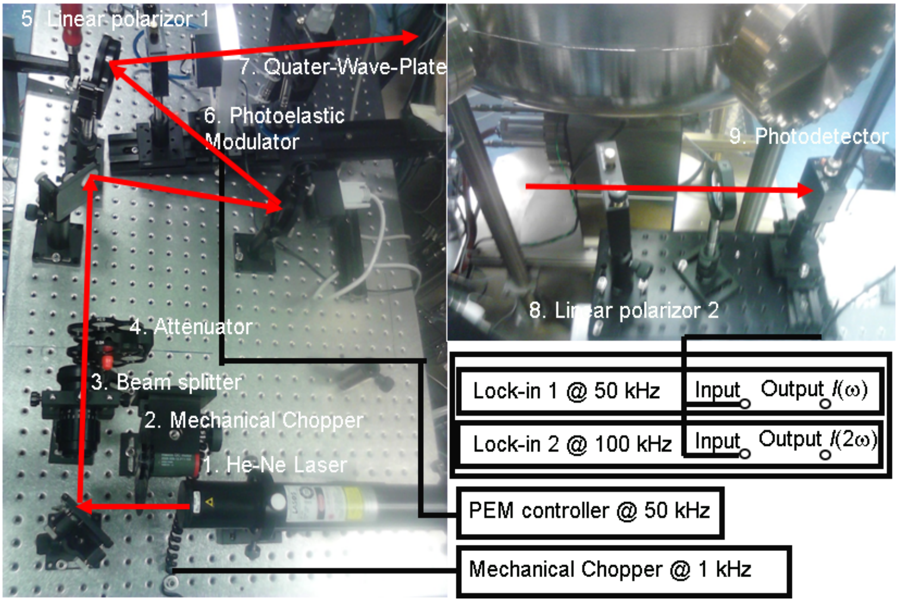

Figure 3.8 *The optical and electrical elements in OIRD system with the primary construction*

The purpose of the optical tables is to reduce vibrations possibly generated from the ground. Indeed, with this setup one OIRD curve with low noise level has been observed. However, a weak reproducibility of the signals has been observed between measurements. The reason could be following: Although all the optical elements are mounted on an optical table with damping mechanism, where the noise influence from the ground on the optical elements is strongly reduced, the chamber and the two optical tables have distinguishable vibrations (illustrated in Figure 3.9). This effect may not strongly deteriorate one measurement, but results in strong discrepancies between different measurements and reduces the reproducibility of experimental OIRD results.

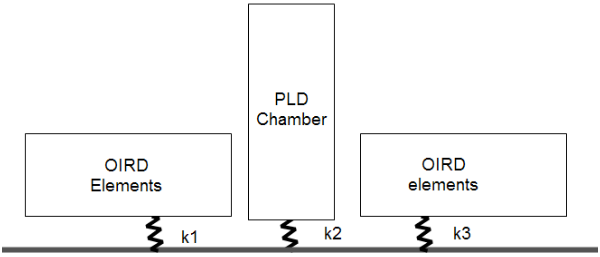

Figure 3.9 *Simplified mechanical models for the PLD chamber and the OIRD elements, when the optical tables are applied. The PLD chamber, the OIRD elements for the incidents and the OIRD elements for the output have different oscillation strengths, which are represented by k1, k2 and k3. Therefore they have different oscillation frequencies and can vary heavily from experiment to experiment. It is also possible that the components drift during the measurements and then deteriorate the reproducibility.*

3.2.3.3 Set-up improvement

To overcome the problem raised by the different oscillations of PLD chamber and the two optical tables, a new construction principle is developed by me. All the optical elements are encapsulated in two boxes (Figure 3.10) and the PLD chamber and the other optical elements have a mechanical static connection.

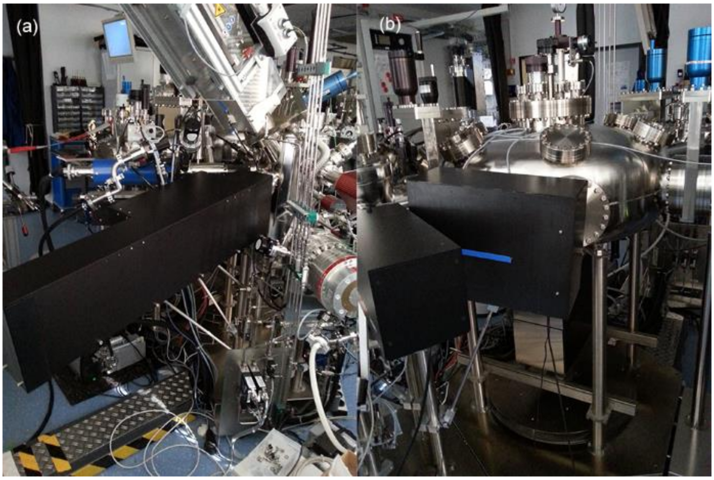

Figure 3.10 *(a) The box encapsulating the optical elements for the incidence of the laser beam. (b) The box encapsulating the optical elements for the output of the laser beam. The box marked with the blue marker is the OIRD box with signal detection elements.*

By establishing the encapsulation, the vibration of three elements is kept similar to each other (Figure 3.11). As discussed above, the former setup has low noise level but bare reproducibility of the results. By new setup, the reproducibility is strongly increased with moderate noise level. The reproducible results are presented in chapter 5.

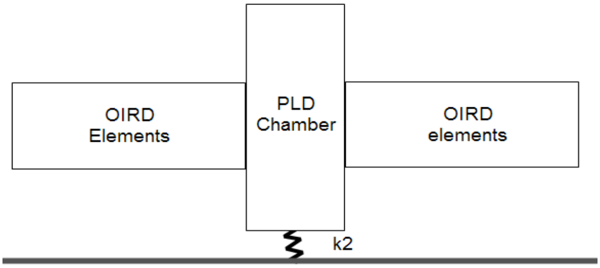

Figure 3.11 *Illustration of the whole OIRD system with the PLD chamber as a vibration unit. The spring with a force constant of k2 represents the unified oscillation of the PLD and OIRD boxes as a whole.*

3.2.4 Cold cathode gauge (CC)

For high vacuum with pressure $p < 10^{-3}$ mbar in the PLD chamber, a cold cathode gauge (CC) (IKR 270© from Pfeiffer GmbH) is applied. The cold cathode gauge measures the ionized particle number (n) in the given gauge volume (V) at controlled temperature (T), where the pressure can be determined with the ideal gas law:

$$p = \frac{n}{V} RT \tag{3.30}$$

, where R is the universal gas constant as a product of the Boltzmann constant and the Avogadro constant.

The general working principle of a cold cathode gauge is illustrated in Figure 3.12. The electrons are generated from the emitting cathode (K), where a strong electrical field is applied. The electrons are accelerated by the field between the emitting cathode (K) and the anode (A) and have a high kinetic energy. These high energetic electrons will knock electrons off the neutral gas molecules M and ionize the molecules into M^{n+}. The positively charged ions will be collected by the collecting cathode (C), as the electrons are collected by the anode.

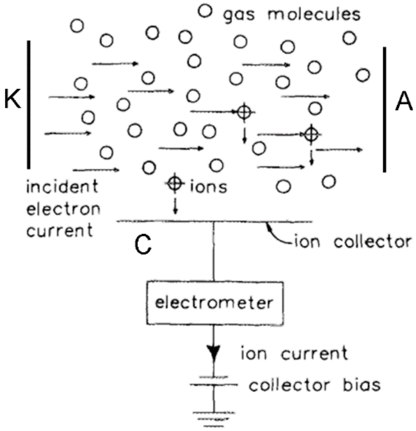

Figure 3.12 *Working principle of the cold cathode gauge. The image is reproduced from ref. [114].*

The ionization process of the gas molecules becomes hardly accessible as the pressure is reduced to 10^{-5} mbar, where the mean free path of the gas molecules approaches 10 m. Therefore the cold cathode gauge, which is capable of measuring pressures down to 10^{-10} mbar, employs normally a collimated magnetic field to focus the electrons and increase the possibility for electrons to hit the molecules. This magnetic field and the distribution of electrons are illustrated in Figure 3.13. The gas molecules can thus be heavily ionized and the measurement of the pressure becomes more accurate.

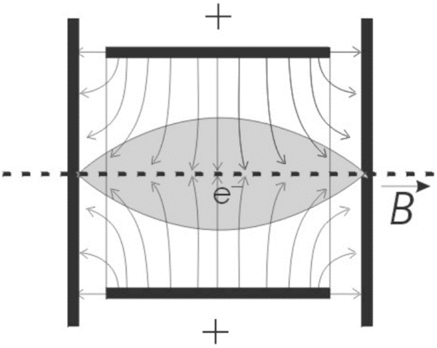

Figure 3.13 *Field distribution within a cold cathode gauge. The arrows show the directions of the electric field in the cold cathode gauge. The grey region is for the electron space charge. The image is reproduced from ref. [115].*

The heavy ionization process can further influence the gas equilibria and thereby on the defect equilibria of samples heated within the PLD chamber. One example is the generation of H^0 from H_2O molecules, which can be absorbed by the LAO surface and change the interface conductivity of LAO/STO [87]. This effect may furthermore have strong impact on the redox process in the PLD chamber and is discussed in the chapter 6.

3.2.5 Mass spectrometer (MS)

Quadrupole mass spectrometry (*PrismaPlus*© from Pfeiffer GmbH) is used to identify the residual gas species at low total pressures in chapter 6. The working principle for a quadrupole mass spectrometry is illustrated in Figure 3.14. The incoming neutral molecules or atoms from the PLD chamber are firstly ionized by an electron impact ionizer. The ions travel to a region with four rod-shaped electrodes parallel to each other. A mixed DC+AC potential $U+V\cos(\omega t)$ is applied on the four electrodes, two positive in the horizontal and two negative in vertical directions. Therefore the potential of a specific position can be described as:

$$\Phi = [U + V\cos(\omega t)]\frac{x^2 - y^2}{2r_0{}^2} \tag{3.31}$$

, where Φ is the potential for the particle at the position (x, y) with respect to the central line of the four electrodes. The r_0 is the distance from the center of the four electrodes to the surface of all electrodes, which are symmetrically arranged.

Neglecting the gravitation, which is not playing a crucial role for the high field case, the electrostatic interaction is the only source of force. The electrostatic field is the gradient of the local potential:

$$E = \nabla\Phi = ([U + V\cos(\omega t)]\frac{x}{r_0{}^2}, -[U + V\cos(\omega t)]\frac{y}{r_0{}^2}, 0)\,. \tag{3.32}$$

And the corresponding force components in three directions are:

$$\begin{aligned} F_x &= q\frac{\partial\Phi}{\partial x} = q[U + V\cos(\omega t)]\frac{x}{r_0{}^2} \\ F_y &= q\frac{\partial\Phi}{\partial y} = -q[U + V\cos(\omega t)]\frac{y}{r_0{}^2}\quad. \\ F_z &= q\frac{\partial\Phi}{\partial z} = 0 \end{aligned} \tag{3.33}$$

Since the velocity of the particles is much lower than the light speed, no relativistic effects have to be taken into consideration. Therefore the simple Newton’s rule can be applied to describe the movement of the charged particles as:

$$
\begin{aligned}
m\frac{\partial^2 x}{\partial t^2} &= q[U + V\cos(\omega t)]\frac{x}{r_0{}^2} \\
m\frac{\partial^2 y}{\partial t^2} &= -q[U + V\cos(\omega t)]\frac{y}{r_0{}^2} \; . \\
m\frac{\partial^2 z}{\partial t^2} &= 0
\end{aligned}
\tag{3.34}
$$

The three equations are called Mathieu's equations and describe a set of properties. The most important one is that the solution for the ($x(t)$, $y(t)$, $z(t)$), which is the trajectory of the particles, is solely dependent on the ratio between U/V and q/m, but not dependent on the initial conditions [116]. Therefore, at given U and V, only particles with certain q/m ratio have the trajectory that converges to the center of the four electrodes, which is also the position of the detector. The other particles will have unstable trajectory and hit the electrodes before arriving at the detector, where the electrons are directly collected by a Faraday-cup for pressures up to 10^{-4} mbar or amplified by a secondary electron multiplier (SEM) for lower pressures. For a full spectra scan, U/V will be varied over a large range, while for a transient scan for a typical q/m ratio the U/V is kept constant during the scanning time. For a detailed description for the quadrupole filter please refer to ref. [117].

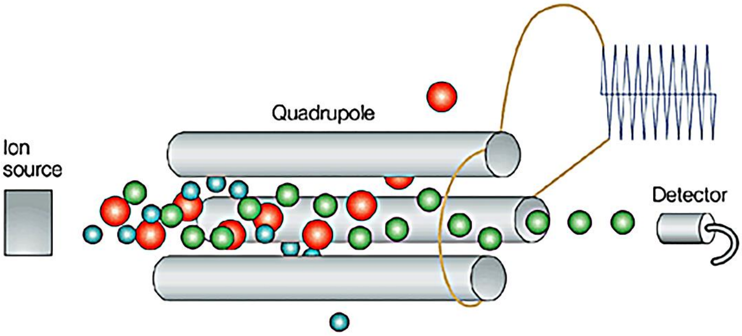

Figure 3.14 *The working principle of a quadrupole mass spectrometer. The image is reproduced from ref. [118].*

Similar as the cold cathode, the quadrupole mass spectrometer utilizes the ionization of the gas molecules to increase the sensitivity at low pressures. This in turn, feeds ionized or dissociated species back to the PLD chamber and thus influences the redox processes. The impact of the mass spectrometer on the redox process in the chamber will be discussed in the chapter 6 as well.

3.3 Thin film characterization methods

3.3.1 AFM

Ever since its invention in 1986 [119], atomic force microscopy (AFM) is a widely used technique for the material surface characterization, especially for the non-conducting material surface without possibility for scanning tunneling microscopy (STM) characterization. In the following, the basic principles about the contact mode AFM and tapping mode AFM will be illustrated.

The basic working principle for a ***contact mode AFM*** with constant amplitude is illustrated in Figure 3.15. The changed interaction between the tip of the cantilever and the sample surface results in a change of the deflection of the laser beam focused on the tip (Figure 3.15). By adjusting the position of the cantilever, the deflection can be compensated and the relative height of this position is acquired. By scanning through the surface, the whole surface morphology can be reconstructed.

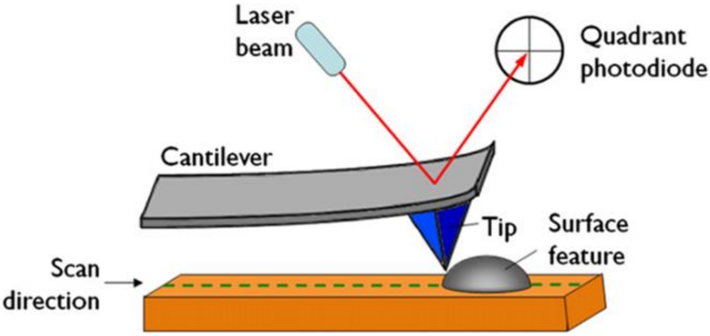

Figure 3.15 *The working principle of the AFM working in contact mode. The figure is reproduced from ref. [120].*

For an AFM working in ***tapping mode*** with constant amplitude, the situation is different. The AFM cantilever is connected to a piezo-element that is driven by an AC voltage signal, while the deflection of the cantilever is measured through the laser beam reflection to a photodetector (Figure 3.16 (a)). The free oscillating AFM cantilever has a resonance frequency (ω_0) around several hundreds of kHz (solid curve in Figure 3.16 (b)). The amplitude at the resonance frequency is measured by a lock-in element. By approaching the tip on the cantilever to the surface, the interaction between tip and surface sets in and the resonance frequency is shifted, which introduces a reduction of the oscillation amplitude (broken curves in Figure 3.16 (b)). A set-point (ω_{sp}) is given by defining the relative shift of the resonance frequency, either in the attractive regime or the repulsion regime. During the scanning of this cantilever over the surface, height changes can change the tip-surface interaction and change the oscillation amplitude at a chosen frequency. The feedback loop will adjust the cantilever heights to shift the resonance curve back to a defined frequency shift. The signal of the cantilever height thus represents the surface morphology. Due to the high sensibility of the resonance curve to the surface-tip interaction, the tapping mode supplies a high resolution not purely restricted to the tip radius.

In chapter 4, contact Mode AFM by *Omicron*© *VT SPM module*® with a single crystalline diamond tip with a tip radius lower than 10 nm (*NaDiaProbes*® from *nanoScience instruments*©) is used to characterize the morphology of sub-monolayer STO. Other experiments with low requirement on the UHV condition have been characterized *ex-situ* with tapping mode AFM in air, where the AFM system is *PICOStation*™ from *S.I.S. GmbH* and the tip radius of the Si cantilever is around 7 nm.

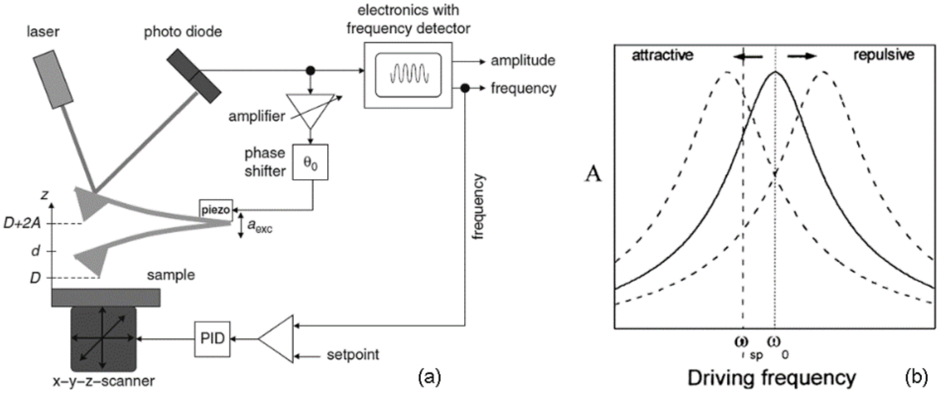

Figure 3.16 *(a) The basic elements in the tapping mode AFM. (b) The resonance curve for a free cantilever with tip (solid line) and for cantilever with tip-surface interaction, which are either attractive (broken curve left) or repulsive (broken curve right). (a) is adapted from ref. [121] and (b) is adapted from ref. [122].*

3.3.2 LEED

Low energy electron diffraction (LEED) employs electrons with a low kinetic energy typically between 10 and 200 eV, which enable 2D diffraction restricted to the surface atomic layer. Two characteristics are important for the LEED: the short de Broglie wavelength enables the 2D diffraction, whereas the low mean free path of electrons confines the interaction between electrons and matter to the surface atom layer. For the electrons with low speed, the relativistic effects can be neglected. Therefore, the wavelength of the electrons can be estimated as:

$$\lambda = \sqrt{\frac{1.5(eV)}{E_0}} nm \tag{3.35}$$

Taking 100 eV as kinetic energy of electrons, we get ~ 0.122 nm as the de Broglie wavelength, which is in the same order of magnitude as the lattice constant of most materials.

The inelastic mean free path (IMFP) is dependent on the kinetic energy of the electrons as well. E.g. for 100 eV the mean free path of electrons is lower than 1 nm [123], which can also be treated as the information depth of LEED. Therefore LEED is surface sensitive.

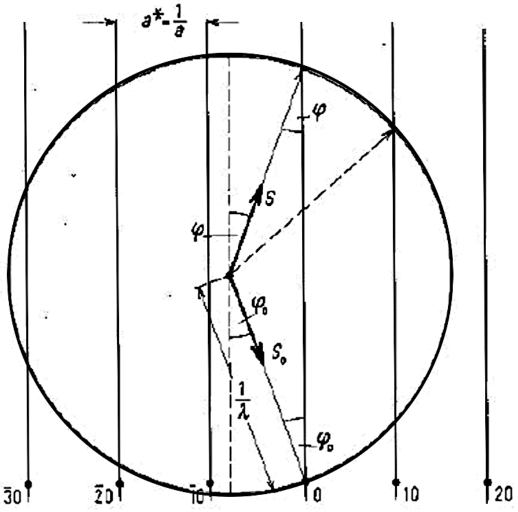

Figure 3.17 *Side view for an Ewald sphere and reciprocal rods from a cubic surface in LEED. The upper part of the Ewald sphere is the position of the screen. The image is reproduced from ref. [124].*

Similar as for RHEED, the diffraction pattern by LEED can be determined by the Ewald sphere and the reciprocal lattice of the surface (Figure 3.17), whereas the difference to RHEED is the almost normal incidence of LEED:

$$\varphi_0 \sim 0 \tag{3.36}$$

The diffraction has also to satisfy the Bragg condition, which can be expressed in the form of wave vectors:

$$\vec{S} - \vec{S}_0 = \vec{G} \tag{3.37}$$

, where $\vec{G}$ is the reciprocal lattice vector that is variable, $\vec{S}_0$ the wave vector of the incident beam and $\vec{S}$ the diffracted wave vector. For $\vec{G} = 0$ as shown in the Figure 3.17, the diffracted spot is the (0 0) spot or specular spot. The index for $\vec{G}$ is the name of the diffracted spot. In practice if the incidence is not normal, the specular spot can be found as follows: one can adjust the de Broglie wavelength of electrons by tuning the kinetic energy of electrons. The specular spot (0 0) stays at the same position, whereas the other spots are shifted due to the changed radius of the Ewald sphere.

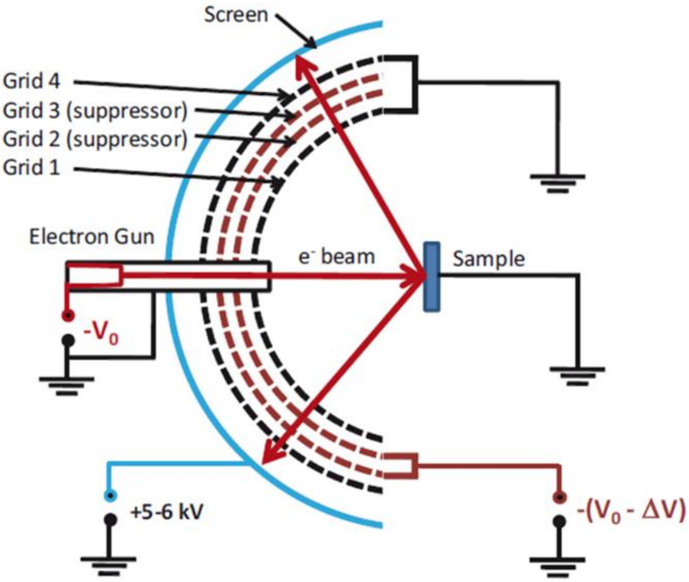

Figure 3.18 *Working principle of LEED. The image is adapted from ref. [125].*

A typical construction is depicted in Figure 3.18. The electrons are generated by an electron gun and accelerated by a voltage bias (V_0). The electron beam is diffracted on the surface of the sample and propagate further to the screen. The screen is negatively charged with typically 5-6 kV, which attracts electrons electrostatically to increase the diffraction spots intensity. A set of grids lies between the screen and the sample to optimize the resolution.

There are many possible interpretations of the LEED pattern (Figure 3.19):

1) The most intuitive information delivered by LEED pattern is the short range order like e.g. surface reconstruction. A detailed discussion on the STO surface reconstructions during STO growth will be carried out in chapter 4.

2) With the analysis of the spot’s intensity change with variation of incident electron kinetic energy, the absorption of electrons at different energies can be determined. As a consequence, the corresponding surface electron band structure can be determined. For more details about this kind of analysis please refer to ref. [127].

3) From the spot profile analysis, the long range order like the terrace length can be obtained. Similar to the situation in RHEED, the additional periodicity introduced by the terraces on a vicinal surface can lead to modulation of 2D reciprocal rods, which result in the modification of specific spots.

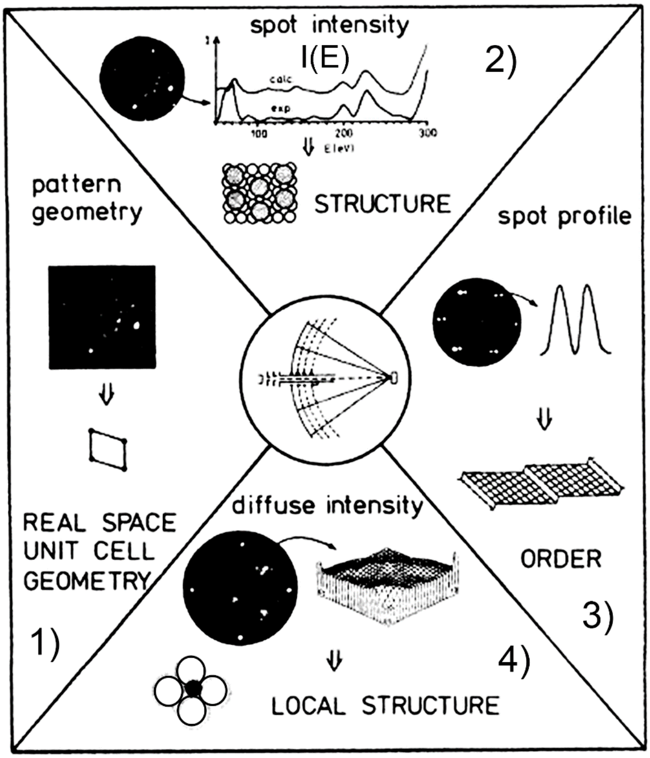

Figure 3.19 *The different analysis possibilities by LEED. The image is adapted from ref. [126]. The discussion on each possibility is carried out in the following text.*

4) The diffuse intensity of the spot reveals the local structure for specific atoms. The relative shift of local atoms to the average position that is responsible for the LEED spot is the origin of the diffuse spot. By analyzing the shape of the diffuse spot, the relative shift of local atoms can be investigated. This analysis is useful for the disordered adsorption of molecules on the surface, which is not in the scope of this thesis. For more about the diffuse intensity analysis plea refer to ref. [128].

In this work *in-situ* LEED is carried out on a *SPA-LEED*© system from *Omicron Nanotechnology GmbH*, whereas the *ex-situ* LEED is carried out on a home-built LEEM system in cooperation with the physics department of Leiden University.

3.3.3 Hall measurement

Hall measurements are widely applied for the determination of the charge carrier concentration in different material systems. Hall measurement is developed based on the Hall-effect that has been discovered by Edwin H. Hall in 1879 [129].

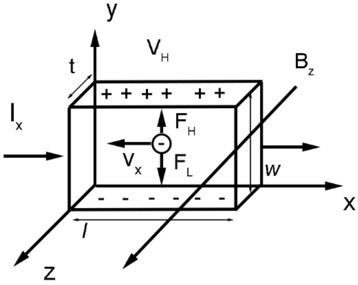

Figure 3.20 *Principle of the Hall Effect at a stationary state, where the electron flow is parallel to the x-direction. The directions of different fields and the corresponding forces are marked with arrows.*

The principle of the Hall-effect is shown in Figure 3.20. Considering an n-conducting semiconductor as an example, the majority charge carriers are electrons. By applying a magnetic field (B_z) perpendicular to the sheet sample plane with a width of w, a thickness of t and a length of l, in which a current flow (I_x) is present, the electrons experience a Lorentz force (F_L) in y-direction as a vector product of v_x and B_z. The electrons flow to one side of the plate and build up an electrical potential, which is named as Hall voltage V_H and enables the steady flow of electrons. The Lorentz force and the electrostatic force (F_H) for such a potential is in equilibrium in y-direction, which leads to:

$$ev_xB_z = e\frac{V_H}{w} \tag{3.38}$$

The current flow in the x-direction can be expressed as:

$$I_x = -nwtev_x \tag{3.39}$$

, where n is the electron concentration, v_x the electron velocity in the direction of the current flow and e the elementary charge. The negative sign comes from the fact that the flow direction of current is opposite to the electron movement.

For a sample without defined conductive layer thickness t, like the LAO/STO interface, the sheet carrier concentration (n_S) is used to describe the carrier number per area with the relation:

$$n_S = n \cdot t \tag{3.40}$$

, therefore the sheet electron concentration can be determined:

$$n_S = -\frac{I_x B_z}{eV_H} \tag{3.41}$$

, where the term $\frac{V_H}{I_x B_z}$ is often referred as the Hall resistance R_H.

The sheet carrier concentration is related to the Hall resistance simply through:

$$n_S = -\frac{1}{eR_H}. \tag{3.42}$$

The sheet resistance (R_S, sometimes referred as R_{xx}) is also frequently used:

$$R_S = \frac{\rho}{t} \tag{3.43}$$

, where ρ is the electrical resistivity.

Since the electrical resistivity is expressed as:

$$\rho = \frac{V_x wt}{I_x l} = -\frac{E_x}{nev_x} \tag{3.44}$$

, where E_x is the electrical field in x-direction, the electron mobility is:

$$\mu = \frac{v_x}{E_x} = -\frac{1}{ne\rho}. \tag{3.45}$$

The electron mobility can also be expressed by the sheet carrier concentration and sheet resistance:

$$\mu = \frac{v_x}{E_x} = -\frac{1}{en_S R_S}. \tag{3.46}$$

As a short summary, by measuring the sheet resistance (R_S) and the Hall resistance (R_H) both the sheet carrier concentration (n_S) and the electron mobility (μ) can be acquired in the n-type semiconductor. The same principle holds for p-type semiconductors. However, the sign of Hall-voltage should be positive since the flow direction of holes in p-type semiconductor is the current flow direction. This leads to the possibility of distinguish p-and n-semiconductors from the sign of Hall-voltage.

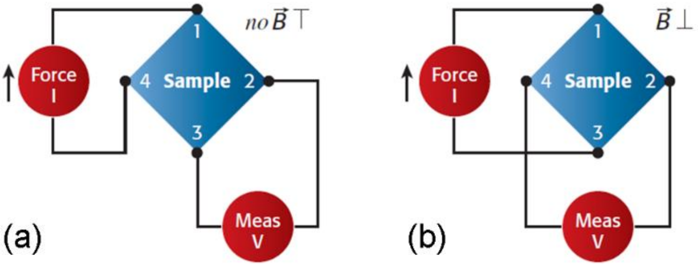

Figure 3.21 *Van der Pauw configuration for (a) sheet resistance and (b) Hall resistance measurements. The image is adapted from ref. [130].*

For the measurement of both, sheet resistance (R_S) and Hall resistance (R_H), the van der Pauw configuration is used. The configurations are illustrated in Figure 3.21. For the sheet resistance (R_S) measurement (Figure 3.21 (a)), the current is applied through the contacts 14 (or 12) and the voltage is measured through 23 (or 43). The corresponding resistances are $R_{14,23}$ and $R_{12,43}$. The sheet resistance R_S can be determined from an implicit function [131]:

$$e^{-\pi\frac{R_{14,23}}{R_S}}+e^{-\pi\frac{R_{12,43}}{R_S}}=1 \tag{3.47}$$

For the measurement of the Hall resistance (Figure 3.21 (b)), the current is applied between 1 and 3 (or 2 and 4) and the Hall voltage is measured between 2 and 4 (or 1 and 3). The corresponding resistances are $R_{13,24}$ and $R_{24,13}$. The Hall resistance is thus an average of the two measurements:

$$R_H=\frac{R_{13,24}+R_{24,13}}{2}\,. \tag{3.48}$$

All Hall measurements are carried out in a *Lakeshore*® *8400H*© system. For the samples with a low resistance $< 10\ \mathrm{k}\Omega$, only DC measurements are necessary. For the samples with a higher resistance $> 100\ \mathrm{k}\Omega$, AC Hall measurements are applied. For details about DC and AC measurements, please refer to ref. [132].

3.3.4 X-ray diffraction (XRD)

As discussed in chapter 2, the negatively charged cation vacancies in STO will lead to a lattice expansion because of the electrostatic force between them and the oxygen ions [12]. The *c*-lattice expansion in the STO thin film represents the concentration of the cation vacancies. The lattice expansion is characterized by the difference of *c*-lattice constant between films and substrates which can be measured using the X-ray diffraction.

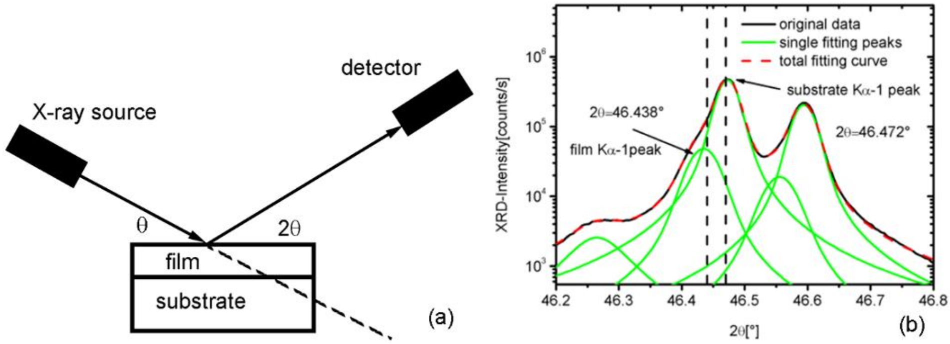

Figure 3.22 *(a) Working principle of XRD for thin film and substrate system. (b) a typical XRD scan for the crystalline STO thin film on a STO single crystal substrate. The black curves are for the measured data, while the green curves are for the fitted peaks. The red line is the sum of the fitted peaks. The broken lines are the expected positions of the* $K_{\alpha 1}$ *peaks of film and substrate, respectively.*

The X-ray diffraction analysis works with the following principle (see Figure 3.22 (a))): After generated from the X-ray tube, where not only X-rays with the characteristic wavelength, but also X-rays with a continuous spectrum are generated, the X-ray beam will be focused and filtered to hit the sample just in a small region. The periodic lattice planes of the single crystal sample result in a constructive interference of the incoming X-rays at a certain angle, which is called the Bragg angle. The determination of the Bragg angle follows the Bragg equation:

$$n\lambda = 2d\sin\theta \tag{3.49}$$

, where θ is the emission angle of the diffracted electrons, λ the de Broglie wavelength of the electrons, d is the distance between two diffraction centers and n the diffraction order.

At the angle of constructive interference an intensity peak can be received by the detector at the position 2θ. By rotating the sample (θ) and detector (2θ) the angle for the peak intensity can be found, thus the distance between lattice planes can be calculated.

For the determination of the out-of-plane lattice parameter, 200 nm thick homoepitaxial STO films were grown and characterized by XRD with an *X'pert MRD 3040®* system. The Cu-$K_{\alpha 1}$ and $K_{\alpha 2}$ X-ray with a wavelength of 0.154 nm is used. Only a Nickel-filter is used for suppression of Cu-K_{β} line.

For all the samples in chapter 4, the distance between (001) lattice planes, which is the length of the *c*-axis of $SrTiO_3$, will be investigated. Since the substrate and the film have almost the same lattice parameters, the only difference is the cation vacancies induced increase in *c*-lattice constant and reduction of the Bragg angle for the film. The Bragg-angle shift will be observed as extra peaks in the vicinity of substrate peaks, thus the observation range in this work is restricted to the $K_{\alpha 1}$, $K_{\alpha 2}$ peaks and the Bremsstrahlung peaks around the $SrTiO_3$(001) lattice plane.

The position of the highest and the second highest peaks should be the $K_{\alpha 1}$ and $K_{\alpha 2}$ peaks from substrates because the substrate is much thicker than the film and the X-ray beam penetrates not only the film but also the substrate. The film peaks (both $K_{\alpha 1}$, $K_{\alpha 2}$ and the Bremsstrahlung) are then fitted using the software *Fityk*©. The 2θ position of the $K_{\alpha 1}$ peak from the substrate is normalized to the theoretical value of 46.472° and the 2θ position of the $K_{\alpha 1}$ peak from the film is drawn from the fitting. The *c*-lattice constant of the film can then be calculated using the Bragg equation. An example of fitting is shown in Figure 3.22 (b).

3.3.5 X-ray photoelectron spectroscopy (XPS)

3.3.5.1 Basic principle

X-ray photoelectron spectroscopy (XPS) is based on the photoelectric effect induced by X-ray radiation, which describes the general phenomenon of electron emission from a material's surface by illumination of X-rays. The kinetic energy of the emitted electrons (E_{kin}) depends on the photon energy ($\hbar\omega$), the work function (Φ) and the binding energy of the electrons (E_{binding}):

$$E_{kin} = \hbar\omega - \Phi - E_{binding} \tag{3.50}$$

, where the binding energy is the difference between a specific energy level and the Fermi energy.

Therefore, by measuring the spectrum of the electron kinetic energy with an electron energy analyzer the electronic structure of the material can be represented (Figure 3.23). For more details please refer to ref. [133].

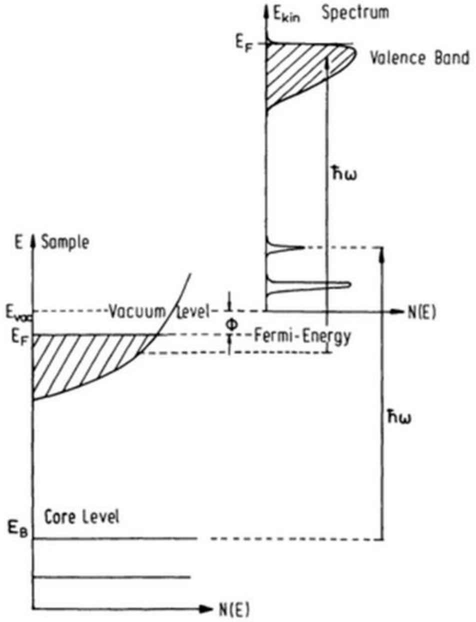

Figure 3.23 *Electronic structure of the material and the spectra of the kinetic energy emitted from the sample surface. The left part is the real electronic structure of the sample, whereas the right part is the measured spectrum. The electrons by different states are activated differently: the core level electrons form discrete peaks, while the electrons in valence band result in continuous broad band in the spectrum. The image is taken from ref. [133].*

The general working principle of XPS is depicted in Figure 3.24. A point source of X-rays is generated by focusing of an electron beam onto the metal anode. The incidence angle of the X-rays (ψ) is constant, whereas the detection of the emitted electrons is carried out at various angles (ϑ). The emitted electrons with different kinetic energy are fed through an electron energy analyzer with a voltage applied between its two hemispheric surfaces. For a given voltage only electrons with corresponding kinetic energy can pass the slit and arrive at the detector. By varying the voltage applied on the two hemispheric surfaces in the electron energy analyzer, the spectrum of electron kinetic energy is determined. In this thesis, the XPS measurements were performed with a PHI 5000 Versa Probe (*Physical Electronics* Inc., USA) with Al K_α X-ray illumination, a pass energy of 29.35 eV at various photoemission angles using electron neutralization.

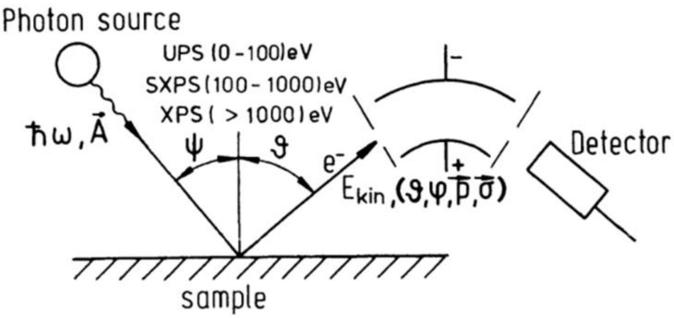

Figure 3.24 Sketch of a XPS system. The image is reproduced from the ref. [133].

In the following, we take STO as an example to show how the surface termination ratio and the thin film stoichiometry can be determined by XPS.

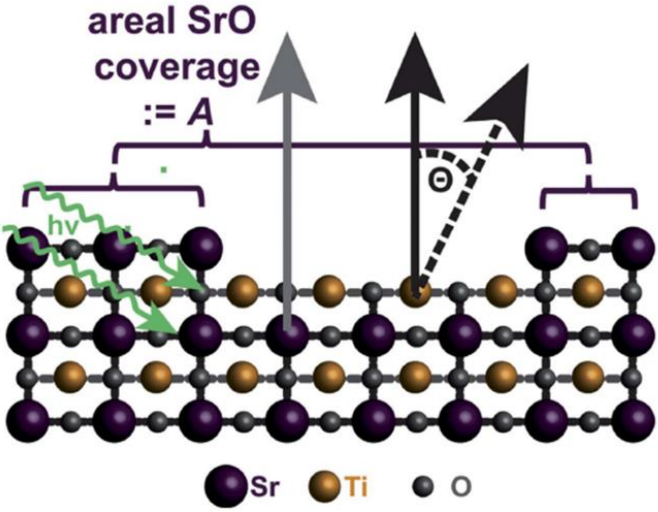

Figure 3.25 Model for the situation of a certain surface termination ratio. The image is reproduced from ref. [134].

Not only the electronic structure of the material has to be taken into consideration, the structural factors of the material, especially the chemistry of the bulk and surface are of importance. For the example of STO(001), the intensity ratio between Sr3d and Ti2p peaks in the XPS spectrum is dependent on the Sr/Ti ratio in thin film (N^{Sr}/N^{Ti}), surface termination ratio of SrO and TiO_2 (A and B) and the emission angle of photoelectrons (θ) [134]:

$$\frac{I_{total}^{Sr3d}}{I_{total}^{Sr3d}+I_{total}^{Ti2p}}=\frac{(A+B\,exp(-\frac{a/2}{cos\theta\lambda^{Sr3d}}))N_0^{Sr}\sigma^{Sr}}{(A+B\,exp(-\frac{a/2}{cos\theta\lambda^{Sr3d}}))N_0^{Sr}\sigma^{Sr}+(A\,exp(-\frac{a/2}{cos\theta\lambda^{Ti2p}})+B)N_0^{Ti}\sigma^{Ti}} \tag{3.51}$$

, where A is the areal coverage of a SrO monolayer, N_0^{Sr} is the total atomic concentration of Sr in the film and σ^{Sr} is the sensitivity factor for a Sr atom. Correspondingly, B = 1 - A is the areal coverage of a TiO_2 monolayer, N_0^{Ti} is the total atomic concentration of Ti in the film and σ^{Ti} is the sensitivity factor for a Ti atom. a is the lattice constant of $SrTiO_3$ which is assumed unchanged and $\cos\theta$ is the emission angle of ejected photoelectrons. λ^{Sr3d} and λ^{Ti2p} are the wavelengths of the ejected photoelectrons for the Sr3d peak and the Ti2p peak, respectively. Therefore, by fitting the ratio between Sr3d peak and Ti2p peak as a function of the incident angle, the thin film stoichiometry (N_0^{Ti} and N_0^{Sr}) and the surface termination ratio (A and B) can be acquired. For a detailed description of the theoretical model see reference [134].

This model is applied for the characterization of the SrO termination for SrO deposition in the PLD chapter 3.4 and the characterization of SrO termination ratio during STO growth in chapter 4.

3.4 Termination control on STO single crystals

The surface termination ratio control is very important for future electronic devices based on surface and interface engineering. One example is the interface between (001)$LaAlO_3$ and (001)$SrTiO_3$, where a conductive interface or a two dimensional electron gas (2DEG) between two band insulators can be generated. This interface is very sensitive to the termination of the $SrTiO_3$ substrate. While the TiO_2 termination can generate the 2DEG, the SrO termination can generate no conductive interface [88]. For details see the discussion in chapter 2.

3.4.1 TiO_2 termination

For as received STO single crystals, the surface is mixed terminated with SrO and TiO_2. Since the SrO region is hydrophilic, adsorption of the water to the surface can hydrate SrO to $Sr(OH)_2$. With a subsequent buffered HF etching, the $Sr(OH)_2$ can be removed and the surface is TiO_2 terminated. Post annealing in air at 950 °C for 2 hours enables the diffusion of surface atoms and the energetically favored terrace structure can be formed with single terrace heights of 0.4 nm. For details please refer to the previous work in our group [31, 135].

3.4.2 SrO termination

By controlled PLD growth of SrO on TiO_2 terminated STO, the surface termination engineering for different ratios of SrO termination can be carried out. The quantitative verification of the surface termination is carried out by XPS measurements. The ratio between Sr3d and Ti2p peak intensity can be utilized to determine the surface termination and the thin film cation stoichiometry. Especially for SrO growth on TiO_2

terminated STO single crystals, where the thin film cation stoichiometry is Sr/Ti = 1, the surface termination can be precisely determined.

For this purpose, sub-monolayer SrO deposition on TiO_2 terminated (001)$SrTiO_3$ single crystal substrates is carried out. A SrO_2 ceramic plate with the radius of 0.5 inch (Producer: *Shinkosha* Co., Ltd) is used as a target and ablated under $pO_2 = 10^{-7}$ mbar with 1 Hz *via* a 248 nm KrF laser with a laser fluence of 1.3 J/cm^2 at a spot size of 2 mm^2. The substrate of 5x5x0.5 mm^3 single crystal (001)$SrTiO_3$ (CrysTec GmbH) is TiO_2 terminated. The substrate is heated up to 800 °C with a laser heater at a substrate to target distance of about 44 mm for deposition. All the samples are quenched with 10 °C/s by switching the heating laser off.

It has been observed for the (1 0) and (-1 0) spots, that the RHEED intensity experiences firstly a reduction and then an increase (Figure 3.26 (a)). For one full oscillation, 9 pulses are needed. On the contrary, the specular (0 0) spot intensity is continuously reduced during the 9 pulses. As shown by the more precisely controlled MBE [42], where a monolayer SrO deposition can be well controlled, similar contrast change in RHEED is observed. Thus we could conclude that the 9 pulses are sufficient to turn the surface of TiO_2 terminated single crystal (001)$SrTiO_3$ to almost 100 % SrO terminated. To further quantify the linear dependence of the SrO surface coverage on the laser pulses, a detailed investigation with AFM and XPS is carried out.

The morphology detected with *in-situ* AFM for sub-monolayer SrO (Figure 3.26 (b), (c), (d) and (e)) shows no significant surface coverage change, which might result from the surface reconstructions that reduces the SrO island height and makes it hard to be detected by AFM. The growth of more than 1 ML SrO introduces extra structures on the step edges (Figure 3.26 (f) and (g)), suggesting SrO growth with more than 10 pulses are not suitable for termination control any more. The 3D growth of SrO might be appearing in this growth stage.

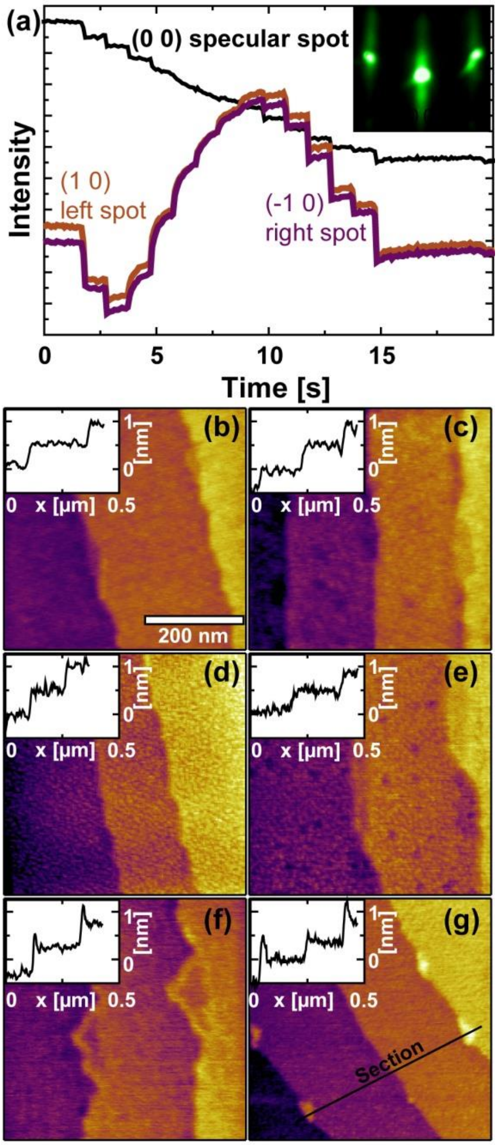

Figure 3.26 *Systematic surface termination variations in SrTiO$_3$ single crystals. (a) Representative RHEED intensity during SrO deposition. Inset: Exemplary RHEED pattern after SrO growth. (b)-(g) AFM-morphology after deposition of 2, 4, 6, 8, 10 and 12 pulses of SrO, respectively. Step terraces are of unit cell height (0.4 nm). Insets: representative line profiles from the AFM scans along sections like the one depicted in (g). Vertical scale is 1.75 nm. The results were published in ref. [134].*

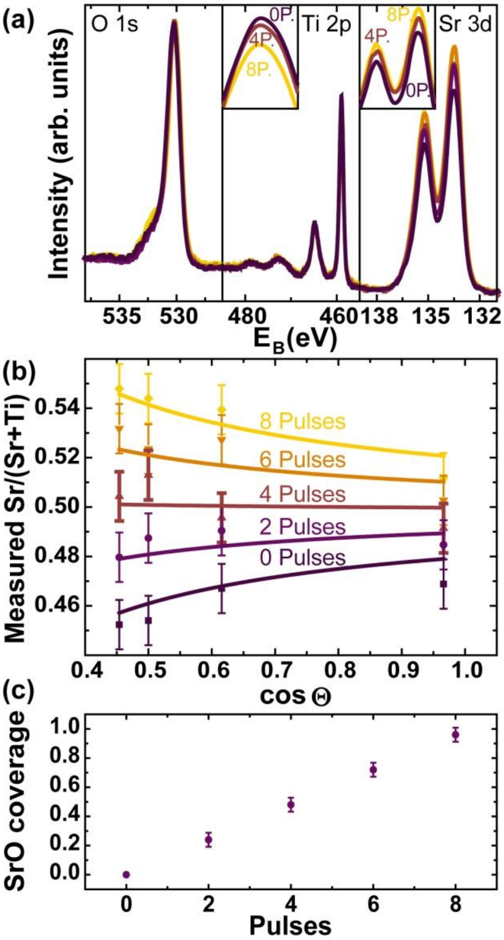

Figure 3.27 *XPS analysis and termination determination of $SrTiO_3$ single crystals. (a) Representative XPS spectra for $SrTiO_3$ crystals with increasing amounts of SrO coverage normalized to the O 1s peak intensity. The Ti2p and Sr3d peaks have the same shape and binding energy for each sample, indicating the absence of a second phase. Insets: Zoom-in on the peaks for films with 0, 4 and 8 pulses of SrO. (b) Measured cation ratios (data points) as a function of the photoemission angle and fits (solid lines) according to Equation (3.51). (c) SrO coverage extracted from the fits in (b). The results were published in ref. [134].*

The XPS spectra for 0, 2, 4 and 8 pulses are shown in Figure 3.27 (a) with the corresponding Sr3d/Ti2p peak intensity ratio summarized in Figure 3.27 (b). Since for the $SrTiO_3$ single crystal substrate the Sr/Ti ratio in thin film is 1, the termination ratio is the only factor to be fitted. As a result, we see in Figure 3.27 (c) that the termination ratios of SrO fit well into a linear form with respect to the number of pulses. This does not only verify that the sub-monolayer SrO can be deposited with PLD as a method to control the surface termination ratio for $SrTiO_3(001)$, but also proves the accessibility of measuring surface termination with angle dependent XPS signals. A possible error in the termination ratio can be present due to the error in XPS fitting process and the absence of AFM resolved island dimension. However, the linear dependence of the SrO coverage with laser pulse number is proved. This enables the engineering of the surface termination of SrO and makes the further work on the interface engineering possible.

3.5 Special holder design for UV-radiation study

To study the influence of the UV-radiation emitted from the plume during the PLD process, a series of holders are designed and tested. The basic idea is to permit the photons to pass by inserting an optical window that has transmittance for a specific wavelength range. This principle is depicted in Figure 3.28.

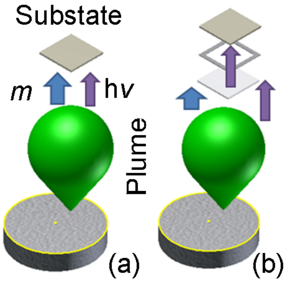

Figure 3.28 *The principles of experiments for (a) influence from massive particles and photons; (b) the influence only from photons.*

To study the influence of UV-radiation from the LAO plume on the STO properties, double side polished Al_2O_3 single crystals from *CrysTech GmbH* are used as window material. As a band insulator with 8 eV band gap, the Al_2O_3 single crystal (commercial name: sapphire) shows a fairly wide transmission range from 140 nm to 5500 nm of more than 50 % transmittance (Figure 3.29). This range comprises the part of UV, all visible and part of the infrared spectra. During the growth process, amorphous LAO is accidentally deposited on the front side of the window and influences the transmittance of the window. However, as reported by Edge et. al [136], amorphous $LaAlO_3$ has a band gap around 6.2 eV, which is also high enough to prevent absorption of wavelengths above 200 nm. Thus the transmission of the used window is guaranteed for all photons with a wavelength above 200 nm.

With the sapphire window, three different types of holders are developed for different purposes:

1) **UV1:** the holder with complete coverage by the sapphire window, where the sapphire window is mechanically pressed to a metallic spacer. The spacer between sapphire window and the sample is

a quadratic frame. This holder is illustrated in Figure 3.30 (a) and applied in chapter 6.2 for discussion on the role of the UV-radiation on the morphology.

2) **UV2:** the holder with complete coverage by the sapphire window, where the sapphire window is mechanically pressed to four 1x1x1 mm^3 sapphire single crystals (Figure 3.30 (b)). This holder is applied in chapter 6.2 for discussion on the role of the UV-radiation on the conductivity.

3) **UV3:** the holder for 50 % coverage by the sapphire window of the STO substrate. This holder is shown in Figure 3.30 (c) and will be applied in chapter 6.3 for disentanglement of influences from kinetical particles and UV-radiation from the plume.

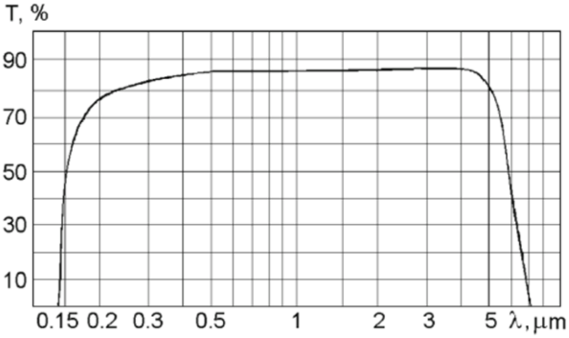

Figure 3.29 *Transmission spectrum of single crystal* Al_2O_3*. The scale is logarithmic. Reproduced from ref. [137].*

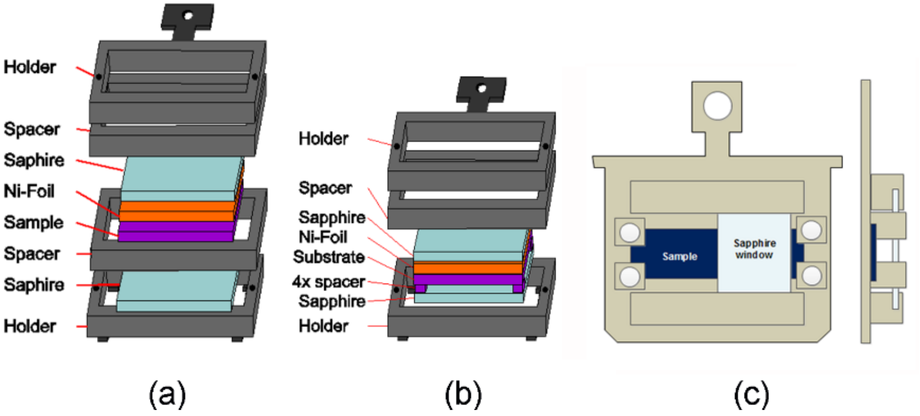

Figure 3.30 *The holders for the experiments related to UV-radiation emitted from plume during PLD. (a) UV1, (b) UV2 and (c) UV3.*

4 Cation non-stoichiometry during homoepitaxial PLD growth of STO

In this chapter we discuss the origin of cation non-stoichiometry during PLD homoepitaxial growth of $SrTiO_3$ (STO) (chapter 4.1) and the impact of non-stoichiometry on the thin film growth, with respect to the surface diffusion (chapter 4.2), surface atomic rearrangement (chapter 4.3), defects formation (chapter 4.4) and growth mode (chapter 4.5).

4.1 Origin of the cation non-stoichiometry of homoepitaxial STO growth via PLD

4.1.1 Experiments

In order to address the aspect of cation non-stoichiometry on the film growth, we investigate STO thin films deposited in the different fluence and pressure regimes by the XRD analysis. 200 nm STO thin films are deposited on a STO(100) single crystal substrate (provided by Crys Tec GmbH). The STO single crystals are annealed prior to the deposition in ambient atmosphere at 950 °C for 4 hours, exhibiting a regular step-terrace structure afterwards. The target substrate distance d_{ST} is set to 44 mm and the ablation spot measured 1.8 mm^2. The O_2 background pressure p and the laser fluence F_{L} are varied from 0.1 mbar - 10^{-6} mbar and 0.6 Jcm^2 - 2 $\mathrm{J/cm}^2$, respectively. The laser fluence is varied by tuning the laser energy with an attenuator in front of the laser port of the chamber, while the laser spot size is fixed by using an aperture within the optical path.

The XRD system used to determine the out-of-plane lattice parameter is an X'pert MRD 3040® system. The Cu-$K_{\alpha 1}$ X-ray with a wavelength of 0.154 nm is used. The software Fityk® is used to simulate the peak curves and to fit the measured Cu-$K_{\alpha 1}$, Cu-$K_{\alpha 2}$ and Cu-K_{β} peaks, while only the Cu-$K_{\alpha 1}$ peak position is used to determine the STO(001) lattice constant for thin film and substrate. For the details about peak fitting see chapter 2. The difference between the film and substrate lattice constant is defined as lattice expansion Δc.

4.1.2 Results

The corresponding lattice expansion Δc with laser fluence variation is summarized in Figure 4.1. For the laser fluence series deposited at p = 0.1 mbar depicted in Figure 4.1, Δc exhibits a clear minimum at a laser fluence of 1.4 $\mathrm{J/cm}^2$. Either increase or decrease of the laser fluence increases the Δc. The maximum of Δc with low laser fluence is ~ 0.1 pm at 0.6 $\mathrm{J/cm}^2$, while the maximum of Δc with high laser fluence reaches ~ 0.45 pm at ~ 2.7 $\mathrm{J/cm}^2$.

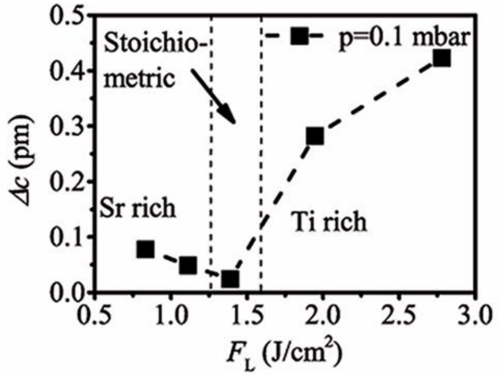

Figure 4.1 *Laser fluence dependence of the c-lattice constant of 200 nm STO thin film on STO. The oxygen partial pressure is 0.1 mbar and the temperature is 800 °C. The results were published in ref. [63].*

Since the stoichiometry of the STO film also depends on the scattering of plume species with the background gas molecules, the STO film stoichiometry and the out-of-plane lattice expansion, respectively, are investigated for various background pressures as depicted in Figures 4.2 (a)-(c).

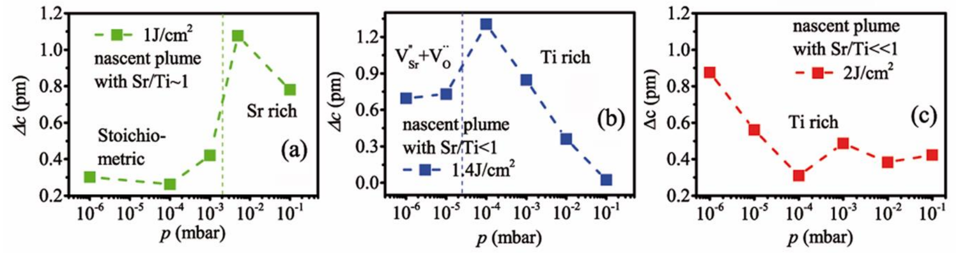

Figure 4.2 *The pressure sequences for three different laser fluences: (a) 1 J/cm^2, (b) 1.4 J/cm^2 and (c) 2 J/cm^2. The results were published in ref. [63].*

In Figure 4.2 (a) for the laser fluence of 1 J/cm^2, Δc for p = 0.1 mbar is around 0.8 pm and increased slightly to 1.1 pm for p = 0.01 mbar. By further reducing the pressure, Δc is reduced to below 0.4 pm or even close to 0.2 pm. In Figure 4.2 (b) for the laser fluence of 1.4 J/cm^2, Δc increases with a reduction of the pressure till 10^{-4} mbar. Decreasing the pressure further to 10^{-5} and 10^{-6} mbar, however, does not further increase Δc. Δc stays constant around 0.75 pm. In Figure 4.2 (c) for the laser fluence of 2 J/cm^2, Δc stagnates between 0.3 and 0.5 pm between p = 0.1 mbar and $p = 10^{-4}$ mbar. For pressures lower than 10^{-4} mbar, Δc increases to 0.6 at $p = 10^{-5}$ mbar and to 0.9 at $p = 10^{-6}$ mbar.

4.1.3 Discussion

Firstly we discuss the clear minimum in the ***fluence series*** around 1.4 J/cm^2 (Figure 4.1). This minimum of c-lattice constant indicates the stoichiometric point as illustrated in chapter 2. As revealed by X-ray photoelectron spectroscopy (XPS) and plume imaging [58] the nascent plume for low laser fluence is nearly stoichiometric. However, it loses lighter Ti-species during the propagation to the substrate by interaction with the background gas molecules, giving rise to a Sr-rich STO film and a significant increase in Δc. When the laser fluence is increased, the nascent plume becomes Ti-rich due to incongruent ablation [4]. This compensates the lost Ti species, resulting in a stoichiometric STO film with bulk lattice parameters. When the laser energy is further increased, the concentration of Ti-species in the nascent plume proliferates and yields Ti-rich STO films resulting in an increase in Δc.

Secondly we focus on the ***pressure dependence*** of Δc at different laser fluences. Under the growth conditions depicted in Figure 4.2 (a) the nascent plume is stoichiometric. Due to preferential scattering of Ti-species the STO film for $p = 0.1$ mbar is Sr-rich and shows an expanded c-axis lattice parameter. By reducing the background pressure the scattering effects of Ti gradually decrease and the STO film renders stoichiometric with a very small or no Δc. When STO films are deposited at $F_L = 1.4$ J/cm^2 the emerging plume is Ti-rich, i.e. Sr/Ti < 1. At elevated background pressure the scattering of Ti-species can help in producing a stoichiometric STO film. Therefore, by reducing the pressure fewer Ti-species are scattered, resulting in an increase in the Ti content and finally in Ti-rich films with increased Δc. The obvious drop in increase in Δc for STO films grown at 10^{-5} and 10^{-6} mbar could be explained by the facilitated incorporation of oxygen vacancies, which counteracts the Coulomb repulsion due to the cation vacancies in the STO film [138]. When the laser fluence is increased even further and the background pressure is decreased, the STO films become extremely Ti-rich. Therefore, when the scattering of Ti can be neglected at low pressures, F_L should be sufficiently low in order to prevent the formation of Ti-rich films. This is in good agreement with the experimental results reported in [139].

In summary, we could demonstrate that stoichiometric thin films can only be obtained in a limited pressure-fluence regime. Therefore, the lattice strain and vacancy defects present under non-stoichiometric conditions have to be considered when the impact of fluence and background pressure on the growth mode are regarded.

4.2 Surface diffusion with cation non-stoichiometry

4.2.1 Experiments

To study the surface diffusion in dependence of cation stoichiometry, three different stoichiometries are chosen for the growth of STO films in the early growth stages with thickness less than 1 monolayer (ML). The pressure is 0.1 mbar and temperature is 800 °C. The laser fluences are 1.05, 1.4 and 2.0 J/cm^2, corresponding to Sr/Ti ratios of 1.17, 1.0 and 0.92. *In-situ* AFM scanning is carried out for samples with deposition stopped after different numbers of pulses and at different surface coverages.

4.2.2 Results

We show the morphology evolution overview in the Figure 4.3 for three stoichiometries for different growth stages in a relatively big area around 400 nm x 700 nm. The surface coverage ratio is determined for 400 pm island areas on every terrace. In general, Figure 4.3 shows how the morphology of homoepitaxial sub-monolayer STO evolves during the PLD growth and how the completion of a monolayer is achieved. The detailed discussions about different aspects are presented in the following. The discussions are based on the selected areas on corresponding pictures, which are also applicable for the whole scan area in Figure 4.3.

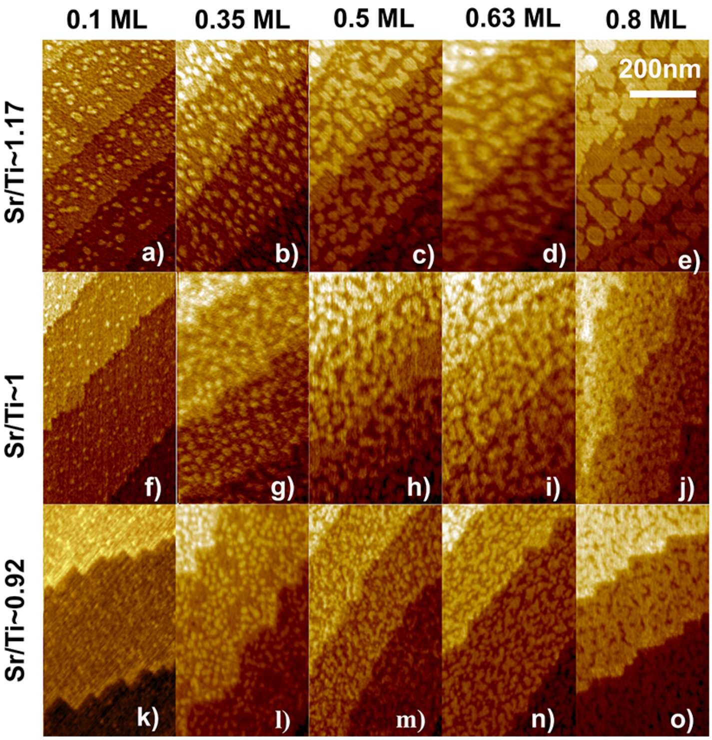

***Figure 4.3** The overview of the morphology evolution for three cation stoichiometries within one monolayer. The corresponding stoichiometries are marked at the left of every row and the corresponding surface coverage ratios are marked on top of each column. The area of scan is 400 nm x 700 nm.*

Firstly, we observed that the sub-monolayer growth of STO occurs in a 2D layer-by-layer growth mode for all three different stoichiometries since all islands have heights of around 400 pm, which is the unit cell height of STO (line profiles in Figure 4.4 (j)–(l)). The coalescence of the 2D islands is indicated in the histograms of Figure 4.4 by a strong decrease of the mean island number, which goes along with a strong increase of the width of the island area distribution. It is observed that island coalescence occurs at different coverages for the three stoichiometries (Figure 4.4 (a)-(i)). In particular, the coalescence of 2D islands under stoichiometric conditions already takes place when the coverage is less than 0.35 ML (Figure 4.4 (d) and (e)), while under both, Sr rich (Figure 4.4 (b) and (c)) and Ti rich conditions (Figure 4.4 (h) and (i)), the coalescence occurs between 0.35 ML and 0.5 ML. For possible scenarios behind this phenomenon see discussion below.

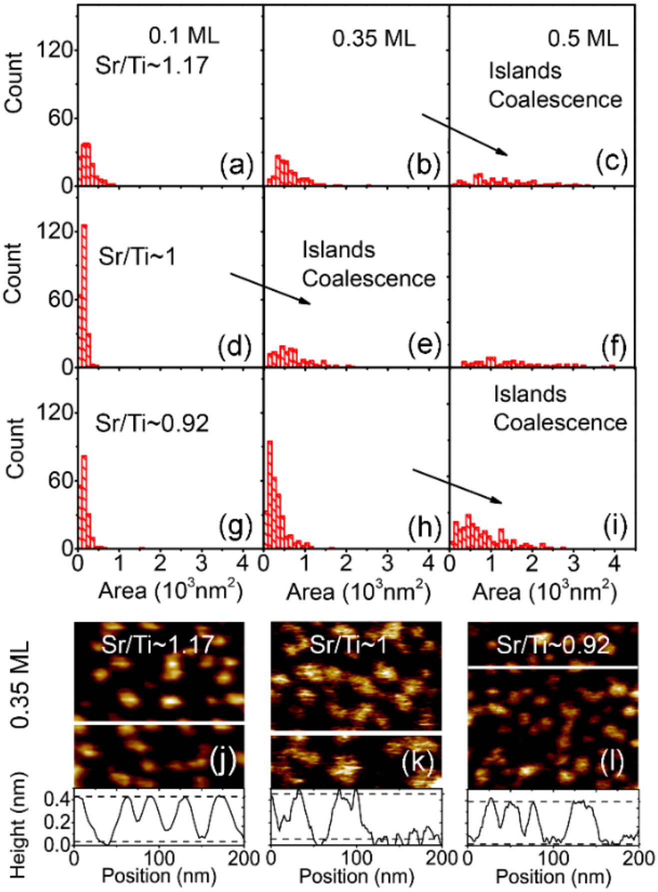

Figure 4.4 *(a) to (i): Statistics of the island area from the in-situ AFM measurements in a 400 nm x 700 nm area shown in Figure 4.3. Vertical: change of stoichiometry from Sr rich to Ti rich. Horizontal: change from 0.1 to 0.5 monolayers. (j) to (l): AFM scans and selected line profiles of the three different stoichiometries at 0.35 ML. The corresponding positions of the line profiles are marked with white lines in the figure. The area of the scans is 200 nm x 200 nm. The results were published in ref. [140].*

The earlier start of the coalescence under stoichiometric conditions in comparison with non-stoichiometric conditions is also visible from the morphologies at 0.35 ML (Figure 4.4 (j)-(l)): Only under stoichiometric conditions, a strong coalescence between the islands can be detected at 0.35 ML, while under Sr rich and Ti rich conditions the islands remain almost isolated from each other at 0.35 ML.

Figure 4.5 (a)-(f) depicts the morphology at 0.1 ML and 0.8 ML for samples with different stoichiometries. The coverage ratio is determined by the large area scans (400 nm × 700 nm, Figure 4.3 (a)-(o)). The morphology of the three stoichiometries differs with respect to both the nuclei density (0.1 ML, Figure 4.5 (a)-(c)) and the islands shape close to layer completion (0.8 ML, Figure 4.5 (d)-(f)).

A statistical comparison of nuclei densities performed at larger area scans (400 nm × 700 nm, Figure 4.3 (a)-(o)) is listed in Table 4.1. Under Sr rich conditions, the nuclei density N_n at 0.1 ML is the lowest (Figure 4.5 (a)), while under Ti rich conditions it is the highest (Figure 4.5 (c)). The stoichiometric conditions result in a medium nuclei density (Figure 4.5 (b)). Since an increased Ti content is obtained by increasing the laser fluence, it goes along with a higher deposition rate and mass flux from the target to the substrate [63], resulting in a higher supersaturation [8]. Thus, the increase of the nucleation density for the Ti-rich sample could be a direct result of an increased supersaturation [75, 141-142]. Likewise, the low nucleation density observed for the Sr rich thin films is a result of the low supersaturation obtained at low laser fluence. Considering the stochastic nature of diffusion, particles can diffuse in opposite directions with equal probability and the averaged diffusion length for particles is half the averaged islands distance. From the morphology at low coverage (0.1 ML), we could estimate the distance between two formed islands, i.e. the distance between two bright spots in Figure 4.5 (a). The distances between formed islands are averaged for all islands in the 180 nm × 180 nm AFM scan area and can be identified with the diffusion length ($L_{\mathrm{D},0.1\,\mathrm{ML}}$) of particles moving on the substrate to the island edge [143, 144]. In analogy, we can also average the distances between uncovered areas, i.e. the distances between the edges of unconnected dark areas in Figure 4.5 (d). The averaged diffusion length ($L_{\mathrm{D},0.8\,\mathrm{ML}}$) is half of this distance and can be attributed to the diffusion length of the particles on the formed islands to the island edges (for details about the principle see chapter 2).

The diffusion lengths at a coverage of 0.1 ML and 0.8 ML for the three stoichiometries are summarized in Table 4.1. It is interesting to note that the diffusion lengths at both 0.1 ML and 0.8 ML for all three stoichiometries are almost identical considering the error bars.

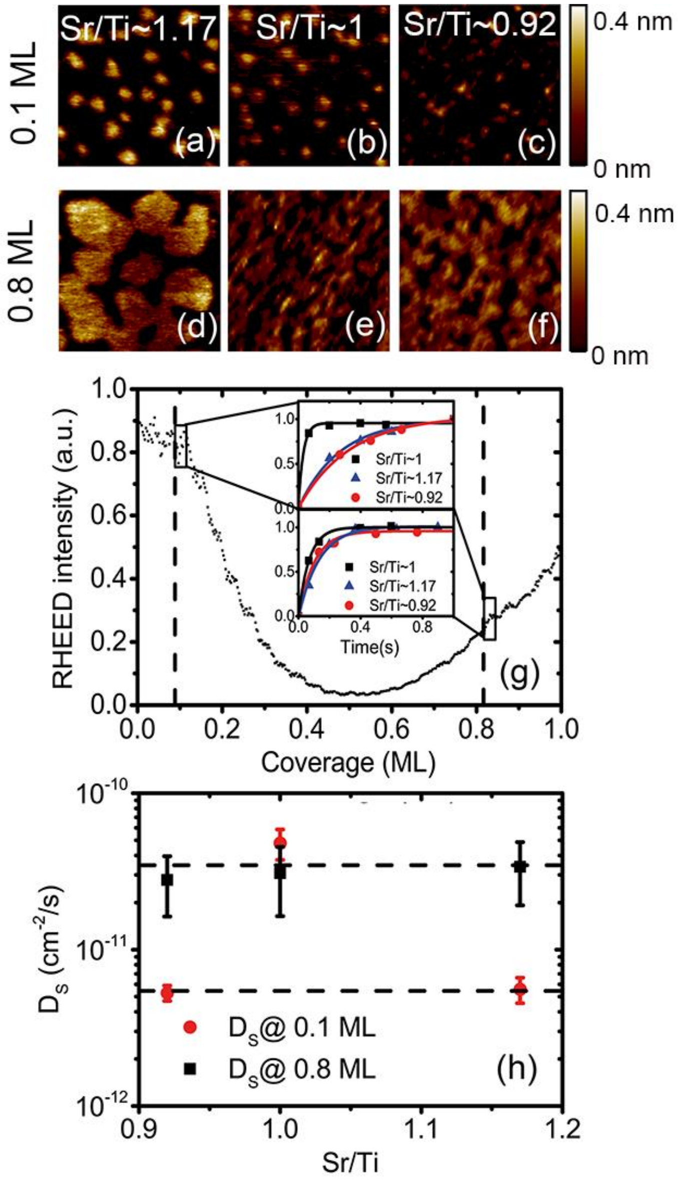

Figure 4.5 *From the surface morphology of 0.1 ML ((a)-(c)) and 0.8 ML((d)-(f)) along with the diffusion time from RHEED intensity relaxation (g) the apparent surface diffusion coefficients can be estimated (h). The details for this approximation can be found in chapter 2 and in the discussion below. The AFM scans are acquired in area of 180 x180 nm*^{2}*. The results were published in ref. [140].*

***Table 4.1** Island density and diffusion lengths for different Sr/Ti ratios at 0.1 ML and 0.8 ML coverage are listed. L_D is the diffusion length, τ is the diffusion time and N_n the island density. The diffusing species are in this approximation, formally, one unit cell of STO. The reason for such an approximation can be found in chapter 2.*

	$L_{D,0.1\ ML}$ (nm)	$L_{D,0.8\ ML}$ (nm)	$\tau_{0.1\ ML}$ (s)	$\tau_{0.8\ ML}$ (s)	$N_{n,0.1\ ML}$ (10^{10}cm^{-2})
Sr/Ti~1.17	24±10	42±14	0.26±0.04	0.13±0.01	5.4±0.6
Sr/Ti~1	25±10	29±14	0.03±0.005	0.07±0.003	6.9±1.2
Sr/Ti~0.92	26±11	34±14	0.33±0.04	0.10±0.01	10.6±1.9

Figure 4.5 (g) illustrates the typical RHEED intensity oscillation for the growth of one monolayer. The upper inset shows the corresponding RHEED intensity at 0.1 ML coverage for the three different stoichiometries. The RHEED intensity after one laser pulse relaxes to higher intensities (separated spots in the upper inset of Figure 4.5 (g)). This can be as attributed to the diffusion process of the arriving species on the substrate to the islands edges at low coverages of 0.1 ML [8, 68, 68] and can be fitted as a single relaxation function (solid lines in the inset of Figure 4.5 (d)):

$$I_{RHEED}(t) = I_0(1-\exp(-\frac{t}{\tau})) \ . \tag{4.1}$$

The corresponding relaxation time (τ) is a good approximation of the diffusion time of the particles [9]. Under stoichiometric conditions, the diffusion time at 0.1 ML is the lowest, whereas the diffusion time under Sr and Ti rich conditions are over one magnitude higher (see Table 4.1). Similarly, the RHEED intensity relaxation after 1 laser pulse at a high coverage of 0.8 ML (separated spots in the lower inset of Figure 4.5 (g)) can be as attributed to the surface diffusion processes on the formed islands, which can be divided into diffusion to the edges and subsequent downwards diffusion over the Ehrlich-Schwoebel barrier [68]. Since the Ehrlich-Schwoebel barrier is below 5 % of the surface diffusion barrier for STO on STO diffusion at 800 °C [145], its influence on the diffusion process is insignificant. Thus, we can attribute the relaxation time determined from the 0.8 ML RHEED oscillations to the diffusion time on the formed islands. It is important to note that in contrast to the situation at 0.1 ML, the diffusion times of the three stoichiometries only slightly differ at 0.8 ML (Table 4.1). See discussion below.

Utilizing the Einstein relation for 2D diffusion $D_S = L_D/\tau$ we can estimate the apparent surface diffusion coefficients for different stoichiometric conditions (Figure 4.5 (h)). For 0.1 ML, the diffusion coefficient is significantly higher at stoichiometric conditions than for the non-stoichiometric conditions. However, for 0.8 ML, the diffusion coefficients of the three stoichiometries are almost identical. Whereas the diffusion of the arriving species at the 0.1 ML growth stage solely occurs on the TiO_2 terminated STO substrate, at the 0.8 ML growth stage, the diffusion of the arriving species to the edges of the formed islands mainly takes place on the preexisting islands. Therefore, the discrepancy between the diffusion coefficients observed for the different growth stages can be assigned to the difference in the diffusion on the STO substrate and the preexisting STO thin film islands, respectively. As illustrated in Figure 4.6 with the filled spheres representing diffusing STO unit cells, we can explain this difference as follows: while the diffusion of Ti- or Sr-rich non-stoichiometric STO unit cells on the STO substrate has to be regarded as heteroepitaxial diffusion, the diffusion of non-stoichiometric STO unit cells on the formed films can be regarded as homoepitaxial diffusion.

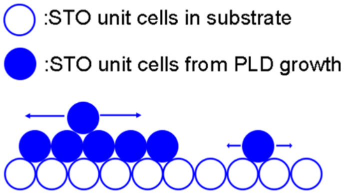

Figure 4.6 *The diffusion of STO on STO substrate (blue filled spheres with two short arrows) and formed STO islands (blue filled spheres with two long arrows). The solid spheres indicate STO unit cells grown via PLD and the empty spheres indicate STO unit cells of the single crystal substrate. The lengths of the arrows indicate the diffusion length.*

At a high coverage of 0.8 ML, we see significant differences in the morphology of Sr rich islands (Figure 4.5 (d)) and Ti rich islands (Figure 4.5 (f)). Whereas the Sr rich islands are compact, the Ti rich islands are much more ramified, indicating a preliminary stage of fractal structure. We attribute this to the differences in the deposition rate for Sr rich (160 pulses/u.c.) and Ti rich (26 pulses/u.c.) conditions, since a similar transition from a compact structure into a more ramified structure is observed for antimony nanostructure growth with increasing deposition rates [146, 147]. It can be explained by the kinetic limitation for the formation of energetically favorable circular islands imposed by the steady flux of material to the island edges. For the Sr rich conditions, the deposition rate is sufficiently low to enable the formation of circular islands prior to the arrival of new atoms at the edges. Therefore, the islands are comparably large and have a compact shape. In contrast, the deposition rate under Ti rich conditions is too high for the edge rounding process to finish before new atoms arrive. Therefore, the islands are much smaller and more ramified than in case of Sr rich samples.

In order to correlate the experimentally observed RHEED oscillation with our AFM analysis in the simplest way, we consider the step density model [86], which is generally employed for interpreting the influence of deposition parameters on the RHEED specular intensity both in MBE [148-150] and PLD [8]. However, for a more detailed analysis of the RHEED data, a kinematical or dynamical approach is needed to include both the diffraction from the surface/interface [151, 152] and the step edge scattering and shadowing effects [107]. In the step density model, the loss of specular RHEED intensity can be described by the scattering at step edges of the islands [84] in the form:

$$\frac{I}{I_0} = 1 - \frac{S}{S_{\max}} \tag{4.2}$$

, where *I* is the specular RHEED intensity, I_0 the maximum of specular intensity, *S* the density of island edges, and $S_{\max}$ the maximum step edge density. The corresponding model for the description of the 2D step density evolution suggested by [8, 86] is

$$S(t) = \frac{1}{c(t)}\frac{d\theta}{dt} = 2\sqrt{\pi N_n}(1-\theta(t))\sqrt{-\ln(1-\theta(t))} \tag{4.3}$$

, where N_n is the island density and *c*(t) the velocity of the island edge movement. Since the islands are supposed to have a 2D circular shape, the total step edge length (*S*) and the coverage (θ), which corresponds to the total island area, are related with each other in a simple way within the step density model. As a result, the RHEED intensity minimum should always be at around 0.39 [8]. This is true for the stoichiometric STO monolayer growth (Figure 4.7 (a), black data points) but for the growth with insufficient diffusion coefficients, e.g. for Sr and Ti rich STO, the RHEED minimum is shifted to around 0.5 (Figure 4.7 (a), blue and red data points). Therefore, the model for the step density evolution originating from insufficient diffusivity has to be modified. The apparent surface diffusion coefficients are not included in the original step density model [86], since, as a result of the assumed infinitely high surface diffusion resulting in an instantaneous arrangement of the particles in the position of the minimum surface energy, the islands are considered to grow in a 2D circular shape in the step density model as mentioned above. For PLD growth with high diffusion coefficients like in the case of stoichiometric STO, we can see the coalescence from the compact circular shape islands, which is illustrated by the compact circular shapes in Figure 4.7 (b) and (c). However, for Ti rich conditions, a slightly ramified shape with strong deviation from the compact circular shape can be seen at 0.5 ML, which becomes more pronounced at a coverage of 0.63 ML, illustrated by the solid frames in Figure 4.7 (d) and (e). The deviation from the circular islands, in turn, increases the step edge length compared to stoichiometric conditions at the same coverage. Based on this observation, we suggest an additional term in the step density formula to describe the increase of step density induced by the deviation from the 2D circular island shape, which is dependent on diffusivity and coverage. A linear approximation can be made to account for this increased step density:

$$S(t) = 2\sqrt{\pi N_n}\left((1-\theta)\sqrt{-\ln(1-\theta)} + C\cdot\xi\theta\right). \tag{4.4}$$

The factor ξ describes the finite diffusion coefficients:

$$\xi = \frac{D_{S0} - D_S}{D_{S0}} \tag{4.5}$$

, where D_{S0} is the diffusion coefficient under stoichiometric condition and D_S under different conditions. *C* is a constant independent of the diffusion coefficients and coverages. The expression for the RHEED minimum is:

$$\theta_0 = 1 - \exp\left(-\frac{(C\xi\sqrt{(C^2\xi^2+2} + C^2\xi^2+1)}{2}\right). \tag{4.6}$$

Based on the diffusivities measured for Sr rich, stoichiometric and Ti rich conditions in this work (Table 4.1), C = 0.32 results in the best fit for the RHEED minimum position for each condition.

With Equation (4.5) and (4.6), we obtain a qualitative link between the diffusion constant and the RHEED minimum for the sub-monolayer STO homoepitaxial growth.

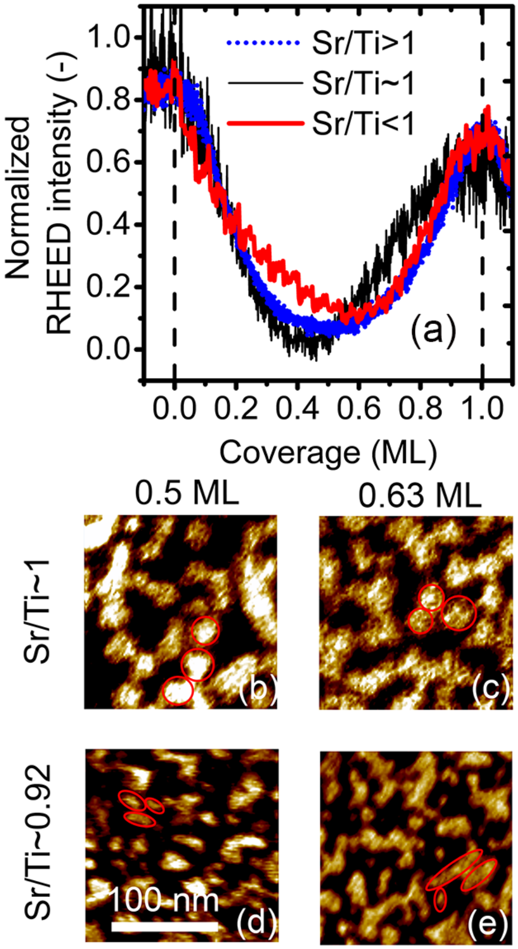

Figure 4.7 *(a) Normalized RHEED intensity for the growth of one complete monolayer. (b) to (e): AFM images (180 nm x 180 nm) for two stoichiometries and two coverages. Horizontal: from 0.5 ML to 0.63 ML. Vertical: stoichiometric and Ti rich. The results are published in ref. [140].*

4.2.3 Discussion

Next we discuss the influence of the cation stoichiometry on the diffusion process, which we could clearly deduce from the analysis of the sub-monolayer growth of STO on STO.

In order to do so, we have to clarify the diffusing species on the surface. Since the crystallization time for STO unit cells is in the time scale of μs [10] and the STO unit cell diffusion process on the STO surface is in the time scale of seconds [153], the relaxation process that happens within the time resolution of RHEED analysis can be properly interpreted as the diffusion process of STO unit cells. Since the time we need for completion of cooling down from 800 °C to 300 °C is around 50 second, it will be sufficiently long to enable crystallization as well. Our AFM analysis performed after the cooling-down procedure also provides information about the morphology evolution of STO unit cells.

We will now discuss possible reasons for the decreased diffusivity at non-stoichiometric conditions. As shown in Figure 4.5 (h) the decrease of diffusivity for non-stoichiometric conditions happens only in the case of the Ti- or Sr-rich non-stoichiometric STO unit cell diffusion on STO substrate. The interaction between the non-stoichiometric deposited STO unit cells and the stoichiometric substrate is thus dominating the diffusion process. As reported before [41], cation non-stoichiometry in STO is accommodated by point defects like Sr vacancies (V_{Sr}''), Ti vacancies (V_{Ti}'''') or extended defects in the grown film, resulting in a considerable lattice expansion in the STO thin films [12]. Without digging into the microscopic processes, the point defects are distributed in all nucleated Ti- or Sr-rich non-stoichiometric STO structures within nucleation stage. Effectively all the non-stoichiometric STO structures with various amount of STO unit cells are electrostatically expanded. Taking the STO unit cells as the diffusion units (for explanation see chapter 2), each STO unit cell is effectively “expanded”. As a result, the growth at non-stoichiometric conditions on the STO single crystal substrate occurs under compressive strain. As a result of the compressive strain, the diffusion barrier of STO unit cells might be increased as observed for the diffusion of Ge on a Si surface [154, 155]. This is consistent with the fact that the reduction of the apparent diffusion coefficient occurs only for the diffusion of non-stoichiometric STO on the stoichiometric substrate and not on the 2D islands, since there exists no strain between relaxed non-stoichiometric STO islands and non-stoichiometric diffusion units.

An alternative explanation for the changed apparent surface diffusion coefficient are the defect sites in the formed islands. They can trap the diffusing unit cells and then release them, thereby slowing down the diffusion process as observed for Si diffusion on defective Si(001) surfaces [156]. This effect should be stronger on the formed defective islands than on the substrate. However, this is in contradiction to our observations. So the trapping effect can be neglected for the diffusivity reduction for the non-stoichiometric diffusion. Therefore, we conclude that the impact of the compressive strain effectively imposed to the diffusing STO particles is the main reason for the decrease of diffusivity at non-stoichiometric conditions.

In summary, the cation non-stoichiometry has strong impact on the surface diffusion process during homoepitaxial STO growth via PLD. The inhibition of the surface diffusion results from the strain between diffusion species and the surface underneath.

4.3 Atomic rearrangement on the surface with cation non-stoichiometry

Besides the apparent surface diffusion coefficient that can be strongly influenced by the cation non-stoichiometry (see chapter 4.2), the atomic rearrangement on the surface during the PLD growth process is another important factor that determines the growth process. To study this point, Sr rich STO growth is analyzed regarding the surface structure with AFM and LEED.

4.3.1 Experiments

Epitaxial growth of Sr rich STO on STO is carried out. 1.5 u.c. STO at laser fluence of 1.05 J/cm^2 is grown on single crystal STO substrate at 0.1 mbar and 800 °C, which is subsequently quenched at 10 °C/s. *Ex-situ* AFM scanning is carried out for the substrate and the 1.5 u.c. STO thin film. LEED measurements are carried out for the substrate and 1.5 u.c. Sr rich STO *ex-situ* as well.

4.3.2 Results

LEED pattern (Figure 4.8 (a) and (b)) and AFM morphologies (Figure 4.8 (c) and (d)) for TiO_2 terminated STO substrate and 1.5 u.c. Sr rich STO are compared. The line profiles for two island features marked in Figure 4.8 (d) are shown in Figure 4.8 (e).

Firstly we take a look on the substrate with TiO_2 termination. Figure 4.8 (c) shows flat terrace structures with 0.4 nm terrace step edges, indicating an almost single termination situation. Figure 4.8 (a) shows clear (1x1) diffraction spots (white arrows) and vague $(\sqrt{13}\times\sqrt{13})$-R33.7° reconstructions (green arrows) in LEED pattern. This indicates the TiO_2 terminated STO surface is covered mostly by the TiO_2 and has tiny amount of Sr excess atoms that form the $(\sqrt{13}\times\sqrt{13})$-R33.7° reconstruction. Generally, the reconstructions on the STO(001) surface can be interpreted as ordered oxygen vacancies by vacuum annealing [157, 158], Sr adatoms at Sr rich condition [101, 159] or the TiO_2 double layers at Ti rich condition [160-162]. In this experiment, since the substrate and the thin film are both handled in oxidizing condition and without Ti excess, the reconstructions on the surface should originates from Sr ad-atoms and the discussions in the following is carried out within this model.

The model for this reconstruction is illustrated in Figure 4.9 (a) and this reconstruction is reported by literature for the almost 100 % TiO_2 terminated surface [101]. The reason for this broad and diffuse pattern may originate from the long coherence length between reconstructed domains, which results from small amount of Sr excess.

Next we focus on the surface for the 1.5 u.c. Sr rich STO. Figure 4.8 (b) shows not only significant (1x1) spots, but also clear $(\sqrt{13}\times\sqrt{13})$-R33.7° and (2x2) reconstructions in LEED pattern. Compared to the weak $(\sqrt{13}\times\sqrt{13})$-R33.7° spots by the TiO_2 terminated substrate, the increased intensity of $(\sqrt{13}\times\sqrt{13})$-R33.7° reconstructions by 1.5 u.c. Sr rich STO indicates the increased amount of Sr adatoms in such a configuration. The appearance of (2x2) reconstruction indicates the increase of Sr atoms on the surface as well. As shown in the literature, the (2x2) reconstruction can only be observed at high concentrations of surface Sr atoms [101] . Since the Sr atoms for (2x2) reconstruction coordinate with reduced distances between each other in comparison with (√13x√13)-R33.7° reconstruction, the area density of Sr atoms at (2x2) reconstruction is higher than the (√13x√13)-R33.7° reconstruction.

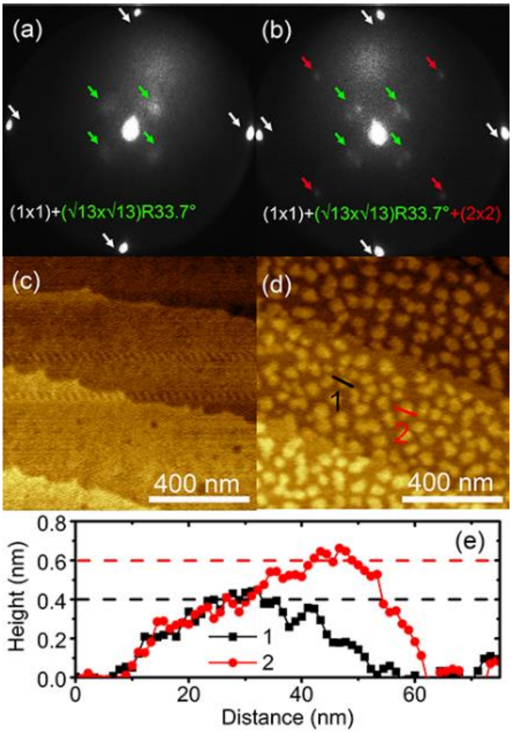

Figure 4.8 *Comparison between substrate and the 1.5 u.c. Sr rich STO on STO. (a)-(b): the LEED pattern with white arrows for (0 0) diffraction spots, green for (√13x √13)R33.7 ° reconstructions and red for (2x2) reconstructions; (c)-(d): ex-situ AFM topographies for substrate and 1.5 u.c. Sr rich STO on STO, respectively. The substrate is flat with 0.4 nm high terrace steps. The 1.5 u.c. Sr rich STO shows two types of islands on the terraces. (e): the AFM line profiles for the marks in (d), showing the exact height and width of two types of islands.*

The configuration of the (2x2) reconstruction is shown in Figure 4.9 (b). Supporting the assumption of an increase of Sr atoms on the surface, the AFM shows not only 0.4 nm high STO islands (profile 1 in Figure 4.8 (e)), but also structures with 0.2 nm heights and ~ 20 nm diameter on the top of 0.4 nm high STO islands with ~ 50 nm diameter (profile 2 in Figure 4.8 (e)). The 0.2 nm high islands on the 0.4 nm islands indicate the formation of both Sr related surface reconstruction regions and SrO 2D islands [163]. The formation of SrO, however, may introduce only contrast change in (1x1), which is not easy to observe due to the bright nature of the (1x1) spots. The atomic configuration of the (1x1) SrO islands is illustrated in Figure 4.9 (b) at the lower right corner.

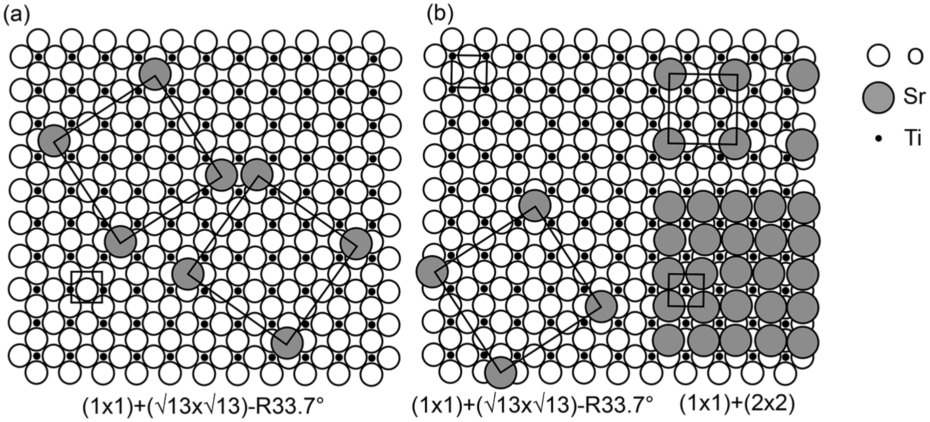

Figure 4.9 *Model for possible surface structures on (a) TiO_2 terminated STO substrate and (b) 1.5 u.c. Sr rich STO thin film.*

4.3.3 Discussion

For the Sr rich STO with 1.5 u.c. thickness, the formation of 0.2 nm high islands on top of the 0.4 nm STO islands is observed and indicates SrO formation on TiO_2 terminated STO islands.

However, the formation of 0.2 nm high islands cannot be observed for film thicknesses in the sub-monolayer regime (Figure 4.3). The impact of the Sr excess is only observed by the reduced surface diffusion coefficient and delayed island coalescence as discussed in chapter 4.2. In this case, it can be possible that Sr atoms are already present on the 0.4 nm STO islands, but are not resolved due to the lack of atomic resolution of the AFM tips. This indicates the presence of fewer Sr atoms on the sub-monolayer islands than on the 1.5 u.c. Sr rich STO islands.

Regarding the low formation energy of SrO on the surface and in the bulk of STO [164], the excess of Sr in STO thin film may introduce atomic rearrangement both on the surface and in the bulk at the thermodynamic equilibrium. However, during the thin film growth process, the kinetic effects are important. For this we have to consider the time needed for each process. Given the deposition time for the 1.5 u.c. STO as ~ 240 s as a good approximation, we can estimate the diffusion length of the cations during the whole process according to the 1D relation:

$$l_D \cong \sqrt{Dt}\,. \tag{4.7}$$

Considering the diffusion coefficient of the Sr ions in the undoped STO bulk in the range of 10^{-20} m^2/s [165], the diffusion length of the cations in such a time scale is only around 0.17 nm. As for STO, this diffusion length is around 0.5 u.c. of the STO lattice. Thus only the exchange between the surface atoms and the next neighbors underneath is possible. It has to be mentioned that the estimation above is based on the measurements in a STO single crystal, where the defect concentration is low. It is possible that the diffusion of ions via exchange with cation vacancies is increased for the high configuration freedom or increased entropy [166]. However, this effect might not be so strong in the Sr rich STO thin film, since the amount of Ti vacancies in Sr rich STO is low due to the high formation energy of the Ti vacancies [25, 26]. Therefore the diffusion length of Sr ions in STO is less than 1 u.c. and we can conclude that the atomic rearrangement cannot extend into the bulk.

Therefore the process of the atomic arrangement on the surface can be interpreted as following: as the Sr atoms on the STO islands may already exist at sub-monolayer stage, they can float to the new STO island surface on top of them. Since the incoming new STO islands are also Sr rich, the total amount of the Sr atoms on the STO new islands is higher than on the STO islands below. The increased amount of Sr atoms on the surface results in the formation of reconstructions and AFM visible 0.2 nm islands.

In summary, the upwards-floating of Sr atoms in the Sr rich STO growth process may be the main reason for the existence of 0.2 nm surface islands at 1.5 u.c. film thickness.

4.4 Defect formation with cation non-stoichiometry

4.4.1 Experiments

To determine the termination evolution during STO homoepitaxial growth on STO single crystal, the deposition of 20 nm thick STO thin films with four different laser fluences is carried out. The TiO_2 terminated (001)STO substrates with identical miscut angle of ~ 0.1° (i.e. terrace length around 250 nm) are heated up to 800 °C under $pO_2 = 10^{-1}$ mbar. The depositions are carried out with four different laser fluences of 1.05 J/cm^2, 1.44 J/cm^2, 1.62 J/cm^2 and 2.25 J/cm^2. During growth, *real-time* RHEED monitoring is carried out. The thin films are subsequently characterized with an *in-situ* angle resolved XPS method to characterize the termination change. *In-situ* AFM scans are carried out on all four samples to study the morphology.

For the $LaAlO_3$ (LAO) growth on STO, the different terminated homoepitaxial STO thin films are employed as substrates. Single crystal LAO is used as target. The repetition rate is 1 Hz and the laser fluence is 1.9 J/cm^2. Deposition is carried out at 700 °C and 10^{-4} mbar pO_2 for 10 u.c.. The surface of LAO grown on STO homoepitaxial thin films is characterized by *ex-situ* AFM operating in tapping mode. After AFM, Hall measurements are carried out for all four samples and the sheet carrier concentration and mobility are obtained. The LAO on Sr rich STO is further characterized by the TEM with atomic resolution in order to clarify the formation of extended defects for these films.

4.4.2 Results

Figure 4.10 (a)-(d) shows the surface morphology with the line profiles of the RHEED pattern across (1 0), (0 0) and (-1 0) in the inset. For the films with lower fluences of 1.05 and 1.4 J/cm^2 (Figure 4.10 (a) and (b)), the terrace structure of the substrate can be observed after the 20 nm film growth. For films with higher fluences of 1.62 and 2.25 J/cm^2 (Figure 4.10 (c) and (d)), no clear terraces can be observed. However, from the statistic point of view, the surfaces for all four samples are equally smooth with a root-mean-square roughness below 0.25 nm. RHEED intensity profiles are obtained through line-by-line integration of the RHEED intensity perpendicular to the diffraction streaks of (1 0), (0 0) and (-1 0). They are presented in the inset of Figure 4.10 (a)-(d). An increased contrast between the first order diffracted electrons ((1 0) and (-1 0)) and the specular spot (0 0) is observed for a decreased laser fluence, indicating an increase of the SrO-termination fraction [42].

Figure 4.10 (e) shows the XPS peak intensity ratio between Sr3d and Ti2p at different angles with error bars. The fitting of the data points is according to the method described in Equation (3.51) in chapter 3.3.5 and the best fitting curves are shown as solid lines.

The corresponding SrO termination ratio and atomic Sr concentration in the thin film obtained from fitting are listed in Table 4.2. In Table 4.2 we see that the surface termination of SrO is 100 % for 1.05 J/cm^2, whereas the atomic Sr concentration with respect to Sr+Ti is ~ 54 %. This means not only the surface termination is switched from TiO_2 to SrO, but also in the thin film there is an excess of Sr atoms. As the laser fluence increases to 1.44 J/cm^2, the surface termination of SrO is ~ 76 % and the atomic Sr concentration in the thin film is ~ 49.8 %. Thus the thin film is stoichiometric within the measurement error of XPS ~ 2 % [134]. For the laser fluence of 1.62 J/cm^2, the surface termination of SrO is 0 % and the Sr atomic concentration is 48.5 %, which is slightly Ti rich. With further increasing the laser fluence to 2.25 J/cm^2 not only the SrO surface termination is 0 %, the thin film stoichiometry becomes $N_{\mathrm{Sr}}/(N_{\mathrm{Sr}} + N_{Ti})$ ~ 47.7 %, which is heavily Ti rich.

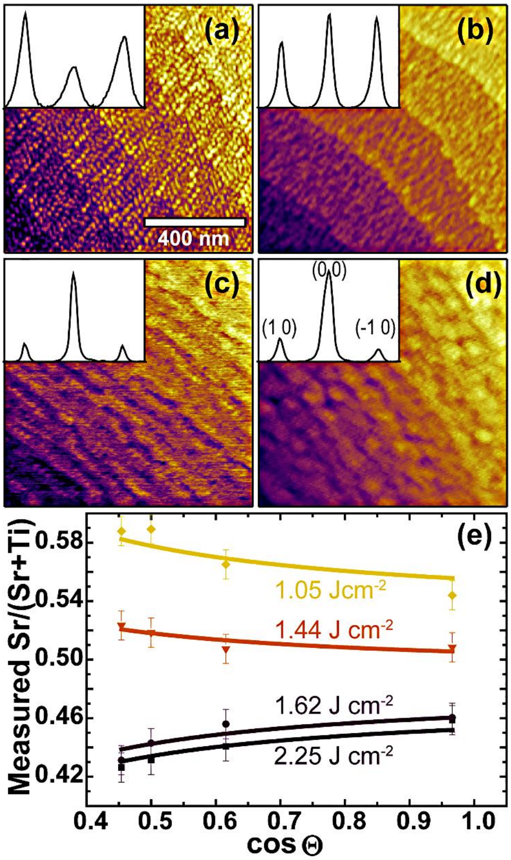

Figure 4.10 *Termination and stoichiometry determination for STO thin films. (a)-(d) AFM-morphology of 20 nm homoepitaxial STO thin films grown with a laser fluence of 1.05, 1.44, 1.62 and 2.25 J/cm^2, respectively. Step terraces are of unit cell height (400 pm). Inset: Line profiles extracted from the RHEED pattern after growth. For each case, only the specular spot and 1st order diffracted electrons are detected (each peak is labeled exemplary in (d)). (e) Measured cation ratios (data points) from XPS as a function of the photoemission angle and fits (solid lines) according to the principle illustrated in chapter 3. The results were published in ref. [134].*

Table 4.2 *Sr atomic ratio ($N_{Sr}/(N_{Sr}+N_{Ti})$) and the SrO surface termination ratio (θ_{SrO}) for four different laser fluences. The results were published in ref. [134]. The standard deviation for Sr atomic ratio is given, while the SrO surface termination ratio is a manually given fitting parameter that has no standard deviation. The best values for SrO surface termination that gives the fitting curves in Figure 4.10 (e) are shown.*

Laser fluence F_L (J/cm^2)	**1.05**	**1.44**	**1.62**	**2.25**
$N_{Sr}/(N_{Sr}+N_{Ti})$	54 % ± 2 %	49.8 % ± 1.6 %	48.5 % ± 1.6 %	47.7 % ± 1.6 %
θ_{SrO}	100 %	76 %	0 %	0 %

Figure 4.11 (a) to (d) shows the morphology obtained by AFM of the LAO grown on STO homoepitaxial films with different stoichiometries on STO substrate. We see the surface morphology of STO thin films is preserved with slightly modified surface morphology with less pronounced small islands. This indicates a layer-by-layer growth for LAO, whereas the islands on STO are possibly broken due to the high kinetic energy in the LAO growth process at low oxygen pressures.

Figure 4.11 (e) shows the electrical data of the Hall measurements, including the sheet carrier concentration (n_S) (left y-axis) and the electron mobility (μ_n) (right y-axis). For both the Sr rich and the stoichiometric samples with surface terminations of 100 % and 76 % SrO respectively, the LAO/STO heterostructures have higher resistances than the 10 MΩ detection limit. On the contrary, the slightly Ti rich and heavily Ti rich condition, resulting in a surface termination of 100 % TiO_2, have shown high sheet carrier concentrations (n_S) between 10^{13} and 10^{14} cm^{-2}. This is a similar value to the literature for LAO/STO fabricated with similar growth conditions on TiO_2 terminated (100)STO single crystals [88, 167-169]. Since the sheet carrier concentration of LAO/STO heterostructures is strongly dependent on the surface termination of the STO, where TiO_2 termination results in conductive interface and SrO results in an insulating interface (see chapter 2), the sheet carrier concentration can be used as a tool to evaluate the surface termination of STO. The difference in the sheet carrier concentration thus verifies again the change in surface termination for the four different samples.

The room temperature mobility (μ_{300K}) for the Ti rich samples is between 2 and 5 cm^2/(Vs). This is also in the right order of magnitude for the mobility in STO [30]. Comparing the slightly Ti rich sample and the heavily Ti rich sample, we found both the sheet carrier concentration and mobility are lower for heavily Ti rich samples. The reduction of the sheet carrier concentration may be attributed to the incorporated defects that trap electrons of the interface, whereas the decrease of the electron mobility may originate in the defective lattice and the increased phonon scattering at the room temperature.

As a short summary, the surface termination of STO is strongly influenced by the thin film stoichiometry. The thin film stoichiometry influences the surface termination in a monotone way: the Ti rich thin film preserves the TiO_2 termination, while the stoichiometric and the Sr rich film of STO have a converted SrO termination. The Sr rich conditions result in a surface termination of 100 % SrO, whereas the stoichiometric conditions lead to a partial SrO termination of around 76 %.

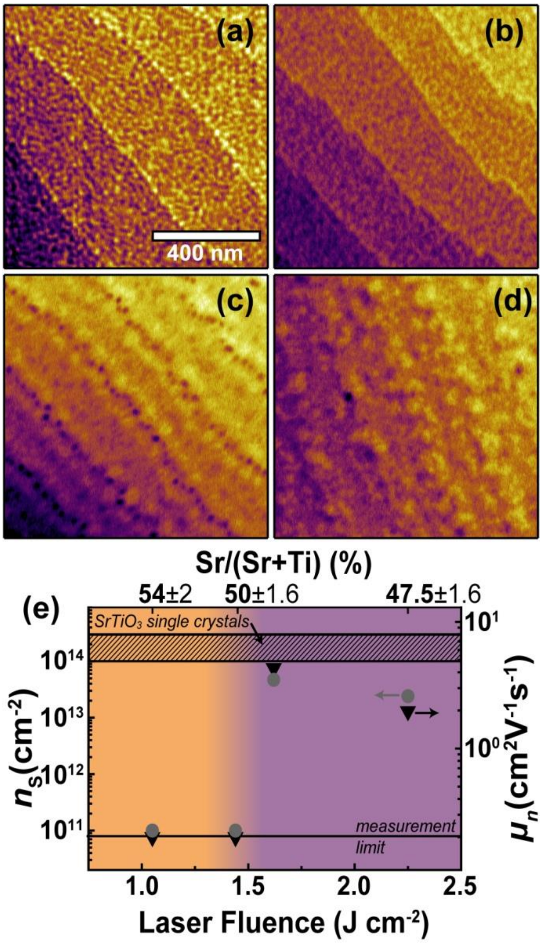

Figure 4.11 *Characterization of LAO/STO thin film heterointerfaces. (a)-(d) AFM-morphology of 10 unit cells heteroepitaxial LAO thin films grown on the films shown in Figure 4.10. Step terraces are of unit cell height (400 pm). (e) Sheet carrier concentration* n_S *(grey dots) and electron mobility* μ_n *(black triangles) extracted from Hall measurements for each heterostructure. The STO stoichiometry is shown at the top axis. The surface termination is indicated with a color gradient from complete SrO termination (orange) to complete* TiO_2 *termination (violet). The sheet carrier concentration and mobility range expected for LAO/STO interfaces fabricated with STO single crystals is indicated by the shaded area. For the SrO terminated STO films, the sheet resistance of the resulting heterostructures is barely above the measurement limit, which inhibits the extraction of quantitative values for the sheet carrier concentration and mobility. The results were published in ref. [134].*

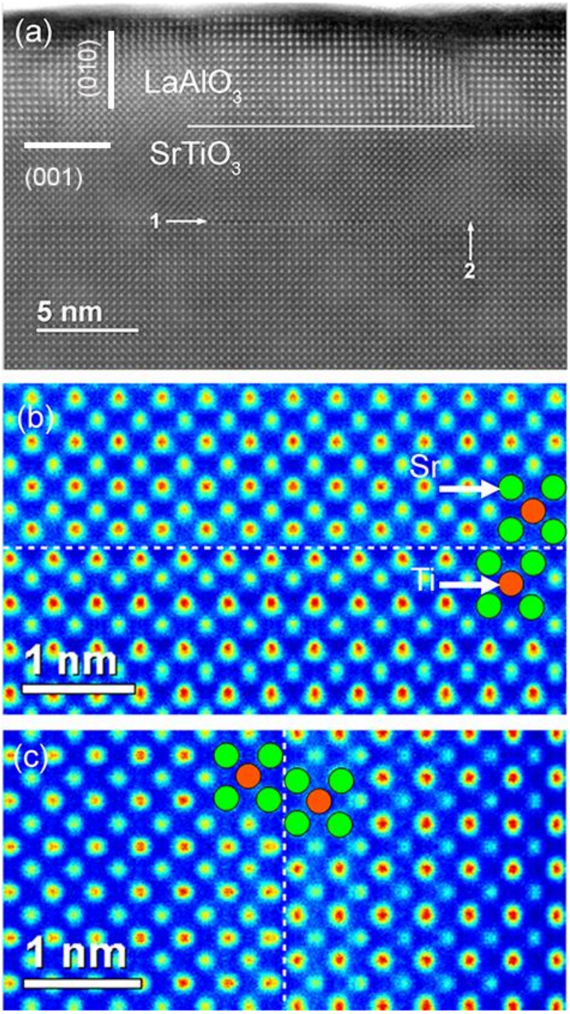

***Figure 4.12** (a) HAADF of part of a 50 u.c. Sr rich STO(001) thin film with 10 u.c. of LAO on top obtained by STEM. We see two kinds of anti-phase boundaries (APB) 1 and 2. (b) and (c) are HAADF images averaged along the APB 1and APB 2, respectively (images are encoded in false color scale for easy recognition of the type of atomic columns (green: Sr, orange: Ti-O). STEM measurements were carried out by Hongchu Du.*

A more detailed look into the atomic structure of LAO on Sr rich STO thin film is enabled by STEM. Figure 4.12 (a) shows the high-angle annular dark field (HAADF) image of the Sr rich STO with 10 u.c. LAO on top of it. The boundary between LAO and STO is qualitatively marked with the horizontal white line, keeping in mind that the surface of both STO and LAO is not flat and with 2 nm roughness. The following discussion is focused on the STO below the LAO. We see two different types of the anti-phase boundaries (APB), which are on the (001) plane (APB 1) and the (010) plane (APB 2), respectively. The HAADF images averaged along APB 1 and APB 2 are presented in Figure 4.12 (b) and (c). The orange circles represent the Ti-O column and the green circles represent the Sr column in [100] direction. We see in Figure 4.12 (b) on the APB 1, two Sr rows are accommodated with 0.5 u.c. parallel shift in [010] direction, indicating a rock-salt-type SrO structure in plane (001). On the APB 2 (Figure 4.12 (c)), two Sr columns are arranged with 0.5 u.c. parallel shift in [001] direction, indicating a rock-salt-type SrO structure in plane (010).

Figure 4.12 (a) also shows that the lateral extension of the APB 1 in the (001) plane is around 10 nm. Since the islands on the surface of 50 u.c. Sr rich STO have around 20 nm diameter (Figure 4.10 (a), 10 islands on the 200 nm wide terrace), Figure 4.12 (a) should represents a cross section comprising two islands without APB 1 and an island with APB 1. The two interfaces between these three islands should be two APB 2. However, only one clear APB 2 between the central region and the right region is visible in Figure 4.12 (a), whereas on the left side a diffuse region is observed with overlapped intensities of Sr and Ti-O columns. This indicates that the cross section for TEM meets only the APB 2 on the right side with perpendicular configuration, whereas the APB 2 between the left and the middle islands has oblique angle to the cross section or lamella plane. The 3D model for the islands with APB is depicted in Figure 4.13.

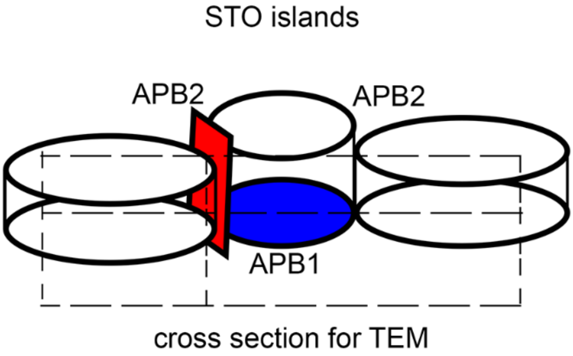

Figure 4.13 *3D model for the different configurations of APB 2 formed between three different STO islands.*

As revealed by the STEM picture in Figure 4.12, the anti-phase boundary in the (001) plane (APB 1) and in the (010) plane (APB 2) are observed within the region of 12 u.c. beneath the surface of 50 u.c. of the Sr rich STO thin film. However, the first 38 u.c. of the STO are completely homogeneous and have a high lattice perfection.

4.4.3 Discussion

Combining the results from chapter 4.2, 4.3 and 4.4, we see that the defects generated during the Sr rich STO growth can be divided into three stages: (1) for ***sub-monolayer growth*** the diffusion coefficient is reduced by the cation non-stoichiometry, which indicates the presence of ***point defects***; (2) at small thickness (***1.5 u.c.***) the surface is enriched of Sr atoms with ***clear Sr rich reconstruction and even SrO islands*** on top of STO islands; (3) ***at larger thickness (like 38 u.c. shown in Figure 4.12 (a)),*** the ***APB*** start to form. This change of the defect formation at different growth stages can be understood by the upwards-floating process of Sr atoms to the surface, which has been suggested in the discussion in chapter 4.3. Furthermore the change of the defect formation may also be a result of a thermodynamic stabilized rock-salt-type SrO in STO. At the initial growth stage, the sub-monolayer regime, the Sr excess atoms flow to the surface but their number density is not sufficient to form large area structures visible by AFM. Above 1.5 u.c., the upwards-flow of Sr to the surface continues and the formation of large area Sr rich reconstructions and 0.5 u.c. island is started. As the surface amount of Sr further increases to larger thicknesses, a rock-salt-type SrO double layer may form on the surfaces both perpendicular and parallel to the growth direction. The formation of SrO double layer islands with increased amount of SrO has been observed by Takahashi et. al [104] and in our termination experiments. Theses SrO double layer islands remain stable in the Sr-rich STO. The STO layers grown on the rock-salt-type SrO islands (marked region with broken lines in Figure 4.14) and the neighboring normal STO lattice lead to a phase shift between SrO and TiO_2 semi-monolayers. As a result, APB 1 and APB 2 are formed.

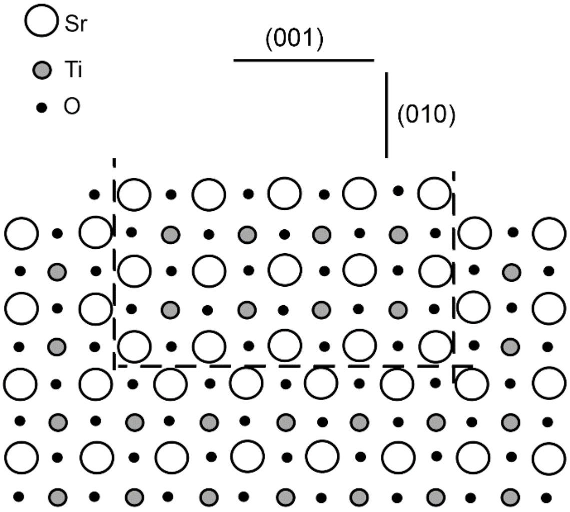

Figure 4.14 *A sketch of the atomic configuration of APB 1 in (001) and APB 2 in (010) during growth*

One has to pay attention to the point that even at nearly stoichiometric growth conditions, the surface termination is not 50 % SrO but slightly SrO rich (76 %). This fact implies that the excess of Sr atoms are consumed rather through self-organized termination conversion than the incorporation into the thin film as defects. This further verifies the mechanism of the floating of the Sr to the surface and indicates the surface chemistry is different from bulk.

As the laser fluence increases to 1.62 J/cm^2 and 2.25 J/cm^2 respectively, the thin film becomes Ti rich and the TiO_2 termination is preserved. The accommodation of the Ti excess in STO is in the form of amorphous TiO_2 phase with high Ti concentration [170], whereas by low Ti excess mainly Sr vacancies are formed. These Sr vacancies in the STO thin film have also been identified qualitatively by positron annihilation lifetime spectroscopy (PALS) [41, 171-172].

4.5 Growth modes with cation non-stoichiometry

As discussed in the previous chapters, the cation non-stoichiometry has a strong impact on surface diffusion, surface atomic rearrangement and defect formation. The detailed study on these microscopic processes leads to a better understanding of the growth modes of STO thin films with cation non-stoichiometry. In the following discussion, a correlation between the cation non-stoichiometries and the growth modes is presented.

4.5.1 Experiments

Three 200 nm STO thin films are grown at 10^{-1} mbar and 800 °C with a target-substrate distance of 44 mm and repetition rate of 5 Hz. Laser fluences of 0.69, 1.6 and 2.02 J/cm^2 are applied to achieve Sr rich, near stoichiometric and Ti rich STO films, respectively. The miscut is kept constant for all three samples with a constant terrace length of ~ 250 nm.

4.5.2 Results

As depicted in Figure 4.14 the laser fluence significantly influences the final topography of 200 nm STO thin films (see Figure 4.14 (c), (f) and (i)). The difference in morphology between near stoichiometric and Ti-rich samples is most pronounced near the terrace edges, which are better defined for the near stoichiometric film. Furthermore, the decrease in the diffusion length from the stoichiometric condition to the Ti-rich condition becomes obvious by comparing the respective surface morphologies on the terraces. In Figure 4.14 (f) and (i) the smallest distance between the islands and the holes is marked with arrows. This distance is twice the diffusion length, since all the small islands in this region succeeded in diffusing to the step edges at holes or islands. The distance marked by the arrows can be used as a qualitative estimation of the diffusion length, whereas the exact determination of the diffusion length needs statistics. Keeping this in mind we see the diffusion length of the stoichiometric conditions is larger than for the Ti rich conditions, which indicates that the surface diffusion is stronger at stoichiometric conditions. This is in good accordance with the results in chapter 4.2. The Sr-rich films grown with a lower laser fluence show a completely different surface containing many small islands with a height of around 20 nm. The different topographies can be explained by the different growth modes, which can be deduced from the shape of the RHEED pattern and the oscillation behavior of the RHEED intensity at the specular point (Figure 4.14 (a), (b), (d), (e), (g) and (h)).

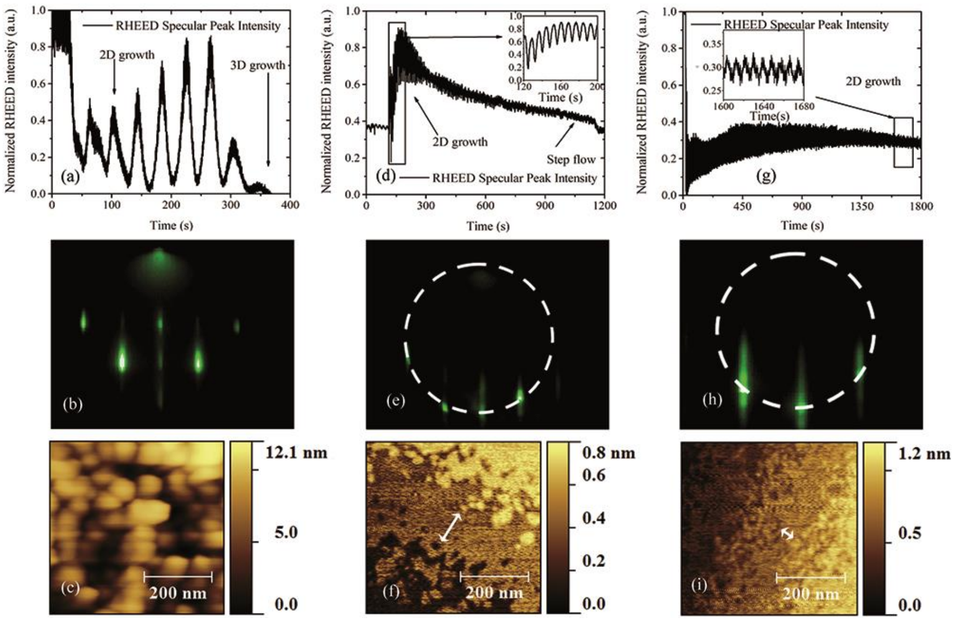

Figure 4.14 RHEED oscillations, final RHEED pattern, and the morphology from NC-AFM for STO thin films grown with different fluence and corresponding stoichiometry. (a), (b) and (c) Sr-rich with F_L = 0.69 J/cm^2; (d), (e) and (f) near stoichiometric with F_L = 1.6 J/cm^2; (g), (h) and (i) Ti-rich with F_L = 2.02 J/cm^2. The oxygen partial pressure is 10^{-1} mbar for all three samples. The terrace length of all three substrates is 200 nm to obtain a comparable growth process. The arrows in (f) and (i) show the distances between nearest holes and islands. The results were published in ref. [63].

For the Sr-rich films the RHEED oscillations disappear after several periods (Figure 4.14 (a)) and the RHEED pattern (Figure 4.14 (b)) changes from points on the Laue circle expected for a 2D surface to the reciprocal lattice of a cubic structure, which can be attributed to the three-dimensional (3D) diffraction of the perovskite structure, indicating a transition to 3D island growth. This indicates that for the Sr-rich films the 3D island growth starts after several monolayers, resulting in the islands observed on the surface in Figure 4.14 (c).

For the stoichiometric film, the RHEED oscillations disappear after several periods and the intensity of specular point remains constant (Figure 4.14 (d)). All points of the RHEED pattern are still on the Laue circle indicating the preservation of a 2D surface (Figure 4.14 (e)). This reveals that the growth of the stoichiometric film starts with 2D growth but it is converted to step-flow growth after several monolayers. The step flow mode results in a step terrace structure with a very low density of holes on a terrace (Figure 4.14 (f)). Since the terrace length of all substrates is around 200 nm, the diffusion length of 50 nm under stoichiometric conditions is insufficient to enable step-flow growth at the early stage, as indicated by the RHEED oscillations (Figure 4.14 (f)) and the early stage morphology shown in Figure 4.3 (f)-(j).

However, after several monolayers the step edges are roughened and the effective terrace length is reduced, which is already visible at 0.8 ML in Figure 4.3 (j). The reduced terrace length enables most of the small islands to diffuse to the terrace edges. Thus a transition between 2D to step flow is observed under near stoichiometric conditions.

For the Ti-rich films, the RHEED oscillations last until the end of the deposition (Figure 4.14 (g)) and the diffraction points are all on the Laue circle (Figure 4.14 (h)), indicating a 2D type growth. Compared with the terraces of the stoichiometric film (Figure 4.14 (h)), where the distance between nearest holes and islands is bigger than the island diameter, the islands and holes on Ti-rich terraces (Figure 4.14 (i)) have a distance equal to the island diameter. This indicates that no perfect 2D layer-by-layer growth can be achieved under Ti-rich conditions but a more realistic two-layer growth mode occurs as reported in [68] or even multi-layer growth mode. In the two-layer growth mode and multi-layer growth, the next layer starts to grow before the last layer is finished, thus islands and holes occur on the same terrace. Since the growth mode of the first monolayer of Ti rich STO is layer-by-layer growth (see chapter 4.3), there should be a growth mode transition from 2D layer-by-layer growth to the 2D multi-layer growth mode. The exact start of this transition, however, is not obtainable from the RHEED oscillations.

Since the samples presented in Figure 4.14 are grown at 0.1 mbar, the kinetic energy of the particles is insufficient to influence the growth kinetics for all investigated fluence values (see ref. [63] and chapter 2). However, the kinetic energy of the impinging species for a growth pressure below 0.01 mbar is sufficient to break up 2D islands thereby resulting in a smoothening of the growing film surface. This is confirmed by Figure 4.15, which depicts a STO film grown at $p = 10^{-3}$ mbar, exhibiting an atomically flat surface. Despite of the strongly pronounced non-stoichiometry under these conditions and the resulting *c*-lattice elongation $\Delta c \sim 1$ pm, the step-terrace structure is still visible for 200 nm thick films, indicating a steady layer-by-layer growth. This demonstrates that the inhibited surface diffusion present at significant non-stoichiometries can in principle be compensated by the surface fragmentation process induced by energetic particles present at low oxygen pressures. In another word, the ion bombardment leads to a roughening of the surface and the diffusing species need shorter diffusion lengths for obtaining a homogeneous film.

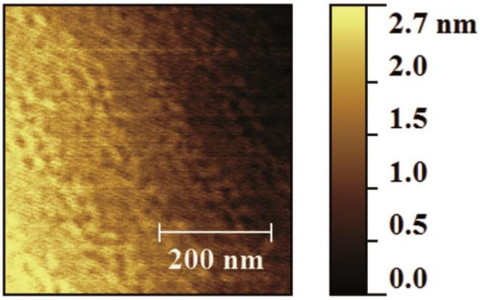

Figure 4.15 *Surface morphology of a 200 nm thick STO film determined by NC-AFM scans (2×2 μm²). With* $T_S = 800$ *°C,* $F_L = 1.4$ *J/cm²,* $p = 10^{-3}$ *mbar,* $f_L = 5$ *Hz. The result was published in ref. [63].*

4.5.3 Discussion

The growth mode transition from 2D layer-by-layer to 3D featured growth for the Sr rich sample is a complex process. The cation non-stoichiometry, which introduces different defects at different growth stages (as discussed in chapter 4.4.3), should have strong impact on the growth mode transition process. As revealed by the STEM picture in Figure 4.12, the epitaxial nature of the growth exists for almost 40 u.c. Sr rich STO, whereas only 12 u.c. Sr rich STO show APBs and islands-like growth. Combined with the fact that the growth of such Sr rich STO experienced a 2D to 3D growth mode transition, it is qualitatively clear that the APB formation influences the 2D to 3D growth mode transition. However, as STEM shows only the local atomic structure in the scale of 100 nm, which comprises only three islands, it is hard to establish quantitative comparison between STEM and the *real-time* growth monitoring RHEED that covers the whole surface of STO within the mm scale. Moreover, as the *c*-lattice of Sr rich thin film is expanded (see chapter 4.1), there should be a lattice strain in the film. The relief of the strain during the growth process could be another reason for the coherent 3D growth after reaching a certain thickness. As a conclusion, for the thin film growth with a certain cation non-stoichiometry, both the strain relief and the defect formation from the cation non-stoichiometry should be responsible for the growth mode transition during Sr rich STO homoepitaxy.

The high diffusion coefficient and the roughening of the terrace edges are the main reasons for the growth transition from 2D layer-by-layer to step flow growth for stoichiometric STO homoepitaxy. At this point, the right stoichiometry plays a key role to establish this kind of growth mode. Deviations form stoichiometry would lead to extended defect structures or reduced diffusion coefficients and may reduce the diffusion length or even lead to 3D growth. Thus for the stoichiometric homoepitaxial growth, the exact cation stoichiometry plays an important role.

For the Ti rich homoepitaxial growth, the growth mode evolves towards a multi-layer growth mode with formation of islands before completing one monolayer. This indicates the nucleation rate on the formed island is higher than the growth rate of the not yet finished island underneath. However, this decrease is not strong enough to trigger 3D islands growth. Moreover, as the point defect like Sr vacancies have a low formation energy in Ti rich STO, the lattice is stable despite of the non-stoichiometry and no extended defects are observed.

As a short summary for the growth of STO with different stoichiometries on single crystal STO substrates, both the defect formation and the surface diffusion are important for the determination of the growth mode. For growth with extended defect formation and inhibited surface diffusion (Sr rich condition), the 2D growth mode becomes 3D growth mode as the thickness increases. For growth without extended defect formation and inhibited surface diffusion (Ti rich condition), the 2D growth mode can be sustained, however it is turned from 2D layer-by-layer growth to a 2D multi-layer growth. For the growth without extended defect formation or inhibition of surface diffusion (stoichiometric condition), the 2D layer-by-layer growth can be even enhanced to step-flow growth with roughened step edges.

4.6 Conclusions

The impact of cation non-stoichiometry on the growth process for complex oxide thin films in the PLD has been identified by the systematic study on the epitaxial growth process of STO thin films with different cation non-stoichiometries. The cation non-stoichiometry is introduced by the preferential scattering of Ti species during the propagation process of the plume. The cation non-stoichiometry can influence the surface diffusion and the defect formation. The cation non-stoichiometry can decrease the diffusion coefficient for the initial growth stage through the strain between non-stoichiometric STO unit cells and the stoichiometric substrate. With increasing film thickness, the defect formation both on the film surface and in the thin film bulk gain importance. For the near stoichiometric condition with a low defect concentration, the growth at optimized condition is 2D step flow growth with a perfect lattice and surface structure. If only point defects are present, like Sr vacancies in Ti rich STO, the growth remains 2D type without transition towards 3D growth. For Sr rich conditions, the non-stoichiometry cannot be accommodated by point defects. Instead of extended defects like antiphase boundaries are formed and the growth experiences a transition from 2D towards 3D.

The extended defect formation process in Sr rich STO revealed the upwards floating of Sr atoms to the surface during the PLD growth process. This effect accumulates with increasing layer thickness and explains the different defect types for different stages in Sr rich STO growth: in sub-monolayer regime, the defects are not visible; as the thickness increases to several monolayers, the surface Sr amount increases. Thus the surface reconstruction changes and 2D island formation due to Sr excess is observable. A termination change is achieved after tens of monolayers of Sr rich STO, after which rock-salt-like SrO 2D islands start to form. Theses rock-salt-like SrO 2D islands are responsible for the formation of antiphase boundary in both (010) and (001) planes and the growth mode transition from 2D to 3D at a later stage of growth. This helps understanding the formation of the Ruddlesden-Popper type of defects observed for Sr rich STO thin films in the literature [43].

5 In-situ study on the heteroepitaxial growth in PLD

In this chapter, the heteroepitaxial growth of $LaAlO_3$ (LAO) on $SrTiO_3$ (STO) is studied *in-situ* with a combination of RHEED and OIRD. The OIRD signal of LAO growth on TiO_2 terminated STO is presented in chapter 5.1 and discussed with a transition matrix method. The pressure sequence of LAO on TiO_2 terminated STO is presented in chapter 5.2 and the annealing time sequence in chapter 5.3.
Since the termination can also change the heterostructure properties, the OIRD signal for LAO growth on different terminated STO is discussed in chapter 5.4. and 5.5 with 100 % SrO termination and 55 % SrO termination, respectively.

5.1 LAO growth on TiO_2 terminated STO

5.1.1 Experiments

LAO single crystals are used as targets, while TiO_2 terminated (001)STO single crystals are used as substrates. The laser fluence is 1.5 J/cm^2. For this standard deposition process, $8x10^{-4}$ mbar O_2 with 10^{-9} mbar UHV background pressure is used as deposition ambient. During the deposition, the target to substrate distance is kept at 44 mm while the substrate temperature is kept at 800 °C. The averaged intensity of the (0 0) reflex of the RHEED pattern is taken to monitor the thickness of the LAO film. The imaginary part of the reflectivity difference is selected as OIRD signal. LAO with thicknesses of 3 u.c., 7 u.c., 11 u.c. and 14 u.c. is deposited.

5.1.2 Results

Figure 5.1 shows the RHEED (Figure 5.1 (a)) and OIRD (Figure 5.1 (b)) intensity during the growth and the AFM morphologies for STO substrate (Figure 5.1 (c)) and the 8 u.c. LAO film (Figure 5.1 (d)).

The RHEED intensity depicted in Figure 5.1 (a) firstly oscillates superimposed with a strong reduction until a thickness of 3 u.c. of LAO is reached, whereafter it oscillates around a constant value with a constant amplitude. Therefore the deposition rate of LAO can only be determined by the oscillations after 3 u.c., which is ~ 40 pulses/u.c.. The averaging of the first 3 u.c. deposition time gives the same deposition rate.

The OIRD signal shows also oscillations within one monolayer (Figure 5.1 (b)), which might be attributed to the morphology change during one monolayer growth [173] or the mechanical vibrations (see chapter 3) from the environment. However, since the morphology change during LAO growth is experimentally hard to follow, the study on the correlation between OIRD signal and the morphology will not be carried out here. Instead, the focus is on the OIRD at each completed monolayer, i.e. at the maximum of RHEED intensity. The OIRD intensity can be fitted into two straight lines with oscillations on them (Figure 5.1 (b)). These two lines have distinguishable slopes with the transition point at 3 u.c.. This means the OIRD intensity increases with a constant rate within 3 u.c., whereas this constant is changed after 3 u.c. of LAO. Similar measurements carried out in our group were published in ref. [174].

In Figure 5.1 (c) and (d) the AFM morphology for the STO substrate and the 8 u.c. of LAO on STO are compared. Since the surface terrace structure is preserved during growth, the growth of 8 u.c. of LAO on STO takes place in 2D layer-by-layer mode.

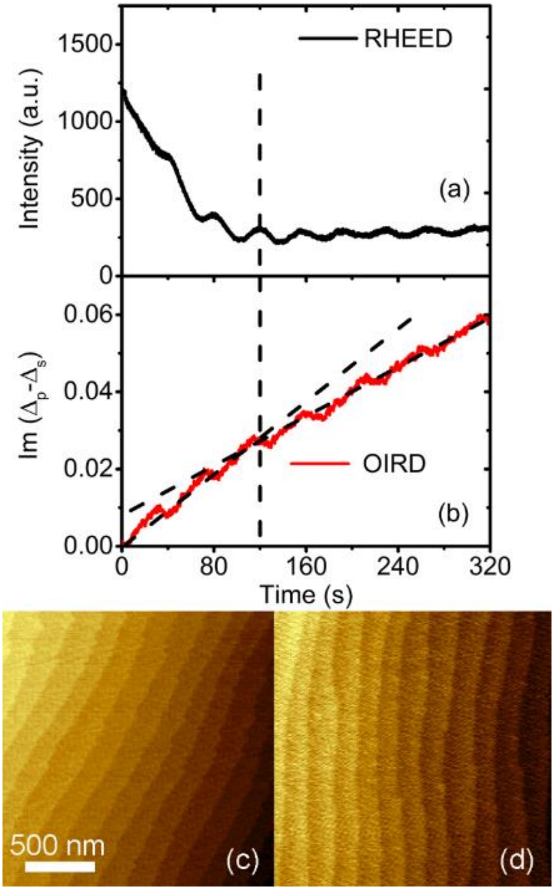

Figure 5.1 *The peak intensity of the specular spot (0 0) (a) and the imaginary reflectance difference measured by OIRD (b) for the growth of 8 u.c. of LAO on* TiO_2 *terminated STO. The vertical broken line is for the indication of 3 u.c.. The two broken lines along the OIRD signal in (b) are the guide to the eye for the OIRD signal at complete monolayers. (c) and (d) are the AFM morphology for the STO substrate and the 8 u.c. LAO on STO, respectively. All the terraces have a height of 0.4 nm.*

In Figure 5.2 the thickness dependence of the OIRD signal is depicted for the growth of 7 u.c., 11 u.c. and 14 u.c. LAO. The slope change at 3 u.c. for LAO growth on STO can be seen for all the thicknesses. This confirms that the slope change is a reproducible phenomenon.

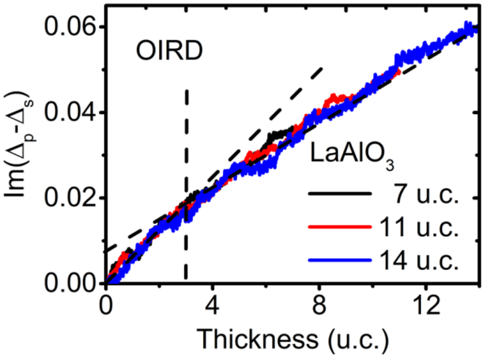

Figure 5.2 *OIRD signal of LAO on TiO$_2$ terminated STO with different LAO thicknesses*

5.1.3 Discussion

As shown by the Figure 5.1 and Figure 5.2, the slope change in the OIRD signal is a reproducible effect that is independent on any surface structure formation. To understand this phenomenon, a detailed look into the theoretical interpretation of the OIRD signal is necessary.

For a general substrate-film system, the OIRD signal can be expressed as [108, 175-176]:

$$\Delta_p - \Delta_s \approx i\frac{4\pi n_0 \cos\varphi_0 \tan^2\varphi_0 \varepsilon_s}{\lambda(\varepsilon_s - \varepsilon_0 \tan^2\varphi_0)(\varepsilon_0 - \varepsilon_s)}\left(\frac{d_f(\varepsilon_d - \varepsilon_s)(-\varepsilon_0 + \varepsilon_d)}{\varepsilon_d}\right) \tag{5.1}$$

, where n_0 is the refractive index of the ambient, φ_0 is the incidence angle, ε_0 is the relative optical permittivity of the ambient and λ is the wavelength of incident light. d is the thin film thickness, ε_s is the optical permittivity of the (assumed) semi-infinite substrate and ε_d is the optical permittivity of the thin film.

Specifically for the LAO/STO system, where the imaginary part of the optical permittivity of LAO [94, 177] and STO [178, 179] are both negligible at the applied wavelength, the OIRD signal can be correlated to the properties of LAO and STO as follows:

$$\mathrm{Im}(\Delta_p - \Delta_s) \approx \frac{4\pi \cos\varphi_0 \tan^2\varphi_0 \varepsilon_{SrTiO_3}}{\lambda(\varepsilon_{SrTiO_3} - \tan^2\varphi_0)(1 - \varepsilon_{SrTiO_3})}\left(\frac{d_{LaAlO_3}(\varepsilon_{LaAlO_3} - \varepsilon_{SrTiO_3})(-1 + \varepsilon_{LaAlO_3})}{\varepsilon_{LaAlO_3}}\right) \tag{5.2}$$

, where φ_0 is the incidence angle ~ 83°, and λ is the wavelength of incident He-Ne laser of ~ 632.8 nm. These parameters are constant during the PLD process. In contrary, the thickness of each LAO monolayer ($d_{\mathrm{i,LAO}}$), the effective optical permittivity of the STO substrate ($\varepsilon_{\mathrm{STO}}$) and the LAO monolayers ($\varepsilon_{\mathrm{LAO}}$) can be changed during the growth process. In the following we will discuss which of the 3 parameters is responsible for the slope change observed in Figure 5.2.

Firstly we take a look at the STO side. The most important concern are the delocalized electrons on the STO side of the LAO/STO interface [97]. As illustrated by Dubroka et.al., the conductive interface between LAO/STO lies on the STO side and has a plasmonic response to the photons with energies around 100 meV at a temperature below 300 K [180]. This optical response originates from delocalized electrons condensed at the interface on the STO side, however, it can't contribute to the OIRD signal for two reasons: firstly, the temperature for the LAO growth on STO is 800 °C, which is much higher than the visibility limit of the plasmonic response from the 2DEG in STO; secondly, the photon energy used for OIRD is ~ 1.98 eV, which is much higher than the plasmonic response energy level. Thus the contribution from the ***delocalized electrons on the interface can be excluded***.

The structural change in STO may also change the optical properties at 1.98 eV. The first possibility is the existence of point defects or defect clusters that can generate in-gap states that influence the optical transition processes e.g. of reduced STO [181]. However, as indicated in ref. [181], for the moderate reduction conditions, the increase of the charge carrier density in STO is not enough to introduce any increased response at ~ 2 eV. Only if the reduction progresses to an extend that the surface morphology is strongly changed and the charge carrier density is reduced due to possible extended defect formation (e.g. 2 hours in H_2 at 1000 °C, where the cations are mobile as well), a significant change of optical permittivity is visible at ~ 2 eV. Thus for the growth condition of LAO on STO, where the reduction is very moderate and no surface change is observed, the ***response from defects in STO at 1.98 eV can be neglected***.

Furthermore the strain and A- or B-site doping in STO can also change the inter-band transition [182]. However, these two effects have minimal influence on the response at ~ 2 eV for the optical permittivity. Thus the ***response from strain or extrinsic doping in STO at 1.98 eV can also be neglected.*** Thus the influence of STO is not the source of the OIRD signal change.

The experimental proof for the absence of optical permittivity change for interface STO layers is given by Asmara et. al [94], where the optical permittivity at 1.98 eV does not differ for interface STO at 4-6 u.c. LAO/STO and at 2-3 u.c. LAO/STO.

On the contrary, the contribution of the structural transition in the LAO thin film to the OIRD signal can be significant, where the thickness of each LAO monolayer ($d_{\mathrm{i,LAO}}$) and the effective optical permittivity of LAO monolayer ($\varepsilon_{\mathrm{LAO}}$) have to be considered. Different possibilities for these two factors are discussed in the following.

Firstly we discuss the possibility of changing the LAO monolayer thickness or the *c*-lattice constant. As shown by Cancellieri et.al, the *c*-lattice constant of the first 3 u.c. LAO on STO is higher than the nominal value due to the presence of the electrical field in LAO, so called electrostriction [95], which follows the relation:

$$\Delta d_{LAO} = \alpha E_{dc}^{2}. \tag{5.3}$$

In this paper, the *c*-lattice constant of LAO thin films within 3 u.c. is around 0.382 nm, whereas the LAO film has *c*-lattice constant around 0.3745 nm for the thicker 4 u.c. film. This means the averaged *c*-lattice constant is reduced by 2 % when the build-in field is compensated after 4 u.c.. It has to be mentioned that this averaged *c*-lattice change is gradual. This gradual change implies that the lattice constant change happens only in the first 3 u.c., whereas the rest LAO has no thickness-dependent *c*-lattice parameter change.

Secondly, we discuss a possible change in the effective optical permittivity of LAO monolayer ($\varepsilon_{\mathrm{LAO}}$). As shown by the ellipsometry measurements carried out by Asmara, the effective optical permittivity of the LAO is around 3.8 after 4 u.c., which is smaller in comparison to the effective optical permittivity of LAO with thickness less than 3 u.c. of 4.8 [94]. As proposed by Asmara, this change in LAO originates from the charge transfer process that can influence the optical transition strength and thus the optical permittivity. However, other microscopic mechanisms can also play a role. For example, the optical permittivity can be influenced by the applied DC electrical field if the crystal has non-linear susceptibility, which is called DC electro-optical Kerr effect [183]. The DC electro-optical Kerr effect is described through the formula [184]:

$$\frac{\Delta n}{n^{3}} = \frac{1}{2} R E_{dc}^{2} \tag{5.4}$$

, where Δn is the relative change of the refractive index n, R is the second order electro optical Kerr coefficient and E_{dc} is the strength of the DC electrical field. For small changes of Δn, the relative optical permittivity change $\Delta\varepsilon_{\mathrm{r}}$ can be estimated as:

$$\frac{\Delta \varepsilon_{r}}{\varepsilon_{r}^{2}} \cong \frac{1}{2} R E_{dc}^{2} . \tag{5.5}$$

Since bulk LAO shows no significant electro-optical Kerr effect, it is hard to make a quantitative estimation of the absolute change of optical permittivity with the build-in field in LAO. For a qualitative comparison we assume the R of LAO is around 10^{-20} $\mathrm{m^2/V^2}$ to 10^{-21} $\mathrm{m^2/V^2}$, which is around 2 to 3 orders of magnitude smaller than the typical values of electro-optical Kerr effect materials like $LiNbO_3$ [185], $KNbO_3$ [186], $Pb_xZr_{1-x}TiO_3$ [184], $Ba_{1-x}Sr_xTiO_3$ [187] and $BaTiO_3$ [188]. Even with such a small R, the build-in DC field around 2.4×10^{9} V/m in the 3 u.c. LAO film on STO [95, 189] will still introduce a significant change in optical permittivity of LAO. With 4.26 as the relative optical permittivity in LAO [177], the absolute change in the optical permittivity is 0.1 to 1 according to Equation (5.5). Thus this change is another possibility to explain the optical permittivity change in LAO after 3 u.c. thickness.

As a short summary, both the *c*-lattice constant and the optical permittivity in LAO can be changing during growth. Although the microscopic mechanisms for both effects are still under discussion, the absolute value for the changes can be used for the models in OIRD signal interpretation.

In order not to lose the universality, we will start a qualitative discussion of the OIRD signal firstly with the analytical formula Equation (5.2). According to Equation (5.2) and the discussion above, we get the expression for the slope of OIRD signals, which is only dependent on the monolayer thickness and the optical permittivity of the LAO as discussed before:

$$\frac{\delta(\mathrm{Im}(\Delta_p-\Delta_s))}{\delta d_{LaAlO_3,0}} \approx \alpha\left(d_{LaAlO_3}\frac{\delta}{\delta d_{LaAlO_3,0}} f(\varepsilon_{LaAlO_3}) + f(\varepsilon_{LaAlO_3})\frac{\delta}{\delta d_{LaAlO_3,0}} d_{LaAlO_3}\right) \tag{5.6}$$

, where $\alpha = \dfrac{4\pi n_0 \cos\varphi_0 \tan^2\varphi_0\, \varepsilon_{SrTiO_3}}{\lambda(\varepsilon_{SrTiO_3}-\varepsilon_0 \tan^2\varphi_0)(\varepsilon_0-\varepsilon_{SrTiO_3})}$ is constant since the substrate does not contribute and the incident angle φ_0 is a constant throughout the experiment. $\delta d_{LaAlO_3,0}$ is the unit cell thickness after 4 u.c..

Within the two thickness regions of less than 3 u.c. LAO and more than 3 u.c., the variation of 1 u.c. LAO does not introduce any change in optical permittivity and the first term on the right side of (5.6) is zero. Only the second term has to be considered. Taking optical permittivity change and lattice constant change into consideration, the Equation (5.6) can be simplified to:

$$\frac{\delta(\mathrm{Im}(\Delta_p-\Delta_s))}{\delta d_{LaAlO_3,0}} \approx \begin{cases} \alpha f(\varepsilon_{LaAlO_3}+\delta\varepsilon_{LaAlO_3})\cdot(1+\Delta d_{LaAlO_3}), & n_{LaAlO_3}\le 3 \\ \alpha f(\varepsilon_{LaAlO_3}), & n_{LaAlO_3}\ge 4 \end{cases} \tag{5.7}$$

, where $\delta\varepsilon_{LaAlO_3}$ is the increased optical permittivity for the whole stack and Δd_{LaAlO_3} is the monolayer lattice expansion. This can explain the slope change in a qualitative way. The most important information derived from this simplified formalism is that the latter monolayers do not influence the monolayers already grown, otherwise the slope change should not be abrupt and an additional OIRD signal change is expected. This indicates that the charge transfer does not change the unit cell properties of the first 3 unit cells and only the monolayers for more than 4 u.c. have a normal optical permittivity and lattice constant. However, the quantitative discussion with respect to the parameter changes requires simulations.

The next step is the quantitative interpretation of the OIRD signal. Therefore an optical simulation with the transfer matrix method (TMM) model is applied [190] (using a MATLAB© code, which can be found in the appendix), where the wave propagation and reflection on every interface is included. The basic idea is to treat every unit cell of LAO as a single layer with reflection on surface and interface and transmission through this monolayer. The incoming and outcoming strength of the electromagnetic wave is thus:

$$\begin{bmatrix} E_{LaAlO_3\ surface,incoming} \\ E_{LaAlO_3\ surface,reflected} \end{bmatrix} = \left(\prod_{i=1}^{n_{LaAlO3}} \frac{1}{1+\rho_i} \begin{bmatrix} e^{jk_il_i} & \rho_i e^{-jk_il_i} \\ \rho_i e^{jk_il_i} & e^{-jk_il_i} \end{bmatrix} \right) \begin{bmatrix} E_{SrTiO_3\ substrate,+} \\ 0 \end{bmatrix} \tag{5.7}$$

, where j is the imaginary unit, k_i the wave vector in the corresponding material, l_i the propagation length in the thin slice for light propagation, specifically the thickness of each monolayer of LAO d_{LAO}. ρ_i is the elementary reflectance on each interface that differs for *p*-and *s*-polarizations as:

$$\rho_{i,p} = \frac{\dfrac{n_{i,p}}{\cos\theta_{i,p}} - \dfrac{n_{i+1,p}}{\cos\theta_{i+1,p}}}{\dfrac{n_{i,p}}{\cos\theta_{i,p}} + \dfrac{n_{i+1,p}}{\cos\theta_{i+1,p}}} \tag{5.8}$$

and

$$\rho_{i,s} = \frac{n_{i,s}\cos\theta_{i+1,s} - n_{i+1,s}\cos\theta_{i+1,s}}{n_{i,s}\cos\theta_{i+1,s} + n_{i+1,s}\cos\theta_{i+1,s}} \tag{5.9}$$

, where $\theta_{i+1,p}$ and $\theta_{i+1,s}$ are the incident angles into each layer for *p*- and *s*-polarization, respectively. $n_{i,p}$ and $n_{i,s}$ are the corresponding refractive indices in each layer for *p*- and *s*- polarization, respectively. For the first approximation they are treated equally for homogeneous media and are both the square root of the optical permittivity with $\varepsilon = n^2$.

As the other configuration parameters are illustrated at the beginning of chapter 5.1.3, only the parameters for the materials in the simulations are listed in Table 5.1. It has to be noticed that the refractive index for STO is extrapolated from the room temperature (26.6 °C) value 2.39 with the thermal coefficient ~ $-5.1\text{x}10^{-5}$ °C^{-1} from literature [191] to the deposition temperature (800 °C) value of 2.35. This reduces the optical permittivity of STO from 5.71 at room temperature to around 5.52 at 800 °C. Since the optical permittivity of LAO is not sensitive to temperature, which has been verified by the absence of optical permittivity change at ~ 2 eV from room temperature to 800 °C measured by spectroscopy (not shown here), no extrapolation is needed and the optical permittivity at room temperature ~ 4.26 is used for the 800 °C condition for LAO layer later than 4 u.c... The extrapolation of the lattice constant from room temperature to the high temperature of 800 °C is done by applying thermal expansion coefficients for STO ($9.4\text{x}10^{-6}$ °C^{-1}) [192] and LAO ($10\text{x}10^{-6}$ °C^{-1}) [193]. The room temperature values of STO are 0.3905 nm, 0.3905 nm and 0.3905 nm for *a*-, *b*- and *c*-lattice constants, respectively [194]. Therefore the lattice constant at 800 °C for STO is 0.3912 nm. Due to the tensile strain the room temperature lattice constants of LAO are 0.3905 nm, 0.3905 nm, and 0.3730 nm [95], which is shortened compared to the 0.3789 nm for bulk materials [21]. Following the same consideration for strained LAO thin film at room temperature, the lattice constant at 800 °C for LAO is estimated to be 0.3738 nm. Assuming the electron transfer happens strictly at 3 u.c., the built in field exists in the first three monolayers. Thus the LAO lattice constant for the first three monolayers increase by 2 % to reach 0.3813 nm due to electrostriction. For the simulation, the optical permittivity of

LAO of the first three unit cells is the manually varied fitting parameter. The simulation details and MATLAB code are summarized in the Appendix.

It has been found that the best fitting is achieved by the optical permittivity of first three u.c. of LAO around 5.26. The best fitted OIRD signal is plotted for complete monolayers in Figure 5.3 as separated dots. We see these dots lie very well on the corresponding places of OIRD data from experiment. Thus we can conclude the optical permittivity change and lattice constant change can explain the observed slope change in OIRD signals, which means the OIRD signal represents the ***structural transition in LAO***. More importantly, the abrupt change of the slope at 3 u.c. in the OIRD signal suggests strongly that the charge transfer to the interface does not change the first three grown LAO monolayers, but only influences the latter monolayer of LAO grown on it.

Table 5.1 *The parameters for each monolayer applied in the simulation*

Parameter for each monolayer @ 800 °C	**LAO**		**STO**
	<3 u.c.	>4 u.c.	
***c*-lattice constant *d* (nm)**	0.3813	0.3738	0.3912
Relative optical permittivity ε_r (-)	5.26	4.26	5.52

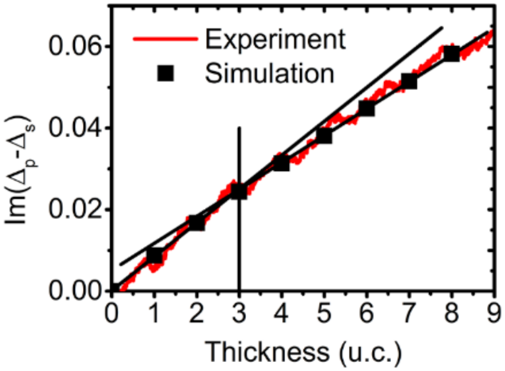

Figure 5.3 *The experimental OIRD signal (red curves) and the calculated OIRD signal at each unit cell with the parameters shown in Table 5.1 (black square spots). The optical permittivity of the first 3 u.c. LAO is the fitting parameter.*

As shown by different techniques, the conductive interface between crystalline LAO and STO is only visible for LAO thicker than 4 u.c. and the samples with 3 u.c. or less than 3 u.c. show no interface charge carriers [18, 92, 103, 195]. However, the exact thicknesses for electronic transition (conductivity transition) and structural transition (lattice parameter and optical permittivity change) are not clear. As a matter of fact, the electronic transition and structural transition are correlated with each other. As shown in other *ex-situ* experiments, the conductivity transition happens at 4 u.c. and the 3 u.c. including 3.5 u.c. LAO/STO samples always show unstable results [92, 103, 195]. Our *in-situ* OIRD measurement shows the charge transfer may happen during the growth at 3 u.c.. We think the adsorbents in air by the *ex-situ* measurements may suppress the conductivity and “delay” the conductivity transition. The influence of the adsorbates on the interface conductivity was also demonstrated by a variation of surface polar adsorbates in different aqueous solutions [87, 196].

As discussed with the theoretical model, the slope change of the OIRD signal can be interpreted as a charge transfer induced lattice constant change and optical permittivity change, where the electronic contribution from the STO should theoretically be small. However, the electronic contribution of STO is not experimentally confirmed yet. To further complete the picture of the mechanism of the OIRD signal change, the disentanglement between the electronic conduction in STO and the OIRD signal is necessary. This disentanglement can be achieved by investigating the OIRD signal and electrical properties by (a) the growth of LAO on STO at different oxygen pressures and (b) the growth of LAO on STO with different annealing times. The reason is that for both cases the electrical properties of the STO vary heavily. The two aspects will be discussed separately in the following chapter.

5.2 Oxygen pressure dependence of the LAO growth on TiO_2 terminated STO

5.2.1 Experiment

The growth of 8 u.c. LAO on STO is carried out under different pO_2, namely 10^{-1}, 10^{-3} and 10^{-5} mbar. Laser fluence is fixed at 1.5 J/cm^2. Target to substrate distance is kept as 44 mm, while the substrate temperature is kept at 800 °C. For all three samples, both *in-situ* RHEED and OIRD are carried out. The signals of RHEED and OIRD for three pressures are normalized to illustrate the transient change during the growth in a better way. The morphologies and surface reconstructions are checked with AFM and RHEED, respectively. The *ex-situ* conductivity, sheet carrier concentration and electron mobility are measured using AC-Hall measurements. All samples are quenched with 10 °C/s cooling rate by switching off the laser heating in the PLD. The aim of quenching is to minimize the effect of the post annealing processes.

5.2.2 Results

We firstly discuss the electrical properties of the LAO/STO heterostructure fabricated under different pressures. In Table 5.2 the electrical properties including the sheet carrier concentration (n_S), sheet conductivity (G_S) and room temperature mobility (μ_{300K}) are summarized. As for $pO_2 = 10^{-3}$ mbar and 10^{-5} mbar the interface is still conductive, the LAO/STO heterostructure for $pO_2 = 10^{-1}$ mbar is insulating. The difference of the sheet carrier concentration between 10^{-1} mbar and 10^{-3} mbar is at least four orders of magnitude, the difference between 10^{-3} mbar and 10^{-5} mbar is still two orders of magnitude.

Both the $pO_2 = 10^{-3}$ mbar and 10^{-5} mbar samples have higher sheet electron concentration than the predicted sheet carrier concentration at the interface, indicating contributions from the STO bulk. The contribution of bulk reduced STO is higher at $pO_2 = 10^{-5}$ mbar than at 10^{-3} mbar. This oxygen pressure dependence of the sheet carrier concentration is in good accordance to literature [88, 96, 169, 197-198].

Table 5.2 *The sheet carrier concentration (n_s), sheet conductance (G_S) and room temperature mobility (μ_{300K}) for $pO_2 = 10^{-1}$, 10^{-3} and 10^{-5} mbar*

pO_2 (mbar)	10^{-1}	10^{-3}	10^{-5}
$\boldsymbol{n}_S$ (cm^{-2})	$<10^{10}$ Under detection limit	$\sim 6.5 \times 10^{14}$	$\sim 3.6 \times 10^{16}$
$\boldsymbol{G}_S$ (Ω^{-1})	$<10^{-6}$ Under detection limit	$\sim 7 \times 10^{-4}$	$\sim 3.8 \times 10^{-2}$
$\boldsymbol{\mu}_{300K}$ ($cm^2/(Vs)$)	-	~ 6.4	~ 6.8

Secondly the details about the LAO growth will be discussed. Figure 5.4 (a) to (f) show the AFM morphology for the substrate and the film with corresponding RHEED pattern for 10^{-1}, 10^{-3} and 10^{-5} mbar, respectively. Figure 5.4 (g) shows the RHEED intensity for three deposition pressures, while the corresponding OIRD signals are summarized in Figure 5.4 (h).

As illustrated in Figure 5.4 (a) to (f), the 8 u.c. LAO on STO still show a similar terrace structure as the substrates for all $pO_2 = 10^{-1}$ mbar, 10^{-3} mbar and 10^{-5} mbar. Together with the fact that the RHEED intensity oscillations are conserved till the end of 8 u.c. for all three conditions (Figure 5.4 (g)), we can conclude the growth of 8 u.c. LAO on STO is still in 2D layer-by-layer growth. The OIRD signal can thus be interpreted with the same principle as in chapter 5.1.3.

In Figure 5.4 (h) the OIRD signals are shown. We see for $pO_2 = 10^{-1}$ mbar, 10^{-3} mbar and 10^{-5} mbar, the OIRD signals ***all experience a slope change at 3 u.c.***. It has to be mentioned that the noise level in OIRD is higher at 10^{-1} mbar than 10^{-3} mbar and 10^{-5} mbar. The reason for this can be an imperfect 2D layer-by-layer growth which is also indicated by the streakier RHEED diffraction pattern, which is a sign for a surface with a higher roughness (the inset of Figure 5.4 (d)) considering the morphology obtained with AFM (Figure 5.4 (d)).

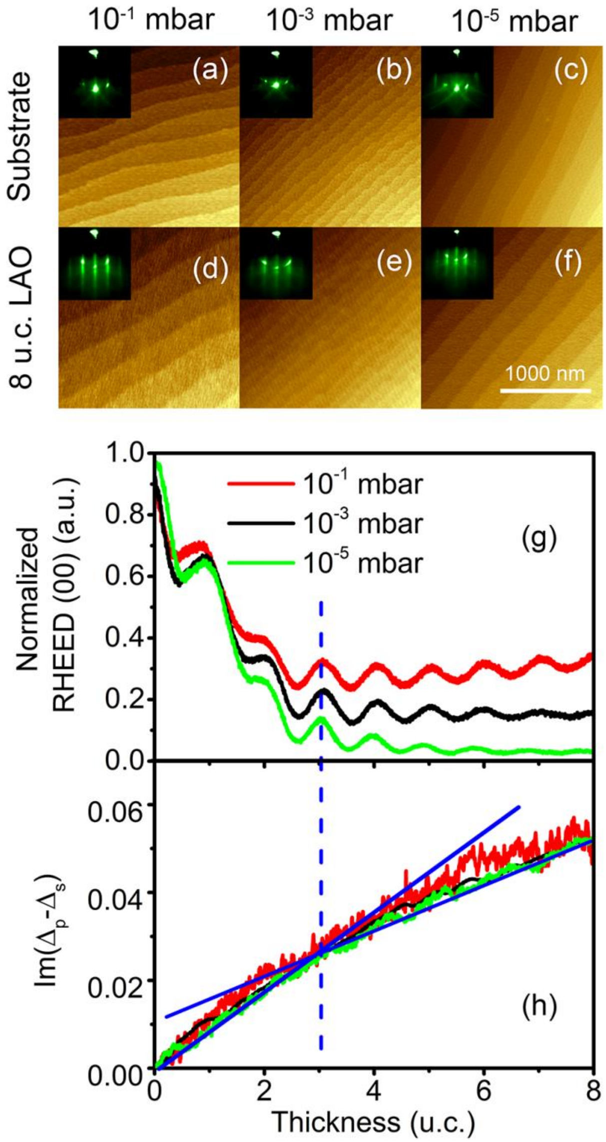

Figure 5.4 *RHEED pattern and AFM morphology for substrates ((a)-(c)) and deposited 8 u.c. LAO/STO thin films ((d)-(f)) for different* pO_2*. (g) the RHEED intensity oscillations for different* pO_2*. (h) the OIRD signal for different* pO_2*. Both RHEED and OIRD are shown as a function of the film thickness.*

5.2.3 Discussion

The difference between the final electronic states of LAO on STO grown at $pO_2 = 10^{-1}$ mbar, 10^{-3} mbar and 10^{-5} mbar originates mainly from the growth process, since all the samples are quenched with minimal influence from the post annealing process. The electrical properties of the LAO/STO heterostructures grown at 10^{-1}, 10^{-3} and 10^{-5} mbar (Table 5.2) are representative for three different states of the interface and the bulk of STO. LAO/STO deposited at 10^{-1} mbar shows no conductivity, which indicates the absence of both interface conductivity and bulk conductivity. LAO/STO deposited at 10^{-3} mbar shows an interface sheet carrier concentration that is only slightly higher than the typical value of a 2DEG between LAO and STO ~ $1x10^{14}$ cm^{-2} [88, 169, 197]. This indicates that the STO bulk is slightly reduced during the growth and a low concentration of oxygen vacancies is present in STO. The LAO/STO deposited at 10^{-5} mbar exhibits a sheet carrier concentration of around $4x10^{16}$ cm^{-2}, which corresponds to a highly reduced STO substrate with a high concentration of oxygen vacancies. For a detailed discussion of the electrical properties of the low pressure deposited LAO on STO see chapter 6. As a summary, the interface conductivity as well as the bulk conductivity of LAO/STO is different for different growth oxygen pressures, where the oxygen vacancy concentration in STO is heavily changed.

However, the OIRD signals for the three different oxygen growth pressures do not have distinct differences. They all have similar features, especially the slope change at 3 u.c.. Therefore we can conclude that the slope change in OIRD signal ***during the growth*** is not influenced by the oxygen vacancies in the STO substrate. If the influence from STO ***after the growth*** can also be excluded, the disentanglement of the oxygen vacancies in the STO substrate and of the OIRD signal is accomplished. This is the point to be discussed in chapter 5.3.

5.3 Post annealing time sequence

5.3.1 Experiments

The growth procedures have identical parameters and are carried out with 10^{-3} mbar and 1.5 J/cm^2 with LAO single crystal as a target and STO single crystals as the substrates. Only the post annealing time after deposition is varied between samples with 0 s, 40 s, 120 s and 200 s with pO_2 kept at 10^{-3} mbar, whereas the heating, cooling, adjustment and deposition time are controlled to be identical (Figure 5.5(a)). After each deposition and annealing process, the sample is characterized *ex-situ* with Hall-effect measurement.

5.3.2 Results

For the OIRD signals for different annealing times (Figure 5.5 (b)), we observe once again the reproducibility of the 3 u.c. slope change. This means that the structural transition in LAO is reproduced. After the stop of deposition at 8 u.c. the samples with different annealing times show almost identical OIRD signals. Only noise that may originate from mechanical vibrations in the environment can be seen. Thus the annealing time has no impact on the OIRD signal.

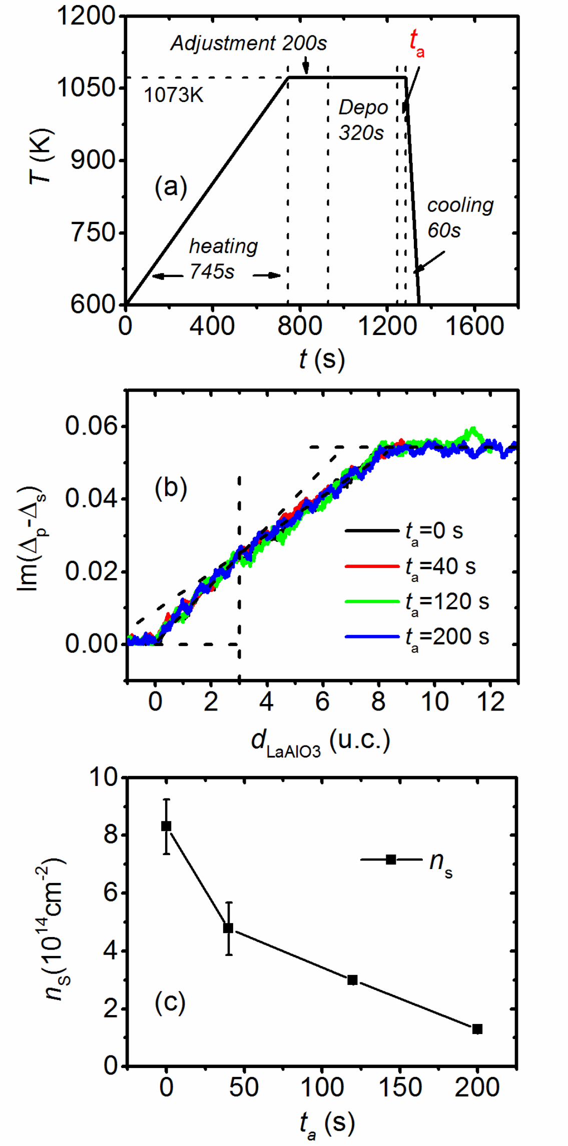

Figure 5.5 *(a) The time dependence of the STO temperature during the experiments. Only the annealing time (t_a) is variable. (b) the OIRD signals for the different annealing times. (c) the sheet carrier concentration for the samples with different annealing time.*

Although the annealing time has no impact on the OIRD signal, the sheet carrier concentration can be strongly reduced by increasing the annealing time (Figure 5.5 (c)). By increasing the annealing time from 0 s to 200 s, the sheet carrier concentration is reduced from ~ $8x10^{14}$ cm^{-2} to ~ $1x10^{14}$ cm^{-2}. This change is almost one order of magnitude.

5.3.3 Discussion

As illustrated by our previous work [199], the decrease of the sheet carrier concentration by increasing the post annealing time for LAO growth on STO originates from the reoxidation of the reduced STO substrate, whereas the interface electrons are undisturbed. The oxygen vacancies that are introduced during the growth process by the high energetic plume are then compensated by the incorporation of oxygen ions from ambient [200]. Thus the oxygen vacancy concentration in STO is changed by the post annealing process.

However, the OIRD signal for the post annealing process stays constant. Moreover, the similarly grown LAO with different annealing times show also identical OIRD signals. Thus the oxygen vacancy concentration change in STO does not have an influence on the OIRD signal ***during the post annealing process*** or ***after growth***.

As a summary for the pressure sequence and the annealing time sequence, we observe that the change of the oxygen vacancy concentration in the STO substrate neither influences the OIRD signal during growth (pressure sequence) nor influence the OIRD signal after growth (annealing time sequence).

Based on this verification, ***the OIRD slope change*** originates ***purely from the LAO thin film***. Two main changes in LAO might be responsible for the OIRD slope change: the optical permittivity change and the *c*-lattice expansion change. The optical permittivity of LAO at ~ 2 eV is different for LAO thin films on STO with thicknesses higher than 4 u.c. and lower than 3 u.c. [94]. The optical permittivity change is supposed to be influenced by the charge transfer to the interface. The averaged *c*-lattice constant is much higher than the bulk value for LAO for films with thicknesses below 4 u.c., where the electrostriction induced by the build-in field in LAO might be responsible [95]. The averaged *c*-lattice constant relaxes to the bulk value as the LAO thickness increases and the absence of the build-in field in LAO layers after 4 u.c. is assumed. The absence of build-in field after 4 u.c. might originate from the electron transfer to the interface.

5.4 LAO growth on 100 % SrO terminated STO

5.4.1 Experiments

TiO_2 terminated 5x5x0.5 mm^3 STO is used as the substrate. The sample is heated up in the PLD chamber to 800 °C under atmosphere of $2x10^{-7}$ mbar pressure with oxygen inlet. 9 pulses SrO are deposited from a SrO ceramic target with a laser fluence of 1.4 J/cm^2. The 9 pulses correspond to ~ 1 u.c. SrO according to chapter 3. Afterwards the pressure is increased to $1x10^{-3}$ mbar while the temperature of the substrate is kept at 800 °C. With rotation of the target carrousel the single crystal LAO is in use for the deposition of 8 u.c. LAO with a laser fluence of 1.4 J/cm^2. The interval between the end of SrO deposition and the begin of LAO deposition is ~ 300 s. The RHEED measurements for both SrO and LAO are carried out, while the OIRD measurement is only carried out for LAO due to the short deposition time of SrO. After the deposition of LAO the sample is quenched and characterized by *ex-situ* AFM and Hall measurements.

5.4.2 Results

The growth process is summarized in Figure 5.6 with the RHEED diffraction pattern at 800 °C substrate temperature (Figure 5.6 (a)), after deposition of SrO (Figure 5.6 (b)) and after deposition of LAO (Figure 5.6 (c)), respectively. The averaged RHEED intensity of spots (0 0), (0 1) and (0 -1) during SrO and LAO growths are shown in Figure 5.6 (d) and Figure 5.6 (e), respectively.

The substrate shows a strong contrast between (0 0) and (0 1) or (0 -1) (Figure 5.6 (a)), whereas the RHEED pattern of SrO shows a weak contrast between the (0 0) and (0 1) or (0 -1) reflections (Figure 5.6 (b)). This can also be visualized by the RHEED intensity variation in Figure 5.6 (d): the (0 0) spot experiences a strong decreased for the 9 pulses, whereas the (0 1) and (0 -1) spots firstly decreas and then increas to almost the same level of (0 0) . This contrast change of the RHEED spots is in good accordance with the literature for the growth of one monolayer of SrO with molecular beam epitaxy [42]. Since the diffraction pattern remains in Laue ring form, the growth of the SrO monolayer is 2D layer-by-layer growth.

The layer thickness of 8 u.c. is estimated through the oscillation number of the (0 0) spot in Figure 5.6 (e) represented by the black curve. Although the first two oscillations are overlapped by a strong decrease of the intensity, the deposition rate of 42 pulses can be extracted by averaging the duration of 8 oscillations, thus verifying the number of oscillations to be two during the first significant drop of intensity. The deposition is stopped at the 8th maximum of the RHEED oscillations. It has to be mentioned that at the beginning of deposition a oscillation with only half the periode is observed for the (0 1) and (0 -1) spots (red and blue curves in Figure 5.6 (e)). The origin of such half oscillations needs further investigation.

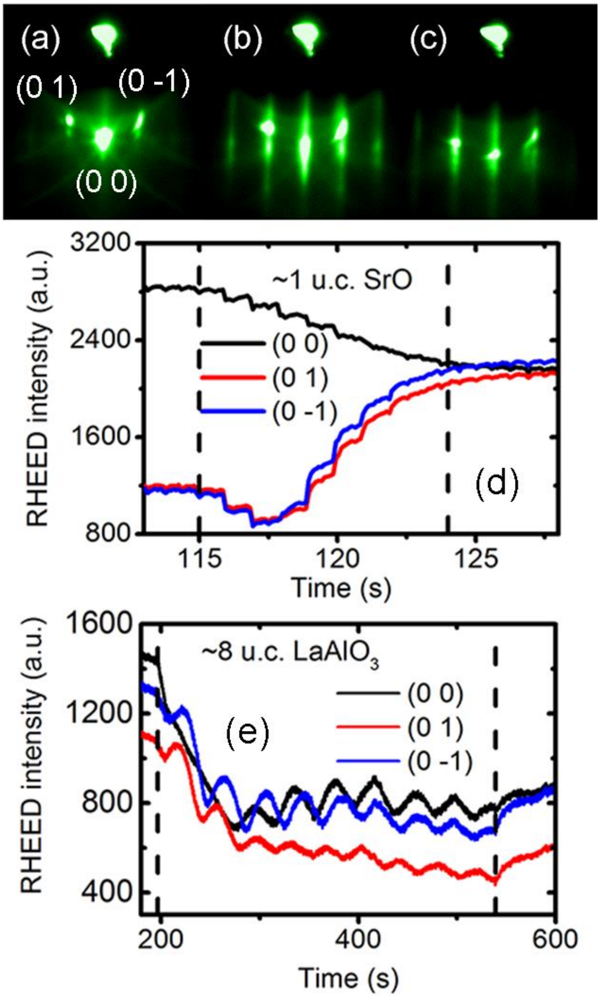

Figure 5.6 *RHEED pattern for (a) TiO$_2$ terminated STO substrate, (b) 1 u.c. SrO and (c) 8 u.c. LAO. The corresponding RHEED intensity for 1 u.c. SrO and 8 u.c. LAO are shown in (d) and (e), respectively.*

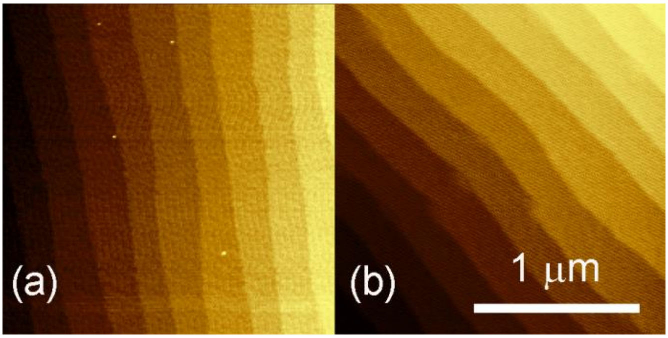

Figure 5.7 *AFM morphology for (a) the substrate and (b) the LAO on 1 u.c. SrO terminated STO. For both 0.4 nm high flat terrace structures are observable.*

However, it is certain that the small oscillation at the beginning is not related to any significant structure formation on the surface of LAO, since at the end of LAO deposition the surface is as flat as before deposition as shown in Figure 5.7 (a) and (b).

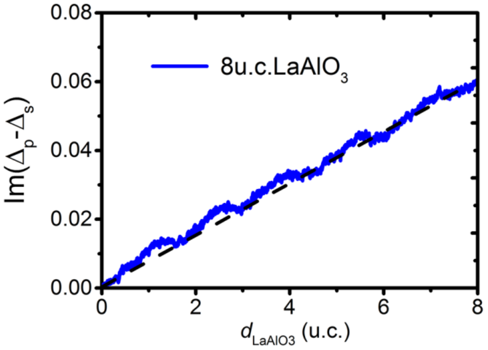

Figure 5.8 *OIRD signal for the growth of LAO on the SrO terminated STO*

Taking the deposition rate ~ 42 pulses per unit cell for LAO revealed by Figure 5.6, the OIRD signal can be plotted against the increasing LAO thickness in Figure 5.8. In contrast to Figure 5.1 (b) in chapter 5.1, we see no slope change at 3 u.c. or at any point. The signal can be interpreted as a straight line with small oscillations, which can originate from the surface roughness change during the growth. Alternatively, the OIRD signal can also be interpreted as two straight lines with a slope change at 1 u.c., which is not as obvious as the slope change in Figure 5.1.

The Hall measurement is carried out on this sample with van der Pauw configuration. The sheet electron concentration (n_S) is ~ $6x10^{11}$ cm^{-2}, whereas the sheet resistance (R_S) is ~ 350 kΩ.

5.4.3 Discussion

As a comparison of the electronic properties, we see that the n_S of LAO/(SrO)STO is over three orders of magnitude lower than the one of the LAO/(TiO_2)STO heterostructure (see Table 5.2). As discussed in chapter 2, the LAO/(SrO)STO should be insulating. The existence of the conductivity should originate in the reduction of STO that is caused by a low pressure SrO deposition. It has been shown that at low pressures, the laser plume will have a high kinetic energy and can kick out the oxygen atoms of the substrate and the growing thin film, leaving electrons and oxygen vacancies in the STO substrate [70-71, 201].

As discussed in chapter 5.2 and 5.3, the oxygen vacancies in STO do not change the OIRD signal. Only the processes in LAO are responsible for the OIRD signal change. Therefore the absence of an obvious slope change in OIRD signal for the LAO growth on (SrO)STO indicates the absence of a change in the LAO thin film properties during growth.

As an *in-situ* observation method, the OIRD signal does not investigate the mechanism behind the process, but gives information about the transient processes. Assuming the build-in field in LAO is compensated by the oxygen vacancies generated during the growth process of LAO on (SrO)STO, this compensation might be accomplished at a very early stage e.g. within 1 u.c. of LAO. Therefore an obvious slope change is absent.

As a summary for the LAO growth on (SrO)STO, two main processes may take place: one is the reoxidation of the STO substrate, which might be reduced during the SrO growth; the other one is the compensation of the build-in field in LAO, which can be finished at an early growth stage. The first process could explain the conductivity, while the second process could be responsible for the absence of an obvious slope change.

5.5 Growth of LAO on mixed terminated STO

5.5.1 Experiments

A similar procedure for the deposition of SrO and LAO as in chapter 5.4 is carried out. The only difference is that for 0.55 u.c. SrO, 5 pulses are used. 5 pulses correspond for ~ 55 % coverage by SrO. To exclude influences from the substrate and make the comparison strictly trustable, the 5x5x0.5 mm^3 substrates used in chapter 5.4 and 5.5 are selected from 4 samples diced from the same 10x10x0.5 mm^3 STO sample with identical terrace structures. RHEED and OIRD are recorded during the growth, and *ex-situ* Hall measurement is carried out for the sample.

5.5.2 Results

The RHEED diffractions and the corresponding intensity oscillations for different spots are summarized in Figure 5.9. In contrast to 1 u.c. SrO, 0.5 u.c. SrO shows higher intensities for the (0 0) spot than for the (0 1) or (0 -1) spot, as do the substrates (Figure 5.9 (a) and (b)). This can also be observed in the corresponding intensity change transiently in Figure 5.9 (d). In contrast to the growth of SrO we can observe good oscillations for LAO. Clear oscillations can be seen for the LAO growth, where the 8 u.c. RHEED oscillations are all visible (Figure 5.9 (e)), while the RHEED diffraction pattern is also still in the 2D Laue ring form and indicates a flat surface (Figure 5.9 (c)). This indicates the growth is 2D layer-by-layer growth.

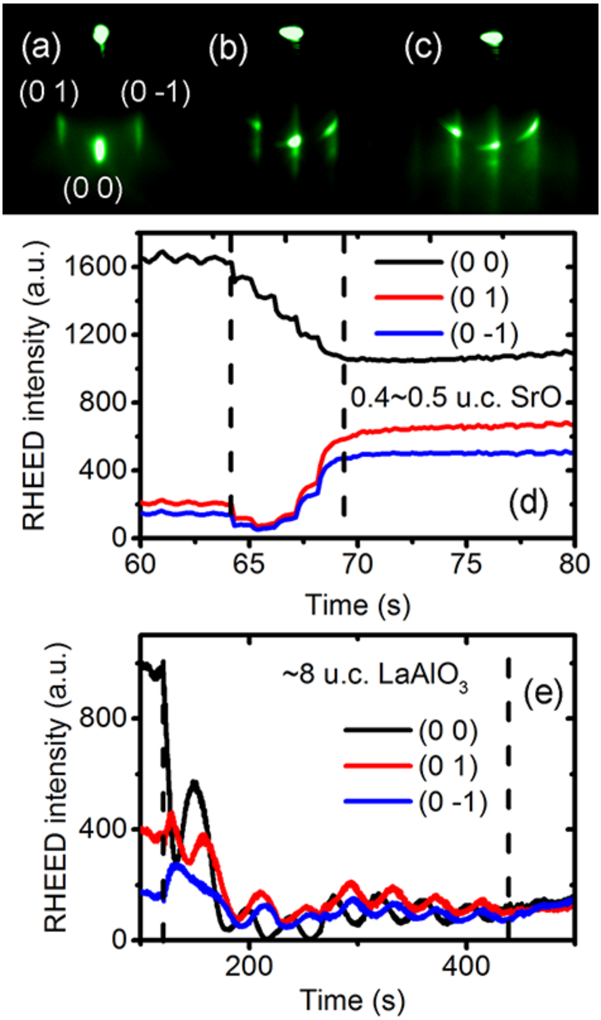

Figure 5.9 *RHEED pattern for (a) a TiO$_2$ terminated STO substrate, (b) 0.55 u.c. SrO and (c) 8 u.c. LAO. The corresponding RHEED intensity for 0.55 u.c. SrO and 8 u.c. LAO are shown in (d) and (e), respectively.*

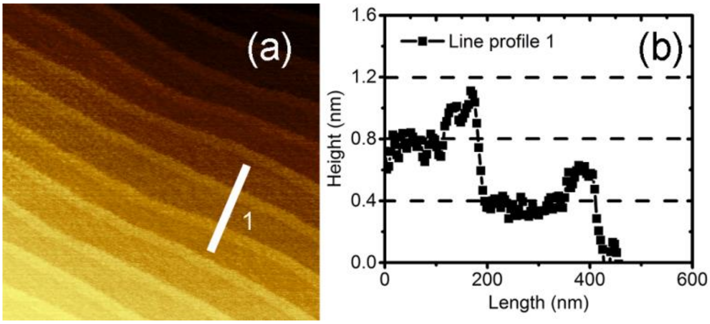

Figure 5.10 *(a) 2 μm x 2 μm AFM morphology for LAO on 0.55 u.c. SrO terminated STO. (b) is the line profile marked in (a) from left down to right up. The substrate morphology is identical to that in Figure 5.7 (a), so it is not shown here.*

However, the AFM results contradict with the growth model suggested by the RHEED oscillation. As shown in Figure 5.10 (a), the surface still shows a step-terrace structure that is similar to the substrate in Figure 5.7 (a). However, on each terrace edge, there is a stripe with universal width of around 100 nm, which is ~ 40 % of the whole terrace width of 250 nm. The stripes on the terrace edges have 200 pm height. Figure 5.10 (b) shows a line profile across one terrace edge as a representative example. (The profile is the averaged data by a width of 13 pixels with total 512 x 512 pixels for the whole image. The purpose is to reduce the influence of the noise.)

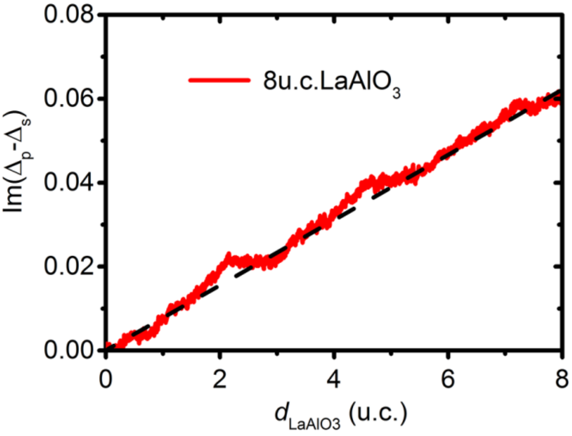

Figure 5.11 *OIRD signal for the growth of LAO on the ~ 55 % SrO terminated STO*

The OIRD signal is shown in Figure 5.11. Similar as for the 100 % SrO terminated STO, the OIRD signal for the growth of LAO on the 55 % SrO terminated surface shows no obvious slope changes. A weak slope change can be suggested at 2 u.c., which is not verifiable with respect to the noise level.

From room temperature Hall measurement directly after the growth (after 1 day), it is observed that the sheet electron concentration (n_S) is ~ $4x10^{13}$ cm^{-2}, whereas the sheet resistance (R_S) is ~ 37 kΩ.

5.5.3 Discussion

It has been observed that the growth of LAO on a mixed terminated STO substrate can generate a mixture of conductive and insulating areas [105]. However, since the SrO termination in that work has been generated using thermal handling, the SrO areas on STO are elliptical stripes. As an improvement, we have parallel ordered stripes with uniform separation on the LAO/(SrO)STO heterostructure.

It is still hard to understand the absence of an obvious slope change for the OIRD signal. A possible explanation is the phase shift introduced by the stripe structures, which reduces the strength of the reflectivity change for both *p*-and *s*-polarization that are responsible for OIRD signal. However, this is hard to verify. Further detailed studies on the growth of LAO on mixed terminated STO should be carried out.

5.6 Conclusions

As an *in-situ* method, OIRD supplies information on the transient processes happening during the LAO growth on STO.

For TiO_2 terminated STO the OIRD signal shows a slope change when 3 u.c. of LAO are deposited. This slope change is verified as not being related to the oxygen vacancy concentration change in STO via the growth pressure series and post annealing time series. Therefore the change can only originate in the grown LAO: The first 3 u.c. of LAO might keep the high *c*-lattice constant and optical permittivity throughout the growth process, while the latter LAO monolayers have bulk *c*-lattice constant and optical permittivity.

For the SrO termination, the OIRD signal shows no slope change at all for 8 u.c. of LAO growth, which indicates the absence of a build-in field or the fast finishing of the compensation of the build-in field in LAO.

Interesting stripe like structures are observed for the LAO growth on 55 % SrO terminated STO, where no obvious slope changes in the OIRD signal are observed. The mechanisms behind the stripe formation and optical signal change are not clear.

6 Oxygen incorporation during thin film growth in pulsed laser deposition

6.1 Role of residual gas species and equipment

The pressure of oxygen needed for PLD for reduction is much higher than the partial pressure of oxygen in the equilibrated reducing gas mixture. For instance, with the same oxygen pressure used in the PLD process for reduction (e.g. 10^{-5} mbar ~ 10^{-7} mbar [202]), the $SrTiO_3$ sample is never reduced in the oxygen pump system (for details refer to ref. [16, 17]). The scenario behind this phenomenon, however, has never been studied systematically. In the following the analysis for the low pressure annealing in PLD is carried out to investigate the role of residual gas species and equipment during low pressure reduction of STO in PLD chamber.

6.1.1 Experiments

Pressure sequence: 5x5 mm^2 $SrTiO_3$ samples with TiO_2 termination are mounted on the normal *Omicron* sample-holder with silver paste. All the samples are annealed at 800 °C for 513 s and 3600 s under different pressures ranging from 10^{-7} mbar to 10^{-3} mbar with the cold cathode gauge (CC) switched on. All the samples are quenched directly after the annealing. The sheet carrier concentration (n_S) is measured with *ex-situ* Hall measurements.

Mass spectrometry: One 5x5 mm^2 $SrTiO_3$ sample is annealed at $p = 10^{-6}$ mbar for 513 s while both the cold cathode gauge and mass spectrometer are switched on. During annealing mass spectrometry is carried out. The UHV base pressure is around 5×10^{-9} mbar. After a full range scan we choose the following specific mass-charge ratio to be detected by the mass spectrometer: 1 for H atoms, 2 for H_2 molecules, 16 for O atoms, 18 for H_2O molecules (where CH_4 is also possible but not as frequent as H_2O in a typical UHV chamber), 28 for N_2 or CO and 44 for CO_2. The sample is quenched directly after the annealing.

Measurement equipment sequence: Four 5x5 mm^2 $SrTiO_3$ sample**s** with TiO_2 termination are mounted on the standard omicron sample holder with silver paste. All the samples are annealed at 800 °C for 513 s at 10^{-6} mbar under four different conditions: with cold cathode gauge, with both cold cathode gauge and mass spectrometer, with mass spectrometer and without cold cathode gauge or mass spectrometer switched on. All the samples are quenched directly after the annealing. The sheet carrier concentration (n_S) is measured with *ex-situ* Hall measurements.

6.1.2 Results

Figure 6.1 (a) shows that the Ag paste mounted $SrTiO_3$ samples with both 513 s (red dots) and 3600 s (black squares) annealing time have sheet carrier concentrations (n_S) of around 10^{17} cm^{-2} at 10^{-7} mbar and 10^{-6} mbar, respectively. As the total pressure is increased to 10^{-5} mbar, the difference between the samples annealed for 513 s and 3600 s gets obvious. For the 513 s annealed sample, the n_S decreases from ~ 10^{17} cm^{-2} to under the detection limit < 10^{10} cm^{-2}. On the contrary, the n_S of the 3600 s annealed sample is reduced from ~ 10^{17} cm^{-2} to under detection limit < 10^{10} cm^{-2} at 10^{-4} mbar. For both annealing times10^{-6} mbar is the highest pressure at which the reduction of STO can be still observed. To understand the reduction process at this pressure mass spectrometry is carried out.

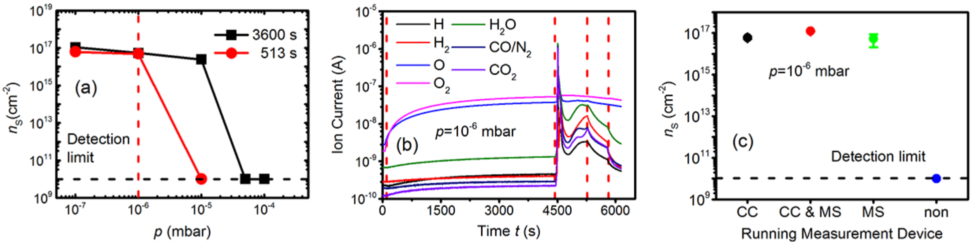

Figure 6.1 *(a) The pressure dependence of the sheet carrier concentration of STO annealed for different durations. During the annealing processes in this case only the cold cathode gauge is switched on. (b) The mass spectrometry data for the sample annealed at 10^{-6} mbar. In this case both the cold cathode gauge and mass spectrometry are running. (c)The sheet carrier concentration for different conditions: with cold cathode gauge (CC), with both cold cathode gauge and mass spectrometer (CC & MS), with mass spectrometer (MS) and without both (non). The experiment was carried out by F. Hensling.*

Figure 6.1 (b) shows the content of different gas species for a silver paste mounted STO sample. At the beginning, the UHV with p = 5x10^{-9} mbar shows a low ion current for all gas species. At this point O_2 and O are the dominant species with a two times higher ion current than H_2O, which is the dominant species of the residual gases. After gas inlet through a leak valve, the ion current measured for O_2 and O increases over 20 times, while the amount of residual gases remains almost unchanged. The total pressure is adjusted to 10^{-6} mbar at room temperature and the content of O_2 and O reaches a stable level after 1500 s. After around 1 hour, the laser heater is switched on and we observe a drastic increase of all gas species, where an overshoot of H- and C- related gas species is obvious below 300 °C. This sudden increase of the residual gas is accompanied by an increase of the total pressure to 3x10^{-6} mbar. It is reasonable since the silver paste has an organic binder that contains H and C and is easily decomposed at temperatures below 300 °C. As the temperature increases further, the emission of all the residual gas species increase. The amount of H_2O and H_2 reaches ***almost the same level*** as O_2 and O, whereas the other species strongly increase as well. However, as 800 °C is reached and the laser power stays constant, the emission of residual gas species decreases to a level two or three times smaller than the one of O_2 and O. When switching off the laser heater, the emission of the residual gases decreases further. However, since for this sample both, the cold cathode gauge and the mass spectrometer, are switched on, the pure influence of the residual gases is not clear.

Therefore, an equipment sequence is carried out. The data is summarized in Figure 6.1 (c). With cold cathode gauge (CC), with mass spectrometer (MS) and with both cold cathode gauge and mass spectrometer (CC & MS) the n_S remains over 10^{17} cm^{-2}, which hints to a heavily reduced STO single crystal. For the sample annealed without cold cathode gauge or mass spectrometer (non), however, the sheet carrier concentration is under the detection limit, which indicates that STO is not reduced in this case. As a conclusion, ***the sole residual gas*** observed in Figure 6.1 (b) is ***not sufficient for the reduction*** observed in Figure 6.1 (a).

6.1.3 Discussion

We showed with Figure 6.1 (a) to (c) that the residual gas species in the PLD chamber, which might derive from the silver paste or other sources, will not reduce the STO single crystal without a running cold cathode gauge or mass spectrometer. The reduction is possible if at least one of the two measurement devices is switched on. This indicates that the ***residual gas molecules*** are ***not able to reduce STO in the thermodynamic equilibrium***.

Interestingly, both mass spectrometer and cold cathode gauge utilize ionization processes (see chapter 3). The ionization process has two effects: Firstly the generation of ionized reducing species e.g. H_2 to H^+ [203], which increases the activity of the reducing species like H_2; secondly the cracking of non- reducing species into reducing species, like cracking of H_2O into $H^{0,+1}$ and $(OH)^{0,+1}$ [204] or CO_2 into $CO^{0,+1}$ and $O^{0,+1}$ [205]. It has to be mentioned that the collision between electrons and neutral molecules mostly produces neutral and positively charged ions, since the negative ions need attachment of electrons that is unlikely to happen [204, 205]. As a consequence of the ionization and cracking process, the molecular gas species e.g. H_2 is decomposed into a mixture of H^0 and H^+.

It has been observed that with running cold cathode gauge during the inlet of H_2 or H_2O with relative high pressure of 10^{-3} mbar at room temperature [87], the LAO/STO interface resistance is continuously reduced, whereas switch off the cold cathode gauge ceases the reduction. It is suggested in [87] that through the absorption on the LAO surface H^0 can donate electrons to the LAO/STO interface:

$$H^0 + O^{2-} \rightarrow e^- + (O-H)^- .$$

Similarly, the reduction process in STO can also be related to H^0. However, since the process of the adsorption of H^0 takes place at elevated temperature during our annealing process at 800 °C, the defect reaction at the oxygen site can be active (see chapter 2) and the generation of oxygen vacancies has to be taken into consideration. One possible scenario is:

$$2H^0 + O_O^x \rightarrow V_O^{\bullet\bullet} + H_2O(g)\uparrow + 2e^- .$$

These oxygen vacancies are preserved after the quenching process and are hardly influenced by the ambient adsorbates. Other microscopic processes may also play a role, but for simplicity we only discuss the oxygen vacancies as being responsible for the majority of the delocalized electrons in STO.

The distribution of oxygen vacancies in STO is dependent on the diffusion and surface reaction. Taking the high diffusion coefficient of oxygen vacancies in STO at 800 °C into consideration [206], the diffusion length exceeds the sample thickness (0.5 mm) for 513 s already [106]. Therefore, the surface reaction process mentioned above is the rate determining process. The incorporation of oxygen vacancies or the removal of oxygen atoms from the STO surface generates electrons in STO and is strongly dependent on the amount of the H^0 delivered to the surface, which determines the final reduction state of the STO.

Two factors might be responsible for the pressure dependence of n_S in Figure 6.1 (a). The first factor is the competition of the ***relative amount*** between reducing H^0 and oxidizing O_2. As the total pressure increases by the increased amount of oxygen, the oxidation should be stronger than the reduction. Therefore the sheet carrier concentration is reduced by the increased pressure.

The second one is the ***absolute amount*** of H^0, which is strongly dependent on the scattering of H^0 on the way to the STO surface. The absolute amount of H^0 generated by the cold cathode gauge or mass spectrometer should be constant if O_2 is the inlet gas. Considering the high mean free path of gas molecules at 10^{-6} mbar, around 10 m according to the ideal gas law, which is much higher than the PLD chamber dimension (~ 1 m), the scattering of H^0 within the PLD chamber is low. As the pressure increases to 10^{-5} mbar, the mean free path is decreased to 1 m, which means the H^0 could be scattered within the PLD chamber by other gas molecules like O_2. At this pressure regime, the delivering of H^0 takes more time and thus the reduction of STO by 513 s is much less pronounced than after 3600 s. By further increase of total pressure to 10^{-4} mbar with increased O_2 inlet, the mean free path falls to only 0.1 m, which means the H^0 scattering is much stronger than at low pressures, which is the reason for the absence of conductivity at 10^{-4} mbar (Figure 6.1 (a)). The scattering strength with different mean free path can explain the abrupt change of the reduction in STO and difference between the 533 s annealed and 3600 s annealed STO at the same pressure like 10^{-4} mbar. The discussion of the time dependent reduction or oxidation will be carried out in the next section

As a summary, we are able to show that at low pressures in the PLD (10^{-7} mbar and 10^{-6} mbar) the reduction in STO during ***annealing processes*** originates from the ionization and cracking process by the cold cathode gauge or mass spectrometer. The increase of the pressure in the PLD chamber with increased inlet of oxygen molecules helps both the reoxidation of the STO and scattering of H^0 or other reducing species, whereas the scattering of H^0 is the rate limiting step.

6.2 The role of UV-radiation from plume

It has been shown in chapter 2 that the high energy photons with wavelength in the UV region can be generated during PLD processes. The role of UV-radiation from the plume can be studied with a sapphire window in front of the STO sample during PLD growth. The principle for such experiments has been illustrated in chapter 3.

6.2.1 Experiments

The impact of UV-radiation on the morphology: The annealing experiments for two STO samples with and without laser plume UV-radiation are carried out. The laser fluence is 1.5 J/cm^2 on single crystal STO target with target-to-substrate distance about 44 mm. The annealing temperature is 800 °C and the pressure is 10^{-4} mbar. Both samples are quenched after the given annealing time of 513 s.

The impact of UV-radiation on the conductivity: The pressure dependent annealing time series of STO samples is carried out with two different experiments: one has a sapphire window in front of the holder and UV-radiation from ignited plume (UV), while the other has also a sapphire window but no ignition of laser plume (w/o UV). For both experiments the holder without silver paste is used to avoid high emission of residual gas species. For a detailed description of the holders please refer to chapter 3. All the samples are annealed at 800 °C with pressures of 10^{-4} mbar and 10^{-5} mbar for different annealing times. For the holder that permits UV-radiation, a plume is generated with 1.5 J/cm^2 laser fluence on a $SrTiO_3$ single crystal target. The target-substrate distance is 44 mm. The samples are characterized with *ex-situ* Hall measurements.

6.2.2 Results

Figure 6.2 shows that the surface structure of the UV annealed sample (Figure 6.2 (d)) is distinguishably different from the annealed sample without UV-radiation (Figure 6.2 (b)). While the sample only annealed without UV-radiation shows almost identical morphology before and after annealing, the sample with UV-radiation shows many holes with diameter around 20-50 nm after the annealing. The averaged depth of these holes is around 1 u.c. of STO around 0.4 nm.

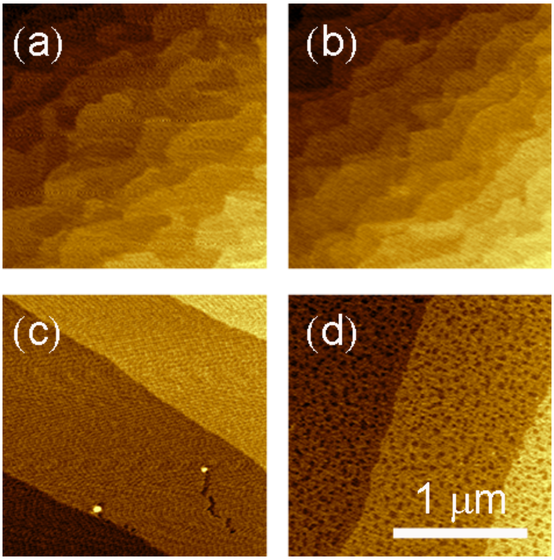

Figure 6.2 *The AFM morphologies of the annealed sample at 10^{-4} mbar without UV-radiation before (a) and after annealing (b); annealed sample with UV-radiation before (c) and after (d) annealing. Both samples are annealed at 800 °C for 513 s. The bright spots in (c) may come from dirt that has not been removed completely.*

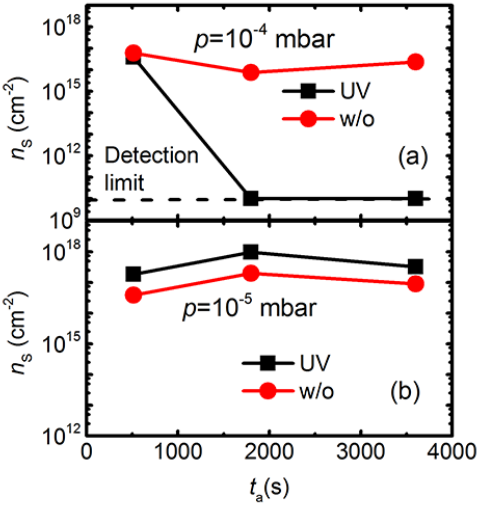

Figure 6.3 *Annealing time series with (a) $p = 10^{-4}$ mbar and (b) $p = 10^{-5}$ mbar. The black squares are with UV-radiation during the annealing and the red dots are without UV-radiation during the annealing. The experiment was carried out by F. Hensling in ref. [106].*

Figure 6.3 shows that at $p = 10^{-4}$ mbar the sample in the holder without UV-radiation has a stable $n_S \sim 10^{17}$ cm^{-2} from 513 s to 3600 s, whereas the sample with UV has at first a similar sheet carrier concentration $n_S \sim 10^{17}$ cm^{-2}, which declines below the detection limit ~ 10^{10} cm^{-2} after annealing. The samples annealed with $p = 10^{-5}$ mbar show a different trend. The samples without UV show a similar initial value around 10^{17} cm^{-2} but with a slight increase from 513 s to 1800 s and then slightly reduced for 3600 s. The UV radiated samples show even higher $n_S \sim 10^{18}$ cm^{-2} with a similar trend as the samples annealed without UV.

6.2.3 Discussion

It is shown that at the same annealing condition, the STO surface without UV-radiation shows no voids (Figure 6.2 (b)) and the surface with UV-radiation shows a high density of voids with 0.4 nm depth (Figure 6.2 (d)). A possible mechanism related to the ***defect coalescence on the surface*** can be suggested. Schottky defect pairs like Sr vacancy and oxygen vacancy ($V_{Sr}''+V_O^{\bullet\bullet}$) pairs or Ti vacancy and oxygen vacancy ($V_{Ti}''''+2V_O^{\bullet\bullet}$) pairs can be observed in the vicinity of the surface of reduced STO [172, 207]. These Schottky defect pairs are normally not mobile at annealing temperatures ~ 800 °C [26] and under detection limit of AFM, therefore no visible changes are observed for the solely annealed STO surface (Figure 6.2 (b)). However, the UV-radiation can generate electrons and holes, which could compensate the charges of oxygen vacancies and cation vacancies, respectively. The Schottky pair can be thus dissociated into two neutral vacancies, whose mobility should be higher than the defect pairs. Therefore the coalescence of the vacancies can be enhanced and large voids within AFM resolution could be formed. The quantitative description and explanation for the surface morphology change of STO under UV-radiation, however, needs further investigation. Another possible scenario is the ***nanoscale ablation process***. Similar to the ablation process on the target, the UV photons from plume can be absorbed by the electrons in STO. Given sufficient energy, these electrons can leave the surface and generate a local field to drag ions out from surface. However, as the ablation process is a strongly non-linear process that needs high intensity of photons with high coherence, the UV-radiation from plume may not be strong enough to trigger such kind of ablation process. Therefore the most probable scenario is the ***defect coalescence on the surface***.

The physical scenario behind the reduction of STO under UV-radiation is the UV mediated desorption of the oxygen atoms on-site, which has been discussed by T. Hara et. al in ref. [208]. Such desorption process of oxygen atoms can generate charge carriers and thus influence the carrier density in the STO bulk, which will be discussed in the following.

The influence of UV-radiation on STO during annealing experiments is bidirectional. For oxidizing conditions, the oxidation is accelerated as shown in Figure 6.3 (a). On the contrary, for reducing condition the reduction is further increased.

Via UV-radiation with a photon energy higher than the direct optical bandgap of STO (~ 3.2 eV [181]), electron-hole pairs are generated. At oxidizing conditions, the oxidation of reduced STO samples takes place in the thermodynamic equilibrium as follows:

$$V_O^{\bullet\bullet} + 2e^- + O_2 \rightarrow 2O_O^x \ .$$

This process can be divided into many partial processes and the ionization process of the oxygen molecule on the surface is often the rate limiting step [209, 210]. The already existing electrons will help the ionization of oxygen molecules and thus accelerate the reoxidation speed.

On the contrary, at reducing conditions, the oxygen atoms on-site can be removed as discussed in chapter 6.1:

$$2H^0 + O_O^x \rightarrow V_O^{\bullet\bullet} + H_2O(g)\uparrow + 2e^- \ .$$

In this process the presence of holes will consume the electrons generated by this reaction and may accelerate the reaction. However, as discussed before, the rate limiting step is not the reaction on the surface, but the delivering of H^0 onto the surface with scattering by other molecules. Therefore, the UV-radiation influence during the reduction process is rather weak as shown in Figure 6.3 (b).

6.3 Disentanglement of impinging particles and UV-radiation in the plume

Impinging particles with high kinetic energy and the UV-radiation present in the plume are the main aspects that can influence the surface oxygen exchange process in STO during the growth process of PLD. In the following the influence of UV-radiation and impinging particles with high kinetic energy on the STO substrate will be disentangled at room temperature and at high temperature.

6.3.1 Experiments

Room temperature experiment: Around 21 u.c. LAO thin film is deposited on 5x10 mm^2 STO substrates at room temperature (300 K) with a target-to-substrate distance of 44mm and a laser fluence of 2 J/cm^2 at p = 2x10^{-7} mbar and 10^{-4} mbar. Since no RHEED oscillations can be acquired for such growth conditions, the deposition time is estimated according to other depositions with the same laser fluence at a higher temperature. The sample is partially covered by a sapphire window, ensuring two regions: one with only ultra-violet (UV) radiation and one with both UV-radiation and impinging particles with high kinetic energy. These two regions are separated by cutting the sample into two pieces. A detailed description and the construction ideas are illustrated in chapter 3. The Hall measurements are carried out for the two pieces.
Around 8 u.c. LAO thin film is deposited on 5x5 mm^2 STO substrates at room temperature (300 K) with a target-to-substrate distance of 44 mm and a laser fluence of 2 J/cm^2 at p = 10^{-4} mbar.

High temperature experiment: The 20 u.c. LAO is deposited on TiO_2 terminated STO at 800 °C with a laser fluence of 2 J/cm^2 and pO_2 = 1x10^{-4} mbar. The sample is partially covered by a sapphire window, ensuring two regions: one with only UV-radiation and one with both UV-radiation and particles. These two regions are separated by cutting the sample into two pieces. The Hall measurements are carried out for the two pieces.

6.3.2 Results

Table 6.1 shows the sheet carrier concentration (n_S) of the LAO/STO heterostructure with LAO deposited at 800 °C of ~ 2x10^{15} cm^{-2}, which is over one order of magnitude higher than that at room temperature of ~ 1.4x10^{14} cm^{-2}. For both room temperature (25 °C) and high temperature (800 °C), the UV-radiation from the plume is not able to reduce the sample, where the conductivities for both are under the detection limit. As a straightforward conclusion, the influence of the UV-radiation at the given growth conditions is too weak to reduce the STO at all.

Table 6.1 *The sheet carrier concentration (n_S) of different regions on a STO sample after growth of LAO at different conditions*

n_S (cm^{-2})	**25 °C @ 10^{-7} mbar**	**25 °C @ 10^{-4} mbar**	**800 °C @ 10^{-4} mbar**
particles + UV	1.35x10^{14}	Under detection limit, <10^{10}	2.04x10^{15}
UV	Under detection limit, <10^{10}	-	Under detection limit, <10^{10}

6.3.3 Discussion

Firstly we consider the influence of impinging particles with high kinetic energy and UV-radiation at room temperature. It has been reported that at room temperature, the UV-radiation can introduce oxygen vacancies or oxygen vacancies related defects in $SrTiO_3$, which makes the $SrTiO_3$ conductive. One example is the generation of Ti-O vacancy clusters during the irradiation with a 325 nm Cd laser [73]. However, the UV-radiation in such experiments was continuous radiation with relatively high intensity. In the PLD process, the UV-radiation from the plume exists as long as the laser plume exist, whose lifetime is only in the μs regime [5-6, 10, 57, 60]. The short duration of the UV-radiation from the plume is therefore assumed to have only a very weak influence because the radiation dose is rather small.

On the contrary, the kinetic energy of particles in the LAO plume can exceed 10 eV with $p < 10^{-5}$ mbar [71], which can kick out the oxygen atoms to generate the oxygen vacancies and electrons as compensating defects. Although the impact from impinging particles with high kinetic energy is discussed by Sambri et. al with variation of PLD ambient pressure, the UV-radiation influence has not been really excluded in that experiment. The disentanglement between the UV-radiation and the kinetic energy of particles at room temperature is experimentally achieved by our experiments: the main influence from the plume derives from the kinetic energy of the particles in the plume.

Secondly we discuss the influence of the UV-radiation at high temperature for the PLD growth process. The n_S for this quenched sample fabricated with standard deposition parameters is one order of magnitude higher than the value for a typical LAO/STO at the thermodynamic equilibrium ~1×10^{14} cm^{-2} [16, 31, 199]. The excess charge carriers may derive from non-equilibrium processes, which are mainly induced by the high kinetic energy of the particles in the plume. As for a similar system with 2 J/cm^2 laser fluence, target-substrate-distance of 45 mm and $p = 10^{-4}$ mbar, the kinetic energy of the plume front is around 10 eV [71]. This energy is enough to trigger the removal of oxygen atoms from STO. However, the same kinetic energy is not able to reduce the STO sample at room temperature. This indicates the diffusion of oxygen vacancies is crucial for the reduction of STO, which is only strong enough at 800 °C [106].

As a summary, we experimentally confirmed the dominant role of the kinetical energy of the particles from the plume for the reduction process during thin film growth process e.g. LAO on STO. This influence is mainly assigned to the formation and diffusion of oxygen vacancies in the STO substrate and therefore strongly temperature dependent.

6.4 The disentanglement between growth dynamics and thermodynamics

6.4.1 Influence of thermodynamics

6.4.1.1 Experiments

Four 25 u.c. $LaAlO_3$ on TiO_2 terminated $SrTiO_3$ are grown at 700 °C with a laser fluence of 1.89 J/cm^2 and $pO_2 = 1x10^{-4}$ mbar. The samples are post annealed with different oxygen partial pressures for identical time length of around 1 hour. The pressures are 10^{-2} mbar, 10^{-3} mbar and 10^{-4} mbar. The temperature dependent sheet resistance has been measured by Physical Properties Measurement System (PPMS®, *Quantum Design* Inc.).

6.4.1.2 Results

From Figure 6.4 we see that while the sample annealed at 10^{-4} mbar is similar to the as grown sample with metal-like temperature dependence of sheet resistance, the samples annealed at 10^{-2} mbar and 10^{-3} mbar exhibit a distinct Kondo-like minimum that indicates scattering centers on the interface. This is similar to the results on samples deposited at these pressures in the literature [96]. Another phenomenon indicating the increased scattering on the interface is the strongly increased low temperature resistance (e.g. at 2 K) of the samples annealed at 10^{-2} and 10^{-3} mbar in comparison to the as grown sample and the sample annealed at 10^{-4} mbar.

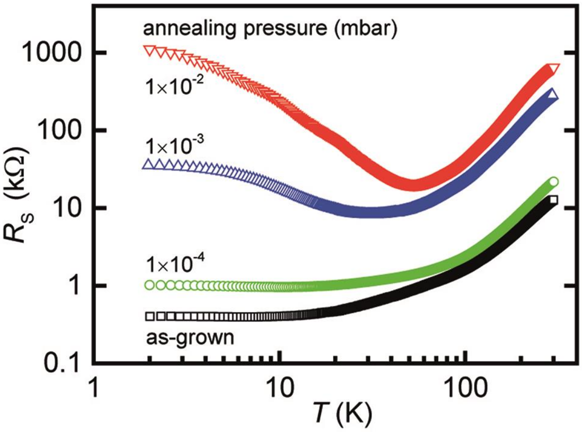

Figure 6.4 *Sheet resistances of LAO/STO heterostructures deposited with T = 700 °C and* $pO_2 = 1x10^{-4}$ *mbar. The samples were post-annealed at 700 °C in varying* pO_2 *for one hour. The fabrication and the low temperature characterization were carried out by R. Heinen. The results were published in ref. [199].*

6.4.1.3 Discussion

As shown in the literature [96], the increase in sheet resistance with increasing oxygen partial pressure is mainly caused by a decrease in electron mobility, indicating that *additional* defects are induced at the interface during annealing and equilibration at an increased pO_2.

Since the defects appear at increased oxygen pressures, oxygen vacancies are unlikely to be the relevant defect species here, as their concentration should be reduced at an increased pO_2. The main thermodynamic process on the interface of the heterostructure of $LaAlO_3/SrTiO_3$ is the Schottky-equilibrium (for details see chapter 2) on the $SrTiO_3$ side that shifts towards ionic charge compensation at an increased oxygen pressure, where cation vacancies are generated in the vicinity of the interface. In particular these cation vacancies at the interface should be Sr vacancies, since the formation energy of the Ti vacancies is too high [26].

Thus one can conclude that the thermodynamic properties influence the interface conductivity through the mobility change due to Schottky-equilibrium generated cation vacancies at the interface.

6.4.2 Influence of growth dynamics

6.4.2.1 Experiments

The deposition of LAO on 5x5x0.5 mm^3 STO samples is carried out with a laser fluence of 1.4 J/cm^2 at 800 °C. The deposition pressure is set to $1x10^{-3}$ mbar (growth rate 42±2 pulses/u.c.) and $1x10^{-4}$ mbar (growth rate 45±2 pulses/u.c.), respectively, by oxygen inlet with an UHV background pressure of 10^{-8} mbar. Note that the different laser fluence results from independent parameter optimization for each individual PLD setup in use. For $1x10^{-3}$ mbar, the thickness of the LAO films is 8 u.c., while for $1x10^{-4}$ mbar, the thickness is 5 u.c. (in order to enable XPS characterization). After switching off the ablation laser, the sample is kept at the deposition temperature for different durations t_a, ranging from 0 s up to 3600 s. Subsequently, the samples are quenched by switching off the heating laser. Both sequences of LAO/STO films are characterized with room temperature Hall measurements in an 8404 HMS© (*Lakeshore* Inc.). The post-annealed samples grown at $1x10^{-4}$ mbar are also characterized by *in-situ* X-ray Photoelectron Spectroscopy (XPS) before being removed from UHV conditions. The XPS measurements are performed with a PHI 5000 Versa Probe© (*Physical Electronics* Inc., USA) with Al Kα X-ray illumination, a pass energy of 29.35 eV and at a photoemission angle of 45° using electron neutralization.

6.4.2.2 Results

Figure 6.5 (a) shows the room temperature sheet conductance, G_S, of LAO/STO heterostructures measured *ex-situ* after annealing for various t_a. The corresponding sheet carrier concentrations, n_S, are presented in Figure 6.5 (b). The Ti^{3+} content determined by XPS for corresponding t_a with normal incidence is shown in Figure 6.5 (c), which is fitted from the XPS spectrum with the help of the ratio between Ti^{3+} and Ti^{4+} peak maximum in Figure 6.5 (d). For XPS analysis, we use the sample sequence obtained at $1x10^{-4}$ mbar. The LAO layer thickness is 5 unit cells to minimize signal attenuation introduced by LAO layer.

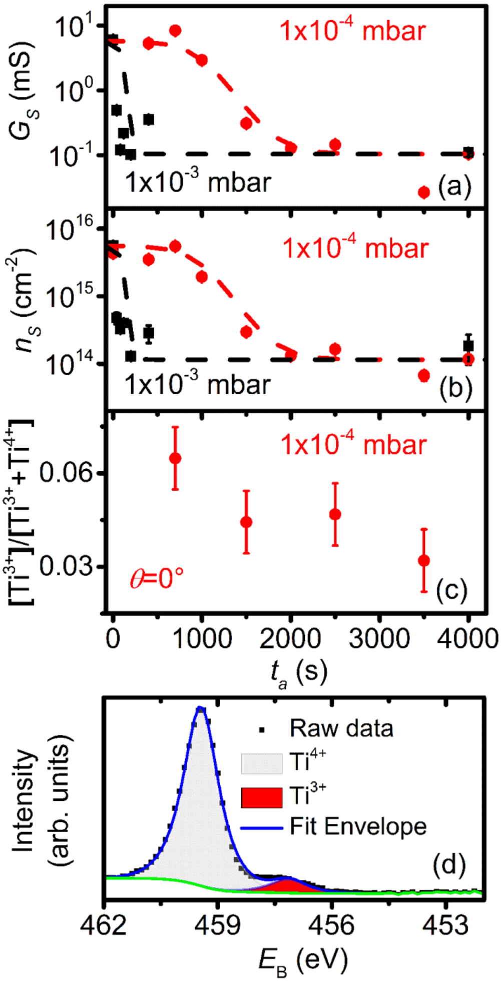

Figure 6.5 *Transient properties of LAO/STO heterostructures after PLD growth. (a) Room temperature sheet conductance, G_S, of LAO/STO samples quenched at a defined time after growth. (b) Corresponding sheet carrier concentration, n_S. (c) Ti^{3+} fraction obtained from XPS spectra (principle depicted in (d)) recorded on samples quenched after various periods of time. The solid lines are a guide to the eyes. The results were published in ref. [199].*

For both growth pressures, the conductance measured for samples quenched immediately after growth ($t_a \approx 0$ s) is almost two orders of magnitude larger than the conductance measured for samples quenched after annealing for one hour ($t_a \approx 3600$ s). The initial values are also much larger than the room temperature conductance of the samples cooled down slowly as shown in Figure 6.4. For intermediate t_a, the conductance relaxes from its high value obtained directly after growth towards its lower (equilibrium) value, which is obtained after one hour and remains unchanged upon further annealing. We thus monitor how the as-grown LAO/STO heterostructures relax from a non-equilibrium state (varying in time) to their equilibrium state (stable over time) inside the PLD chamber. The relaxation rate strongly depends on the actual pO_2. In particular, equilibrium is reached after ~100 s at $1x10^{-3}$ mbar (black symbols) and after ~1800 s at $1x10^{-4}$ mbar (red symbols), respectively.

As shown in Figure 6.5 (b), the sheet carrier concentration shows a similar trend as observed for the conductance. While n_S is of about $5x10^{15}$ cm^{-2} for t_a = 0 s, it relaxes to an equilibrium value of about $1x10^{14}$ cm^{-2} at t_a = 3600 s. This equilibrium value is the typical carrier density reported for the interfacial 2DEG. [88, 169, 197] The non-equilibrium value, however, is too large to be accommodated at the confined interface only (it would correspond e.g. to a volume concentration of $1x10^{22}$ $cm^{-3} \approx 60$ at% considering a 2DEG thickness of about 5 nm). Therefore, the high concentration of electrons observed immediately after the growth has to be attributed to the formation of charge carriers inside the STO substrate. In other words, during the growth process the STO substrate is strongly reduced, resulting in the formation of oxygen vacancies inducing conduction in the bulk of STO. The bulk conduction in STO originating from oxygen vacancies has been discussed in chapter 2 for the point defect part. As a consequence, the relaxation process observed for various t_a (Figure 6.5 (a), (b)) has to be attributed to the reoxidation of the bulk of the STO substrate inside the PLD chamber. Thus, this reoxidation process is an additional relaxation process occurring after PLD growth of LAO/STO heterostructures, superimposed by the establishing of the Schottky-equilibrium in the near-interface region (Figure 6.4).

This reoxidation process can also be visualized and the contributions of interface and bulk conduction can be separated by monitoring the Ti^{3+} content determined by XPS (Figure 6.5 (c)). A drop in the $[Ti^{3+}]/[Ti^{3+}+Ti^{4+}]$ ratio can be observed from about 6 at% for t_a = 0 s to about 3 at% at t_a = 3600 s. Based on a model comprising both interface and bulk contributions (see supplementary material of ref. [199]), we can attribute this drop by 3 at% to a vanishing bulk contribution, while the interface contribution is constant over time accommodating the entire Ti^{3+} content of about 3 at% found for t_a = 3600 s. This percentage of Ti^{3+} is in good accordance with the sheet carrier concentration at t_a = 3600s of ~$1.2x10^{14}$ cm^{-2} (Figure 6.5 (a)). The constant interface contribution forms immediately at t_a = 0 s. The vanishing bulk contribution is associated with the oxidation process of the sample during relaxation from non-equilibrium after the growth to equilibrium, as discussed above.

6.4.2.3 Discussion

Our findings are in good accordance with the phenomena observed by Basletic et. al [97] with conductive AFM for the bulk and interface properties in LAO/STO system, where the interface of LAO/STO remains almost unchanged after the post annealing process and the charge carrier concentration in the STO bulk decreases by over 2 orders of magnitude because of the reoxidation processes during post annealing. Our results do not only verify the existence of this oxidation process, but also allow us to study the pressure-dependent kinetics of this process to disentangle the growth dynamics and thermodynamics on the interface of LAO/STO.

As a matter of fact, the observation of a reoxidation effect in the bulk of STO indicates that the equilibrium state of STO for the whole range of investigated deposition pressure in the absence of a plume for LAO/STO is a well-oxidized one. The observation of bulk conduction in LAO/STO is hence related to the non-equilibrium into which the growing sample has been pushed during growth. The non-equilibrium in the PLD process has been discussed in chapter 2 as a basic aspect of PLD processes.

Interestingly, for both growth pressures the non-equilibrium states obtained directly after growth are almost identical with $G_S \approx 60$ mS ($n_S \approx 5x10^{15}$ cm^{-2}). However, the equilibration process differs depending on the ambient pressure and exhibits distinct features. At 1x10^{-3} mbar, the reduction of conductance starts immediately as the post-annealing begins. Equilibrium is reached already after a few hundreds of seconds. At 1x10^{-4} mbar, annealed samples firstly remain almost unchanged for about 1000 s before the sheet carrier concentration starts to drop. Moreover, the time needed for the (inhibited) conductance equilibration is larger at 1x10^{-4} mbar than at 1x10^{-3} mbar (slope of dashed lines in Figure 6.5 (a) and (b), which are guides to the eye). The almost identical initial non-equilibrium states at 1x10^{-3} mbar and 1x10^{-4} mbar indicate that the reduction of the STO substrate is induced predominantly by the plasma plume dynamics, while the actual partial pressure seems less important. The plasma dynamics are essentially unchanged in the considered pressure range [71], which leads to the fact that the oxidation states of the incoming plasma species are rather similar in this pressure range [71]. Thus, oxygen gettering [211, 212] by the growing layer should be similar, too.

In contrast to this, the pO_2 is much more important for reoxidation inside the PLD chamber. The reoxidation happens through two main steps: surface incorporation and bulk diffusion. For a specific condition either of the two is slower than the other and acts as the rate limiting step. At growth temperature, oxygen vacancy or oxygen ion diffusion is rather fast in the bulk of STO ($D_{\text{Vö}} \approx 3x10^{-6}$ cm^2/s at 800 °C [213]). In contrast to that, the surface incorporation rate of oxygen into perovskite is low ($k_S \approx 10^{-9}$cm/s [214]). Hence, the rate limiting step for the reoxidation process should be surface incorporation. Therefore, the difference in the transient behavior observed for different growth and annealing pressures indicates that the incorporation of oxygen ions into the STO bulk is hindered at a physical pressure of 1x10^{-4} mbar, while it is considerably faster at 1x10^{-3} mbar. One possible scenario could be a varied surface exchange coefficient, k_S, of the LAO thin film due to the different growth conditions. We explicitly tested this scenario by comparing samples grown even below 1x10^{-4} mbar and annealing them in 1x10^{-3} mbar, which resulted in a similar equilibration time as observed for the samples grown at 1x10^{-3} mbar. Therefore, we can exclude a modification of k_S at lower *growth* pressure and assign the increased equilibration time to the *annealing* pressure. The observed relaxation behavior is thus consistent with the reduced attempt frequency of oxygen attaching to the sample at 1x10^{-4} mbar, or in other words, the delivering rate of oxygen to the oxide surface at vacuum conditions.

As a summary, the growth dynamics do have an influence on the bulk properties of STO through the introducing of oxygen vacancies, which can be compensated by the oxygen delivered back to the system heading towards the thermodynamic equilibrium. The equilibration process differs due to the different amount of oxygen delivered to the oxide system.

6.4.3 The interaction between thermodynamics and growth dynamics

In order to illustrate how far away the initial non-equilibrium state introduced by the growth kinetics is from thermodynamic equilibrium, we compare the results of the quenching experiments with the high temperature equilibrium conductance (HTEC) data obtained experimentally for single crystal $SrTiO_3$ and $LaAlO_3/SrTiO_3$ heterostructures in previous work in our group [15, 17]. A detailed discussion of the oxygen pressure dependence of the conductance can be found in the corresponding publication [15].

From the data, it is directly displayed how the equilibration process observed for LAO/STO heterostructures inside the PLD chamber compares with the equilibrium states probed in *ex-situ* HTEC experiments. For this, we rescale the Hall data from room temperature (Figure 6.5 (b)) to high temperature (800 °C) applying the temperature dependence of the electron mobility reported in the literature [30]. For temperatures between 873 K and 1573 K the electron mobility (μ) can be estimated as $\mu = 3.95\text{x}10^4\ (T/K)^{-1.62}\ \text{cm}^2/(\text{V}\cdot\text{s})$ [24]. By replacing the room temperature mobility by this estimated mobility at high temperature of 800 °C, the conductance data of the anneal time sequence (Figure 6.5 (b)) can be rescaled and compared to the conductance from HTEC.

Figure 6.6 shows typical HTEC data as a function of ambient pO_2 obtained at a temperature of 800 °C for a $SrTiO_3$ single crystal (open symbols) and a $LaAlO_3/SrTiO_3$ heterostructure (closed symbols), exhibiting an additional thermally stable conductance contribution observable at intermediate pO_2 values (deviation between open and closed symbols). In addition, we plot the scaled conductance values obtained in this study after quenching directly after growth ($t_a = 0$ s) and after 1 hour of equilibration ($t_a = 3600$ s).

The initial non-equilibrium states for both pressures correspond to the equilibrated state obtained for LAO/STO at an ambient pO_2 of about $1\text{x}10^{-16}$ mbar (dashed lines), which is 12-13 (!) orders of magnitude lower than the nominal growth pressure. Hence, the sample is pushed far away from equilibrium during growth. In this reduced state, the HTEC of $LaAlO_3/SrTiO_3$ heterostructure and $SrTiO_3$ single crystal overlap, indicating that the non-equilibrium state from PLD is mainly originating from the reduced STO bulk. A similarly strong reduction of $SrTiO_3$ caused by PLD plasma is also observed by Scullin et. al [215].

During equilibration (Figure 6.5), the conductance of the $LaAlO_3/SrTiO_3$ heterostructures virtually follows the isobaric lines at $1\text{x}10^{-3}$ and $1\text{x}10^{-4}$ mbar, respectively (black arrow, Figure 6.6) drifting towards equilibrium. After $t_a = 3600$ s, the equilibrated states of $LaAlO_3/SrTiO_3$ in the PLD chamber are in good accordance with the HTEC data of the $LaAlO_3/SrTiO_3$ 2DEG at $1\text{x}10^{-4}$ mbar and $1\text{x}10^{-3}$ mbar. At these pressures, the bulk $SrTiO_3$ yields only a minor contribution to the total HTEC of the $LaAlO_3/SrTiO_3$ heterostructure, confirming that the equilibrated samples exhibit merely interfacial conduction.

Thus, samples equilibrated under growth conditions exhibit negligible contributions of bulk conduction within the substrate. As a consequence, post-deposition annealing at growth pressure is sufficient to suppress the effect of electronic carriers in the bulk of $SrTiO_3$. So far, it has been typically assumed that annealing in oxygen-rich atmospheres (10-1000 mbar) is required to achieve a sufficiently insulating $SrTiO_3$ substrate. However, while such high oxygen pressures may give similar conductance values at room temperature, they may result in considerably increased resistance at low temperature as shown in chapter 6.4.1 (Figure 6.4).

In particular, higher oxygen pressures during equilibration lead to an increase in residual resistances corresponding to a decrease in electron mobility. This can be attributed to cationic defects existing at the interface (Figure 6.4), while the conductance variation at room temperature (Figure 6.5) stems mainly from a changing concentration of oxygen vacancies in the bulk. Our results therefore indicate that equilibration at growth pressure is sufficient to suppress bulk contributions to the conductance and is beneficial for the increased carrier mobility in comparison to post annealing at higher pressures.

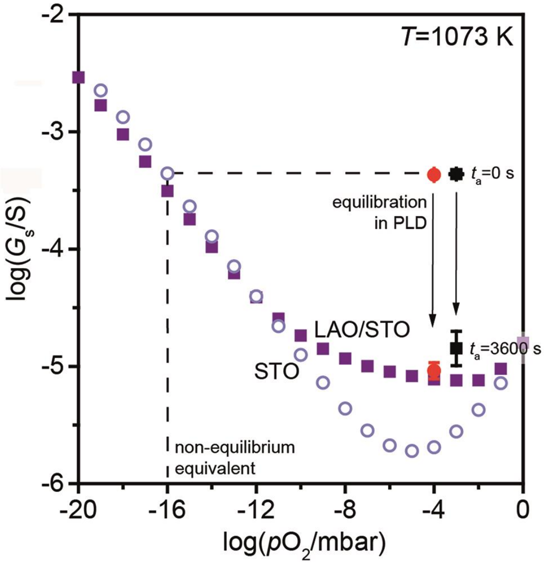

Figure 6.6 *High temperature equilibrium conductance (HTEC) of $SrTiO_3$ (open symbols) and $LaAlO_3/SrTiO_3$ (closed symbols) at 800 °C between for (-20) < log(pO_2/mbar) < 0. Initial and equilibrated sheet conductance obtained for quenched $LaAlO_3/SrTiO_3$ samples are plotted as black (for $1x10^{-3}$ mbar) and red (for $1x10^{-4}$ mbar) filled symbols. The equilibrium pressure corresponding to the initial quenched state is about 10^{-16} mbar (dashed lines). The results were published in ref. [199].*

Interestingly, the oxygen pressure for which bulk conduction is typically observed in $LaAlO_3/SrTiO_3$ (10^{-6} mbar - 10^{-4} mbar) corresponds to highly oxidizing conditions, if compared to typical oxygen partial pressures obtained in chemically controlled reducing atmospheres. For instance, Ar/H_2 gas mixtures typically deliver $pO_2 < 10^{-17}$ mbar at typical growth temperatures. This emphasizes the crucial role of non-equilibrium effects involved in the growth process for the varying sample properties obtained by different groups. This extreme importance of the non-equilibrium created by PLD is also illustrated clearly through the comparison between non-equilibrated and equilibrated states in Figure 6.6. The reoxidation process triggered in the bulk of $SrTiO_3$ manifests itself mainly in the sheet carrier concentration in the substrate's bulk. As oxygen exchange with the surrounding atmosphere is involved, the equilibration rate strongly depends on the ambient pressure. At typical growth pressures, the equilibration time scales from hundreds of seconds to thousands of seconds. This time scale coincides with the typical time scale on which grown samples are still at elevated temperatures after growth in most PLD setups (typically a few minutes). As the electrical properties of $LaAlO_3/SrTiO_3$ heterostructures and in particular those of the $SrTiO_3$ substrate are still very sensitive within this time, kinetic limitations for oxidation may explain the observed scatter in the properties of samples grown at comparable growth conditions by different research groups and setups. In particular, at a growth pressure of $1x10^{-4}$ mbar, a sample cooled down directly after growth may exhibit significant parasitic conduction in the bulk, while a sample cooled down slowly or kept at growth conditions for about 30 minutes shows merely interface conduction (such as for samples discussed in Figure 6.4). At a growth pressure of $1x10^{-3}$ mbar, almost any sample cooled down immediately after the growth (unless intentionally quenched within seconds as described here) should exhibit interface conduction only because equilibration is sufficiently fast. Based on the discussion above, we can suggest a preferred growth recipe for fabricating an electron gas at the LAO/STO interface with minimal scattering centers and without parallel conduction in the bulk: after the typical growth of LAO on STO for a conductive interface (e.g. $1x10^{-4}$ mbar and 800 °C), a post annealing process on the order of one hour should be carried out under growth conditions, rather than with higher oxygen pressures.

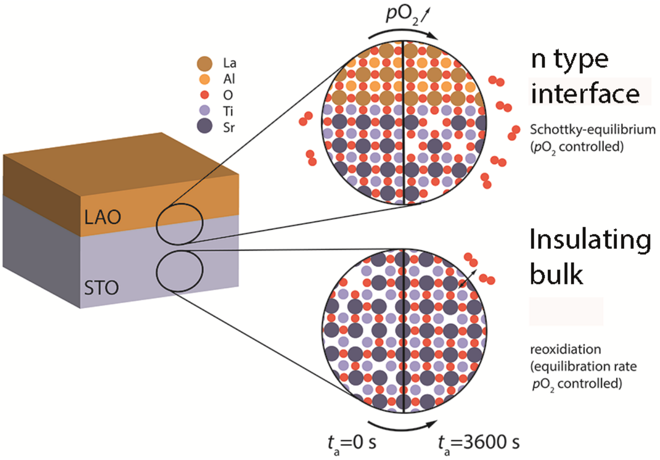

Figure 6.7 *Thermodynamic processes in LAO/STO heterostructures. 1) incorporation of strontium vacancies in the n-type near-surface region upon high-pressure annealing controlled via pO_2 (top); 2) reoxidation of the STO substrate as acceptor doped bulk after reduction during the PLD process controlled via annealing time, t_a (bottom). This figure was published in ref. [199].*

In summary, the growth kinetics and the thermodynamics are strongly interlinked during the fabrication processes for $LaAlO_3/SrTiO_3$ heterostructures. Firstly the growth kinetics shift the $SrTiO_3$ bulk to extreme non-equilibrium. Secondly, two distinct thermodynamic processes are involved in the equilibration of the defect structure of LAO/STO heterostructures after being pushed far away from equilibrium during the PLD process: (1) reoxidation of the STO substrate after reduction during the PLD process; (2) incorporation of Sr vacancies in the near-surface region upon high-pressure annealing. The two thermodynamic processes are summarized in Figure 6.7.

6.5 Complexity of the redox processes

6.5.1 Experiments

The deposition of LAO on 5x5x0.5 mm^3 STO samples is carried out with a laser fluence of 1.4 J/cm^2 at 800 °C. The deposition pressure is set to 1x10^{-5} mbar by oxygen inlet with an UHV background pressure of 10^{-8} mbar. Three samples are annealed at the growth pressure with different annealing times (t_a) ranging from 0 s to 3600 s and quenched afterwards. After *ex-situ* Hall measurements, two samples with an annealing time of 0 s and 3600 s are annealed a second time at 800 °C with 10^{-3} mbar pO_2 for 3600 s and subsequently quenched. These two samples are again characterized by *ex-situ* Hall measurements. During all growth processes and annealing processes the cold cathode gauge is switched on for pressure measurement.

6.5.2 Results

As shown in Figure 6.8 for the LAO deposited at 10^{-5} mbar with 0 s annealing time, the absolute value of n_S is ~ 5x10^{16} cm^{-2}. As the annealing time increases to 3600 s, n_S increases slightly ~ 8x10^{16} cm^{-2}. This value is almost identical to that of the STO sample that is only annealed at 10^{-5} mbar for 3600 s (the point at 10^{-5} mbar in Figure 6.1 (a)). After annealing at pO_2 = 10^{-3} mbar for 3600 s, n_S decreases to ~10^{14} cm^{-2}, which is similar to the equilibrated value shown in Figure 6.5.

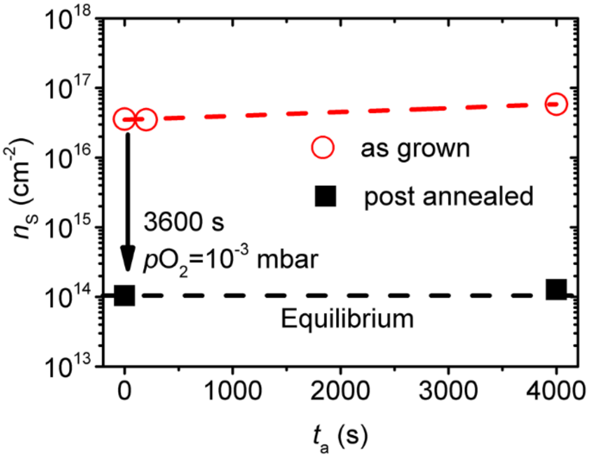

Figure 6.8 *The sheet carrier concentration (n_S) for LAO grown and annealed at 10^{-5} mbar with different annealing times (t_a) (red circles). The 0 s and 3600 s annealed samples are annealed again for 3600 s at 10^{-3} mbar and characterized with ex-situ Hall measurements again (black squares).*

6.5.3 Discussion

The high value of n_S is ascribed to bulk conductivity of STO. Different influences are discussed for the growth and annealing processes.

The quenched sample deposited at 10^{-5} mbar shows an n_S that is around one order of magnitude higher than the one of quenched samples deposited at 10^{-4} mbar and 10^{-3} mbar (the red/black dots in Figure 6.5 (b) with $t_a = 0$ s). The origin of this difference may be assigned to the different oxygen content in LAO as suggested by A. Sambri et. al [71]. The kinetic energy of the plume species at 10^{-5} mbar is almost identical to the ones at 10^{-4} mbar and 10^{-3} mbar around 10 eV [71], whereas the oxidized species in the LAO plume by 10^{-5} mbar can be less. It has been measured at ~ 40 mm target-substrate-distance that the LaO/La ratio is reduced by 10 % by changing oxygen pressure from 10^{-3} mbar to 10^{-4} mbar [71]. The oxygen in STO may be extracted by the LAO film due to the low formation energy of oxygen vacancies in STO and the high kinetic energy of the incoming species of the LAO plume and accommodated into the oxygen deficient LAO thin film.

The annealing process of the LAO/STO samples at 10^{-5} mbar results in a slightly increased n_S. This is similar to STO annealed at 10^{-5} mbar with running cold cathode gauge (Figure 6.3 (b)), where the n_S increases from under detection limit to the same level of around 8×10^{16} cm^{-2}. This similarity indicates the annealing process for LAO/STO samples is dominated by the reducing species generated by the cold cathode gauge like H^0, which has been discussed in chapter 6.1. The STO underneath LAO is thus reduced by annealing at 10^{-5} mbar. The STO substrate can be reoxidized at an increased oxygen pressure of 10^{-3} mbar with an annealing time of 3600 s. The reason for this difference may be the same as for annealing STO at different pressures (chapter 6.1), including the relative delivering rate of reducing and oxidizing species to the LAO/STO surface. However, the process of the incorporation of oxygen or oxygen vacancies into STO in the LAO/STO heterostructure should be different from pure STO. For the LAO/STO heterostructure, both the LAO thin film and the interface between LAO/STO with delocalized electrons can influence the incorporation processes. With regard to this point further investigation is needed.

6.6 Conclusions

In this chapter the different factors that can influence the redox process during PLD processes are studied.
The residual reducing gas species and attached ionizing equipment, like a cold cathode gauge and a mass spectrometer, play an important role in the reduction of STO during annealing at low pressures below10^{-5} mbar. As the total pressure increases to 10^{-4} mbar, the STO sample is not reduced by the annealing process. At this pressure or higher, the kinetic energy of the plume species acts as the main factor for the reduction in STO. This reduction, however, is also dependent on the amount of oxidized species in the LAO plume. Nevertheless, all the oxygen vacancies incorporated in STO during LAO growth can be compensated by annealing at pressures around ~ 10^{-3} mbar, resulting in a reoxidation of the STO single crystal.

7 Summary and Outlook

In this thesis we investigated three important aspects of PLD growth with various methods, namely:

(1) the impact of cation non-stoichiometry on STO homoepitaxy (chapter 4) with *in-situ* AFM, RHEED, LEED and STEM;
(2) the conductive interface formation during LAO growth on STO (chapter 5) with OIRD and Hall-measurement;
(3) the incorporation and removal of oxygen during PLD growth and post-annealing (chapter 6) with mass-spectrometry and Hall-measurement.

For the homoepitaxial growth of STO with PLD, both the laser fluence and the pressure can change the cation non-stoichiometry in the STO thin film and thus the *c*-lattice expansion (chapter 4.1). The laser fluence variation at high pressure oxygen ambient ~ 0.1 mbar is thus utilized for the variation of the cation non-stoichiometry in the thin STO films, namely low laser fluence (1.0 J/cm^2) result in Sr rich STO, medium laser fluence (1.4 J/cm^2) in stoichiometric STO and high laser fluence (2 J/cm^2) in Ti rich STO.
The influence of the cation non-stoichiometry is demonstrated at different growth stages, namely the initial growth stage ($d < 1$ u.c.), the medium growth stage (1 u.c. $< d <$ 50 u.c.) and the late growth stage ($d <$ 500 u.c.).

For the initial growth stage, the surface diffusion and the 2D island coalescence for all three stoichiometries are investigated (chapter 4.2). The surface diffusion coefficients of STO unit cells with different stoichiometries are compared with the diffusion time estimated from RHEED relaxation time and the diffusion length estimated from the averaged island edge separation. It is observed that the ***diffusion of unit cells of non-stoichiometric STO on the stoichiometric substrate is inhibited***, while the diffusion of these cells on existing non-stoichiometric islands is not inhibited. We therefore conclude that reduced diffusion coefficients originate from the surface strain. As a result of the reduced diffusivity, the island shape of non-stoichiometry STO unit cells deviates from the circular shape. Moreover, the island coalescence is delayed for non-stoichiometric thin films, which is observed by *in-situ* AFM investigations and a shift of the RHEED minimum. A modified step density model is suggested to describe the correlation between the reduced diffusivity and the delay of the island coalescence, where the island shape deviation is taken into consideration.

For the intermediate stage of the growth, ***the different solubility of point defects*** influences the ***defect formation processes*** (chapter 4.3 and 4.4). Since the formation energy of Ti vacancies in STO is high, the formation of Ti vacancies in Sr rich STO is energetically unfavorable. Instead, SrO islands on the surface are observed by LEED and AFM, while rock-salt-type SrO layers within STO as well as anti-phase boundaries (APBs) are observed by TEM. For the growth of stoichiometric STO thin film on the TiO_2 terminated STO, the thin film is stoichiometric while the surface is Sr rich. This verifies the strong trend of the formation of SrO islands on the STO surface during PLD growth. However, no extended defects are observed in the stoichiometric STO thin film. In the Ti rich STO thin film, the surface termination of TiO_2 is preserved and no extended defects are formed. The reason for the important role of Sr vacancies could be their low formation energy Sr vacancies with respect to Ti vacancies.

During the late growth stage, ***the defect formation and the surface diffusion in combination determine the growth mode*** of homoepitaxial grown STO with cation non-stoichiometry (chapter 4.5). For Sr rich STO, where extended defects are formed, the growth mode changes from 2D growth to 3D growth. This transition happens after several STO unit cells, where the surface diffraction pattern acquired by RHEED changes from a Laue circle to a 3D ordering. As revealed by the TEM analysis for the APBs, a perfect lattice is observed below the horizontal APBs, which indicates a perfect 2D growth before the formation of APBs takes place. The growth mode transition from 2D to 3D could be correlated to the formation of extended defect in Sr rich STO. The exact comparison between the growth mode transition and the defect formation is difficult, since the growth mode transition observed by RHEED covers the whole surface and TEM supplies only local information. For Ti rich STO, the absence of extended defects prevents a similar transition from 2D to 3D growth. Instead, the inhibited surface diffusion turns the growth from 2D layer-by-layer to 2D double-layer growth. For stoichiometric STO, the growth changes into the step flow mode after several layers. During the growth, the distances between the terrace edges are effectively reduced by the terrace edge roughening, which is observed by AFM for 200 nm films. Therefore, the surface diffusion lengths of STO unit cells can be higher than the terrace width and step flow takes place rather than the 2D island growth on terraces. This means that the ***cation non-stoichiometry*** influences the diffusion and the defect formation processes.

For the heteroepitaxial growth of LAO on STO, 8 u.c. of LAO are grown on different terminated STO with RHEED and OIRD for *in-situ* observation. The different STO terminations are 100 % TiO_2, 100 % SrO and 55 % SrO, where the corresponding heterostructures are LAO/(TiO_2)STO, LAO/(SrO)STO and LAO/(55 % SrO + 45 % TiO_2)STO. For all surface terminations, the subsequently deposited LAO layers grow in 2D growth mode.

For LAO/(TiO_2)STO the heterostructure has a sheet carrier concentration of 10^{14} cm^{-2} at equilibrium. The OIRD signal for the growth of 8 u.c. LAO changes after the first 3 u.c. LAO. The linear slope is steeper for the first 3 u.c. than for the latter 5 u.c. (chapter 5.1). This indicates that the properties of the first 3 u.c. LAO differ from the subsequent LAO unit cells. An influence from the STO substrate can be excluded by the deposition oxygen pressure sequence (chapter 5.2) and post annealing time sequence (chapter 5.3), where the electronic conductivity of STO varies to a great extent but the OIRD signals stay identical. Simulation with a transition matrix method (TMM), taking into account the electrostriction in LAO and the optical permittivity change in LAO allow an explanation of the OIRD signal change. Since the electrostriction and optical permittivity change are correlated to the electron transfer to the LAO/STO interface, the ***electron transfer*** should take place ***at 3 u.c. during the growth of LAO***. It is known that a critical thickness above 3 u.c. LAO is needed for the conductivity of this heterostructure, whereas it is not clear if the conductivity is generated during the growth or after the growth. The OIRD signal indicates that the conductivity of the heterostructure is formed during the growth process. It has to be mentioned that the conductive interface formation does not change the properties of the initial 3 u.c. LAO, only the later grown 5 u.c. LAO differ from the initial 3 u.c..

For LAO/(SrO)STO heterostructure fabrication, the OIRD signal for the 8 u.c. LAO growth process exhibits no slope change, indicating no lattice constant change or optical permittivity change in LAO. The sheet carrier concentration of this heterostructure is just around 10^{11}cm^{-2} and is over three orders of magnitude lower than the LAO on TiO_2 terminated STO. The absence of the slope change and the low sheet carrier concentration indicates ***no electronic transfer to the interface during the growth***. This result verifies the assumption that no electron transfer should happen on LAO/STO interface if STO is 100 % SrO terminated.

For LAO/(55% SrO + 45 % TiO_2)STO, the growth of 8 u.c. LAO is complex. Stripe structures with ~ 0.2 nm height are observed on the LAO surface occurring at the terrace edges. The OIRD shows no significant slope change. The microscopic reason for the surface structure formation and the absence of a slope change need further investigation.

The incorporation of oxygen during pulsed laser deposition is not only a process determined by the thermodynamics, but also strongly influenced by the growth dynamics (impinging particles) and reoxidation kinetics. Taking the peripheral effects like residual gases in the PLD chamber into consideration, the discussion on the incorporation of oxygen during pulsed laser deposition is carried out by carefully investigating each factor.

For the low pressure (< 10^{-4} mbar) annealing of STO (chapter 6.1), the activated residual species like H^0 induced by the ionizing equipment such as the cold cathode and mass spectrometer are found to be responsible for the reduction and incorporation of oxygen vacancies into the STO. However, this effect is insignificant for high pressures (> 10^{-4} mbar), thus pressures above 10^{-4} mbar are oxidizing for PLD annealing processes.

For the annealing process of STO at 10^{-5} mbar, corresponding reducing conditions, the UV-radiation of a LAO plume has only a slight influence on the reduction process. On the contrary, for oxidizing conditions like 10^{-4} mbar, the UV-radiation accelerates the oxidation process (chapter 6.2).

For the deposition process of LAO on STO, the impinging particles with high kinetic energy and the UV-radiation both originate from the plume and could influence the heterostructure conductivity. However, the disentanglement of these two factors has not been investigated before. As shown in chapter 6, the impinging particles with high kinetic energies play the key role for the increase of the STO conductivity, while the UV-radiation from the plume plays a minor role for the conductivity change (chapter 6.3). Nevertheless, the UV irradiated STO surface at high temperatures shows voids with 0.4 nm depth, indicating the influence of UV-radiation on the surface morphology.

The bombardment of the impinging particles plays a key role even for the typical growth condition of LAO/STO ($pO_2 = 10^{-4}$ mbar and 10^{-3} mbar at 800 °C), where the sheet carrier concentration of quenched LAO/STO heterostructures is around 10^{15} cm^{-2}. In these heterostructures, the STO substrates can be reoxidized by annealing at deposition pressure with different annealing times, while the LAO/STO interface remains unchanged (chapter 6.4). The sheet conductance of the equilibrated LAO/STO at growth pressure is consistent with the high temperature equilibrium conductance. However, if the samples are annealed at oxygen pressure higher than the growth pressure, the sheet resistance shows a defect related temperature dependence. As a conclusion, while the substrate reduction relies on growth-induced non-equilibrium effects in the bulk, the incorporation of strontium vacancies is related to thermodynamic equilibrium effects in the interface-near region (controlled via pO_2) deriving from the natural reaction of STO to accommodate charge at the interface. Both effects have to be taken into account when comparing different samples grown by PLD. Annealing time and cooling rates as well as ambient annealing pressure are especially important for these processes, as they act not only as thermodynamic state variables but also control the equilibration kinetics. Based on the discussion above, we can suggest a preferred growth recipe for fabricating an electron gas at the LAO/STO interface with minimal scattering centers and without parallel conduction in the bulk: after the typical growth of LAO on STO for a conductive interface (e.g. 10^{-4} mbar and 800 °C), a post annealing process on the order of one hour should be carried out under growth conditions, rather than with higher oxygen pressures.

Outlook

In this work a qualitative description of the correlation between cation non-stoichiometry induced defects and the growth process of STO homoepitaxy has been established, whereas a quantitative and mechanistic description of this correlation awaits further investigation. Furthermore, the correlation observed here should be transferred to the heteroepitaxial growth in order to design a more general and advanced growth routine for PLD. Especially the APBs observed for the Sr rich STO are of interest as they may act as localized switching paths in resistive switching STO devices. Thus the control of the APB formation through growth engineering should be further explored.

The OIRD signals indicates that for LAO/STO growth the first 3 u.c. have a higher *c*-lattice constant and a higher optical permittivity than the subsequently deposited LAO unit cells. This is difficult to understand based on the present results for LAO/STO studies. This peculiar phenomenon has to be investigated further by other techniques, since other evidence is not available yet. Nevertheless, the OIRD method is an adequate method for the *real-time* observation of heteroepitaxy. Material systems with a certain critical thickness for specific properties such as ferroelectricity, magnetism or optical dichroism could be subjects to be studied.

The incorporation of the oxygen vacancies during low pressure annealing after PLD growth ($< 10^{-5}$ mbar), is caused by the ionized residual gas species in the PLD chamber. By elimination of the ionization sources or residual gas species, this effect can be reduced. This may help further design of low oxygen pressure annealing of low valence complex metal oxides.

Bibliography

[1] D. G. Schlom, Perspective: Oxide molecular-beam epitaxy rocks!, *APL Mater.* **3**, 62403/1-5 (2015)

[2] W. Doolittle, A. Carver and W. Henderson, Molecular beam epitaxy of complex metal-oxides: Where have we come, where are we going, and how are we going to get there?, *J. Vac. Sci. Technol. B* **23**, 1272-1276 (2005)

[3] H. M. Christen and G. Eres, Recent advances in pulsed-laser deposition of complex oxides, *J. Phys. Condens. Mat.* **20**, 264005/1-16 (2008)

[4] B. Dam, J. H. Rector, J. Johansson, J. Hujibregtse and D.G. De Groot, Mechanism of incongruent ablation of STO, *J. Appl. Phys.* **83**, 3386 - 3389 (1998)

[5] S. Amoruso, A. Sambri and X. Wang, Plume expansion dynamics during laser ablation of manganates in oxygen atmosphere, *Appl. Surf. Sci.* **253**, 7696 - 7701 (2007)

[6] S. Amoruso, R.Bruzzese, R.Velotta, N.Spinell, A.Vitiello and X.Wang, Characterization of $LaMnO_3$ laser ablation in oxygen by ion probe and optical emission spectroscopy, *Appl. Surf. Sci.* **248**, 45-49 (2005)

[7] S. Amoruso, C. Aruta, P. Aurino, R. Bruzzese, X. Wang, F. M. Granozio and U. S. di Uccio, Oxygen background gas influence on pulsed laser deposition process of $LaAlO_3$ and $LaGaO_3$, *Appl. Surf. Sci.* **258**, 9116-9122 (2012)

[8] G.Rijnders, The initial growth of complex oxides: Study and Manipulation, *PhD Thesis, University of Twente, Netherlands* (2001)

[9] M. Lippmaa, N. Nakagawa, M. Kawasaki, S. Ohashi and H. Koinuma, Growth mode mapping of $SrTiO_3$ epitaxy, *Appl. Phys. Lett.* **76**, 2439-2441 (2000)

[10] J. Tischler, G. Eres, B. Larson, C. M. Rouleau, P. Zschack and D. H. Lowndes, Nonequilibrium interlayer transport in pulsed laser deposition, *Phys. Rev. Lett.* **96**, 226104/1-4 (2006)

[11] D. Ielmini and R. Waser, *Resistive Switching - From Fundamentals of Nanoionic Redox Processes to Memristive Device Applications*, Wiley-VCH, Weinheim, Germany (2016)

[12] T. Ohnishi, M. Lippmaa, T. Yamamoto, S. Meguro and H. Koinuma, Improved stoichiometry and misfit control in perovskite thin film formation at a critical fluence by pulsed laser deposition, *Appl. Phys. Lett.* **87**, 241919/1-3 (2005)

[13] E. Breckenfeld, R. Wilson, J. Karthik, A. R. Damodaran, D. G. Cahill and L. W. Martin, Effect of growth induced (non)stoichiometry on the structure, dielectric response, and thermal conductivity of $SrTiO_3$ thin films, *Chem. Mater.* **24**, 331-337 (2012)

[14] C. H. Lee, N. J. Podraza, Y. Zhu, R. F. Berger, S. Shen, M. Sestak, R. W. Collins, L. F. Kourkoutis, J. A. Mundy, H. Wang, Q. Mao, X. Xi, L. J. Brillson, J. B. Neaton, D. A. Muller and D. G. Schlom, Effect of reduced dimensionality on the optical band gap of $SrTiO_3$, *Appl. Phys. Lett.* **102**, 122901/1-5 (2013)

[15] F. Gunkel, S. Wicklein, P. Brinks, S. Hoffmann-Eifert, M. Huijben, G. Rijnders, R. Waser and R. Dittmann, Transport limits in defect-engineered $LaAlO_3/SrTiO_3$ bilayers, *Nanoscale* **7**, 1013-1022 (2015)

[16] F. Gunkel, S. Hoffmann-Eifert, R. Dittmann, S.B. Mi, C.L. Jia, P. Meuffels and R. Waser, High temperature conductance characteristics of $LaAlO_3/SrTiO_3$-heterostructures under equilibrium oxygen atmospheres, *Appl. Phys. Lett.* **97**, 12103/1-3 (2010)

[17] F. Gunkel, P. Brinks, S. Hoffmann-Eifert, R. Dittmann, M. Huijben, J. E. Kleibeuker, G. Koster, G. Rijnders and R. Waser, Influence of charge compensation mechanisms on the sheet electron density at conducting $LaAlO_3/SrTiO_3$-interfaces, *Appl. Phys. Lett.* **100**, 52103/1-3 (2012)

[18] S. Thiel, G. Hammerl, A. Schmehl, C. W. Schneider and J. Mannhart, Tunable quasi-two-dimensional electron gases in oxide heterostructures, *Science* **313**, 1942-1945 (2006)

[19] A. Savoia, D. Paparo, P. Perna, Z. Ristic, M. Salluzzo, F. M. Granozio, U. S. di Uccio, C. Richter, S. Thiel, J. Mannhart and L. Marrucci, Polar catastrophe and electronic reconstructions at the $LaAlO_3/SrTiO_3$ interface: Evidence from optical second harmonic generation, *Phys. Rev. B: Condens. Matter* **80**, 75110/1-6 (2009)

[20] K. Momma and F. Izumi, VESTA 3 for three-dimensional visualization of crystal, volumetric and morphology data, *J. Appl. Crystallogr.* **44**, 1272-1276 (2011)

[21] S. Hayward, F. Morrison, S. Redfern, E. Salje, J. Scott, K. Knight, S. Tarantino, A. Glazer, V. Shuvaeva, P. Daniel, M. Zhang and M. Carpenter, Transformation processes in $LaAlO_3$: Neutron diffraction, dielectric, thermal, optical, and Raman studies, *Phys. Rev. B: Condens. Matter* **72**, 54110/1-17 (2005)

[22] D. M. Smyth, *The defect chemistry of metal oxides*, Oxford University Press, UK (2000)

[23] J. Maier, *Physical Chemistry of Ionic Materials*, Wiley, Chichester, UK (2004)

[24] R. Moos and K. H. Härdtl, Defect chemistry of donor-doped and undoped strontium titanate ceramics between 1000 °C and 1400 °C, *J. Am. Ceram. Soc.* **80**, 2549-62 (1997)

[25] M. J. Akhtar, Z.-U.-N. Akhtar, R. A. Jackson and C. R. A. Catlow, Computer simulation studies of strontium titanate, *J. Am. Ceram. Soc.* **78**, 421-428 (1995)

[26] T. Tanaka, K. Matsunaga, Y. Ikuhara and T. Yamamoto, First-principles study on structures and energetics of intrinsic vacancies in $SrTiO_3$, *Phys. Rev. B: Condens. Matter* **68**, 205213/1-8 (2003)

[27] K. Szot and W. Speier, Surfaces of reduced and oxidized $SrTiO_3$ from atomic force microscopy, *Phys. Rev. B: Condens. Matter* **60**, 5909-26 (1999)

[28] K. Szot, W. Speier, U. Breuer, R. Meyer, J. Szade and R. Waser, Formation of micro-crystals on the (100) surface of $SrTiO_3$ at elevated temperatures, *Surface Science, Netherlands* **460**, 112-28 (2000)

[29] S. N. Ruddlesden and P. Popper, The compound $Sr_3Ti_2O_7$ and its structure, *Acta Crystallographica* **11**, 54-55 (1958)

[30] R. Moos, W. Menesklou and K. H. Hardtl, Hall-mobility of undoped n-type conducting strontium-titanate single-crystals between 19 K and 1373 K, *Appl. Phys. A-Mater. Sci. Process.* **61**, 389-395 (1995)

[31] F. Gunkel, The role of defects at functional interfaces between polar and non-polar perovskite oxides, *PhD Thesis, RWTH Aachen, Germany* (2013)

[32] T. Ohnishi, K. Shibuya, T. Yamamoto and M. Lippmaa, Defects and transport in complex oxide thin films, *J. Appl. Phys.* **103**, 103703/1-6 (2008)

[33] C. L. Jia, L. Houben and K. Urban, Atom vacancies at a screw dislocation core in $SrTiO_3$, *Philosophical Magazine Letters* **86**, 683-90 (2006)

[34] C. L. Jia, A. Thust and K. Urban, Atomic-scale analysis of the oxygen configuration at a $SrTiO_3$ dislocation core, *Phys. Rev. Lett.* **95**, 225506/1-4 (2005)

[35] C. M. Brooks, R. B. Wilson, A. Schaefer, J. A. Mundy, M. E. Holtz, D. A. Muller, J. Schubert, D. G. Cahill and D. G. Schlom, Tuning thermal conductivity in homoepitaxial $SrTiO_3$ films via defects, *Appl. Phys. Lett.* **107**, 51902/1-5 (2015)

[36] K. H. Lee, S. W. Kim, H. Ohta and K. Koumoto, Ruddlesden-Popper phases as thermoelectric oxides: Nb-doped $SrO(SrTiO_3)_n$ (n=1,2), *J. Appl. Phys.* **100**, 63717/1-7 (2006)

[37] K. Shibuya, R. Dittmann, S. Mi and R. Waser, Impact of defect distribution on resistive switching characteristics of Sr_2TiO_4 thin films, *Adv. Mater.* **22**, 411-414 (2010)

[38] C. H. Nien and H. Y. Lu, Crystallographic orientation relationships between $SrTiO_3$ and Ruddlesden-Popper phase, *J. Am. Ceram. Soc.* **95**, 1676-1681 (2012)

[39] C. M. Brooks, L. F. Kourkoutis, T. Heeg, J. Schubert, D. A. Muller and D. G. Schlom, Growth of homoepitaxial $SrTiO_3$ thin films by molecular-beam epitaxy, *Appl. Phys. Lett.* **94**, 162905/1-3 (2009)

[40] K. Shibuya, S. Mi, C.L. Jia, P. Meuffels and R. Dittmann, Sr_2TiO_4 layered perovskite thin films grown by pulsed laser deposition, *Appl. Phys. Lett.* **92**, 241918/1-3 (2008)

[41] D.J. Keeble, S. Wicklein, L. Jin, C. L. Jia, W. Egger and R. Dittmann, Nonstoichiometry accommodation in $SrTiO_3$ thin films studied by positron annihilation and electron microscopy, *Phys. Rev. B: Condens. Matter* **87**, 195409/1-11 (2013)

[42] Y. F. Nie, Y. Zhu, C. Lee, L. F. Kourkoutis, J. A. Mundy, J. Junquera, Ph. Ghosez, D. J. Baek, S. Sung, X. X. Xi, K. M. Shen, D. A. Muller and D. G. Schlom, Atomically precise interfaces from non-stoichiometric deposition, *Nat. Commun.* **5**, 4530/1-8 (2014)

[43] Y. Tokuda, S. Kobayashi, T. Ohnishi, T. Mizoguchi, N. Shibata, Y. Ikuhara and T. Yamamoto, Growth of Ruddlesden-Popper type faults in Sr-excess $SrTiO_3$ homoepitaxial thin films by pulsed laser deposition, *Appl. Phys. Lett.* **99**, 173109/1-3 (2011)

[44] B. Chichkov, C. Momma, S. Nolte, F. vonAlvensleben and A. Tunnermann, Femtosecond, picosecond and nanosecond laser ablation of solids, *Appl. Phys. A Mater. Sci. Process.* **63**, 109-115 (1996)

[45] E. Gamaly, A. Rode, B. Luther-Davies and V. Tikhonchuk, Ablation of solids by femtosecond lasers: Ablation mechanism and ablation thresholds for metals and dielectrics, *Phys. Plasmas* **9**, 949-957 (2002)

[46] A. Vogel, J. Noack, G. Huttman and G. Paltauf, Mechanisms of femtosecond laser nanosurgery of cells and tissues, *Appl. Phys. B-Lasers Opt.* **81**, 1015-1047 (2005)

[47] S. Amoruso, R. Bruzzese, N. Spinelli and R. Velotta, Characterizaion of laser-ablation plasmas, *J. Phys. B Atom. Mol. Opt. Phys.* **32**, R131-R172 (1999)

[48] B. Dam, J.H. Rector, J. Johansson, S. Kars and R. Griessen, Stoichiometric transfer of complex oxides by pulsed laser deposition, *Appl. Surf. Sci.* **96-98**, 679-684 (1996)

[49] C. Guguschev, D. Klimm, F. Langhans, Z. Galazka, D. Kok, U. Juda and R. Uecker, Top-seeded solution growth of $SrTiO_3$ crystals and phase diagram studies in the SrO-TiO_2 system, *Crystengcomm* **16**, 1735-1740 (2014)

[50] D.B. Geohegan and A.A. Puretzky, Laser ablation plume thermalization dynamics in background gases: Combined imaging, optical absorption and emission spectroscopy, and ion probe measurement, *Appl. Surf. Sci.* **96-98**, 131-138 (1996)

[51] S. Amoruso, J. Schou and J. G. Lunney, Influence of the atomic mass of the background gas on laser ablation plume propagation, *Appl. Phys. A Mater. Sci. Process.* **92**, 907-911 (2008)

[52] S. Amoruso, B. Toftmann and J. Schou, Thermalization of a UV laser ablation plume in a background gas: From a directed to a diffusionlike flow, *Phys. Rev. E: Stat. Nonlinear Soft Matter Phys.* **69**, 56403/1-6 (2004)

[53] M. Predtechensky and A. Mayokov, Expansion of laser-plasma in oxygen at laser deposition of HTSC films - theoretical-model, *Appl. Supercond.* **1**, 2011-2017 (1993)

[54] S. Amoruso, C. Aruta, R. Bruzzese, D. Maccariello, L. Maritato, F. M. Granozio, P. Orgiani, U. S. di Uccio and X. Wang, Optimization of $La_{0.7}Ba_{0.3}MnO_{3-\delta}$ complex oxide laser ablation conditions by plume imaging and optical emission spectroscopy, *J. Appl. Phys.* **108**, 043302/1-8 (2010)

[55] C. Aruta, S. Amoruso, R. Bruzzese, X. Wang, D. Maccariello, F. M. Granozio and U. S. di Uccio, Pulsed laser deposition of $SrTiO_3$/$LaGaO_3$ and $SrTiO_3$/$LaAlO_3$: Plasma plume effects, *Appl. Phys. Lett.* **97**, 252105/1-3 (2010)

[56] S. Amoruso, R. Bruzzese and X. Wang, Plume composition control in double pulse ultrafast laser ablation of metals, *Appl. Phys. Lett.* **95**, 251501/1-3 (2009)

[57] S. Amoruso, A. Sambri and X. Wang, Propagation dynamics of a $LaMnO_3$ laser ablation plume in an oxygen atmosphere, *J. Appl. Phys.* **100**, 013302/1-11 (2006)

[58] S. Wicklein, A. Sambri, S. Amoruso, X. Wang, R. Bruzzese, A. Koehl and R. Dittmann, Pulsed laser ablation of complex oxides: The role of congruent ablation and preferential scattering for the film stoichiometry, *Appl. Phys. Lett.* **101**, 131601/1-5 (2012)

[59] N. Arnold, J. Gruber and J. Heitz, Spherical expansion of the vapor plume into ambient gas: an analytical model, *Appl. Phys. A Mater. Sci. Process.* **69**, S87-S93 (1999)

[60] S. Amoruso, J. Schou and J. G. Lunney, Energy balance of a laser ablation plume expanding in a background gas, *Appl. Phys. A Mater. Sci. Process.* **101**, 209-214 (2010)

[61] A. Sambri, S. Amoruso, X. Wang, M. Radovic, F. Miletto Granozio and R. Bruzzese, Substrate heating influence on plume propagation during pulsed laser deposition of complex oxides, *Appl. Phys. Lett.* **91**, 151501/1-3 (2007)

[62] A. Sambri, S. Amoruso, X. Wang, F. Miletto Granozio and R Bruzzese, Plume propagation dynamics of complex oxides in oxygen, *J. Appl. Phys.* **104**, 053304/1-8 (2008)

[63] Chencheng Xu, Sebastian Wicklein, Alessia Sambri, Salvatore Amoruso, Marco Moors and Regina Dittmann, Impact of the interplay between nonstoichiometry and kinetic energy of the plume species on the growth mode of $SrTiO_3$ thin films, *J. Phys. D Appl. Phys.* **47**, 034009/1-11 (2014)

[64] R. Dömel, Untersuchung der Transporteigenschaften von SNS-Kontakten mit $SrRuO_3$ Barriere, *Berichte des Forschungszentrum Jülich (Dissertation Universität Gießen)* (1994)

[65] D. Adamovic, V. Chirita, E. P. Munger, L. Hultman and J. E. Greene, Kinetic pathways leading to layer-by-layer growth from hyperthermal atoms: A multibillion time step molecular dynamics study, *Phys. Rev. B: Condens. Matter* **76**, 115418/1-7 (2007)

[66] P.R. Willmott, R. Herger, C.M. Schlepuetz, D. Martoccia and B.D. Patterson, Energetic surface smoothing of complex metal oxide thin films, *Phys. Rev. Lett.* **96**, 176102/1-4 (2006)

[67] W. M. Haynes, *CRC Handbook of Chemistry and Physics*, CRC press, Boca Raton (2013)

[68] G. Eres, J. Z. Tischler, C. m. Rouleau, P. Zschack, H. m. Christen and B. C. Larson, Quantitative determination of energy enhanced interalyer transport in pulsed laser deposition of $SrTiO_3$, *Phys. Rev. B: Condens. Matter* **84**, 195467/1-12 (2011)

[69] G. J. H. M. Rijnders, G. Koster, D. H. A. Blank and H. Rogalla, In situ monitoring during pulsed laser deposition of complex oxides using reflection high energy electron diffraction under high oxygen pressure, *Appl. Phys. Lett.* **70**, 1888-1890 (1997)

[70] G. Herranz, M. Basletic, O. Copie, M. Bibes, A. N. Khodan, C. Carretero, E. Tafra, E. Jacquet, K. Bouzehouane, A. Hamzic and A. Barthelemy, Controlling high-mobility conduction in $SrTiO_3$ by oxide thin film deposition, *Appl. Phys. Lett.* **94**, 12113/1-3 (2009)

[71] A. Sambri, D. V. Cristensen, F. Trier, Y. Z. Chen, S. Amoruso, N. Pryds, R. Bruzzese and X. Wang, Plasma plume effects on the conductivity of amorphous-$LaAlO_3$/$SrTiO_3$ interfaces grown by pulsed laser deposition in O_2 and Ar, *Appl. Phys. Lett.* **100**, 231605/1-4 (2012)

[72] J. Hermann, A. Thomann, C. Boulmerleborgne, B. Dubreuil, M. Degiorgi, A. Perrone, A. Luches and I. Mihailescu, Plasma diagnostics in pulsed-laser TiN layer deposition, *J. Appl. Phys.* **77**, 2928-2936 (1995)

[73] F. Fujishiro and S. Mochizuki, Photo-induced phenomena in $SrTiO_3$, **21**, 142-148 (2005)

[74] M. C. Tarun, F. A. Selim and M. D. McCluskey, Persistent photoconductivity in strontium titanate, *Phys. Rev. Lett.* **111**, 187403/1-5 (2013)

[75] I. V. Markov, *Crystal growth for beginners*, World Scientific, Singapore (2003)

[76] R. Altsinger, H. Busch, M. Horn and M. Henzler, Nucleation and growth during molecular-beam epitaxy (MBE) of Si on Si(111), *Surf. Sci.* **200**, 235-246 (1988)

[77] R. Gomer, Diffusion of adsorbates on metal-surfaces, *Rep. Prog. Phys.* **53**, 917-1002 (1990)

[78] G. Koster, G. J. H. M. Rijnders, D. H. A. Blank and H. Rogalla, *In situ initial growth studies of $SrTiO_3$ on $SrTiO_3$ by time resolved high pressure RHEED.*, Materials research society symposium proceedings **526**, 33-37 (1998)

[79] K. Oura, V.G. Lifshits, A. Saranin, A.V. Zotov and M. Katayam, *Surface Science: An Introduction*, Springer, New York (2003)

[80] D. Montiel, J. Muller and E. Poire, Morphological instability at the early stages of heteroepitaxial growth on vicinal surfaces, *J. Phys. Condens. Mat.* **14**, L49-L55 (2002)

[81] J. Choi, C. B. Eom, G. Rijnders, H. Rogalla and D. H. A. Blank, Growth mode transition from layer by layer to step flow during the growth of heteroepitaxial $SrRuO_3$ on (001)$SrTiO_3$, *Appl. Phys. Lett.* **79**, 1447-9 (2001)

[82] M. Lippmaa, N. Nakagawa, M. Kawasaki, S. Ohashi, Y. Inaguma, M. Itoh and H. Koinuma, Step-flow growth of $SrTiO_3$ thin films with a dielectric constant exceeding 10^4, *Appl. Phys. Lett.* **74**, 3543-5 (1999)

[83] M. Lippmaa, N. Nakagawa, T. Kinoshita, T. Furumochi, M. Kawasaki and H. Koinuma, Growth dynamics of oxide thin films at temperatures above 1000 degrees C, *Physica C* **335**, 196-200 (2000)

[84] T. Kawamura, Relation between surface step density and RHEED Intensity, *Surf. Sci.* **298**, 331-335 (1993)

[85] M. Ohring, *Materials science of thin films*, Academic Press, San Diego (2002)

[86] S. Stoyanov and M. Michailov, Non-steady state effects in MBE: oscillations of the step density at the crystal surface, *Surface Science* **202**, 109-124 (1988)

[87] P. Scheiderer, F. Pfaff, J. Gabel, M. Kamp, M. Sing and R. Claessen, Surface-interface coupling in an oxide heterostructure: Impact of adsorbates on $LaAlO_3$/$SrTiO_3$, *Phys. Rev. B: Condens. Matter* **92**, 195422/1-9 (2015)

[88] A. Ohtomo and H. Y. Hwang, A high-mobility electron gas at the $LaAlO_3$/$SrTiO_3$ heterointerface, *Nature* **427**, 423-426 (2004)

[89] J. Mannhart and D. Schlom, Oxide interfaces an opportunity for electronics, *Science* **327**, 1607-1611 (2010)

[90] A. Savoia, D. Paparo, P. Perna, Z. Ristic, M. Salluzzo, F. M. Granozio, U. di Uccio, C. Richter, S. Thiel, J. Mannhart and L. Marrucci, Polar catastrophe and electronic reconstructions at the $LaAlO_3/SrTiO_3$ interface: Evidence from optical second harmonic generation, *Phys. Rev. B: Condens. Matter* **80**, 075110/1-6 (2009)

[91] S. A. Chambers, Understanding the mechanism of conductivity at the $LaAlO_3/SrTiO_3(001)$ interface, *Surf. Sci.* **605**, 1133-1140 (2011)

[92] A. Rubano, M. Fiebig, D. Paparo, A. Marino, D. Maccariello, U. S. di Uccio, F. M. Granozio, L. Marrucci, C. Richter, S. Paetel and J. Mannhart, Spectral and spatial distribution of polarization at the $LaAlO_3/SrTiO_3$ interface, *Phys. Rev. B: Condens. Matter* **83**, 155405/1-6 (2011)

[93] M. Sing, G. Berner, K. Goss, A. Mueller, A. Ruff, A. Wetscherek, S. Thiel, J. Mannhart, S. A. Pauli, C. W. Schneider, P. R. Willmott, M. Gorgoi, F. Schaefers and R. Claessen, Profiling the interface electron gas of $LaAlO_3/SrTiO_3$ heterostructures with hard X-ray photoelectron spectroscopy, *Phys. Rev. Lett.* **102**, 176805/1-4 (2009)

[94] T. C. Asmara, A. Annadi, I. Santoso, P. K. Gogoi, A. Kotlov, H. M. Omer, M. Motapothula, M. B. H. Breese, M. Ruebhausen, T. Venkatesan, Ariando and A. Rusydi, Mechanisms of charge transfer and redistribution in $LaAlO_3/SrTiO_3$ revealed by high-energy optical conductivity, *Nat. Commun.* **5**, 3663/1-10 (2014)

[95] C. Cancellieri, D. Fontaine, S. Gariglio, N. Reyren, A. D. Caviglia, A. Fete, S. J. Leake, S. A. Pauli, P. R. Willmott, M. Stengel, Ph. Ghosez and J. Triscone, Electrostriction at the $LaAlO_3/SrTiO_3$ Interface, *Phys. Rev. Lett.* **107**, 56102/1-4 (2011)

[96] A. Brinkman, M. Huijben, M. Van Zalk, J. Huijben, U. Zeitler, J. C. Maan, W. G. Van der Wiel, G. Rijnders, D. H. A. Blank and H. Hilgenkamp, Magnetic effects at the interface between non-magnetic oxides, *Nat. Mater.* **6**, 493-496 (2007)

[97] M. Basletic, J. Maurice, C. Carretero, G. Herranz, O. Copie, M. Bibes, E. Jacquet, K. Bouzehouane, S. Fusil and A. Barthelemy, Mapping the spatial distribution of charge carriers in $LaAlO_3/SrTiO_3$ heterostructures, *Nat. Mater.* **7**, 621-625 (2008)

[98] M. Huijben, A. Brinkman, G. Koster, G. Rijnders, H. Hilgenkamp and D. H. A. Blank, Structure-Property Relation of $SrTiO_3/LaAlO_3$ Interfaces, *Advanced Materials* **21**, 1665-1677 (2009)

[99] V. Vonk, J. Huijben, D. Kukuruznyak, A. Stierle, H. Hilgenkamp, A. Brinkman and S. Harkema, Polar-discontinuity-retaining A-site intermixing and vacancies at $SrTiO_3$/$LaAlO_3$ interfaces, *Phys. Rev. B: Condens. Matter* **85**, 45401/1-5 (2012)

[100] W. Sitaputra, N. Sivadas, M. Skowronski, D. Xiao and R. M. Feenstra, Oxygen vacancies on SrO-terminated $SrTiO_3$(001) surfaces studied by Scanning Tunneling Spectroscopy, *Phys. Rev. B: Condens. Matter* **91**, 205408/1-10 (2015)

[101] T. Kubo and H. Nozoye, Surface structure of $SrTiO_3$(100), *Surf. Sci.* **542**, 177-191 (2003)

[102] R. Bachelet, F. Sanchez, F. J. Palomares, C. Ocal and J. Fontcuberta, Atomically flat SrO-terminated $SrTiO_3$(001) substrate, *Appl. Phys. Lett.* **95**, 141915/1-3 (2009)

[103] J. Mannhart, D.H.A. Blank, H.Y. Hwang, A.J. Millis and J.-M. Triscone, Two-dimensional electron gases at oxide interfaces, *MSRS Bulletin* **33**, 1027-1034 (2008)

[104] R. Takahashi, Y. Matsumoto, T. Ohsawa, M. Lippmaa, M. Kawasaki and H. Koinuma, Growth dynamics of the epitaxial SrO film on $SrTiO_3$(001), *J. Cryst. Growth* **234**, 505-508 (2002)

[105] M. Foerster, R. Bachelet, V. Laukhin, J. Fontcuberta, G. Herranz and F. Sanchez, Laterally confined two-dimensional electron gases in self-patterned $LaAlO_3$/$SrTiO_3$ interfaces, *Appl. Phys. Lett.* **100**, 231607/1-5 (2012)

[106] Felix V. E. Hensling, Influence of UV radiation during Pulsed Laser Deposition on the electrical properties of $SrTiO_3$, *Master Thesis, RWTH Aachen, Germany* (2015)

[107] Ayahiko Ichimiya and Philip I. Cohen, Reflection High Energy Electron Diffraction, *Cambridge University Press, UK* (2004)

[108] X. Zhu, Oblique-incidence optical reflectivity difference from a rough film of crystalline material, *Phys. Rev. B: Condens. Matter* **69**, 115407/1-5 (2004)

[109] X. D. Zhu, H. b. Lu, G. Z. Yang, A. Y. Li, B. Y. Gu and D. Z. Zhang, Epitaxial growth of $SrTiO_3$ on $SrTiO_3$(001) using an oblique-incidence reflectance-difference technique, *Phys. Rev. B: Condens. Matter* **57**, 2515-9 (1998)

[110] X. Zhu, W. Si, X. Xi and Q. Jiang, Oxidation kinetics in $SrTiO_3$ homoepitaxy on $SrTiO_3$(001), *Appl. Phys. Lett.* **78**, 460-462 (2001)

[111] D. Colton and R. Kress, *Inverse Acoustic and Electromagnetic Scattering Theory*, Springer, New York (1998)

[112] J. Mcintyre and D. Aspnes, Differential Reflection Spectroscopy of very thin surface films, *Surf. Sci.* **24**, 417-434 (1971)

[113] X. D. Zhu, Y. Y. Fei, X. Wang, H. B. Lu and G. Z. Yang, General theory of optical reflection from a thin film on a solid and its application to heteroepitaxy, *Phys. Rev. B: Condens. Matter* **75**, 245434/1-14 (2007)

[114] R. Peacock, N. Peacock and D. Hauschulz, Comparison of hot cathode and cold-cathode ionization gauges, *J. Vac. Sci. Technol. A* **9**, 1977-1985 (1991)

[115] K. Jousten and M. Wutz, *Wutz Handbuch Vakuumtechnik*, Vieweg Verlag, Wiesbaden (2006)

[116] Peter H. Dawson, *Quadrupole Mass Spectrometry and Its Applications*, Elsevier, Amsterdam (1976)

[117] P. Miller and M. Denton, The quadrupole mass filter - basic operating concepts, *J. Chem. Educ.* **63**, 617-622 (1986)

[118] G. Glish and R. Vachet, The basics of mass spectrometry in the twenty-first century, *Nat. Rev. Drug Discov.* **2**, 140-150 (2003)

[119] G. Binnig, C. F. Quate and C. Gerber, Atomic force microscope, *Phys. Rev. Lett.* **56**, 930-3 (1986)

[120] D. J. Billingsley, W. A. Bonass, N. Crampton, J. Kirkham and N. H. Thomson, Single-molecule studies of DNA transcription using atomic force microscopy, *Phys. Biol.* **9**, 21001/1-15 (2012)

[121] Hendrik Hoelscher, Encyclopedia of Nanotechnology, **94**, *Springer Netherlands*, Dordrecht (2012)

[122] R. Garcia and R. Perez, Dynamic atomic force microscopy methods, *Surf. Sci. Rep.* **47**, 197-301 (2002)

[123] S. Tanuma, C. J. Powell and D. R. Penn, Calculations of electron inelastic mean free paths. IX. Data for 41 elemental solids over the 50 eV to 30 keV range, *Surf. Interface Anal.* **43**, 689-713 (2011)

[124] G. Ertl and J. Kueppers, *Low Energy Electrons and Surface Chemistry*, VCH, Weinheim (1985)

[125] G. Held, Low energy electron diffraction crystallography of surfaces and interfaces, *Bunsen-Magazin* **12**, 124-131 (2010)

[126] K. Heinz, Structural-analysis of surfaces by LEED, *Prog. Surf. Sci.* **27**, 239-326 (1988)

[127] J. Jobst, J. Kautz, D. Geelen, R. M. Tromp and S. J. van der Molen, Nanoscale measurements of unoccupied band dispersion in few-layer graphene. *Nature Communications* **6**, 1-6 (2015)

[128] D. Saldin, J. Pendry, M. Vanhove and G. Somorjai, Interpretation of diffuse low-energy electron-diffraction intensities, *Phys. Rev. B: Condens. Matter* **31**, 1216-1218 (1985)

[129] E. Hall, On a new action of a magnet on electric currents, *American Jounal of Mathematics* **2**, 287-292 (1879)

[130] R. Green, Hall Effect Measurements in Materials Characterization, *Technical Reports of Keithley Instruments, Inc.* (2011)

[131] L. J. van der Pauw, A method of measuring specific resistivity and Hall effect of discs of arbitrary shape, *Philips Res. Rep.* **13**, 1-9 (1958)

[132] J. Lindemuth and S. I. Mizuta, Hall measurements on low mobility materials and high resistivity materials, *Thin Film Solar Technology Iii* **8110**, 81100I/1-7 (2011)

[133] S. Huefner, *Photoelectron Spectroscopy: Principles and Applications.*, Springer, New York (1995)

[134] C. Baeumer, C. Xu, F. Gunkel, N. Raab, R. A. Heinen, A. Koehl and R. Dittmann, Surface termination conversion during $SrTiO_3$ thin film growth revealed by X-ray Photoelectron Spectroscopy, *Scientific Reports* **5**, 11829/1-11 (2015)

[135] Anja Herpers, Electrical characterization of manganite and titanate heterostructures, *PhD Thesis, RWTH Aachen, Germany* (2014)

[136] L. Edge, D. Schlom, S. Chambers, E. Cicerrella, J. Freeouf, B. Hollander and J. Schubert, Measurement of the band offsets between amorphous $LaAlO_3$ and silicon, *Appl. Phys. Lett.* **84**, 726-728 (2004)

[137] Elena Dobrovinskaya, Leonid Lytvynov and Valerian Pishchik, *Sapphire Materials, Manufacturing, Applications*, Springer, New York (2009)

[138] D. A. Freedman, D. Roundy and T. A. Arias, Elastic effects of vacancies in strontium titanate: Short- and long-range strain fields, elastic dipole tensors, and chemical strain, *Phys. Rev. B: Condens. Matter* **80**, 064108/1-13 (2009)

[139] G. Z. Liu, Q. Y. Lei and X. X. Xi, Stoichiometry of $SrTiO_3$ films grown by pulsed laser deposition, *Appl. Phys. Lett.* **100**, 202902/1-3 (2012)

[140] Chencheng Xu, Marco Moors and Regina Dittmann, Impact of cation stoichiometry on the early stage of growth of $SrTiO_3$ deposited by pulsed laser deposition, *Appl. Surf. Sci.* **359**, 68-72 (2015)

[141] V. Fuenzalida, Pulsed deposition: model for the cluster size distribution after the first pulse, *J. Cryst. Growth* **183**, 497-503 (1998)

[142] V. Fuenzalida, Pulsed deposition and postnucleation: model for the average cluster size as a function of the number of pulses, *J. Cryst. Growth* **213**, 157-160 (2000)

[143] F. Dulot, B. Kierren and D. Malterre, Lineshape analysis of RHEED pattern: scaling behavior and linewidth oscillations, *Thin Solid Films* **428**, 72-75 (2003)

[144] E. Dulot, B. Kierren and D. Malterre, Determination of kinetic parameters in layer-by-layer growth from RHEED profile analysis, *Thin Solid Films* **423**, 64-69 (2003)

[145] J. D. Ferguson, G. Arikan, D. S. Dale, A. R. Woll and J. D. Brock, Measurements of surface diffusivity and coarsening during Pulsed Laser Deposition, *Phys. Rev. Lett.* **103**, 256103/1-4 (2009)

[146] B. Yoon, V. Akulin, P. Cahuzac, F. Carlier, M. de Frutos, A. Masson, C. Mory, C. Colliex and C. Brechignac, Morphology control of the supported islands grown from soft-landed clusters, *Surf. Sci.* **443**, 76-88 (1999)

[147] B. Stegemann, C. Ritter, B. Kaiser and K. Rademann, Crystallization of antimony nanoparticles: Pattern formation and fractal growth, *J. Phys. Chem. B* **108**, 14292-14297 (2004)

[148] T. Shitara, D. Vvedensky, M. Wilby, J. Zhang, J. Neave and B. Joyce, Step density variations and Reflection High-Energy Electron-Diffraction intensity oscillations during epitaxial-growth on vicinal GaAs(001), *Phys. Rev. B: Condens. Matter* **46**, 6815-6824 (1992)

[149] T. Shitara, D. Vvdensky, M. Wilby, J. Zhang, J. Neave and B. Joyce, Morphological model of Reflection High-Energy Electron-Diffraction intensity oscillations during epitaxial-growth on GaAs(001), *Appl. Phys. Lett.* **60**, 1504-1506 (1992)

[150] S. Clarke and D. Vvedensky, Computational investigation of RHEED intensity evolutions during growth by MBE, *Surf. Sci.* **189**, 1033-1040 (1987)

[151] U. Korte and P. Maksym, Role of the step density in reflection high-energy electron diffraction: Questioning the step density model, *Phys. Rev. Lett.* **78**, 2381-2384 (1997)

[152] W. Braun, L. Daweritz and K. Ploog, Origin of electron diffraction oscillations during crystal growth, *Phys. Rev. Lett.* **80**, 4935-4938 (1998)

[153] M. Lippmaa, M. Kawasaki, A. Ohtomo, T. Sato, M. Iwatsuki and H. Koinuma, Observation of $SrTiO_3$ step edge dynamics by real-time high-temperature STM, *Appl. Surf. Sci.* **130**, 582-586 (1998)

[154] D. Shu, F. Liu and X. Gong, Simple generic method for predicting the effect of strain on surface diffusion, *Phys. Rev. B: Condens. Matter* **64**, 245410/1-4 (2001)

[155] L. Huang, F. Liu, G. Lu and X. Gong, Surface mobility difference between Si and Ge and its effect on growth of SiGe alloy films and islands, *Phys. Rev. Lett.* **96**, 16103/1-4 (2006)

[156] Y. Mo, J. Kleiner, M. Webb and M. Lagally, Activation energy for surface diffusion of Si on Si(001) -A Scanning-Tunneling-Microscopy Study, *Phys. Rev. Lett.* **66**, 1998-2001 (1991)

[157] M. Naito and H. Sato, Reflection High-Energy Electron-Diffraction study on the $SrTiO_3$ surface-structure, *Physica C* **229**, 1-11 (1994)

[158] H. Tanaka, T. Matsumoto, T. Kawai and S. Kawai, Surface-structure and electronic property of reduced $SrTiO_3$(100) surface observed by scanning tunneling microscopy spectroscopy, *Jpn. J. Appl. Phys.* **32**, 1405-1409 (1993)

[159] Q. Jiang and J. Zegenhagen, $SrTiO_3$(001)-c(6x2): A long-range, atomically ordered surface stable in oxygen and ambient air, *Surf. Sci.* **367**, L42-L46 (1996)

[160] N. Erdman, K. Poeppelmeier, M. Asta, O. Warschkow, D. Ellis and L. Marks, The structure and chemistry of the TiO_2-rich surface of $SrTiO_3$(001), *Nature* **419**, 55-58 (2002)

[161] N. Erdman, O. Warschkow, M. Asta, K. Poeppelmeier, D. Ellis and L. Marks, Surface structures of $SrTiO_3$(001): A TiO_2-rich reconstruction with a c(4 x 2) unit cell, *J. Am. Chem. Soc.* **125**, 10050-10056 (2003)

[162] Y. Lin, A. E. Becerra-Toledo, F. Silly, K. R. Poeppelmeier, M. R. Castell and L. D. Marks, The (2x2) reconstructions on the $SrTiO_3$(001) surface: A combined scanning tunneling microscopy and density functional theory study, *Surf. Sci.* **605**, L51-L55 (2011)

[163] T. Ohsawa, R. Shimizu, K. Iwaya and T. Hitosugi, Visualizing Atomistic Formation Process of SrO_x Thin Films on $SrTiO_3$, *ACS Nano* **8**, 2223-2229 (2014)

[164] J. H. Lee, G. Luo, I. C. Tung, S. H. Chang, Z. Luo, M. Malshe, M. Gadre, A. Bhattacharya, S. M. Nakhmanson, J. A. Eastman, H. Hong, J. Jellinek, D. Morgan, D. D. Fong and J. W. Freeland, Dynamic layer rearrangement during growth of layered oxide films by molecular beam epitaxy, *Nat. Mater.* **13**, 879-883 (2014)

[165] K. Gomann, G. Borchardt, M. Schulz, A. Gomann, W. Maus-Friedrichs, B. Lesage, O. Kaitasov, S. Hoffmann-Eifert and T. Schneller, Sr diffusion in undoped and La-doped $SrTiO_3$ single crystals under oxidizing conditions, *Physical Chemistry Chemical Physics* **7**, 2053-60 (2005)

[166] K. Gomann, G. Borchardt, A. Gunhold, W. Maus-Friedrichs and H. Baumann, Ti diffusion in La-doped $SrTiO_3$ single crystals, *Physical Chemistry Chemical Physics* **6**, 3639-3644 (2004)

[167] J. Mannhart and D.G. Schlom, Oxide Interfaces An Opportunity for Electronics, *Science* **327**, 1607-1611 (2010)

[168] A. Fete, C. Cancellieri, D. Li, D. Stornaiuolo, A. D. Caviglia, S. Gariglio and J. Triscone, Growth-induced electron mobility enhancement at the $LaAlO_3/SrTiO_3$ interface, *Appl. Phys. Lett.* **106**, 51604/1-4 (2015)

[169] C. Cancellieri, N. Reyren, S. Gariglio, A. D. Caviglia, A. Fete and J. Triscone, Influence of the growth conditions on the $LaAlO_3/SrTiO_3$ interface electronic properties, *EPL* **91**, 17004/1-6 (2010)

[170] T. Suzuki, Y. Nishi and M. Fujimoto, Defect structure in homoepitaxial non-stoichiometric strontium titanate thin films, *Philos. Mag. A-Phys. Condens. Matter Struct. Defec* **80**, 621-637 (2000)

[171] Keeble, Wicklein, Dittmann, Ravelli, Mackie and Eder, Identification of A- and B-site cation vacancy defects in perovskite oxide thin films, *Phys. Rev. Lett.* **105**, 226102/1-4 (2010)

[172] D. J. Keeble, R. A. Mackie, W. Egger, B. Loewe, P. Pikart, C. Hugenschmidt and T. J. Jackson, Identification of vacancy defects in a thin film perovskite oxide, *Physical Review B* **81**, 64102/1-5 (2010)

[173] Y. Fei, X. Zhu, L. Liu, H. Lu, Z. Chen and G. Yang, Oscillations in oblique-incidence optical reflection from a growth surface during layer-by-layer epitaxy, *Phys. Rev. B: Condens. Matter* **69**, 233405/1-4 (2004)

[174] X. D. Zhu, S. Wicklein, F. Gunkel, R. Xiao and R. Dittmann, In situ optical characterization of $LaAlO_3$ epitaxy on $SrTiO_3(001)$, *Europhys. Lett.* **109**, 37006/1-5 (2015)

[175] J. P. Landry, X. Wang, Y. Y. Fei and X. D. Zhu, Effective-substrate theory for optical reflection from a layered substrate, *J. Opt. Soc. Am. B-Opt. Phys.* **25**, 2021-2028 (2008)

[176] P. Thomas, E. Nabighian, M. Bartelt, C. Fong and X. Zhu, An oblique-incidence optical reflectivity difference and LEED study of rare-gas growth on a lattice-mismatched metal substrate, *Appl. Phys. A Mater. Sci. Process.* **79**, 131-137 (2004)

[177] C. M. Nelson, M. Spies, L. S. Abdallah, S. Zollner, Y. Xu and H. Luo, Dielectric function of $LaAlO_3$ from 0.8 to 6 eV between 77 and 700 K, *J. Vac. Sci. Technol. A* **30**, 61404/1-6 (2012)

[178] S. Zollner, A. Demkov, R. Liu, P. Fejes, R. Gregory, P. Alluri, J. Curless, Z. Yu, J. Ramdani, R. Droopad, T. Tiwald, J. Hilfiker and J. Woollam, Optical properties of bulk and thin-film $SrTiO_3$ on Si and Pt, *J. Vac. Sci. Technol. B* **18**, 2242-2254 (2000)

[179] K. van Benthem, C. Elsasser and R. H. French, Bulk electronic structure of $SrTiO_3$: Experiment and theory, *J. Appl. Phys.* **90**, 6156-6164 (2001)

[180] A. Dubroka, M. Roessle, K. W. Kim, V. K. Malik, L. Schultz, S. Thiel, C. W. Schneider, J. Mannhart, G. Herranz, O. Copie, M. Bibes, A. Barthelemy and C. Bernhard, Dynamical response and confinement of the electrons at the $LaAlO_3/SrTiO_3$ interface, *Phys. Rev. Lett.* **104**, 156807/1-4 (2010)

[181] A. Frye, R. French and D. Bonnell, Optical properties and electronic structure of oxidized and reduced single-crystal strontium titanate, *Z. Metallk.* **94**, 226-232 (2003)

[182] A. Dejneka, M. Tyunina, J. Narkilahti, J. Levoska, D. Chvostova, L. Jastrabik and V. A. Trepakov, Tensile strain induced changes in the optical spectra of $SrTiO_3$ epitaxial thin films, *Phys. Solid. State* **52**, 2082-2089 (2010)

[183] M. Melnichuk and L. T. Wood, Direct Kerr electro-optic effect in noncentrosymmetric materials, *Phys. Rev. A: At. Mol. Opt. Phys.* **82**, 13821/1-9 (2010)

[184] J. Lappalainen, J. Hiltunen and V. Lantto, Characterization of optical properties of nanocrystalline doped PZT thin films, *J. Eur. Ceram. Soc.* **25**, 2273-6 (2005)

[185] S. Lee, T. Noh and J. Lee, Control of epitaxial growth of pulsed laser deposited $LiNbO_3$ films and their electro-optic effects, *Appl. Phys. Lett.* **68**, 472-474 (1996)

[186] T. Graettinger, S. Rou, M. Ameen, O. Auciello and A. Kingon, Electrooptic Characterization Of Ion-Beam Sputter-Deposited $KNbO_3$ Thin-Films, *Appl. Phys. Lett.* **58**, 1964-1966 (1991)

[187] D. Y. Wang, J. Wang, H. L. W. Chan and C. L. Choy, Structural and electro-optic properties of $Ba_{0.7}Sr_{0.3}TiO_3$ thin films grown on various substrates using pulsed laser deposition, *J. Appl. Phys.* **101**, 43515/1-6 (2007)

[188] D. Kim and H. Kwok, Pulsed Laser Deposition of $BaTiO_3$ thin films and their optical properties, *Appl. Phys. Lett.* **67**, 1803-1805 (1995)

[189] M. Stengel and D. Vanderbilt, Berry-phase theory of polar discontinuities at oxide-oxide interfaces, *Phys. Rev. B: Condens. Matter* **80**, 241103/1-4 (2009)

[190] C. Katsidis and D. Siapkas, General transfer-matrix method for optical multilayer systems with coherent, partially coherent, and incoherent interference, *Appl. Optics* **41**, 3978-3987 (2002)

[191] E. Schneider, P. Cressman and R. Holman, Temperature dependence of the refractive index of strontium-titanate and prism coupling to lithium-niobate optical waveguides, *J. Appl. Phys.* **53**, 4054-4056 (1982)

[192] F. W. Lytle, X-ray diffractometry of low-temperature phase transformations in strontium titanate, *J. Appl. Phys.* **35**, 2212-2214 (1964)

[193] B. Chakoumakos, D. Schlom, M. Urbanik and J. Luine, Thermal expansion of $LaAlO_3$ and $(La,Sr)(Al,Ta)O_3$, substrate materials for superconducting thin-film device applications, *J. Appl. Phys.* **83**, 1979-1982 (1998)

[194] M. Schmidbauer, A. Kwasniewski and J. Schwarzkopf, High-precision absolute lattice parameter determination of $SrTiO_3$, $DyScO_3$ and $NdGaO_3$ single crystals, *Acta Crystallogr. Sect. B-Struct. Sci.Cryst. Eng.* **68**, 8-14 (2012)

[195] G. Berner, S. Glawion, J. Walde, F. Pfaff, H. Hollmark, L. Duda, S. Paetel, C. Richter, J. Mannhart, M. Sing and R. Claessen, $LaAlO_3/SrTiO_3$ oxide heterostructures studied by resonant inelastic X-ray scattering, *Phys. Rev. B: Condens. Matter* **82**, 241405/1-4 (2010)

[196] Y. Xie, Y. Hikita, C. Bell and H. Y. Hwang, Control of electronic conduction at an oxide heterointerface using surface polar adsorbates, *Nat. Commun.* **2**, 494/1-5 (2011)

[197] A. Kalabukhov, R. Gunnarsson, J. Borjesson, E. Olsson, T. Claeson and D. Winkler, Effect of oxygen vacancies in the $SrTiO_3$ substrate on the electrical properties of the $LaAlO_3/SrTiO_3$ interface, *Phys. Rev. B* **75**, 121404/1-4 (2007)

[198] G. Herranz, M. Basletic, M. Bibes, C. Carretero, E. Tafra, E. Jacquet, K. Bouzehouane, C. Deranlot, A. Hamzic, J. M. Broto, A. Barthelemy and A. Fert, High mobility in $LaAlO_3/SrTiO_3$ heterostructures: Origin, dimensionality, and perspectives, *Phys. Rev. Lett.* **98**, 216803/1-4 (2007)

[199] Chencheng Xu, Christoph Baeumer, Ronja A. Heinen, Susanne E. Hoffmann, Felix Gunkel and Regina Dittmann, Disentanglement of growth dynamic and thermodynamic effects in $LaAlO_3/SrTiO_3$ heterostructures, *Sci. Rep.* **6**, 1-9 (2016)

[200] H. N. Lee, S. S. A. Seo, W. S. Choi and C. M. Rouleau, Growth control of oxygen stoichiometry in homoepitaxial $SrTiO_3$ films by pulsed laser epitaxy in high vacuum, *Sci. Rep.* **6**, 19941/1-7 (2016)

[201] G. Herranz, O. Copie, A. Gentils, E. Tafra, M. Basletic, F. Fortuna, K. Bouzehouane, S. Fusil, E. Jacquet, C. Carretero, M. Bibes, A. Hamzic and A. Barthelemy, Vacancy defect and carrier distributions in the high mobility electron gas formed at ion-irradiated $SrTiO_3$ surfaces, *J. Appl. Phys.* **107**, 103704/1-5 (2010)

[202] M. E. Zvanut, S. Jeddy, E. Towett, G. M. Janowski, C. Brooks and D. Schlom, An annealing study of an oxygen vacancy related defect in $SrTiO_3$ substrates, *J. Appl. Phys.* **104**, 64122/1-5 (2008)

[203] J. S. Yoon, M. Y. Song, J. M. Han, S. H. Hwang, W. S. Chang, B. Lee and Y. Itikawa, Cross sections for electron collisions with hydrogen molecules, *J. Phys. Chem. Ref. Data* **37**, 913-931 (2008)

[204] Y. Itikawa and N. Mason, Cross sections for electron collisions with water molecules, *J. Phys. Chem. Ref. Data* **34**, 1-22 (2005)

[205] Y. Itikawa, Cross sections for electron collisions with carbon dioxide, *J. Phys. Chem. Ref. Data* **31**, 749-767 (2002)

[206] R. A. De Souza, V. Metlenko, D. Park and T. E. Weirich, Behavior of oxygen vacancies in single-crystal $SrTiO_3$: Equilibrium distribution and diffusion kinetics, *Phys. Rev. B: Condens. Matter* **85**, 174109/1-11 (2012)

[207] A. Gentils, O. Copie, G. Herranz, F. Fortuna, M. Bibes, K. Bouzehouane, E. Jacquet, C. Carretero, M. Basletic, E. Tafra, A. Hamzic and A. Barthelemy, Point defect distribution in high-mobility conductive $SrTiO_3$ crystals, *Phys. Rev. B* **81**, 144109/1-9 (2010)

[208] T. Hara, T. Ishiguro and K. Shinozaki, Ultraviolet-light-induced desorption of oxygen from $SrTiO_3$ surfaces, *Jpn. J. Appl. Phys.* **50**, 41502/1-6 (2011)

[209] R. Merkle and J. Maier, How is oxygen incorporated into oxides? A comprehensive kinetic study of a simple solid-state reaction with $SrTiO_3$ as a model material, *Angew. Chem.-Int. Edit.* **47**, 3874-3894 (2008)

[210] R. Merkle and J. Maier, Oxygen incorporation into Fe-doped $SrTiO_3$: Mechanistic interpretation of surface reaction, *Phys. Chem. Chem. Phys.* **4**, 4140-4148 (2002)

[211] Y. Chen, N. Pryds, J. E. Kleibeuker, G. Koster, J. Sun, E. Stamate, B. Shen, G. Rijnders and S. Linderoth, Metallic and insulating interfaces of amorphous $SrTiO_3$-based oxide heterostructures, *Nano Letters* **11**, 3774-3778 (2011)

[212] Y. Z. Chen, N. Bovet, F. Trier, D. V. Christensen, F. M. Qu, N. H. Andersen, T. Kasama, W. Zhang, R. Giraud, J. Dufouleur, T. S. Jespersen, J. R. Sun, A. Smith, J. Nygard, L. Lu, B. Buechner, B. G. Shen, S. Linderoth and N. Pryds, A high-mobility two-dimensional electron gas at the spinel/perovskite interface of gamma-Al_2O_3/$SrTiO_3$, *Nat. Commun.* **4**, 1371/1-6 (2013)

[213] R. Waser, Bulk conductivity and defect chemistry of acceptor-doped strontium titanate in the quenched state, *J. Am. Ceram. Soc.* **74**, 1934-40 (1991)

[214] M. Leonhardt, R. A. De Souza, J. Claus and J. Maier, Surface kinetics of oxygen incorporation into $SrTiO_3$, *J. Electrochem. Soc.* **149**, J19-J26 (2002)

[215] M. L. Scullin, J. Ravichandran, C. Yu, M. Huijben, J. Seidel, A. Majumdar and R. Ramesh, Pulsed laser deposition-induced reduction of $SrTiO_3$ crystals, *Acta Mater.* **58**, 457-463 (2010)

Appendix

Programming code in MatLab 2013a with transition matrix method for the simulation of OIRD signals

```
N_LAO=9;
N_STO=1;
Sub_Critical_thickness=2;
Epsillon_LAO=(2.2)^2;
Epsillon_STO=(2.41)^2;
Epsillon_air=1;
Phi_inc=82.8*pi/180;
Epsillon_total=[Epsillon_air;Epsillon_air*ones(N_LAO,1);Epsillon_STO*ones(N_STO+3,1)];
Elementary_reflectivity_s=zeros(N_LAO+N_STO+1,1);
Elementary_reflectivity_p=zeros(N_LAO+N_STO+1,1);
Wave_vector=2*pi/632.8;
LAO_layer_thickness=0.3789;
STO_layer_thickness=0.3905;
Layer_thickness=[0;zeros(N_LAO,1);STO_layer_thickness*ones(N_STO,1)];

Transmission_matrix_s=zeros(2,2,N_LAO+N_STO+1);
Transmission_matrix_s(1:2*2:end)=1;
Transmission_matrix_s(4:2*2:end)=1;
Transmission_matrix_p=zeros(2,2,N_LAO+N_STO+1);
Transmission_matrix_p(1:2*2:end)=1;
Transmission_matrix_p(4:2*2:end)=1;
Total_transmission_matrix_s=eye(2);
Total_transmission_matrix_s1=eye(2);
Total_transmission_matrix_p=eye(2);
Total_transmission_matrix_p1=eye(2);
Field_vector_s=zeros(2,1);
Field_vector_p=zeros(2,1);

Complex_total_reflectivity_s=zeros(N_LAO,1);
Complex_total_reflectivity_s(1,1)=1;
Complex_total_reflectivity_p=zeros(N_LAO,1);
Complex_total_reflectivity_p(1,1)=1;
Complex_reflectance_ratio_s=zeros(N_LAO,1);
Complex_reflectance_ratio_s(1,1)=1;
```

```
%ratio between the reflactance and the initial value%
Complex_reflectance_ratio_p=zeros(N_LAO,1);
Complex_reflectance_ratio_p(1,1)=1;
Reflectance_ratio_s=zeros(N_LAO,1);
Reflectance_ratio_p=zeros(N_LAO,1);
Real_reflectance_ratio_difference=zeros(N_LAO,1);
Imag_reflectance_ratio_difference=zeros(N_LAO,1);
Epsillon_Lao=zeros(N_LAO,1);
Elementary_reflectivity_second_layer_p=zeros(N_LAO+N_STO+1,1);
Elementary_reflectivity_second_layer_s=zeros(N_LAO+N_STO+1,1);
Time=zeros(N_LAO,1);



for j=0:(N_LAO-1)

    Time(j+1,1)=j;
    Epsillon_total(N_LAO+1-j,1)=(Epsillon_LAO+0.8)-0.8*(j>=Sub_Critical_thickness);
    Epsillon_Lao(j+1)=Epsillon_LAO-Epsillon_total(N_LAO+1-j,1);
    Layer_thickness(N_LAO+1-j,1)=(LAO_layer_thickness*1.02)...
             -LAO_layer_thickness*0.02*(j>=Sub_Critical_thickness);
    Layer_thickness_show=rot90(Layer_thickness(2:N_LAO+1,1),2);

    for k=1:N_STO

       Epsillon_total(N_LAO+N_STO-k+2,1)=Epsillon_STO;
    end



    Elementary_reflectivity_s(N_LAO+1-j,1)=(((Epsillon_total(N_LAO+2-j,1))-…
      (Epsillon_air*(sin(Phi_inc)^2)))^0.5...
      -((Epsillon_total(N_LAO+1-j,1))-(Epsillon_air*(sin(Phi_inc)^2)))^0.5)...
      /(((Epsillon_total(N_LAO+2-j,1))-(Epsillon_air*(sin(Phi_inc)^2)))^0.5...
      +(((Epsillon_total(N_LAO+1-j,1))-(Epsillon_air*(sin(Phi_inc)^2)))^0.5));
   Elementary_reflectivity_s(N_LAO-j,1)=(((Epsillon_total(N_LAO+1-j,1))-…
      (Epsillon_air*(sin(Phi_inc)^2)))^0.5...
      -((Epsillon_total(N_LAO-j,1))-(Epsillon_air*(sin(Phi_inc)^2)))^0.5)...
      /(((Epsillon_total(N_LAO+1-j,1))-(Epsillon_air*(sin(Phi_inc)^2)))^0.5...
      +(((Epsillon_total(N_LAO-j,1))-(Epsillon_air*(sin(Phi_inc)^2)))^0.5));

   Elementary_reflectivity_p(N_LAO+1-j,1)=(Epsillon_total(N_LAO+1-j,1)…
      *(Epsillon_total(N_LAO+2-j,1)-Epsillon_air*(sin(Phi_inc)^2))^0.5...
      -Epsillon_total(N_LAO+2-j,1)*(Epsillon_total(N_LAO+1-j,1)-Epsillon_air*(sin(Phi_inc)^2))^0.5)...
```

```
    /(Epsillon_total(N_LAO+1-j,1)*(Epsillon_total(N_LAO+2-j,1)-Epsillon_air*(sin(Phi_inc)^2))^0.5...
    +Epsillon_total(N_LAO+2-j,1)*(Epsillon_total(N_LAO+1-j,1)-Epsillon_air*(sin(Phi_inc)^2))^0.5);
  Elementary_reflectivity_p(N_LAO-j,1)=(Epsillon_total(N_LAO-j,1)…
    *(Epsillon_total(N_LAO+1-j,1)-Epsillon_air*(sin(Phi_inc)^2))^0.5...
    -Epsillon_total(N_LAO+1-j,1)*(Epsillon_total(N_LAO-j,1)-Epsillon_air*(sin(Phi_inc)^2))^0.5)...
    /(Epsillon_total(N_LAO-j,1)*(Epsillon_total(N_LAO+1-j,1)-Epsillon_air*(sin(Phi_inc)^2))^0.5...
    +Epsillon_total(N_LAO+1-j,1)*(Epsillon_total(N_LAO-j,1)-Epsillon_air*(sin(Phi_inc)^2))^0.5);
  for g=1:N_STO
   Elementary_reflectivity_s(N_LAO+N_STO+2-g,1)=(((Epsillon_total(N_LAO+N_STO+3-g,1))…
     -(Epsillon_air*(sin(Phi_inc)^2)))^0.5...
     -((Epsillon_total(N_LAO+N_STO+2-g,1))-(Epsillon_air*(sin(Phi_inc)^2)))^0.5)...
     /(((Epsillon_total(N_LAO+N_STO+3-g,1))-(Epsillon_air*(sin(Phi_inc)^2)))^0.5...
     +(((Epsillon_total(N_LAO+N_STO+2-g,1))-(Epsillon_air*(sin(Phi_inc)^2)))^0.5));
   Elementary_reflectivity_p(N_LAO+N_STO+2-g,1)=(Epsillon_total(N_LAO+N_STO+2-g,1)…
     *(Epsillon_total(N_LAO+N_STO+3-g,1)-Epsillon_air*(sin(Phi_inc)^2))^0.5...
     -Epsillon_total(N_LAO+N_STO+3-g,1)*(Epsillon_total(N_LAO+N_STO+2-g,1)-
Epsillon_air*(sin(Phi_inc)^2))^0.5)...
     /(Epsillon_total(N_LAO+N_STO+2-g,1)*(Epsillon_total(N_LAO+N_STO+3-g,1)-
Epsillon_air*(sin(Phi_inc)^2))^0.5...
     +Epsillon_total(N_LAO+N_STO+3-g,1)*(Epsillon_total(N_LAO+N_STO+2-g,1)-
Epsillon_air*(sin(Phi_inc)^2))^0.5);
  end

          Transmission_matrix_s(1:2,1:2,(N_LAO-j+1))=[1,...
          Elementary_reflectivity_s(N_LAO-j+1,1)*exp(-2i*Wave_vector*Layer_thickness…
          (N_LAO-j+1));...
          Elementary_reflectivity_s(N_LAO-j+1,1),...
          exp(-2i*Wave_vector*Layer_thickness(N_LAO-j+1))]
          Transmission_matrix_p(1:2,1:2,(N_LAO-j+1))=[1,...
          Elementary_reflectivity_p(N_LAO-j+1,1)…
          *exp(-2i*Wave_vector*Layer_thickness(N_LAO-j+1));...
          Elementary_reflectivity_p(N_LAO-j+1,1),...
          exp(-2i*Wave_vector*Layer_thickness(N_LAO-j+1))];
          Transmission_matrix_s(1:2,1:2,(N_LAO-j))=[1,...
          Elementary_reflectivity_s(N_LAO-j,1)*exp(-2i*Wave_vector*Layer_thickness(N_LAO-j));...
          Elementary_reflectivity_s(N_LAO-j,1),...
          exp(-2i*Wave_vector*Layer_thickness(N_LAO-j))]
          Transmission_matrix_p(1:2,1:2,(N_LAO-j))=[1,...
          Elementary_reflectivity_p(N_LAO-j,1)*exp(-2i*Wave_vector*Layer_thickness(N_LAO-j));...
          Elementary_reflectivity_p(N_LAO-j,1),...
          exp(-2i*Wave_vector*Layer_thickness(N_LAO-j))];

      for b=1:N_STO
```

```
    Transmission_matrix_s(1:2,1:2,(N_LAO+N_STO-b+2))=[1,...
     Elementary_reflectivity_s(N_LAO+N_STO-b+2,1)*exp(-
     …2i*Wave_vector*Layer_thickness(N_LAO+N_STO-b+2));...
     Elementary_reflectivity_s(N_LAO+N_STO-b+2,1),...
     exp(-2i*Wave_vector*Layer_thickness(N_LAO+N_STO-b+2))];
    Transmission_matrix_p(1:2,1:2,(N_LAO+N_STO-b+2))=[1,...
     Elementary_reflectivity_p(N_LAO+N_STO-b+2,1)*exp(-…
     2i*Wave_vector*Layer_thickness(N_LAO+N_STO-b+2));...
     Elementary_reflectivity_p(N_LAO+N_STO-b+2,1),...
     exp(-2i*Wave_vector*Layer_thickness(N_LAO+N_STO-b+2))];
 end


for g=1:(j+N_STO+2)
Total_transmission_matrix_s=Transmission_matrix_s(:,:,(N_LAO+N_STO+2-g))*…
Total_transmission_matrix_s;
Total_transmission_matrix_p=Transmission_matrix_p(:,:,(N_LAO+N_STO+2-g))*
…Total_transmission_matrix_p;
end
Total_transmission_matrix_s1=Total_transmission_matrix_s;
Total_transmission_matrix_p1=Total_transmission_matrix_p;
Total_transmission_matrix_s1;
Total_transmission_matrix_p1;

Field_vector_s=Total_transmission_matrix_s1*[1,1]';
Complex_total_reflectivity_s(j+1,1)=Field_vector_s(2,1)/Field_vector_s(1,1);

Complex_reflectance_ratio_s(j+1,1)=Complex_total_reflectivity_s(j+1,1)/Complex_total_reflectivity
_s(1,1);
Reflectance_ratio_s(j+1,1)=real(Complex_reflectance_ratio_s(j+1,1));
Field_vector_p=Total_transmission_matrix_p1*[1,1]';
Complex_total_reflectivity_p(j+1,1)=Field_vector_p(2,1)/Field_vector_p(1,1);

Complex_reflectance_ratio_p(j+1,1)=Complex_total_reflectivity_p(j+1,1)/Complex_total_reflectivit
y_p(1,1);
Reflectance_ratio_p(j+1,1)=(real(Complex_reflectance_ratio_p(j+1,1)));
Real_reflectance_ratio_difference(j+1,1)= - real(-…
Complex_reflectance_ratio_p(j+1,1)+Complex_reflectance_ratio_s(j+1,1));
Imag_reflectance_ratio_difference(j+1,1)= - imag(-…
Complex_reflectance_ratio_p(j+1,1)+Complex_reflectance_ratio_s(j+1,1));
```

The Real_reflectance_ratio_difference is the Re(Δ_p-Δ_s), while Imag_reflectance_ratio_difference is the Im(Δ_p-Δ_s).

Band / Volume 127
**Dynamics in colloid and protein systems:
Hydrodynamically structured particles, and dispersions with competing attractive and repulsive interactions**
J. Riest (2016), ix, 226 pp
ISBN: 978-3-95806-153-8

Band / Volume 128
Self-purifying $La_{2/3}Sr_{1/3}MnO_3$ epitaxial films: Observation of surface precipitation of Mn_3O_4 particles for excess Mn ratios
A. Steffen (2016), 154 pp
ISBN: 978-3-95806-162-0

Band / Volume 129
Strain and electric field mediated manipulation of magnetism in $La_{(1-x)}Sr_xMnO_3/BaTiO_3$ heterostructures
M. Schmitz (2016), VI, 141 pp
ISBN: 978-3-95806-164-4

Band / Volume 130
High-Throughput Live-Cell Imaging for Investigations of Cellular Heterogeneity in *Corynebacterium glutamicum*
S. Helfrich (2016), xvi, 217 pp
ISBN: 978-3-95806-167-5

Band / Volume 131
Laser-Induced Ultrafast Electron- and Spin-Dynamics in the Electronic Band Structure of Co(001)
M. A. Plötzing (2016), ii, 109, XXXIV pp
ISBN: 978-3-95806-168-2

Band / Volume 132
Robot-Assisted Phenotyping of Genome-Reduced *Corynebacterium glutamicum* Strain Libraries to Draft a Chassis Organism
S. Unthan (2016), 122 pp
ISBN: 978-3-95806-169-9

Band / Volume 133
Characterization of amino acid ammonia lyases & aminomutases for the production of chiral α- and β-amino acids
A. Dreßen (2016), ix, 112 pp
ISBN: 978-3-95806-176-7

Band/Volume 134
7th Georgian-German School and Workshop in Basic Science
Kacharava, A. (Ed.) erscheint nur als CD (2016)
ISBN 978-3-95806-179-8

Band / Volume 135
Crystal growth and scattering studies on two ferrites
S. Adiga (2016), iv, 150 pp
ISBN: 978-3-95806-183-5

Band / Volume 136
Manipulating the Structural and Electronic Properties of Epitaxial $NaNbO_3$ Films via Strain and Stoichiometry
B. Cai (2016), VI, 114 pp
ISBN: 978-3-95806-185-9

Band / Volume 137
Surface Potential of Metallic Surfaces and Self-Assembling Organic Monolayers in Various Electrolytes
J. Wang (2016), ii, 58 pp
ISBN: 978-3-95806-188-0

Band / Volume 138
Ab initio investigation of hybrid molecular-metallic interfaces as a tool to design surface magnetic properties for molecular spintronics
R. Friedrich (2016), 277 pp
ISBN: 978-3-95806-194-1

Band / Volume 139
Topological Matter – Topological Insulators, Skyrmions and Majoranas
Lecture Notes of the 48th IFF Spring School 2017
27 March – 07 April 2017, Jülich, Germany
ed. by S. Blügel, Y. Mokrousov, T. Schäpers, Y. Ando (2017), ca 1000 pp
ISBN: 978-3-95806-202-3

Band / Volume 140
In situ studies of the growth and oxidation of complex metal oxides by pulsed laser deposition
C. Xu (2016), iv, 159 pp
ISBN: 978-3-95806-204-7

Weitere ***Schriften des Verlags im Forschungszentrum Jülich*** unter
http://wwwzb1.fz-juelich.de/verlagextern1/index.asp

Schlüsseltechnologien / Key Technologies
Band / Volume 140
ISBN 978-3-95806-204-7

JÜLICH
FORSCHUNGSZENTRUM